Exposed Ocean Crust on Masirah Island, SE Oman:

Crustal Accretion and Melt Evolution at an Ancient Slow-Spreading Mid-Ocean Ridge

Max N. Jansen

School of Earth and Environmental Sciences

Cardiff University

Submitted in partial fulfilment of the requirements for the degree of

Doctor of Philosophy

February 2023

"Wat is wetenschap? Wetenschap is de titanische poging van het menselijk intellect zich uit zijn kosmische isolement te verlossen door te begrijpen![1]"

Willem Frederik Hermans, Nooit meer slapen

"Wetenschap is pixels verplaatsen[2]"

Jeroen van der Lubbe

[1] What is science? Science is the titanic attempt of the human intellect to redeem themselves from their cosmic isolation through understanding!
[2] Science is moving pixels

Declaration

This work has not been submitted in substance for any other degree or award at this or any other university or place of learning, nor is being submitted concurrently in candidature for any degree or other award.

Statement 1

This thesis is being submitted in partial fulfilment of the requirements for the degree of PhD.

Statement 2

This thesis is the result of my own independent work/investigation, except where otherwise stated, and the thesis has not been edited by a third party beyond what is permitted by Cardiff University's Policy on the Use of Third Party Editors by Research Degree Students. Other sources are acknowledged by explicit references. The views expressed are my own.

Statement 3

I hereby give consent for my thesis, if accepted, to be available online in the University's Open Access repository and for inter-library loan, and for the title and summary to be made available to outside organisations.

Abstract

The accretion of oceanic crust at mid-oceanic ridges (MOR) accounts for the most voluminous magmatism on Earth and occurs across a range of spreading-rates. Slow-spreading ridges represent 50% of the present-day global MOR-system and produce heterogeneous oceanic crust that deviates fundamentally from the conventional 6 – 7 km layer-cake Penrose-crust formed at fast-spreading ridges. Instead, the sparse and intermittent magmatism at slow-spreading ridges requires plate separation to be partly accommodated by faulting, producing ocean lithosphere with a discontinuous igneous crust of variable thickness, commonly disrupted by large 'detachment' faults that exhume the deep crust and shallow mantle directly onto the seafloor. Due to the difficulty in accessing oceanic crust in situ, our knowledge of the processes occurring at MORs is still relatively limited and geologists often turn to ophiolites as their analogues. There is however an increasing awareness of a preservation bias towards ocean lithosphere formed at atypical spreading ridges, such as marginal ocean basins near subduction zones, and that potentially key differences between many ophiolites and 'true' MOR ocean lithosphere (especially in their chemical composition) complicate direct comparisons.

The Masirah Ophiolite, exposed over ~650 km^2 on an isolated island off the southeast coast of the Sultanate of Oman, is near-unique in that it is believed to have formed at a 'true' MOR, unaffected by the influence of subduction. It can therefore provide valuable geological insights into crustal accretion process along modern MORs. Although its basic structure was mapped the 1990s, previous studies did not examine Masirah from the perspective of modern MOR processes in any detail. Previous work determined that Masirah formed at a slow-spreading ridge in the young Indian Ocean at ~150 Ma, followed by an episode of alkaline magmatism during intraplate rifting some 20 Ma later, before being emplaced onto the Arabian continental margin in the late Cretaceous.

The work presented in this thesis updates the geochronological model for the evolution of Masirah, describes a previously unrecognised type of ocean lithospheric architecture ('Penrose on a diet') that accreted at the paleo-spreading ridge, and investigates what mantle processes might be responsible for this style of accretion. In a key finding, new radiometric dates show that the ophiolite formed at 135 – 130 Ma, and that the alkaline magmatic activity overlapped with crustal accretion as an episode of 'near-axis' magmatism. Trace element compositions of the two magmatic suites show a large degree of overlap and define a continuum, supporting a transitional event where magmas, derived by variable degrees of melting of a heterogeneous mantle source, were initially delivered to the ridge axis, whereupon subsequent melts, derived from continued lower-degree melting of a more enriched mantle component, were delivered near off-axis.

The ‘Penrose on a diet architecture’ of the Masirah lithosphere is noteworthy for having a thin igneous crust (2 km) and a thin lower crust with respect to the upper crust (lower crust : upper crust = ~0.4 : 0.6). Despite these characteristics suggesting a low melt supply, field relations nevertheless indicate the crust formed by magmatic spreading. This contradicts current crustal accretion models, which predict the formation of 6 – 7 km thick crust for conditions of high melt supply and spreading dominated by detachment faulting when melt supply is low. The Masirah Ophiolite shows that the variability of permissible slow-spreading crustal geometries is greater than previously thought and that a basaltic seafloor should not automatically be interpreted to correlate with a thick magmatic crust.

The mantle section exposed on Masirah is characterised by highly refractory peridotites with a mineral chemistry indicating high degrees of melting, despite the overlying igneous crust being thin. By considering the effect of mantle fertility on the overall melt production, a model is advanced where upwelling of an ancient domain of depleted mantle led to an overall reduced melt supply and a high proportion of melts from fertile mantle components relative to those from the depleted peridotites. Consequently, observations from Masirah suggest that besides rates of upwelling and seafloor spreading, the time-integrated melting history of the mantle underneath modern MORs exercises an important control on the degree of mantle melting, as well as the resulting lithospheric architecture and compositions of the erupted mid-ocean ridge basalts.

Acknowledgements

First and foremost, many thanks go out to my supervisors Chris MacLeod, Johan Lissenberg and Ian Parkinson, for encouraging me to apply to the project and guiding me throughout this journey over the few past years. Thank you for sharing your expertise and continuously challenging me to question everything. Mohamed Alaraimi, Said Almusharafi and Ibrahim Alsawafi from the Oman Public Authority of Mining are thanked for facilitating the fieldwork in Oman, and Benoit Cordonnier and Chris Tulley are thanked for their help in the field. This PhD project was funded by the Natural Environmental Research Council GW4+ Doctoral Training Partnership (NE/L002434/1) and zircon U-Pb analyses were funded by the NERC Isotope Geosciences Facilities Steering Committee (grant IP-1919-0619).

Much of this work would not have been possible without the excellent facilities that were available to me, and for this I wish to thank Tony Oldroyd (for thin-section preparation), Duncan Muir (for his help with SEM analyses), Iain McDonald (for his help with pXRF analyses), Tony Morris and Louise Koorneeff (for their help with sample preparation and AMS analyses at the University of Plymouth), Diana Sahy and Dan Condon (for their help with zircon mineral separation and U-Pb isotope analyses at the BGS facilities), Nick Dygert (for running LA-ICP-MS analyses on peridotite pyroxenes at the University of Tennessee and the University of Texas, Austin) and Mareli Grobbelaar-Moolman and Riana Rossouw (for running whole-rock major and trace element analyses at the Central Analytical Facilities of Stellenbosch University). Many thanks go out to the staff in the School of Earth and Environmental Sciences at Cardiff University, from the technical and admin staff to the academics, for their continuous outstanding work despite the setbacks posed by a senior management and Westminster government that is set on increasing workloads, cutting pensions and further marketizing higher education. When the Covid-19 pandemic hit, you were the ones that kept things going. I'd like to make a special mention of Emmi Palk of the GW4+ DTP, whose tireless support to the PhD community during the pandemic helped us immensely at a time when we felt all but forgotten.

For parts of this project, I worked with Rengin Ozgoy and Louis McCarthan, two enthusiastic and highly motivated undergraduate students who were looking for extracurricular projects during their degree. Rengin greatly helped with sample preparations and petrography descriptions, and Louis played a significant role in analysing and interpreting the mantle Cr-spinel compositions. Both of you were highly motivated and I thoroughly enjoyed working with you!

I'd also like to thank the many people I had the pleasure of meeting and working with during the OmanDP project, both on the drill site and aboard the Chikyu, as well as the 'post-cruise' conference.

Besides being good fun, the thought-provoking discussions I had during my participation in that project played an important part in shaping my own ideas and helped me place my research into the broader context of ocean geology. Special thanks to Jude Coggon for encouraging me to apply and for her role in the amazing organisation of OmanDP that facilitated this process.

Special thanks are extended to the former participants of the Swiss mapping campaign, especially Edwin Gnos and Adrian Immenhauser, who were very helpful in discussing the previous work on Masirah and generously shared their unpublished data. Additional thanks to Ronny Schoenberg, Igor Villa, Jan Kramers, Robert Frei and Thomas Nägler, for helping me track down the details of their original expedition, which was not always easy, since, in the words of one participant, “a great number of waves have been washed up Masirah Island's beaches and rocky shores since we left this part of the world and compiled and published the data you refer to”. The help you provided was of immeasurable value when it came to making sense of my own data and developing an updated model for Masirah. With regards to the latter, I stand by another pertinent remark of a former member of the Swiss team: “Despite the fact that we spent months and months on this island and mapped every square meter, I do not doubt that Masirah hides many secrets to the present day. I recall the well-established ophiolite aficionados never liked the Masirah ophiolite. Too much complexity, not in agreement with the textbook ophiolites.”

During my years in Cardiff I had many people who I could turn to for friendship, advice, coffee, boardgames, T-Ball, intense discussions, bike rides, fossil hunts, mushroom foraging, culinary adventures and other extracurricular activities. Aidan, Liam, Jaz, Harry, James, Will, Phil, Jeroen, Martijn, Caps, Nat, Chris, Sophie, Evie, Roberto, Emanuela, Adam, George, the Brodies team, and many other, you made all this worthwhile, thank you for being there when I needed you most!

Lastly, thanks to my family for always encouraging my curiosity and introducing me to Oman many years ago, which were the first steps of the path that eventually would take me here. And thank you Deremyre for your endless love, support and patience along the way.

Thanks guys!

Table of contents

Table of figures

List of tables

Supplementary tables in appended excel file

1. Introduction

Hidden in the depths of the ocean is the longest mountain chain in existence on Earth: the mid-ocean ridge (MOR) system. Located at divergent plate boundaries, they form as the result of tectonic plates being pulled apart, in the process producing the largest volumetric flux of magmatism on the present-day Earth and continuously repaving two-thirds of the surface of the planet at an approximately 200 Ma timescale. The processes of ocean crustal accretion and the resulting architecture of the oceanic lithosphere taking place at MORs occur at a range of spreading-rates and have first-order consequences for chemical fluxes between the Earth's interior and the oceans and atmosphere, with implications for mantle heterogeneity, ocean chemistry and Earth's climate. As important as MORs are for our understanding of Earth's geodynamics, scientific research is impeded by the complications involved in accessing the ocean floor and subsurface. Direct observations are limited to bathymetric and geophysical surveys and the dredging of samples from the seafloor, supplemented with samples obtained through ocean drilling under the International Ocean Discovery Programme (IODP, 2013-Present) and its precursors in the form of the Integrated Ocean Drilling Program (IODP, 2003-2013), Oceanic Drilling Project (ODP, 1983-2003) and Deep Sea Drilling Project (DSDP, 1966-1983).

Ocean geology research over the previous decades has established that slower spreading ridges (< 40 mm/yr full spreading rate), representing 50% of the present-day global MOR-system, produce a heterogeneous igneous oceanic crust that deviates fundamentally from the conventional layer-cake crust formed at faster spreading ridges (>80 mm/yr). Instead, the sparse and intermittent magmatism at slow-spreading ridges requires plate separation to be partly accommodated by faulting, producing ocean lithosphere with a discontinuous igneous crust of variable thickness, commonly disrupted by large 'detachment' faults that exhume the deep crust and shallow mantle directly onto the seafloor. Reconstructing the interplay of mantle melting, melt transport and differentiation and tectonic stretching from seafloor observations remains challenging, however, and as a result our understanding remains relatively limited.

For this reason, geologists have historically turned to ophiolites, fragments of oceanic lithosphere that have been emplaced onto the continent, as analogues for modern oceanic crust. Since their recognition as having formed by seafloor spreading, ophiolites have played a pivotal role in models for the formation of oceanic lithosphere at MORs. There is however an increasing awareness of a preservation bias towards ocean lithosphere formed at atypical spreading ridges, such as marginal ocean basins near subduction zones. Direct comparisons are hence complicated by potentially key differences between many ophiolites and 'true' MOR ocean lithosphere, especially in their chemical

composition. A notable exception is the Masirah ophiolite, exposed on an island off the south-eastern coast of Oman, which is thought to represent a fragment of early, slow-spreading Indian Ocean crust (Peters, 2000). As a 'true' MOR ophiolite, it offers a unique opportunity to test current models of seafloor spreading.

This thesis presents an investigation into the geology of Masirah from a mid-ocean ridge perspective. The introductory chapter starts with an overview of the mid-ocean ridge system and our current understanding of slow-spreading oceanic lithosphere, followed by a discussion of how and to what extent ophiolites may serve as their analogues. Subsequently the Masirah ophiolite is introduced, along with the research aims and rationale of this PhD thesis. Finally, the structure of the rest of the thesis is laid out.

1.1 The global Mid-Ocean Ridge system

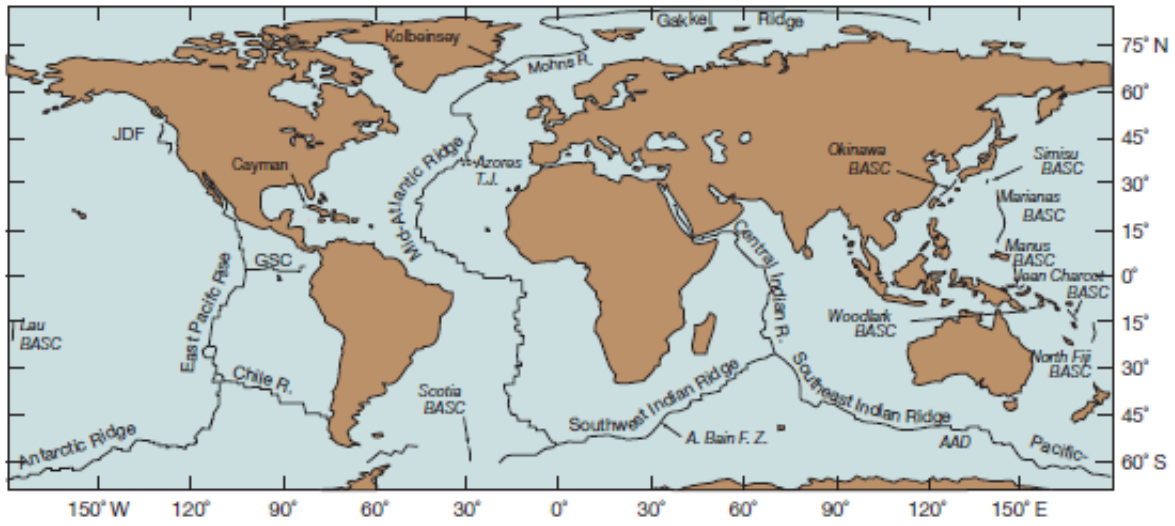

***Figure 1.1**: Map of the mid-ocean ridge system (from White and Klein, 2014).*

1.1.1 Seafloor spreading rates

At a total length of approximately 65 000 km, the mid-oceanic ridge system spans all major oceanic basins and accommodates the bulk of seafloor spreading (Figure 1.1). Early ideas of oceanic lithosphere envisaged an upwelling peridotite mantle underneath MORs that underwent serpentinisation at the ocean floor due to interaction with seawater (Hess, 1962). The recovery of basaltic rocks, rather than serpentinite, from large portions of the ocean floor, however, led to the realisation that most of the ocean basins have a mafic igneous crust that forms at MORs. As mantle material rises and decompresses underneath the ridge, it undergoes polybaric (with mean pressures of 5 – 16 kbar) near-adiabatic partial melting (~8 – 20%), resulting in the formation of an igneous oceanic crust (Klein and Langmuir, 1987). To a first approximation, the variations in the amount of melt produced, the heat budget of the axial lithosphere, the type of crust formed, and the resulting

ridge morphology correlate with the velocity at which the plates are being pulled apart. Hence, MORs are classified as fast (80 – 200 mm/yr full spreading rate), intermediate (40 – 80 mm/yr), slow (20 – 40 mm/yr) and ultraslow-spreading (<20 mm/yr), with some authors including a superfast class (>150 mm/yr, Hey et al., 1985) and a slow-ultraslow transition class (10 – 20 mm/yr, Dick et al., 2003).

1.1.1.1 Ridge-axis morphology

Major differences in axial ridge morphology (Figure 1.2) result from an interplay between tectonic stretching of the lithosphere and the lithosphere rheology, determined by its heat structure (e.g., Chen and Morgan, 1990). Fast-spreading ridges typically have high magma fluxes resulting in a hot system and a thin and weak lithosphere, with deformation taking place in the ductile regime. This results in an elongate, 8 – 10 km wide axial high that typically rises 200 – 400 m above the seafloor and has a smooth topography (Macdonald et al., 1984). Along the crest, a narrow axial summit trough of a few tens of meters deep is the main location of hydrothermal and volcanic activity (Fornari et al., 1998), although off-axis volcanism has been recognised to result in the eruption of lava flows as well as the formation of off-axis seamounts, typically several km to tens of km away from the ridge axis (Niu and Batiza, 1997; Perfit and Chadwick, 1998).

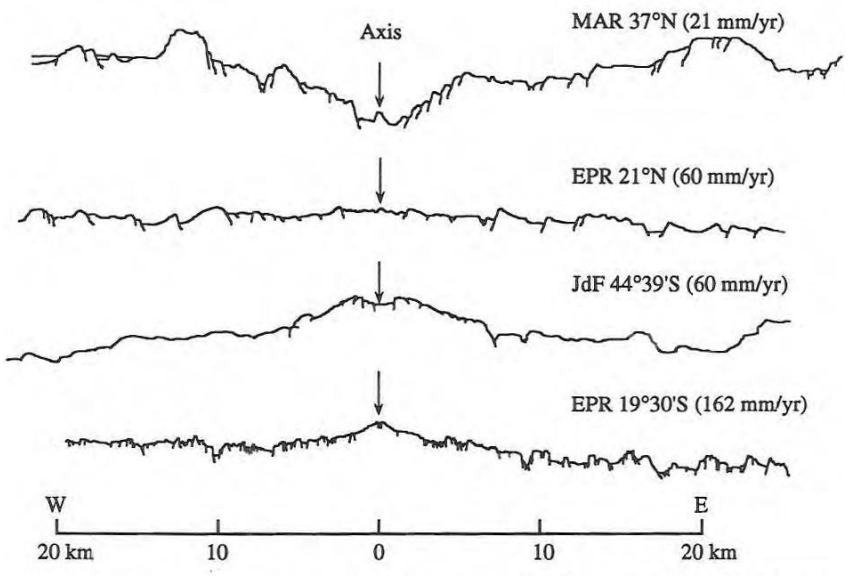

***Figure 1.2**: Cross-sections of several contrasting axial morphologies for different spreading rates. Slow-spreading ridges (MAR 37°N) have wide axial valleys with an axial volcanic ridge. Intermediate-spreading ridges have morphologies that vary from shallow rift valleys (EPR 21°N) and rifted axial highs (JdF 44°39'S). Fast-spreading ridges (EPR 19°30'S) have axial highs with a narrow trough (from Perfit and Chadwick, 1998). MAR = Mid-Atlantic Ridge, EPR = East Pacific Rise, JdF = Juan de Fuca ridge.*

Slow-spreading ridges have a lower magma flux and therefore a thicker and stronger lithosphere, resulting in a dominant role for brittle deformation and a characteristically rough topography with a large, 1.5 – 3 km deep, 30 – 45 km wide, axial rift valley (Macdonald, 1986). The inner valley floor is 5 – 12 km wide and bounded by inward-facing normal faults which displace the crust hundreds of metres creating the crestal mountains. An axial volcanic ridge (AVR), reaching several hundred meters in height, several km wide and tens of km long, is commonly situated in the inner valley and considered the main site for volcanic activity (Smith and Cann, 1993). Additionally, plate separation at slow-spreading ridges can occur through asymmetric tectonic extension along long-lived, low angle detachment faults (Tucholke et al., 1998). These create distinct topographies of shallow sea-floor with domed and spreading parallel corrugated surfaces, named megamullions or oceanic core complexes (OCC, named in analogy to continental metamorphic core complexes).

The morphological features of intermediate-spreading ridges vary widely between those characteristic of fast-spreading and slow-spreading ridges, although rifted axial highs and shallow rift valleys are most common (Cochran and Sempéré, 1997). Rifted axial highs contain a narrow depression distinct from axial summit troughs at fast-spreading ridges (50 – 200 m deep and a few km wide), whereas shallow rift valleys are typically smaller than the valleys found at slow-spreading ridges (<400 m deep and 2 – 4 km wide). Abrupt changes of morphology along the ridge axis suggest there is a threshold response to magma supply, where the steady-state magma reservoir in the crust disappears below a critical magma flux. This, in turn, results in a large increase in strength and thickness of the axial lithosphere (Cochran and Sempéré, 1997).

Notable departures from these previous types of ridge geometry are found at ultraslow-spreading ridges. Ultraslow spreading rates can be the result of very slow plate divergence or ridge orientations that are highly oblique to the spreading direction (Dick et al., 2003). Ultraslow-spreading ridges share features with slow-spreading ridges, such as a wide axial valley with an AVR and common exposures of serpentinised peridotites in ultramafic complexes exhumed by low angle, corrugated detachment faults (Dick et al., 2003; Searle et al., 2003). They also display some unique characteristics, however, such as the occurrence of amagmatic ridge sections that are 100's of km long, with abundant ultramafic outcrops on a smooth, flat and uncorrugated seafloor (Cannat et al., 2006). These domains are interrupted by widely spaced (up to 80 km) regions of highly focussed magmatism, forming large axial volcanoes (>2000 m high) (Cannat et al., 1999; Michael et al., 2003).

1.1.1.2 Along-axis ridge segmentation

Bathymetric surveys in the early 1980's, using improved, high resolution multibeam echosounding systems, revealed that mid-ocean ridges were not, as geologists up until then had imagined, simple

linear features occasionally offset by transform faults. They revealed a whole spectrum of complexities in terms of ridge morphology, segmentation, offsets and misalignments. The ridge is segmented and tectonically offset at a range of scales, thought to coincide with changes in the nature of the underlying magmatic plumbing system (Figure 1.3 and 1.4). The study of the off-axis traces of these structures provides insight in their evolution and longevity, and shows that smaller, non-transform offsets can migrate laterally, merge with each other and/or evolve into larger/smaller offsets (e.g., Hey et al., 1980). Tectonic segmentation correlates to various degrees with geophysical (axial depth and morphology, gravity anomalies and seismic crustal thickness) and geochemical parameters (source composition, extent of melting and degree of fractional crystallisation). Based on correlations between these characteristics, various researchers have developed models to explain the observed segmentation, giving rise to concepts such as spreading cells (e.g., Schouten and Klitgord, 1982) and magmatic segments (e.g., Macdonald et al., 1984), discussed in this section.

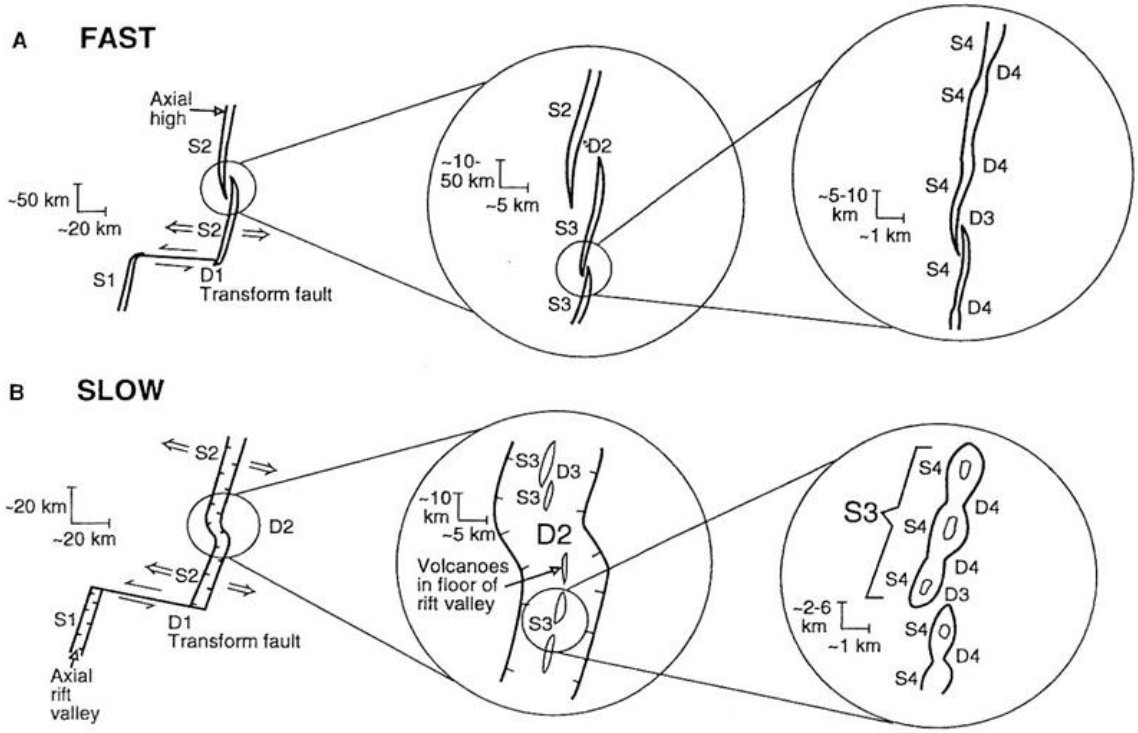

***Figure 1.3**: A schematic diagram illustrating the different styles of ridge segmentation over various scales at fast- (a) and slow-spreading (b) ridges. S = segment, D = discontinuity, numbers denote the order of the segment/discontinuity. Third and fourth order discontinuities at slow spreading ridges are often difficult to identify as such in a consistent manner (from MacDonald et al., 1991).*

At all MORs, first-order segments, 300 – 500 km in length, are offset 30 km or more by large, long lived (from a few to hundreds of millions of years) transform faults, defined as plate tectonic boundaries that accommodate strike-slip movement and are orientated along the small circles

around the Euler pole of the plate's rotation. First-order ridge segments are marked by linear valleys and transform ridges parallel to the spreading direction, from which seismically inactive fracture zones extend, marking past tectonic activity. Transform faults do not migrate along the axis through time, but can evolve into or from non-transform offsets, as has been proposed for the origin of the rotating Easter and Juan Fernandez microplates (Bird and Naar, 1994). Tectonic corridors spanning multiple first-order segments (Figure 1.4) have been described along some parts of the slow- and intermediate-spreading ridge system and are defined as 'corridors' of lithosphere produced at stretches of ridge axis that span multiple first-order segments and have a relatively uniform characteristics (e.g., lithospheric subsidence rates, zero-age depth, ridge asymmetry, Kane and Hayes, 1992; Hayes and Kane, 1994).

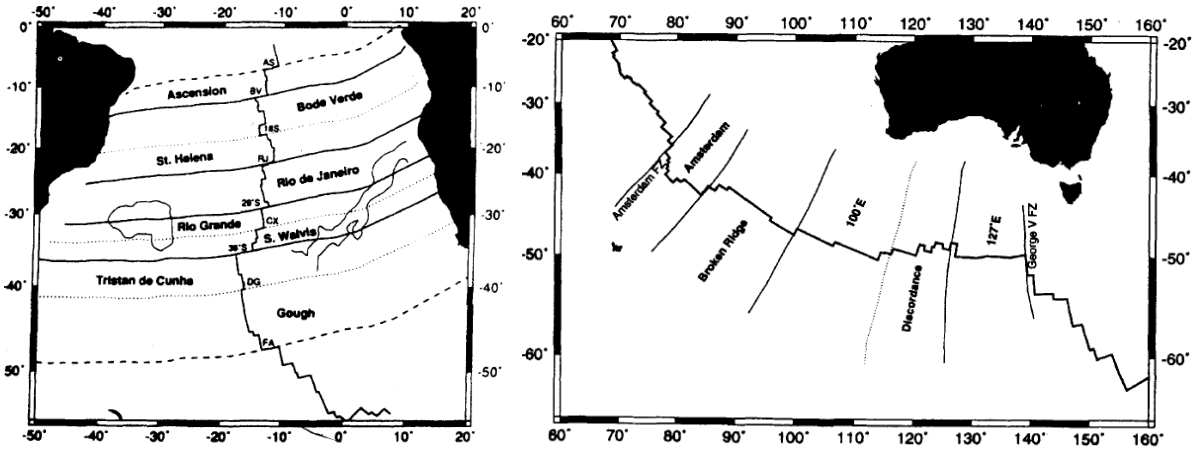

***Figure 1.4**: Tectonic corridors, spanning multiple first-order, transform fault bounded segments, along the Mid-Atlantic Ridge (left) and South East Indian Ridge (right), as described by Kane and Hayes (1992) and Hayes and Kane, (1994) (from Batiza, 1996).*

Second-order segmentation are characterised by several types of ridge-discontinuities known collectively as non-transform offsets (NTO) that last between a few to tens of millions of years. Discontinuities at fast-spreading ridges take the form of large overlapping spreading centres (OSC), forming segments of 50 – 230 km with offsets varying from 1 – 30 km (e.g., Macdonald et al., 1984). At slow-spreading ridges, NTOs can take the form of fault-bounded, steep-sided ridges, oblique shearzones and steps in the volcanic ridge (e.g., Sempéré et al., 1993). Such offsets typically have displacements of 15 – 30 km and can migrate along the ridge, resulting in segment lengths of 20 – 100 km (50 km on average). As with axial morphology, the geometry of second-order discontinuities at intermediate-spreading ridges is variable and related to the strength of the axial lithosphere, taking forms of OSCs, overlapping rift zones and oblique faulted jogs of the axis, typically at scales comparable to those at fast-spreading ridges (Sempéré and Cochran, 1997).

At ultraslow-spreading ridges, second-order discontinuities can occur as orthogonal volcanic domains with oblique basins, and amagmatic domains with highly focussed volcanism. Discontinuities of the first type form segments of 30 – 100 km and are characterised by regions with abundant volcanic centres that form spreading-perpendicular ridges and are separated by wide (up to 50 km) oblique basins that are generally volcanically inactive (e.g., Mendel et al., 1997; Cannat et al., 1999). Amagmatic domains can extend for >200 km and have been termed 'supersegments' (Dick et al., 2003; Carbotte et al., 2016).

Fast-spreading ridges are further segmented by third- and fourth-order discontinuities. Small OSCs partition the ridge in third-order segments of 20 – 80 km (30 km on average), with offsets of 0.5 – 2 km and lasting from 10 – 100 ka (e.g., Macdonald et al., 1984). Fourth-order segmentation, termed devals (short for "deviations from axial linearity", Langmuir et al., 1986) and lasting less than a few thousand years, occurs as bends or small (<500 m) steps in the axial summit at an interval of 5 – 15 km. Third-order segmentation analogous to fast-spreading ridges has also been recognised at intermediate-spreading ridges (e.g., Cochran and Sempéré, 1997). Originally, higher-order segmentation was also proposed for the slow-spreading environment (Macdonald et al., 1991), but due to the complexity of the axial zone at these ridges, these discontinuities can often not be consistently identified as such (e.g., Smith et al., 1995; Carbotte et al., 2016).

1.1.1.3 The scale of the magma plumbing system

The magma plumbing system at MORs extends from the base of the melting regime to the seafloor. During passive mantle upwelling, melting begins at the depth where the mantle adiabat intersects the solidus (a function of mantle temperature and composition) and ceases at the depth where mantle flow turns horizontal. As a consequence of this corner flow, melts are generated over a range of pressures and a relatively large volume of mantle is melted at low percentages while a small volume of mantle rises to the base of the lithosphere and is melted to the maximum extent (e.g., Langmuir et al., 1992). The compositions of mid-ocean ridge basalt (MORB) and the residual mantle are best modelled by polybaric near-fractional melting in the spinel-stability field, with small amounts of melting in the garnet stability field (e.g., Johnson et al., 1990). Ascending melts are seemingly highly focussed towards the spreading axis and melt transport is therefore envisioned as occurring primarily via channelised flow, branching and coalescing at depth (e.g., Kelemen et al., 1995). However, both off-axis eruptions as well as large lava flows extending off-axis have been recognised (Perfit and Chadwick, 1998).

Along-axis variation in the degree of magmatism correlates with ridge segmentation. Originally, magmatic segmentation was envisioned as a hierarchical nested system, where higher order

segments were larger, had greater offsets, were longer lived and resulted from deeper level processes than lower order segments (Macdonald et al., 1988; Sinton et al., 1991). Deep mantle upwelling and melting was thought to occur at the scale of first order segments, where ascending melts would be partitioned to form smaller segments with a shared deep magma plumbing, and are then further subdivided at shallower levels into discrete crustal magma plumbing systems. A recent review by Carbotte et al. (2016), however, concluded that the hierarchical structure of this model is generally not very well supported by observations and that there is little consistency between the nature and magnitude of geochemical boundaries and the order of tectonic segmentation. Nevertheless, they note that 3rd and 4th order partitioning are useful for understanding crustal processes at fast-spreading ridges, and that segmentation observed at scales larger than 1st order, such as amagmatic super-segments at ultraslow-spreading ridges and tectonic corridors at intermediate- and slow-spreading ridges, may be related to processes occurring in the mantle. Principal magmatic segments are defined by Carbotte et al. (2016) as a length of ridge fed by a discrete melt accumulation in the shallow asthenosphere. These segments have similar lengths along ridges of all spreading rates, averaging 30 – 50 km, and correspond to second-order tectonic segments at slow-spreading ridges and third-order tectonic segments at intermediate- to fast-spreading ridges.

Geochemical parameters that are related to mantle source and extent of melting show large jumps across magmatic segments (coinciding with 1st, 2nd and 3rd order tectonic offsets), but there are also many such segment offsets lacking those variations (Carbotte et al., 2016). This may reflect that the jumps are not caused by regional variations in mantle composition and/or extent of melting, but rather by the along-axis focussing of melts in the upper mantle, followed by lateral redistribution at crustal levels, juxtaposing abrupt chemical variability across offsets. Geochemical variations at slow-spreading ridges are typically larger, which may reflect inefficient homogenisation of melts compared to fast-spreading ridges, or possibly a larger degree of variability in the mantle.

MORB compositions are not in equilibrium with mantle peridotite at any pressure (O'Hara, 1968) and indicate that parental melts undergo shallow (~0.1 GPa; ~0.3 km) anhydrous (~0.05 – 0.2 wt%) crystallisation of olivine, plagioclase and clinopyroxene (e.g., White and Klein, 2014). The amount of crystallisation melts undergo (often quantified by Mg#, i.e., molar Mg^{2+} / [Mg^{2+} + Fe^{2+}]), reflects a balance between the rates of cooling and magma supply (Christie and Sinton, 1981). MORBs erupted at slow-spreading ridges generally have a higher mean Mg# and a lower variability in Mg# than at fast-spreading ridges (Rubin and Sinton, 2007). This can be accounted for by ~20% more fractional crystallisation, corresponding to ~20°C lower eruption temperatures, at fast-spreading ridges (Coogan, 2014). Crystallisation of eruptible melts is probably enhanced in the fast-spreading

environment due to the occurrence of shallow, long-lived melt lenses, where hydrothermal cooling is more efficient at removing latent heat (White and Klein, 2014). Slow-spreading ridges may also produce more evolved melts, but their scarce occurrence as MORB implies they are less likely to erupt (Rubin and Sinton, 2007).

Numerous authors have tried to correct for the effects of fractional crystallisation on melt composition to make inferences about the melting conditions. $Na_{8.0}$ and $Fe_{8.0}$ are two commonly used parameters and represent the Na_2O and FeO^T contents of a melt corrected for fractional crystallisation to a MgO content of 8 wt% (Klein and Langmuir, 1987). Since Na_2O behaves as an incompatible element during melting, it is inferred to be inversely related to the mean degree of melting. FeO correlates with the pressure of melting, so that $Fe_{8.0}$ is a proxy for the mean depth of melting (Langmuir and Hanson, 1980). A global compilation of MORB shows that $Na_{8.0}$ and $Fe_{8.0}$ are inversely correlated and that deep mid-ocean ridges with an inferred thin crust were generally formed by smaller amounts of melting (higher $Na_{8.0}$) and shallower melting depths (lower $Fe_{8.0}$, implying shorter melting columns) than shallow ridges with and inferred thick crust (Klein and Langmuir, 1987).

The interpretation of MORB compositions is complicated, however, due to multiple competing processes. Incompatible trace element variations, for example may be affected by both mantle source and degree of melting. Furthermore, magma mixing can obscure geochemical signatures carried by primary MORB magmas. The Mg# in MORB correlates inversely with the variability in various geochemical parameters related to magma source (e.g., La/Sm, K/Ti and isotope ratios of Sr, Nd and Pb are more variable in primitive magmas), indicating magma mixing is more common at faster spreading ridges and at shallow crustal levels (Rubin and Sinton, 2007). Source variability is recorded to a greater extent in melt inclusions (e.g., Sobolev and Shimizu, 1993), phenocrysts (e.g., Lange et al., 2013a), and the lower crust (e.g., Jansen et al., 2018). Additionally, the widespread occurrence of melt-rock reactions during melt transport in the igneous crust has been shown to have a strong control on MORB trace element compositions (e.g., Lissenberg and MacLeod, 2016).

1.1.2 Architecture of oceanic lithosphere: Evaluating the Penrose model

Models of oceanic lithosphere are strongly influenced by seismic surveys that show many seismic velocity profiles of oceanic lithosphere have a consistent, horizontally layered, structure (e.g., Raitt, 1956; White et al., 1992). Early attempts to interpret the jumps in seismic velocities in terms of lithological boundaries (e.g., Fox et al., 1973) coincided with the acceptance of a common definition for ophiolites at the Penrose Conference, as well as the recognition of their formation by seafloor spreading (Anonymous, 1972; Dilek, 2003). The emerging model of oceanic lithosphere, the 'layer-

cake' or 'Penrose model' (Figure 1.5), correlated the litho-stratigraphical succession observed in ophiolites to the layered seismic structure of oceanic crust (e.g., Moores and Jackson, 1974; Christensen, 1978). In this model, seismic layer 1 is correlated with pelagic sediments, whereas seismic layers 2 and 3 comprise the igneous crust. Layer 2 typically has variable seismic velocities and is commonly interpreted as the extrusive lavas and dykes of the upper crust (e.g., White et al., 1992). Layer 3, which typically makes up two-thirds of the igneous crust, is thought to represent the gabbroic lower crust (e.g., White et al., 1992). The Moho at the base of layer 3 marks a sharp increase in seismic velocity and is typically interpreted as the crust-mantle boundary or transition zone.

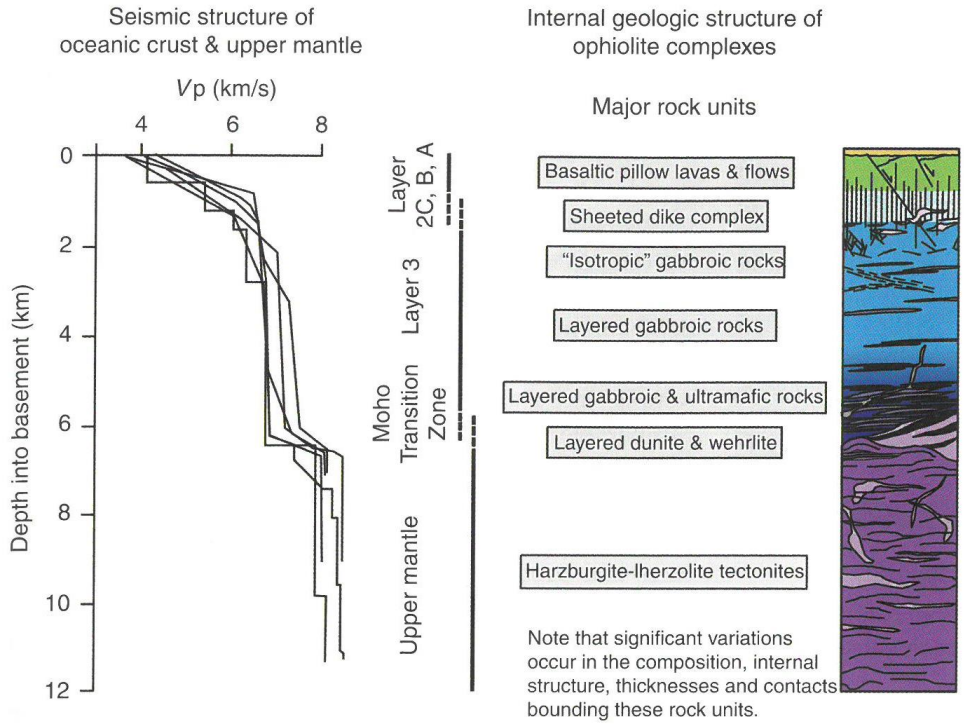

***Figure 1.5**: The Penrose model for oceanic lithosphere, based on the corelation between seismic layering of the oceanic crust (left, White et al., 1992) and the layered lithostratigraphy of ophiolites (right) (from Karson et al., 2015).*

Estimates for the thickness of the igneous oceanic crust derived from the seismic velocity structure of ocean lithosphere are relatively uniform for most spreading rates, ranging from 5 – 8 km (6.5 km on average), where layer 2 is typically 1 – 1.5 km at fast-spreading ridges and 2 – 3 km at slow-spreading ridges, and layer 3 is typically 3.5 – 5.5 km thick (White and Klein, 2014). The seismic estimates generally correspond well to geochemical constraints on the volumes of magma produced by mantle melting, based on major element chemistry and rare earth element inversions of mid-ocean ridge basalts (e.g., Langmuir et al., 1992; White et al., 2001). These observations are

commonly taken to suggest that the mechanisms of crustal accretion are, to a first approximation, similar for slow and fast spreading-rates, with exceptions of fracture zones, which tend to have thinner (2 – 3 km) crust, and hotspot-influenced ridge-sections, which tend to have thicker crust (up to 20 km) (White and Klein, 2014).

It is important to note, however, that models derived from geophysical and geochemical observations are inferences accompanied by an inherent uncertainty and require verification through direct observations. For example, mantle Bouguer anomalies (MBA), free-air gravity anomalies corrected for topography, reflect differences in bulk specific gravity of the subsurface. Though differences result primarily from different proportions of dense peridotite and less dense mafic curst, gravity measurements provide no information on the geometrical distribution of these lithologies, so that lateral variations can be interpreted as thickness variations of a uniform igneous crust or as lateral density compositional changes. Seismic velocity in the oceanic lithosphere is another property commonly measured during in geophysical surveys, but it is affected not only by primary (igneous) lithology but also by the degree of alteration, fracture density and geometry, and fracture-sealing by hydrothermal minerals (e.g., Fox et al., 1973; Christensen, 1978; Wilkens et al., 1991). As a result, the subdivision of seismic layer 2 into 2a and 2b at fast-spreading ridges has been interpreted to represent the boundary between the lava and sheeted dykes units or alternatively an alteration front that may or may not coincide with the unit boundary (Christeson et al., 2007). Similarly, it has been suggested that the seismic Moho at slower spreading ridges may not represent a petrological crust-mantle boundary, but rather a hydrothermal alteration front, due to the lower seismic velocity of hydrated, serpentinised peridotite compared to fresh peridotite, (e.g., Muller et al., 1997, 2000; Dick et al., 2017).

While the presence of a continuous, 6 – 7 km thick igneous crust at the fast-spreading ridges conforms well to the Penrose model (e.g., Cann, 1974; Sinton and Detrick, 1992), it cannot explain the occurrence of gabbros and serpentinised peridotites exposed at the seafloor at slower spreading ridges (e.g., Cannat, 1993). Instead, lower and more episodic melt supplies at slow-spreading ridges result in a thicker axial lithosphere and a greater role for fault-assisted plate separation, which can exhume deeper lithologies. The magma flux at mid oceanic ridges is the primary control on whether a steady-state magma reservoir can exist at the axis, in turn influencing the style of volcanic eruptions and plate separation. Current models for slow-spreading ridges suggest that as melt supply varies in space and time, the modes of crustal accretion vary between symmetrical ‘magmatic spreading’, where extension is accommodated by emplacement of a plutonic lower crust, sheeted dyke complex and lavas, and ‘tectonic spreading’, where extension is accommodated along detachment faults that are typically highly asymmetrical (e.g., Lin et al., 1990; Cannat, 1993, 1996;

Cann et al., 1997; Blackman et al., 1998; Tucholke et al., 1998; Ildefonse et al., 2007). In the following sections the models for seafloor spreading at fast and slow spreading ridges are reviewed, highlighting what uncertainties remain.

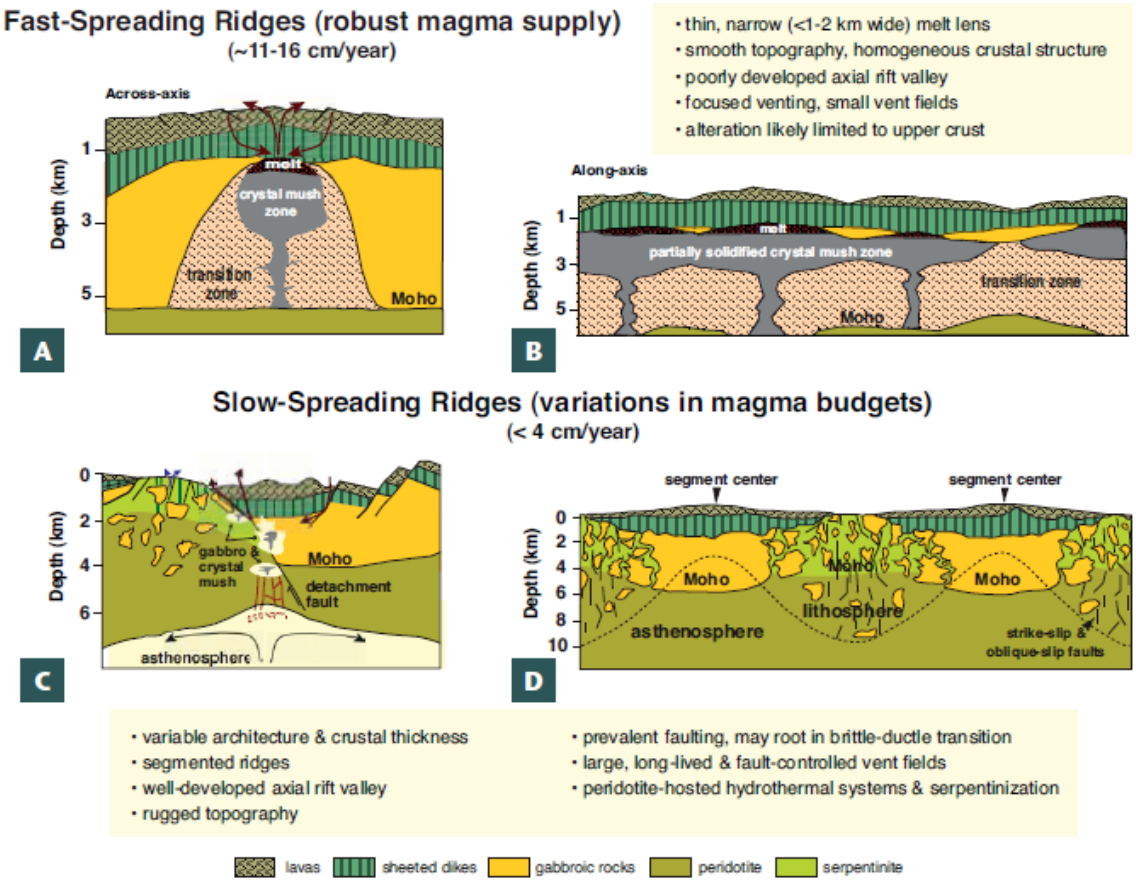

***Figure 1.6**: Current models for oceanic crust at fast- (a & b) and slow- (c & d) spreading ridges with cross-sections across-axis (a & c) and along-axis (b & d) (from Bach and Früh-Green, 2010; modified from Sinton and Detrick, 1992; Boschi et al., 2006 and Cannat et al., 1995).*

1.1.2.1 Magmatic spreading at fast-spreading ridges

Many observations at fast-spreading ridges indicate a robust melt supply and therefore represent the melt-rich endmember of crustal accretion. Magmatism in the upper crust is mainly fed by narrow dykes, leading to frequent (every ~5 years) and small volume fissure eruptions (~1 – 5 x 10^6 m^3 per eruption) that terminate quickly as the feeder-dykes freeze (Perfit and Chadwick, 1998). Sheet flows dominate in the extrusive lavas, indicating higher rates of lava effusion and dyke intrusions at higher pressures compared to pillow lava-dominated systems. At fast- and intermediate-spreading ridges, the observation of a seismically imaged, steady-state, shallow axial melt lens (AML) overlying a large crystal-rich mush zone along large parts of the spreading axis is consistent with a high magma flux, since frequent melt replenishment is required to prevent the

freezing of this body (Detrick et al., 1987; Hooft et al., 1997). A seafloor compliance survey at the East Pacific Rise (EPR) suggests the axial lower crust contains 2.5 – 18% melt distributed in a well-connected network and that additional melt may pond at the base of the crust (Crawford and Webb, 2002). Due to its small size compared to the total volume of melt in the lower crust, the role of the AML in the accretion of the lower crust and feeding the dykes and lavas of the upper crust is debated. Some authors propose the bulk of the crystallisation occurs in the AML and subsequently subsides to form the lower crust (e.g., Phipps Morgan and Chen, 1993). Others assign a smaller role to the AML and propose that crystallisation occurs *in situ* at various levels in the lower crust (e.g., Kelemen et al., 1997). Hybrid models where the lower crust is fed from the top and bottom have also been proposed (Boudier et al., 1996). Along-axis discontinuities of the seismically imaged AML generally coincide with a deepening of the ridge-axis and positive MBA values, interpreted as slightly thinner and/or cooler crust (Carbotte et al., 2016). These variations generally correlate with the lateral density in hydrothermal vents and biological communities and lava morphology (White et al., 2002; Carbotte et al., 2013).

The magmatic crust formed in this fashion is of relatively uniform thickness (6 – 7 km) along the ridge-axis and resembles Penrose crust (Figure 1.6) (e.g., Cann, 1974; Sinton and Detrick, 1992). Sampling of the shallow and deep ocean crust formed at the EPR in ODP Hole 1256D and along exposures in an intra-oceanic rift at Hess Deep show the lithological succession is comparable to that of the Semail Ophiolite in Oman, thought to represent lithosphere formed at a fast-spreading ridge, and conforms well to the Penrose model (e.g., MacLeod and Yaouancq, 2000; Karson et al., 2002; Koepke et al., 2008). Notably, since dykes form by brittle fracturing and the depth of the AML represents the depth of the axial brittle-ductile transition, the presence of a steady-state AML is thought to be related to a relatively sharp gabbro-dyke transition. At Hess Deep and in Hole 1256D this transition is marked by a level of isotropic gabbro interpreted as the remnants of the axial melt lens, as well as high-temperature hornfels-facies metamorphism in the surrounding rocks (e.g., Gillis, 2008; Koepke et al., 2008; France et al., 2009). In the Semail ophiolite, this 'fossil AML' can be traced laterally and dykes are observed rooting in this crustal level (e.g., MacLeod and Rothery, 1992; MacLeod and Yaouancq, 2000). Observations of the fossil melt lens crosscutting and assimilating parts of the sheeted dyke complex are interpreted as the dynamic response of the melt body to the periodic waxing and waning of melt supply (France et al., 2009), whereas the lateral termination of the fossil melt lens coincide with 'penetration zones', where dykes laterally intrude the lower crustal plutons, and are interpreted as ridge discontinuities with a lower melt supply allowing gabbros to cool to the point where dyke intrusion is possible, analogous to ridge segmentation at fast-spreading ridges (Nicolas et al., 1988a; MacLeod and Rothery, 1992).

1.1.2.2 Magmatic spreading at melt-robust slow-spreading ridges

In contrast to fast-spreading ridges, observations at slow-spreading ridges indicate they have a more variable and overall lower melt supply. Volcanism at slow-spreading ridges often has point-source eruptions along magma conduits that are thermally more stable than at fast-spreading ridges and consequently result in larger (50 – 1000 x10^6 km^3), albeit less frequent (every ~5000 years) eruptions (Perfit and Chadwick, 1998). Lower effusion rates compared to fast-spreading ridges result in dominantly pillow morphologies in the lavas. Lavas from slow-spreading ridges are generally more crystal rich than at fast-spreading ridges, suggesting melt crystal separation is less efficient at slow-spreading ridges and eruptible crystal-rich melts are more likely to form there (Coogan, 2014). Seismic surveys indicate stable magma reservoirs are absent along large parts of the ridge (Sinton and Detrick, 1992). Where they have been found, such as at the Reykjanes ridge (North Atlantic, MacGregor et al., 1998) and at 35° N along the Mid-Atlantic Ridge (MAR, Dunn et al., 2005), they are of significant size and predicted to not be thermally stable for periods longer than a few thousand years (MacGregor et al., 1998). Based on this, melt supply at slow-spreading ridges is thought to be of an episodic nature, resulting in ephemeral magma reservoirs and a greater role for tectonic stretching compared to fast-spreading ridges. Seismic imaging of a magma reservoir 3 km underneath the Lucky Strike volcano on the MAR, as well as faults penetrating down to at least 3 – 4 km depth, suggest a continuous interplay between faulting and magmatism (Singh et al., 2006). The lower crust is thought to accrete from multiple, discrete gabbroic plutons, each representing a period of magmatic activity, forming a 'plum-pudding' crust (Cannat, 1993; 1996).

Seismic surveys, 'bulls-eye' patterns in MBA gravity anomalies (e.g., Lin et al., 1990; Tolstoy et al., 1993) and variations in ridge axis depth (e.g., Neumann and Forsyth, 1993), are commonly interpreted as variations in crustal thickness, ranging ~2 – 9 km (e.g., Bonatti et al., 2003; Dunn et al., 2005), with the crust occurring at the centres of ridge segments typically 2 – 3 km thicker than crust at the segment ends (e.g., Hooft et al., 2000). Axial lithospheric thickness, reflecting the thermal structure of the ridge axis, is thick near segment ends and thin near centres. The fluctuations in lithospheric strength along ridge-segments is expressed in the geometry of axial-valley normal faults, with centres generally having smaller fault throws (200 – 400 m) and spacing (<5 km) than segment ends (where throws can exceed 1000 m and faults are spaced >5 km; e.g., Shaw, 1992). These along-axis variations are thought to result from stronger focussing of melt towards segment centres compared to fast-spreading ridges. The thickness of the axial lithosphere is strongly intertwined to this process, since (a) lower melt volumes are produced underneath thick lithosphere due to a shorter melt column, (b) hot melts migrating along the basal topography of the lithosphere towards

the segment centres, and (c) melt migration is an efficient heat transport mechanism that affects the state of the lithosphere (e.g., Cannat et al., 2003; Standish et al., 2008; Carbotte et al., 2016).

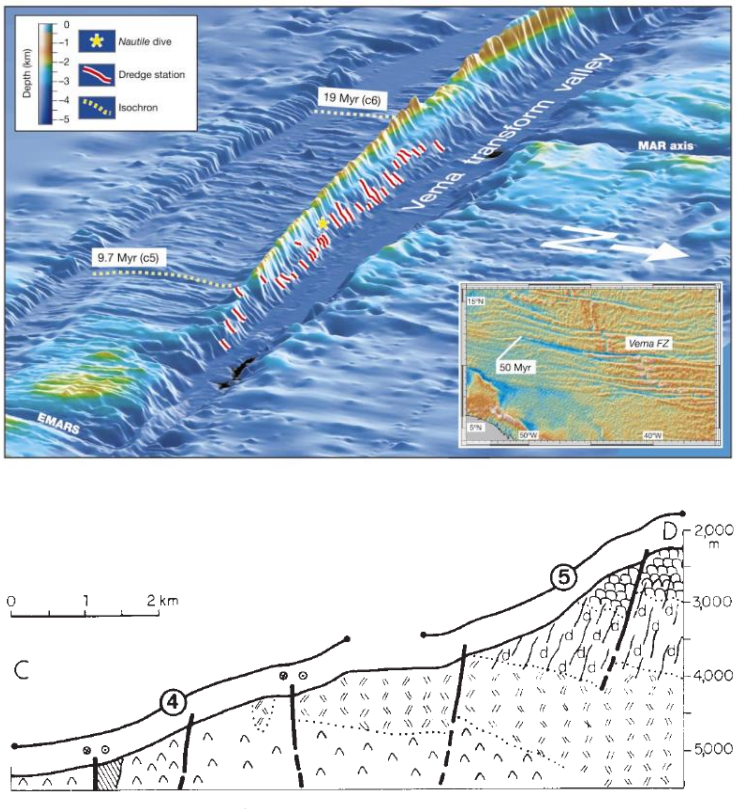

Figure 1.7*: Top: a 3D view of the bathymetry of the Vema transform valley (from Bonatti et al., 2003). Bottom: Cross-section of the southern Vema valley wall, with the four major units from bottom to top being serpentinite, gabbro, dykes and pillow lavas (from Auzende et al., 1989).*

Direct observations of the crust formed by magmatic spreading at segment centres are sparse and limited to the sampling of basalts at the seafloor. Models often implicitly assume that the geophysical observations are consistent with a Penrose style crust (Figure 1.6), but no lower crust has been sampled *in situ* yet due to a lack of exposures. Such exposures have been identified for crust formed at segment ends, however. One of these locations is the Vema transform valley along the MAR, where dives and dredges have revealed that a full crustal section is exposed in the southern valley wall (Figure 1.7, Auzende et al., 1989). The igneous crust at Vema is thin (~2.2 km) compared to the thickness estimates for the crust formed at the segment centre to the south, (Bonatti et al., 2003). Apart from the reduced thickness, the lithostratigraphy is similar to the Penrose model and from bottom-to-top consists of 1 km of serpentinised peridotite, followed by 500 m of predominantly Fe-Ti-oxide gabbros, 700 – 1100 m of dyke complex, and finally 800 m of disrupted and brecciated pillow lavas and lava flows (Auzende et al., 1989). The lava sequence is

thinner than Penrose crust (~1 km), possibly due to mass wasting and/or a period of erosion during subaerial exposure, the latter suggested by the cover of a shallow-water carbonate platform (Bonatti et al., 2005). Most notably, however, the gabbroic section is a lot thinner than predicted by the Penrose model (3.5 – 5.5 km). Additionally, primitive, Mg-rich gabbros and ultramafics are absent, suggesting the section is either incomplete or that the gabbros crystalised from differentiated melts transported along-axis from more melt-rich segment centres (e.g., Abelson et al., 2001). The possibility of the latter process occurring is illustrated by seismic tomography of the magmatic reservoir at 35° N along the MAR, where melt is interpreted to be distributed in vertical pipe-like structures that are deflected laterally to form horizontal, along-axis melt-rich bodies once they intersect the brittle-ductile transition (Magde et al., 2000; Dunn et al., 2005). Taken together, these sparse observations suggest magmatic crustal accretion at slow spreading ridges is highly heterogeneous and involves extra degrees of complexity relating to along-axis as well as temporal variations in melt supply, compared to fast spreading ridges.

1.1.2.3 Tectonic spreading at melt-poor slow-spreading ridges

At portions of slow-spreading ridges with a lower melt supply and a thick axial lithosphere, magmatic crustal accretion cannot keep pace with plate separation and as a result extension is accommodated by faulting. Below a certain threshold value of melt supply, axial normal faults can develop into crustal-scale detachment faults that accommodate run-away displacement. Detachment structures can be active for hundreds of thousands of years and the uplifted footwalls expose lower crust and upper mantle rocks at the ocean floor in structures known as 'megamullions' or 'oceanic core complexes' (OCCs), analogous to continental core complexes (e.g., Tucholke et al., 1998). First recognised at the inside corners of ridge-transform intersects, OCCs are characterised by dome-shaped detachments surfaces on the ocean floor with prominent spreading-parallel corrugations (Figure 1.8, Cann et al., 1997), accompanied by shallower seafloor, higher MBA values, exposures of lower crustal and upper mantle rocks, and a lack of volcanic features (Tucholke et al., 1998). Subsequent investigations have revealed that OCCs may be much more widespread at slow-spreading ridges, with potentially as much as 50% of the Mid Atlantic Ridge between 12.5° and 30° N accommodating seafloor spreading along active detachment faults (Smith et al., 2006; Escartin et al., 2008). Fault rocks with high-strain low-angle fabrics are confined to the detachment surfaces and are dominated by secondary hydrous minerals such as serpentine, chlorite, tremolite and talc (MacLeod et al., 2002). OCCs can be tens of kilometres in length along-axis, 5 – 15 km wide (parallel to the spreading direction) and up to a few kilometres high, although larger examples are known as well (e.g., Ohara, 2001).

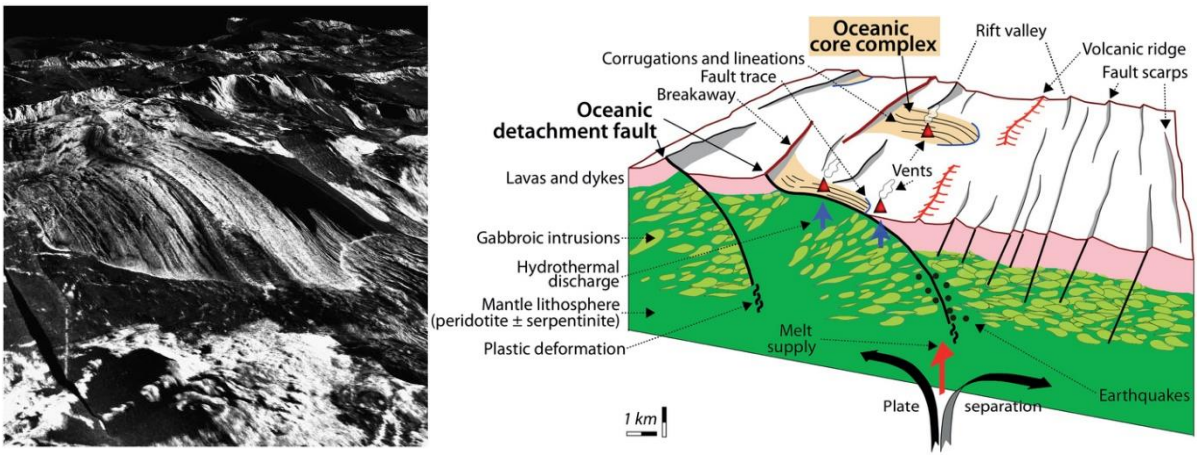

***Figure 1.8**: Left: The corrugated detachment surface of an active OCC emerging from axial valley floor at 13°19'N along the MAR. Distance from emerging toe of detachment to breakaway ridge crest is ~9 km, height difference is ~1.5 km. Sidescan sonar imagery draped over 3D bathymetry model with no vertical exaggeration, (from MacLeod et al., 2009). Right: cartoon model showing the generalised architecture of an oceanic core complex (from Escartin and Canales, 2011).*

Upon their initial discovery, it was unclear what conditions led to OCC formation, since the presence of gabbroic intrusions indicated that magmatic activity was not necessarily absent (e.g., Dick et al., 2000). Models varied from detachment faults requiring a complete cessation of magmatism to form (e.g., Tucholke et al., 1998), to such faults arising from strain localisation around rheologically strong, gabbroic plutons emplaced in weaker serpentinites, and therefore requiring periods of enhanced magmatism (e.g., Ildefonse et al., 2007). More recent numerical modelling has shown that OCC geometries form during periods of intermediate magma supply, when magmatism accounts for 30 – 50% of the total spreading, although these results do not preclude more extreme variations in magmatic spreading on shorter time-scales (Buck et al., 2005; Tucholke et al. 2008). The corrugations on the detachment surface have been suggested to arise from episodic and spatially variable magmatism, resulting in a variable depth of the brittle-ductile transition and hence an uneven detachment surface (Tucholke et al. 2008). Detailed observations along the ridge at 13° N MAR show that oceanic core complexes can initiate when magmatism is supressed on a million-year time scale along 20-30 km of ridge-length (MacLeod et al., 2009). During the waning of magma supply, hydrothermal fluids that penetrate the steep (~65°) axial-valley normal faults are more likely to come in contact peridotite and form hydrous alteration minerals, weakening the fault planes. This leads to strain localisation and a runaway displacement, during which flexural unloading causes rapid flattening of the fault and crustal rotation of the footwall along an "anti-listric" geometry. When magma supply increases again, the lateral along-axis propagation of the neovolcanic zone (NVZ) can

cut across the emerging corrugated OCC surfaces, renewing volcanism and terminating activity along the detachment fault (Figure 1.9; MacLeod et al., 2009).

Oceanic core complexes have been of considerable interest to the scientific community since they expose the otherwise inaccessible gabbroic lower crust and peridotite upper mantle. The two deepest ocean drillholes in slow-spread lower crust are located in OCCs, the first in Atlantis Bank at 57° E at the Atlantis II transform fault along the Southwest Indian Ridge (SWIR, Hole 735B), and the second in the Atlantis Massif at 30° N along the MAR (Hole 1309D). Detailed studies of samples recovered from these near-continuous sections of plutonic crust reveal some important differences between both core complexes. Atlantis Bank is larger (~660 km^2) compared to most known OCC's and besides common olivine-gabbros contains a high abundance of evolved Fe-Ti-oxide rich gabbros, as well as widespread occurrence of shear bands marked by localised ductile deformation and a mineralogy in equilibrium with evolved melts (Dick et al., 1991, 1999, 2000). Atlantis Massif, on the other hand, is smaller (~100 km^2) and more comparable in size to other OCCs along the MAR, consists of mainly gabbro with olivine-rich troctolites as well as minor occurrences of oxide-gabbros, and the main deformation features are brittle (Blackman et al., 2006; Godard et al., 2009). These observations have been interpreted as reflecting differences in magma flux, where a higher melt budget at Atlantis Bank resulted in a larger gabbroic batholith, lower cooling rates, longer-lived crystal-melt mushes with a greater extent of magma differentiation and percolating evolved melts reacting with the gabbroic matrix to form hybridised oxide-gabbros. Continued, syn-magmatic exhumation of the core complex is thought to be accommodated by ductile shear zones towards which the latest, most-evolved melts are focussed, resulting in melt-assisted deformation. A lower, more episodic melt budget at Atlantis Massif, in contrast, resulted in a smaller batholith, higher cooling rates, shorter-lived crystal-melt mushes with limited melt migration, intrusions interlayered with enclaves of mantle peridotite that were incorporated and subsequently hybridised by melts to form troctolites, and a greater role for brittle deformation during exhumation (e.g., Dick et al., 2019a; Boulanger et al., 2020).

It is not clear, however, how representative these rocks are for oceanic lithosphere formed by magmatic spreading. Some models propose that detachment faults truncate an igneous crust that is otherwise similar to crust formed by magmatic spreading, dismembering the lavas and the sheeted dykes of the upper crust from the gabbros of the lower crust (Tucholke et al., 1998; Dick et al., 2000, 2008, 2019b). Other models suggest the crust accreted during tectonic spreading is fundamentally different (Cannat, 1993, 1996). As a consequence of significant asymmetric spreading along detachment faults, the emergence zone of the footwall (i.e., the local plate boundary) will migrate towards, and eventually across the ridge axis (MacLeod et al., 2009). Renewed magmatism

consequently results in plutons to be emplaced into the footwall ("footwall capture") and not immediately contribute to symmetric magmatic extension. In this model, the gabbroic plutons sampled in Hole 735B and 1309D represent former magmatic reservoirs that stalled in the lithosphere and differentiated *in situ* without melts being extracted to form sheeted dykes or lavas (Godard et al., 2009; Boulanger et al. 2020). In the proposed life-cycle of OCCs, footwall capture represents the later stage of OCC formation, when magmatism has increased but the flux is not robust enough to terminate activity along the detachment fault (Figure 1.9; MacLeod et al., 2009).

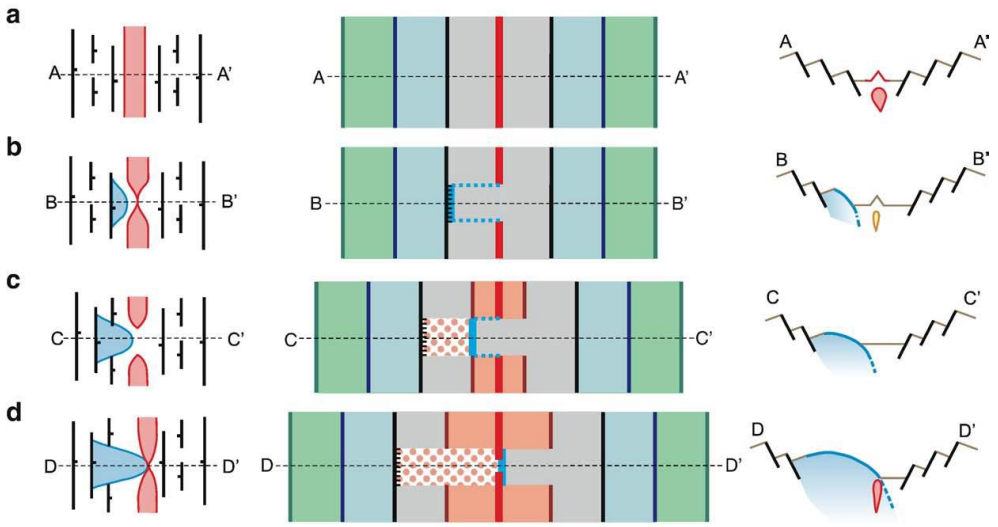

***Figure 1.9**: The life cycle of OCCs as proposed by MacLeod et al. (2009). Left and center show map views of the geology and tectonic plate evolution respectively, and right show cross-sections. (a) Symmetrical magmatic spreading forms the neovolcanic zone (red). (b) Waning magma supply causes the initiation of a detachment fault (blue). (c) Continued activity causes the emergence zone to migrate towards and across the spreading axis. (d) Renewed magmatism leads to footwall capture and will eventually terminate slip along the detachment fault.*

1.1.2.4 Tectonic spreading at amagmatic (ultra)slow spreading ridges

Seafloor spreading under (near-)amagmatic conditions is unique for ultraslow-spreading ridges. At Gakkel Ridge and the easternmost SWIR, portions of the spreading ridge with a volcanic cover alternate with extensive areas that instead expose serpentinised peridotite at the seafloor (Dick et al., 2003; Michael et al., 2003; Cannat et al., 2006). In contrast to the rough topography consisting of volcanic cones, flat-topped volcanoes and spreading-perpendicular fault scarps characteristic for a volcanic seafloor, amagmatic sections of the ridge are characterised by a 'smooth' seafloor, consisting of 15 – 30 km long, 500 – 2000 m high, broad, axis-parallel ridges with a smooth, non-corrugated morphology (Cannat et al., 2006; Cochran, 2008). Some ridges are symmetrical while others have steeper outward-facing slopes than inward-facing slopes. The smooth slopes are interpreted as the surfaces of long detachment faults along which the mantle lithologies were

exhumed, with the overall symmetrical structure resulting from successive changes in fault-polarity as an old detachment fault in abandoned and a new one forms in a 'flip-flop model' (Sauter et al., 2013). The absence of longer lived detachment faults, as occur in oceanic core complexes, is also predicted by numerical models, which show that the strengthening of the lithosphere off-axis in amagmatic conditions favours the formation of a new detachment fault closer to the ridge axis (Tucholke et al., 2008). Amagmatic ridge sections have a relatively thick lithosphere, as indicated by seismicity studies that have detected earthquakes, marking the brittle lithosphere, can reach depths of ~17 km, compared to ~7 km at regular slow-spreading ridges (Grevemeyer et al., 2019). Dramatic variations of maximum earthquake depths along axis are correlated with regions of volcanic seafloor, indicating lithospheric thickness varies with magmatic activity (Schlindwein and Schmid, 2016). In their study, Schlindwein and Schmid (2016) found that microseimicity along ultraslow-spreading ridges could reach depths of ~35 km and that a seismic quite zone exists in the uppermost ~15 km of the lithosphere of amagmatic ridges. They conclude that amagmatic ridges are characterised by extremely thick lithosphere and deep circulation of hydrothermal fluids, leading to serpentinization, rheological weakening of the upper 15 km of lithosphere and deformation being accommodated along aseismic shear zones. The results of this study have been questioned based on the chosen approach for data processing, however, and a more recent interpretation of the data concludes the maximum depth of seismicity is ~17 km whereas the upper aseismic region could not be reproduced (Grevemeyer et al., 2019).

Sampling of this type of lithosphere is limited to dredges of the seafloor, and consequently the lithospheric architecture of this ridge type remains poorly constrained. Rocks recovered from smooth seafloor localities are dominated by peridotites but also include basalts and gabbros, indicating that amagmatic ridges are not completely absent of magmatism (e.g., Seyler et al., 2003). Rare corrugations on some smooth seafloor ridges may indicate locally sustained magmatism (Cannat et al., 2006). Furthermore, the presence of a thick axial lithosphere is likely to favour the crystallisation of melts trapped at various levels in the lithosphere (Cannat, 1996). Seismic surveys of old Atlantic Ocean lithosphere, formed at ultraslow spreading rates, show such trapped gabbroic bodies, thought to have formed by inefficient melt extraction (Lizarralde et al., 2004). In contrast, at the easternmost SWIR areas of volcanic seafloor correlate with MBA anomalies that suggest a substantial underlying igneous crust is present locally (Cannat et al., 2006). Furthermore, off-axis mapping shows that styles of seafloor are not always identical on opposite sides of the ridge axis, indicating the lithospheric accretion processes can be highly asymmetrical (Cannat et al., 2006), while observations of broadly dispersed off-axis volcanism suggest that crustal accretion is not confined to a narrow central spreading axis as is the case at faster spreading ridges (e.g., Standish

and Sims, 2010). These limited observations suggest that melts at ultraslow-spreading ridges are strongly focussed to magmatically robust sections (Cannat et al., 2003), resulting in a lithosphere that is highly variable along-axis in thickness and composition, the precise nature of which remains to be determined.

1.2 Ophiolites: analogues for ocean lithosphere?

1.2.1 The origin of ophiolites

Due to the difficulties in the accessing deeper levels of oceanic lithosphere, much of the work on oceanic crust has been complemented by studies of ophiolites. These sequences of ultramafic peridotites overlain by gabbro, dolerite dykes, pillow lavas and deep-marine sediments were first noted as distinct suites with tectonic contacts occurring in orogenic belts, thus differing from mafic layered intrusions such as Skaergard and Bushveld (Steinmann, 1926; Thayer, 1960). It was suggested that the suite may be derived from partial mantle melting, producing an igneous mafic suite and a residual ultramafic suite (de Roever, 1957), since the volumetric proportions of peridotites versus gabbro and basalt precluded a cumulate origin for the peridotites (Vuagnat, 1964). As geophysical studies and sampling of the seafloor provided increasingly detailed insights into the thickness, the layered structure, and the composition of oceanic crust, comparisons to ophiolites led to the proposition that the latter represented slices of oceanic crust and mantle that were emplaced onto the continent as a consequence of plate tectonics (Dietz, 1963; Hess, 1964; Gass, 1968). Particularly the presence of a sheeted dyke complex, representing 100% extension accommodated by magmatism, is difficult to explain in any other context than seafloor spreading (e.g., Moores and Vine, 1971). This analogy was included in the adoption of an agreed definition for the term ophiolite at the Penrose Conference (Anonymous, 1972). The largest and best preserved of the Penrose-definition ophiolites are the Troodos Ophiolite in Cyprus and the Semail Ophiolite in Oman and the United Arab Emirates (UAE). Consequently, these two ophiolites have historically been most influential for models of seafloor spreading (e.g., Moores and Vine, 1971; Vine and Moores, 1972; Glennie et al., 1974; Nicolas, 1989).

The proposed origin for ophiolites at ancient mid-ocean ridges, and their use as an analogue for oceanic lithosphere was not without controversy. Ophiolites represent unusual oceanic lithosphere per definition, in the sense that they were able to escape subduction. Their crustal sequences are often less thick than the seismic thicknesses of oceanic crust (e.g., Coleman, 1971) and the geochemical composition of ophiolite basalts is not always similar to MORB. Almost immediately after the adoption of the Penrose-definition of ophiolites, it was noted that about a third of the basaltic dykes and lavas in the Troodos ophiolite were not tholeiitic (i.e., MORB-like) in composition, but instead followed a calc-alkalic trend similar to island arc basalts (Miyashiro, 1973). Subsequent

scientific debate focussed, amongst other issues, on the question of how reliably the geochemical compositions of hydrothermally altered rocks could be interpreted, as well as how the widespread extensional features present in ophiolites could form at convergent margins typical of island arcs (Hynes, 1975; Moores, 1975; Gass et al., 1975; Miyashiro, 1975a, 1975b). With regards to the latter, studies of plate boundaries in the western Pacific showed that the island-arcs were separated from the continent by a complex series of ridges and marginal basins, leading to the concept of ocean crust formation at back-arc spreading centres (Karig, 1970, 1971a, 1971b). To overcome the issue of alteration preventing a geochemical comparison between ophiolite lavas and fresh MORB glasses, geochemists focussed on immobile trace elements, concentrations of which are not affected by weathering or metamorphism (Pearce and Cann, 1971, 1973; Pearce, 1996, 2008, 2014). Basalt immobile element geochemistry showed that the Troodos ophiolite had an affinity with basalts from back-arc spreading centres (Pearce, 1975; Smewing et al., 1975) and likely formed during plate separation above a subducting slab of oceanic lithosphere, in what became known as a supra-subduction zone (SSZ) tectonic setting (Pearce et al., 1984).

Subsequent studies of other ophiolites showed that many of these in fact represented oceanic crust formed in marginal basins (Upadhyay and Neale, 1979; Pearce et al., 1984; Dilek and Furnes, 2011). Of the MOR versus SSZ-origin debates regarding various ophiolites, the one concerning the Semail ophiolite has remained contentious to this day (e.g., Warren et al., 2005, 2007; Boudier and Nicolas, 2007). The lava sequence in Oman is subdivided into several units, with the main axial lavas (referred to as the Geotimes lavas) overlain by several later volcanic sequences in the north of the ophiolite, including the Lasail and Alley units (Pearce et al., 1981, Alabaster et al., 1982). These later, discontinuous lava units have depleted incompatible trace elements and have been interpreted to represent products of hydrous melting of a depleted MORB source (e.g., Alabaster et al., 1982; Godard et al., 2006). Boninites, a high-magnesium, trace element depleted variety of andesitic magma found in present-day fore-arc settings, occurring in the Alley unit provide further support for a subduction-origin of the later lavas (Ishikawa et al., 2002). The debate revolves around the question as to what extent the Geotimes unit was also affected by (the early stages of) subduction, and whether that influence is limited to the north of the ophiolite or was pervasive. While some point to the N-MORB character of the Geotimes unit (e.g., Godard et al., 2006), others have argued that the whole of Semail has a SSZ-affinity based on Th enrichments and Nb depletions present in the Geotimes (e.g., Pearce et al., 1981; Alabaster et al., 1982). It has been shown, however, that these trace element anomalies are weak and also present in modern Indian Ocean MORBs, indicating they could therefore reflect an inherent feature of the upper mantle source underneath the Indian Ocean rather than the tectonic setting of the formation of the Semail Ophiolite (e.g.,

Godard et al., 2006). Using a selection of major element trends for which alteration was shown to have a limited effect, MacLeod et al. (2013) demonstrated that the compositions of the earliest dykes and lavas are not consistent with 'dry' MORB (<0.2 wt% H_2O) liquid lines of descent and instead require a small amount of water (~0.2 – 1 wt% H_2O), which they argue is derived from the onset of subduction during the earliest stages of accretion of the oceanic lithosphere. Detailed mapping showed that the later lava sequences had plutonic counterparts that not only occur in the north (Goodenough et al., 2010), but were widespread throughout the ophiolite (Goodenough et al., 2014; De Graaff et al., 2019). High precision geochronology furthermore established that the first and later phases of magmatism occurred within a ~1 – 1.5 Ma period, and that later magmatism took place in the north while primary crustal accretion was still ongoing in the south (Goodenough et al., 2010; Rioux et al., 2012a, 2013). Taken together, the weight of the evidence is against a true MOR origin for the Semail ophiolite.

1.2.2 The effect of water on SSZ-type magmatism

The observation that oceanic crust can also be produced in marginal basins near subduction zones raises the question as to how this lithosphere is similar and/or different to oceanic lithosphere accreted at 'true', open-ocean MORs. Because this is still poorly understood, ophiolites such as Semail continue to be used as MOR analogues, with the significance of SSZ-type volcanism sometimes downplayed (e.g., Nicolas and Boudier, 2011). Marginal ocean basins in the vicinity of subduction zones are potentially crucially different from MORs, however, due to the presence of subduction-derived water in the magmatic system. Consequently, magma generation and subsequent differentiation are affected, as outlined below.

Dehydration of the subducted slab is accompanied by the mobilisation of fluid-mobile elements from the slab into the overlying mantle wedge. Partial melting of the mantle is promoted by the lowering of the solidus temperature by water, allowing previously depleted mantle in SSZ-settings to be molten to a greater extent compared to abyssal (MOR) peridotites, as recorded by residual chrome-spinels compositions (Dick and Bullen, 1984; Arai, 1994). Experiments show that the presence of water and lower melting temperature result in a relative increase in clinopyroxene stability and consequently different melt compositions compared to dry peridotite melting (Gaetani and Grove, 1998). The depleted nature of the mantle source, compared to a MORB mantle source, is apparent from trace element systematics of the erupted basalts, such as lower Y contents for a given Cr content (Pearce et al., 1984), lower Ti and other high field strength element contents and lower La/Yb ratios (Ewart and Hawkesworth, 1987; Woodhead et al., 1993; Godard et al., 2006). Besides a depleted mantle component, an additional enriched mantle component is required for the formation of some back-arc basin basalts (e.g., Price et al., 1990; Pearce and Stern, 2006). The

presence of water during melting also affects the oxidation state of the mantle, which is reflected by a higher incompatibility of vanadium in oxidising condition, resulting in V/Ti enrichments in magmas (Shervais, 1982). Additionally, fluid-mobile elements result in specific trace element anomalies in SSZ basalts, such as Th/Yb enrichments and elevated large ion lithophiles (LIL) with respect to MORB (Pearce et al., 1984).

Although some basalts that erupt at spreading ridges in back-arc basins (back-arc basin basalt, BABB) are similar in composition to MORB, others fall on distinct liquid lines of descent that have lower FeO and TiO_2 and higher Al_2O_3 for a given MgO content (e.g., Fryer et al., 1981). A later appearance of plagioclase as a crystalising phase in more hydrous systems has been proposed as an explanation for the relative enrichment in Al_2O_3 (Sinton and Fryer, 1987). A hydrous control on the mineral phase relations during magmatic differentiation has also been proposed for the Semail ophiolite, where a delayed plagioclase crystallisation and relatively early onset of clinopyroxene crystallisation result in an elevated Al_2O_3 differentiation trend and a less pronounced enrichment of TiO_2, respectively (MacLeod et al., 2013). It is also consistent with the widespread occurrence of wehrlites, indicating clinopyroxene before plagioclase crystallisation, as well as magmatic amphibole, requiring water to form, in the Semail lower crust (e.g., Koepke et al., 2009, 2021; De Graaff et al., 2019).

In summary, although MORs and SSZ-spreading centres are both sites of plate separation and crustal accretion resulting from seafloor spreading, differences in melt generation and subsequent evolution lead to compositional differences in the magmas. Because magma differentiation by progressive crystallisation can also affect magma density and viscosity, the chemical differences can result in differences in physical properties. This in turn potentially affects processes such as melt transport, crystal-melt separation, eruption mechanisms and internal crustal structure, although these remain to be investigated. As such, the analogy between SSZ-type ophiolites and mid-ocean ridges remains contentious.

1.3 Masirah: a rare MOR-type ophiolite

1.3.1 Research aims and rationale

A notable exception to the 'supra-subduction' suite of ophiolites is the Masirah ophiolite, exposed on an island off the south-eastern coast of Oman. It is believed to represent a fragment of slow-spread, N to E-MORB ocean crust from the early stage of formation of the Indian Ocean (Peters, 2000). As a 'true' MOR ophiolite it offers a unique opportunity to test current models of seafloor spreading without the complicating influence of subduction geodynamics.

The most comprehensive study to date on Masirah was carried out by the University of Bern, Switzerland, as part of a geological mapping campaign in the 1990s (Masirah North and Masirah

South, 1:50 000; Peters et al., 1995). It concluded that the magmatic crust at Masirah was thin (1.5 – 2.0 km) due to a reduced magma supply, but nevertheless followed the classical layered ophiolite pseudo-stratigraphy of the Penrose model (Peters et al., 1995; Peters and Mercolli, 1997, 1998; Marquer et al., 1998). The Swiss model was informed by the dominant models of oceanic lithosphere at the time, and as such interpreted any disruptions to the Penrose layer-cake to result from later tectono-magmatic events, unrelated to the initial seafloor spreading. In their reconstruction, the bulk of the igneous crust was formed at a MOR, which, due to the thin nature of the crust, they inferred to be at a low melt-supply spreading-segment end near a transform fault (Peters and Mercoli, 1998). The accretion of primary oceanic crust was followed by the emplacement of an alkaline gabbro-dolerite-granite plutonic suite and associated alkaline seamount volcanism roughly 20 Ma later during renewed, off-axis magmatic activity, accompanied by rifting and differential uplift (Meyer et al., 1996; Immenhauser, 1996; Peters and Mercolli, 1997, 1998; Marquer et al., 1998).

As outlined in this introduction, subsequent oceanic research has however shown that features such as thin or 'missing' gabbroic crust and exposures of mantle at the seafloor may be commonplace along modern slower-spreading MORs (e.g., Cannat, 1993, 1996; Dick et al., 2003; Escartin et al., 2008; Sauter et al., 2013). In itself, therefore, this new insight justifies a re-evaluation of the geological complexities of the Masirah ophiolite: were there indeed separate events relating to on- and off-axis processes, or can the documented complexities instead all be attributed to seafloor spreading?

The aims of this study are to address the following questions:

- What was the nature of the magmatism recorded in the Masirah Ophiolite?
- What was the architecture of the oceanic lithosphere that accreted at the Masirah paleo-ridge?
- What conditions in the mantle were responsible for the lithospheric accretion processes that took place at this particular spreading ridge?
- Should we expect that similar processes are occurring at present-day mid-ocean ridges?

1.3.2 Thesis outline

To address these questions, an integrated multidisciplinary study was undertaken from 2017 to 2022, in which a variety of geological techniques were applied. This thesis presents the results of that study and is organised as follows:

Chapter 2 will review the regional geology of Masirah and summarise the previous work that has been undertaken on the ophiolite, setting the framework for the present study. Chapter 3 outlines the various methodologies and analytical techniques that were used throughout this study. It also presents a compilation of previously collected geochemical data ('MasirahDB') that will be referenced in later chapters. Chapter 4 is a critical assessment of the Swiss model for the evolution of Masirah. By synthesising field observations and presenting new dyke and lava geochemistry, gabbro mineral chemistry and radiometric geochronological constraints, the MOR-origin of the ophiolite is confirmed and the case is made that rather than two separate magmatic events, Masirah records crustal accretion transitioning into 'near-axis' magmatism. The implications of this for the tectonic setting of the Masirah paleo-ridge are discussed. Having established the timing and nature of magmatism on Masirah, Chapter 5 attempts to reconstruct the lithospheric architecture and establish the conditions of crustal accretion by examining magnetic dyke-flow directions, mineral compositions of the plutonic lower crust and estimates of the bulk crustal composition. It concludes that the architecture of Masirah, dubbed 'Penrose on a diet', is very different to what current models predict and discusses the implications for interpreting observations of modern ocean lithosphere. Chapter 6 examines the conditions that could have led to a reduced melt supply at the Masirah paleo-ridge by studying the mineral chemistry of the mantle section. Using spinel geochemistry, it is shown that, contrary to what one might expect, the mantle has undergone extensive melting and the argument is put forward that mantle fertility underneath the Masirah paleo-ridge was the primary control on melt supply and the resulting crustal architecture and geochemistry. Chapters 4, 5 and 6 are intended to each form the basis for a manuscript to be submitted to peer-reviewed journals. Finally, Chapter 7 presents the conclusions of this study and outlines several avenues for future work.

Most of the work and data collection presented in this thesis is the authors own. The high-precision geochronology ID-TIMS U-Pb zircon analyses, as well as the associated cleanlab procedures and data reduction, were performed by Dan Condon at the NERC Isotope Geosciences Laboratories (NIGL) of the British Geological Survey (BGS), Keyworth. Whole-rock major and trace element analyses and data reduction were performed by Mareli Grobbelaar-Moolman and Riana Rossouw at the Central Analytical Facilities, Stellenbosch University, South Africa. Thin-sections were prepared by Tony Oldroyd at Cardiff University.

2. Geological setting and previous work on the Masirah ophiolite

2.1 Regional geology

2.1.1 Geological setting of the Eastern Oman Ophiolite belt

The Eastern Oman Ophiolites (sometimes referred to as the Eastern Ophiolite Belt or the Masirah Ophiolites) comprises a series of ophiolite exposures in the Batain coastal area (between Ra's al Hadd in the north and Ra's Madrakah in the south, Figure 2.1a and b) and Masirah Island. Masirah Island, with most of its ~650 km^2 areal extent consisting of ophiolite exposure, is the largest outcrop of the belt. Other ophiolite outcrops include Ra's Madrakah (~10 km^2), several small hills near Ra's Jibsch (~1 – 2 km^2) and dismembered fragments in the Batain region (ranging hundreds of m^2 to several km^2) (Shackleton et al., 1990; Shackleton and Ries, 1990; Immenhauser et al., 2000). Originally thought to represent a dextral displacement of a dislocated segment of the Tethyan Semail Ophiolite (e.g., Moseley, 1969), later work established that Eastern Ophiolites are entirely unrelated and formed much earlier as part of the young Indian Ocean basin (Peters and Mercolli, 1998). Previous age determinations of Masirah are based on radiometric dating and biostratigraphy of the sedimentary cover, and suggest formation during the Upper Tithonian (Late Jurassic, ca. 150 Ma, Peters et al., 1995; Immenhauser, 1996). The Eastern Ophiolites are thrusted over the Batain group, a series of heavily deformed allochthonous Lower Permian to Upper Maastrichtian sediments and volcanics (Gnos et al., 1997; Immenhauser et al., 1998). The ophiolites and Batain group were emplaced onto the continental margin sometime between the late Maastrichtian and early

Figure 2.1 (next page): *(a) Map of the northwestern Indian Ocean basin (after Gnos et al., 1997) showing the location of Oman with respect to the modern Indian Ocean. Thick black lines represent active spreading ridges, thick brown lines indicate transform and convergent plate boundaries, thick blue lines indicate extinct spreading ridges and magnetic anomalies are shown as labelled thin black lines (M22-M0 are magnetic anomalies between 152 and 118 Ma, while 34-21 indicate anomalies between 84 and 50 Ma). (b) Map of the Owen Basin showing the location of the Eastern Oman Ophiolites (including Masirah), Batain Nappes and Semail Ophiolite (after Beauchamp et al., 1995 and Immenhauser et al., 2000; bathymetry from Whitmarsh, 1979). (c) Simplified interpretation of a seismic cross-section across the Masirah Graben (location in b), showing a double vergent structure within the Batain Nappes that are thrust over the Masirah Graben and crystalline basement (modified from Beauchamp et al. 1995 and Rodriguez et al., 2020). (d) Interpretation of the deep structure of the Owen Basin based on a wide-angle seismic cross-section (location in b) showing the varying depth of the Moho (after Barton et al., 1990 and Peters, 2000). The ophiolite nappes (green) are shown extending into the Owen Basin up to the Owen Ridge (labelled 3), as proposed by Peters (2000). Other authors argue the eastern extent of the ophiolites is situated at the continental margin (1) or within the Owen Basin (2, see also dotted pink line in panel b) (See text for further discussion).*

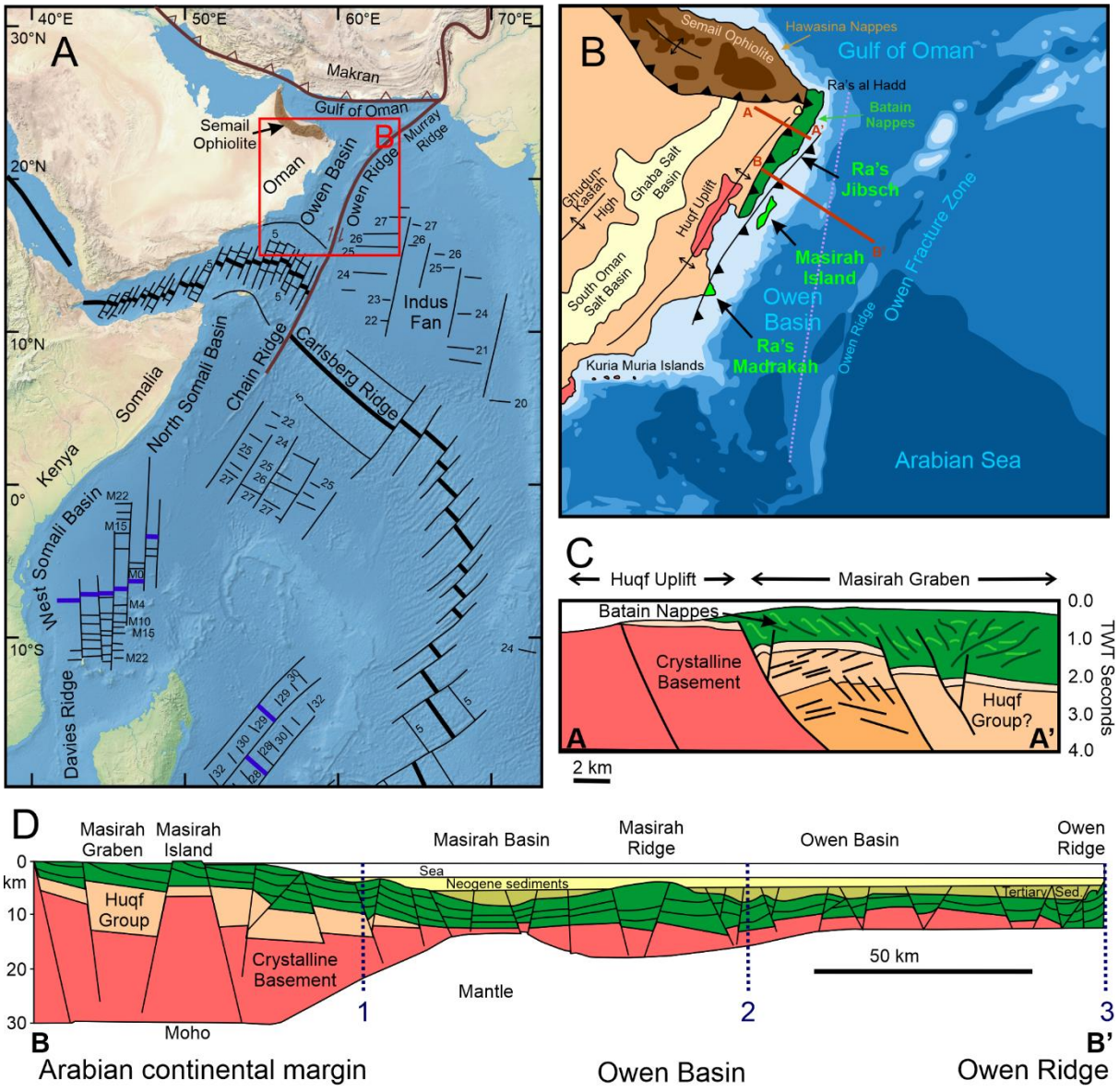

Palaeogene according to stratigraphical constraints, and form a thin-skinned NW-directed fold-thrust belt covering the autochthonous rock units of the Huqf uplift and the Masirah Graben, a Mesozoic sedimentary basin (Figure 2.1c, Beauchamp et al., 1995; Schreurs and Immenhauser, 1999; Immenhauser et al., 2000). Extensional tectonics in the Miocene, related to the opening of the Gulf of Aden, reactivated pre-existing faults and formed a horst-graben structure that exposes the ophiolites today (Immenhauser et al., 2000).

2.1.2 Relation to present-day Indian Ocean Crust

The western Indian Ocean immediately offshore south-east from Oman is marked by the Owen Basin, which is bounded by the Owen Ridge and Owen Fracture Zone (OFZ) to the east (Figure 2.1b). Seismic profiles indicate a continuity between the Eastern Ophiolites and the oceanic crust in the

Owen Basin, implying a common history (Barton et al., 1990; Mountain and Prell, 1990; Beauchamp et al., 1995; Rodriguez et al., 2020). Furthermore, ODP drilling on the continental margin near Ra's Madrakah showed that the sedimentary strata covering basement rock were identical to the post-emplacement sediments that unconformably overly the ophiolites, similarly arguing for a continuity between the basement and the ophiolites (Prell et al., 1990). Based on the seismic continuity and a mapping campaign on Masirah Island, Peters (2000) interpreted that the Eastern Ophiolites expose the top of a series of stacked ophiolite thrust-nappes that extends eastwards into the Indian Ocean (Figure 2.1d). Masirah Island exposes two of these nappes, while Ra's Madrakah likely consists of a third nappe (Marquer et al., 1995; Peters, 2000; Immenhauser et al., 2000). Thrust-nappes are also observed on seismic profiles (Figure 2.1c, Beauchamp et al., 1995; Rodriguez et al., 2020), and on Masirah, the basal detachment fault of the Upper Nappe is sporadically exposed, displaying top-to-south shear deformation (Marquer et al., 1995).

The eastern extent of the ophiolite nappes is debated, however, with different authors placing the boundary at the current Arabian-Indian plate boundary at the Owen Ridge and Fracture Zone (labelled 3 in Figure 2.1d; e.g., Whitmarsh, 1979; Peters, 2000), at the continental margin (1 in Figure 2.1d; e.g., Mountain and Prell, 1990), or in between, at an abandoned transform plate-boundary dissecting the Owen Basin (2 in Figure 2.1d; e.g., Royer et al., 2002; Rodriguez et al., 2016, 2020). The discussion is intertwined with an ongoing debate about the origin of the Owen Basin and changes in location of the Arabian-Indian plate boundary through time (e.g., Whitmarsh, 1979; Mountain and Prell, 1990; Gnos et al., 1997; Peters, 2000; Gaina et al., 2015; Rodriguez et al., 2016, 2020). Peters (2000) proposed the nappes extend to the Owen Ridge, 200 km into the Indian Ocean, where the oceanic crust has a typical seismic structure (Barton et al., 1990). This would suggest a Late Jurassic age for the entire Owen Basin and a long-lived OFZ plate boundary, as proposed by Whitmarsh (1979), linking the basin's formation to the earliest opening of the Indian Ocean, analogous to the North Somali, West Somali and Mozambique basins further south (Gnos et al., 1997; Peters, 2000). DSDP Drilling at the Owen Ridge, however, recovered Late Palaeocene and mid-Eocene sediments overlying sea-floor basalts that can be traced to the centre of the basin along seismic lines (Whitmarsh et al., 1974; Mountain and Prell, 1990). Mountain and Prell (1990) concluded that the oceanic crust of the Owen Basin can therefore not be older than Late Cretaceous, consistent with their depth estimations based on thermal subsidence, and proposed that the Arabian-Indian plate boundary was at the Oman continental margin during Cretaceous times. Their model does not account for the preservation of the Eastern Ophiolites of Late Jurassic age, however. A more recent plate-tectonic reconstruction, based on an extensive geophysical survey of the Owen basin, proposed that the OFZ is a much younger feature and that an abandoned transform plate

margin runs obliquely through the Owen Basin, separating Late Jurassic crust in the western basin from Paleogene crust in the eastern basin, thus reconciling the contradicting ages proposed in previous studies (Royer et al., 2002; Rodriguez et al., 2016, 2020). Such a juxtaposition of oceanic crust with contrasting ages is, however, not reflected in differences in lithospheric subsidence or thickness of sedimentary cover (Gaina et al., 2015). Alternatively, the ophiolites may represent remnants of a Late Jurassic proto-Owen basin that later subducted, whereas the present-day Owen basin formed in the Late Cretaceous (Gaina et al., 2015).

2.1.3 Proposed paleogeographic origin for Masirah

Peters and Mercolli (1998) note that the Late Jurassic age of Masirah places its origin at the earliest phase of the opening of the Indian Ocean, when India-Australia-Antarctica separated from Africa-Arabia. Late Jurassic seafloor has been observed in the present-day Mozambique and West-Somali basins, where magnetic anomalies indicate highly oblique crustal accretion along E-W aligned spreading centres offset by long north-trending transform faults (Segoufin 1978; Segoufin and Patriat 1980; Rabinowitz et al. 1983; Cochran, 1988). A similar origin has been proposed for the North-Somali basin, but is controversial (Bosellini, 1986; Cochran, 1988; Gaina et al., 2015). Half spreading rates during the formation of these basins are estimated to be 10 – 20 mm/yr (Rabinowitz et al., 1983; Cochran, 1988; Gaina et al., 2015).

A paleomagnetic study on Masirah determined a paleo-latitude of 38° S ± 12° at its origin, placing it south of the Arabian continental margin and near the present-day Somali basins (Gnos and Perrin, 1996). As a result of a calculation error, the paleo-latitude was corrected to 48° S ± 12° by Peters (2000). Gnos and Perrin (1996) also concluded that the apparent polar wander path of Masirah fits the Indian Plate. Based on this, Gnos and Perrin (1996) and subsequent tectonic models proposed that Masirah formed off the coast of Africa as part of the Indian Plate during the opening of the Indian Ocean, and that it was subsequently transported northwards when the Indian Plate changed direction to ultimately collide with Eurasia and form the Himalayans (Gnos et al., 1997; Peters and Mercolli, 1998; Peters, 2000). It must be noted, however, that the study of Gnos and Perrin (1996) relies on a tilt correction of the sampled lavas, for which they use the bedding orientation of the overlying sediments. This approach is complicated by the deformation related to nappe thrusting, which is concentrated in the sediments. In absence of further evidence, it is at present not possible to assess the robustness of their polar wander path. Alternatively, a plate reconstruction by Gaina et al. (2015) places the origin of Masirah off the Arabian Margin at 20 – 26° S, in a proto-Owen basin.

2.1.4 Ophiolite emplacement

Multiple authors have suggested that emplacement of the ophiolite thrust nappes occurred during transpressive strike-slip plate motions (Barton et al., 1990; Peters, 2000; Rodriguez et al., 2016, 2020). Geophysical surveys indicate that the continental margin is narrow (< 100 km) and lacks a magnetic anomaly quiet zone usually encountered at passive margins (Mountain and Prell, 1990). Barton et al. (1990) noted that a steep westerly dipping reflector underneath the continental slope, interpreted as the Moho, is the exact opposite orientation of the tectonic fabric predicted by emplacement through simple overthrusting. Instead, the deep seismic structure of the south-eastern Oman continental margin reveals a highly variable thickness of the crystalline crust and a rough seafloor marked by several ridges, suggestive of a strike-slip tectonic regime (Figure 2.1d; Barton et al., 1990). The seafloor ridges are most prominent closest to the continental margin and have been interpreted by Rodriguez et al. (2016, 2020) to be en-échelon structures of an abandoned transform plate-boundary, analogous to modern transform ridges. Their reinterpretation of the seismic profile from Beauchamp et al. (1995) shows the heavily deformed Batain group as a doubly-vergent thrust stack of numerous ophiolite sheets, forming a positive flower structure (Figure 2.1c; Rodriguez et al., 2020). A strike-slip plate motion during emplacement is also consistent with the occurrences of Cretaceous strike-slip features on the Oman mainland (Rodriguez et al., 2016). Furthermore, the lack of an exposed metamorphic sole in the Eastern Ophiolite Belt is compatible with an emplacement mechanism that does not involve subduction (e.g., Wakabayashi and Dilek, 2003).

2.2 Masirah Island

2.2.1 Previous work

Early work and subsequent mapping campaigns on Masirah identified the presence of a full ophiolitic suite, including mantle, gabbros (*sensu lato*), dykes, lavas and an autochthonous sedimentary cover, discordantly overlain by Paleogene limestones (Lees, 1928; Moseley, 1969; Glennie et al., 1974; Moseley and Abbotts, 1984; Le Métour et al., 1992; Peters et al., 1995). The original ophiolite sequence is disrupted by later faulting and local block tilting, hindering the study of an uninterrupted section through the original ocean lithosphere. This structural complexity, especially prominent along the western coast, was initially classified as a tectonic 'ophiolite melange' consisting of metre- to kilometre-sized blocks of ophiolitic lithologies and exotic limestones, and possibly representing a large strike-slip fault or a fossil transform fault zone (e.g., Abbotts, 1979a; Moseley and Abbotts, 1979; Moseley 1990; Shackleton and Ries, 1990). A detailed mapping campaign carried out by the University of Bern (Figure 2.2, Peters et al., 1995) identified a regionally persistent (island-wide) recurring sub-horizontal thrust contact separating the deformed autochthonous sedimentary cover of the ophiolite from overlying mantle harzburgites.

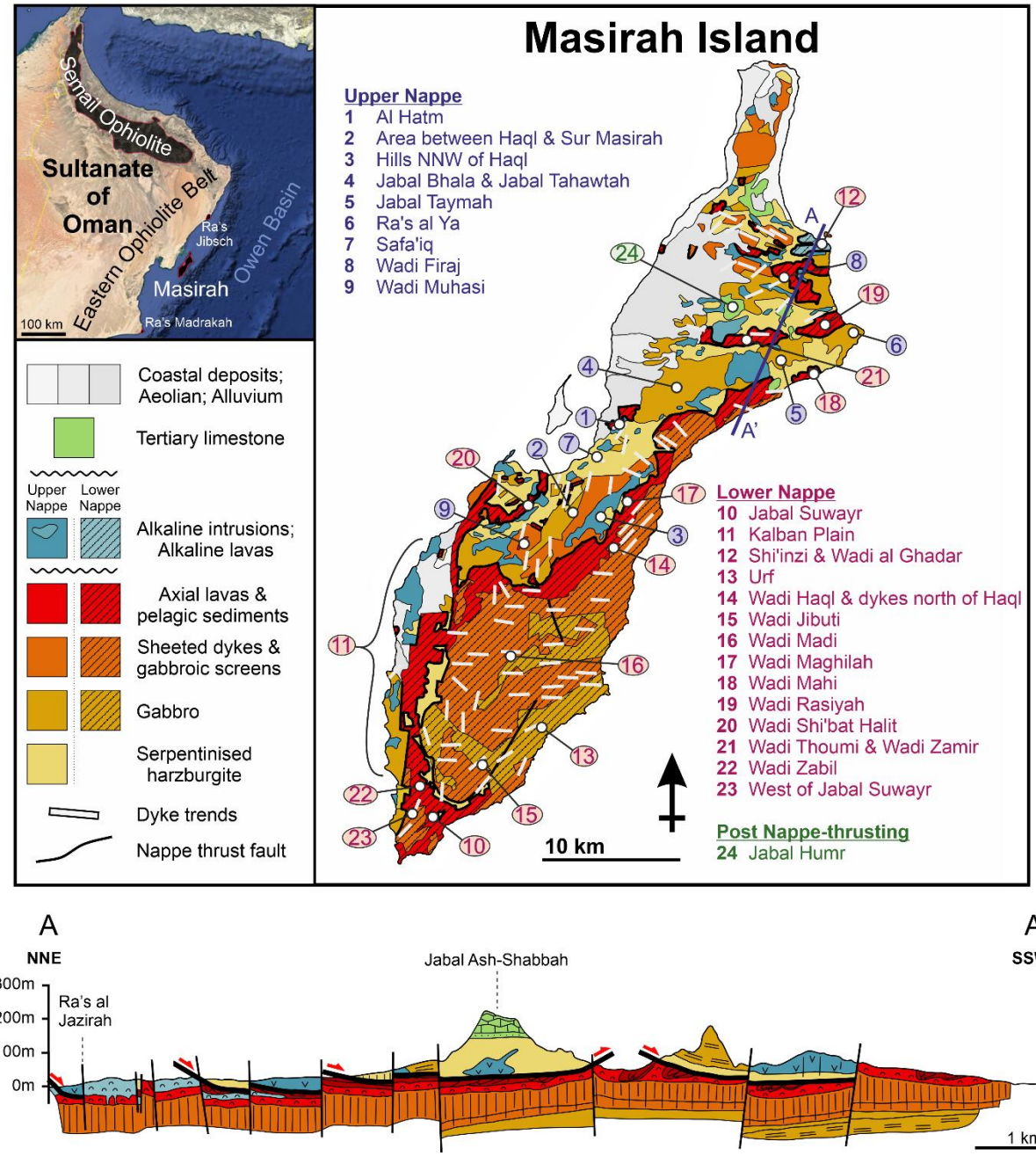

Figure 2.2: *Geological map of Masirah with an overview of the sites mentioned in this thesis. The structural cross section through the north of the island illustrates the relationship between the Upper and Lower Nappes (adapted from Peters et al., 1995).*

They rejected the melange-designation and proposed instead that Masirah exposes two ophiolite nappes. This view has been corroborated by seismic profiles of the region (Beauchamp et al., 1995; Rodriguez et al., 2020). In the revised interpretation of the Swiss group, many lithological contacts on their map are tectonic, arising from interference between Tertiary (i.e., post-emplacement) normal faulting and the low-angle thrust fault (e.g., Marquer et al., 1995, 1998). Despite this apparent complexity, the internal structure of the nappes themselves appears to be relatively

coherent, preserving near-vertical sheeted dykes, layered gabbros sub-parallel to the crust-mantle boundary, and a gradual transition between the upper and lower crust. By combining many different structural sections Marquer et al. (1998) established that the composite thickness of the original igneous oceanic crust was as little as 1.5 – 2.0 km, of which the gabbroic lower crust makes up <500 m, the dyke complex ~1 km and the lavas 250 – 500 m.

The geology of Masirah Island is variable geographically. The south and south-east part of the island contains the main Lower Nappe exposures and resembles a classically layered oceanic crust: a mantle section, a lower crust of layered olivine gabbro intruded by dunitic bodies, succeeded by foliated gabbro intruded by an upward increasing proportion of dolerite dykes that grade into a sheeted dyke complex, which in turn is overlain by volcanics and deep-marine sediments (Peters et al., 1995). The lower-crust/mantle boundary is only rarely exposed. A considerable part of the dolerite dyke complex, which comprises most of the interior of South Masirah, consists of metre-sized parallel dykes and gabbroic screens, with dyke proportions ranging from 0 to 100% and increasing up-section. A true 'sheeted' dyke complex with 100% dyke-in-dyke intrusions is limited to the upper-most part of the dyke complex. Mantle outcrops are sparse, and near Jabal Suwayr (at the southernmost point of the island) they are intruded by swarms of locally parallel dolerite dykes and overlain by shallow-marine limestones. Lavas and overlying sediments of the Lower Nappe are also exposed in parts of the northern part of the island. The dykes and lavas have a N-MORB to E-MORB geochemical character (Peters and Mercolli, 1998). Near Shi'inzi, lavas have a distinct alkaline nature (Abbotts, 1979a) and the presence of volcanic edifices, subvolcanic stock-like intrusions, vent agglomerates, pyro- to epiclastic deposits, and lavas intercalated with marine sediments, were interpreted as the remnants of small submarine seamount volcanoes that originally were up to a few kilometres in diameter and a few hundred metres high (Meyer et al., 1996). Isotopic compositions indicate that the main ophiolite suite and the alkaline suite have distinct mantle sources (Mahoney et al., 1998).

The main Upper Nappe exposures, in the north and north-west of Masirah, consist of more extensive mantle sections, some which are intruded by varying proportions of gabbro and/or dolerite dykes, in addition to a well-exposed lower crust. The dyke complex is less prominent in the north, but better developed in the west near Sur Masirah. Lavas associated with the Upper Nappe are rare, and no sedimentary cover is exposed. Characteristic of this region is the occurrence of an alkaline gabbro-dolerite-granite suite of metre to kilometre-sized bodies that intrudes the pre-existing lithosphere, mainly in the mantle and at the crust-mantle boundary level, and that is absent in the Lower Nappe. Minor ductile deformation in this suite records syn- and post-emplacement extension within the plutons, and brittle extension is indicated by the late crosscutting dykes (Marquer et al., 1998). The

gabbros are isotropic-pegmatoid and have a distinct hornblende-bearing mineral assemblage. The granites are 'true' K-feldspar bearing granites and were previously interpreted to be obduction related (Abbotts, 1978; Smewing et al., 1991; Gaina et al., 2015), although Nägler and Frei (1997) showed that Pb and Nd isotopes were consistent with an oceanic mantle rather than a continental origin.

The pre-Tertiary sedimentary cover is restricted to the Lower Nappe and subdivided into three chrono-stratigraphic units: Maghilah unit, the Kalban unit and the Fayah unit (Peters et al., 1995; Immenhauser, 1996). Although biostratigraphical constraints indicate continued accumulation of sediments on Masirah from formation (Upper Tithonian, ca. 150 Ma) until emplacement (late Maastrichtian, ca. 65 Ma), individual sedimentary sections are incomplete and cross-correlation is complicated by lateral facies variation within the units and the occurrence of non-deposition and/or erosion in some parts of the island (Immenhauser, 1996). The Maghilah unit (~Tithonian – Barremian/Aptian) occurs mainly in the northern and eastern half of the island and concordantly overlies the upper crustal pillow lavas. Beds of radiolarian micrite and ribbon cherts record deep-marine sedimentation that is interrupted by a discontinuous horizon of alkaline volcanic breccia near the top of the unit, interbedded with sediments of Upper Hauterivian – Lower Barremian age (130 – 125 Ma), indicating that the youngest volcanic activity occurred off-axis (Immenhauser, 1996). The Kalban unit (~Barremian/Aptian – Santonian) occurs mainly in the southern and western coastal plain and in the north near Shi'inzi. It is deposited unconformably on an erosional surface and overlies various denuded ophiolite units and the alkaline volcanic breccia where present. The facies of the Kalban unit varies laterally from shallow-marine platform carbonates, to hemi-pelagic limestones and cherts that interfinger with platform detritus, to pelagic radiolarian cherts (Immenhauser, 1996). Although not observed covering the Maghilah Unit, the Kalban Unit is interpreted to be younger based on age constraints from microfossils, while the occurrence of clasts of Kalban carbonates within distal turbidites (consisting of ophiolite material and carbonate breccia) in the upper levels of the Maghilah Unit indicates some overlap in their existence (Immenhauser, 1996). The Fayah unit is the youngest pre-emplacement unit (~Coniacian – Maastrichtian), determined by microfossils rather than a stratigraphic contact with the Kalban Unit. It consists of sandstones, shales, clays and conglomerates, and is characterised by siliciclastic flysch-like sediments and exotic blocks, marking an influx of continental detritus (Immenhauser, 1996).

2.2.2 Outstanding questions addressed in this thesis

The work of the Swiss group has established that the Masirah Ophiolite is exposed in two tectonic nappes and that the MORB-like axial crustal sequence is overprinted by alkaline magmatism which produced plutons, dykes and lavas. The relation between the Upper and Lower Nappes is not well

constrained, however. Additionally, a reconstruction of the axial crustal sequence is complicated by the fact that the later plutonic and volcanic suites cannot always be clearly identified as such based on their field characteristics. Whereas stratigraphical criteria can be used to identify the relative ages of lavas, clear crosscutting relationships for the dykes and plutons are not always present in the field. On the 1:50 000 geological map of Peters et al. (1995), the units are mapped by lithology rather than by magmatic phase (i.e., the axial or alkaline suite), so that the extent of the later magmatism consequently remains poorly defined. It is unclear for example whether the smaller occurrences of isotropic gabbro throughout the Masirah ophiolite belong to the later suite or form a part of the regular lower crust but locally lack typical magmatic fabrics. The geochronology for Masirah also remains relatively poorly constrained. As mentioned, the currently accepted age for the accretion of the Masirah oceanic lithosphere is ~150 Ma, determined by radiometric dating and biostratigraphical constraints. The radiometric dates have not been published in full, however, and contain significant uncertainties (Peters et al., 1995). The sedimentary constraints are also not waterproof, due to the incomplete nature of stratigraphic sections and the difficulties in cross-correlating them, and rest primarily on an accurate interpretation of the microfossil assemblages.

These questions are addressed in Chapter 4. It provides a thorough characterisation of the field characteristics and geochemistry of the gabbros, dykes and lavas of the axial suite and alkaline suite, and assesses their differences and similarities. High precision U-Pb dating of zircons provides a new geochronological framework in which the relation between the Upper and Lower Nappe, as well as the relation between the axial and alkaline magmatism is better constrained. To aid the geochemical characterisation of the various suites and place the results of this study in an overall context, all previously collected geochemical data was compiled into a 'MasirahDB' database, the details of which are described in the methods chapter (Chapter 3).

3. Methodology

3.1 Overview of applied techniques

This chapter presents the methodology of the various analytical techniques that were used throughout this study. The different datasets are presented in the subsequent chapters to address the research aims of this thesis. The field observations are subdivided over chapters 4, 5 and 6, according to their relevance for each chapter. To avoid repetition in later chapters, some sections will reference back to preceding chapters. The whole-rock major and trace element compositions and U-Pb ID-TIMS zircon geochronology are presented and discussed in Chapter 4. The mineral chemistry data for samples from the igneous mafic rocks are discussed in part in Chapter 4 and in part in Chapter 5, whereas the mineral chemistry of the mantle peridotites forms the basis of Chapter 6. The dyke flow directions from anisotropy of magnetic susceptibility (AMS) are presented in Chapter 5. Lastly, MasirahDB, a compilation of all available geochemical data for Masirah, is referenced in Chapters 4, 5 and 6.

3.2 Field Campaign

Fieldwork on Masirah was carried out from the 8th of January to the 10th of February in 2018, during which a total of 29 field days were spent on Masirah Island (Table 3.1), for the most part in campsites set up near outcrops. Observations were made at various localities that together provided a good coverage of the island and overall picture of the ophiolite units mapped by Peters et al., (1995). The accessibility of outcrops was good and most locations could be reached with a 4WD vehicle by navigating graded roads and wadis. A total of 373 samples were collected and shipped to Cardiff University for further petrographic and geochemical analysis (see Table I for an overview). For the nomenclature of villages, capes (ra's) mountains (jabals) and dry riverbeds (wadis), the names and spelling of the map of Peters et al. (1995) were followed as closely as possible, which is based on the series K 768 Masirah North and South topographic maps. Names of features not labelled on the geological map were obtained from the OpenStreetMap project database. All GPS coordinates are UTM grid (WGS84) in decimal format.

Table 3.1. Participants and schedule of the Masirah 2018 field campaign

Name	Affiliation	Dates in the field
Max Jansen	PhD student, Cardiff University	8-16 January; 18-28 January; 2-10 February
Chris MacLeod	PhD supervisor, Cardiff University	8-16 January
Johan Lissenberg	PhD supervisor, Cardiff University	10-16 January
Benoit Cordonnier	Field assistant, University of Oslo & ESRF	18-28 January
Chris Tulley	Field assistant, Cardiff University	2-10 February
Said Almusharafi	Geologist, Public Authority of Mining	3-5 February

3.3 Whole-rock major and trace element geochemistry

3.3.1 Sample selection & trace element characterisation with pXRF

A total of 47 samples were selected for whole-rock (WR) geochemical analysis (12 lavas, 13 dyke margins crosscutting igneous crust, 16 dyke-margins crosscutting mantle peridotites, and 6 of the leucocratic lithologies that were also targeted for geochronology).

Dykes were selected from a larger group of 65 samples based on an initial characterisation of selected trace elements using a portable X-ray fluorescence (pXRF) spectrometer at Cardiff University. A fresh surface of >4 cm^2 was cut using a diamond bladed saw. Samples were positioned in a sandbox for stabilisation and *in situ* elemental analyses were carried out with an Olympus Delta InnovX pXRF device. The excitation source is a 4 W X-ray tube with a rhodium anode providing a beam spot size of ~10 mm in diameter. The pXRF system contains a large area Silicon Drift X-ray Detector (SDD). Analyses were conducted at 20 kV for 30 seconds live time and seven to ten repeat measurements of the same spot were averaged per sample. Precision and accuracy were monitored by repeat measurements of secondary standard reference material spanning a range of mafic to felsic igneous compositions (Bulk SiO_2, 2710a, KC1, HV, MRG, JB1a, JG3, JR1, SDO1 and JA2; reference values from GEOReM, Jochum et al., 2005) and Ti, Zr and Y concentrations were found to be the most quantitatively reliable. A few dyke margins were tested for intra-sample heterogeneity by measuring multiple spots, which were found to be within error.

3.3.2 Sample preparation for whole-rock analyses

Samples were powdered at the rock preparation facilities at the School of Earth and Ocean Sciences, Cardiff University, United Kingdom, and sent to the Central Analytical Facilities, Stellenbosch University, South Africa for further preparation and analysis. Weathered surfaces as well as

alteration veins and patches were removed using a diamond bladed rock saw. Care was taken to minimise the crystal content within dyke and lava samples, and in the case of dykes, to isolate the fine-grained to aphanitic chilled margins – more likely to represent melt compositions – from the coarser dyke cores. Samples were subsequently washed in an ultrasonic bath for 10 – 20 minutes (or until no more material came off), dried and crushed to a coarse grit with a steel jaw crusher. Approximately 80 cm^3 sample material was powdered and homogenised in an agate planetary ball mill.

Powders were ignited to 1000°C to determine the loss on ignition (LOI). Glass fusion disks were prepared for XRF and LA-ICP-MS analysis using 7 g of high purity, trace element and rare earth element-free flux ($LiBO_2$ = 32.83%, $Li_2B_4O_7$ = 66.67%, LiI = 0.50%) mixed with 0.7 g of the powder sample (i.e., a sample : flux ratio of 1 : 10). Mixture of sample and flux were fused in platinum crucibles with Claisse M4 gas fluxer at temp between 1100°C – 1200°C.

3.3.3 Major elements

Whole-rock major element compositions were determined by XRF spectrometry on a PANalytical Axios Wavelength Dispersive spectrometer. The spectrometer is fitted with an Rh tube and with the following analyzing crystals: LIF200, LIF220, PE 002, Ge 111 and PX1. The instrument is fitted with a gas-flow proportional counter and a scintillation detector. The gas-flow proportional counter uses a 90% Argon-10% methane mixture of gas. Major elements were analyzed on a fused glass disk using a 3 kW Rhodium tube. Matrix effects in the samples were corrected for by applying theoretical alpha factors and measured line overlap factors to the raw intensities measured with the SuperQ PANalytical software. The concentration of the control standards that were used in the calibration procedures for major element analyses fit the range of concentration of the samples. Amongst these standards were NIM-G (Granite from the Council for Mineral Technology, South Africa) and BE-N (Basalt from the International Working Group). Major element concentrations at relevant concentrations for reference materials BE-N, JB-1, BHVO-1, JG-1, and in-house standards HUSG-1 and WITS-G monitored over the course of a year are reproducible within 0.4 – 4 % with respect to recommended values (from GeoReM, Jochum et al., 2005; and in-house values).

3.3.4 Trace elements

For trace element analysis, the fusion disks were coarsely crushed and a chip of sample was mounted along with up to 12 other samples in a 2.4 cm round resin disk. The mount was mapped and then polished for analysis. A Resolution 193nm Excimer laser from Applied Spectra connected to an Agilent 7700 Q ICP-MS was used in the analysis of trace elements in bulk rock samples following the guidelines of Eggins (2003) (instrument conditions in Table 3.2). Before analysis the ICP-MS was

optimized for sensitivity and low oxide ratios (< 0.2%) by tuning both the ICP and laser parameters while ablating a line on NIST612 reference material. Ablation was performed in He gas at a flow rate of 0.4 L/min, then mixed with a carrier gas of argon (0.9 L/min) and nitrogen (0.003 L/min) just before introduction into the ICP plasma. Two spots of 104 µm were ablated on each sample using a frequency of 8 Hz and fluence of ~3.5 J/cm^2. NIST 610 glass (values from Jochum et al., 2011) was used for quantification and analysed every 15 samples, along with BCR-2G and BHVO-2G reference material (values from GeoReM: Jochum et al., 2005). A fusion control standard from certified basaltic reference material (BCR-2 and BHVO-1, values from Jochum et al., 2016) is also analysed in the beginning of a sequence to verify the effective ablation of fused material. Additionally, two previously analysed lavas from the Semail Ophiolite were included as unknowns for data quality control (89OC115 and 89OC123 from OmanDB; C. MacLeod, unpubl. Data).

Data processing was done using the LA-ICP-MS data reduction software package LADR from Norris Scientific (Norris and Danyushevsky, 2018). In order to correct for variations in ablation yield between standards and samples, an internal standard element of known concentration is used (Longerich et al., 1996). The Al_2O_3 content of each sample, obtained from XRF analysis, was used for this purpose.

Table 3.2. LA-ICP-MS Instrument conditions

ICP-MS Instrument connected to laser	Agilent 7700
ICP-MS Software	Mass Hunter v 4.5
ICP-MS Settings	
RF Power (W)	1350
Carrier gas (L/min)	0.9
Sample depth (mm)	5.5
He Cell gas flow (ml/min)	n/a
H2 Cell gas flow (ml/min)	n/a
O2 Cell gas flow (ml/min)	n/a
Detector type	Photo multiplier

Laser Ablation Instrument	193nm Resolution M50 LR Excimer
Controlling Software	Geostar v 10.09
Laser Settings	
Frequency (Hz)	8
Fluence (J/cm2)	3.5
Spot size (µm)	104
Ablation gas (He) flow (ml/min)	400
Additional gas (N2) flow (ml/min)	2.5
Background acquisition time (sec)	25
Ablation time (sec)	40
Washout time (sec)	25

Calibration stds	NIST 610
Quality Control stds	BCR-2G, BHVO-2G, BCR-2, BHVO-1
Calibration method	Standard – Sample bracketing every 15 – 20 samples

Data processing software	LADR, Norris Scientific

Data quality for the Masirah samples was assessed for each element using the fused powder secondary standard (BCR-2 and BHVO-1) that had trace element concentrations closest to the Masirah samples. The combined precision and accuracy of the trace element analyses was generally better than 10%. In Table 3.3 accuracy is expressed as % deviation from the reference value and precision is expressed as two relative standard deviations from the mean of repeated secondary standard measurements.

Table 3.3. LA-ICP-MS reproducibility of standards

Element	Accuracy (%)	Precision (%)	% Deviation Lava 89OC115	% Deviation Lava 89OC123	Element	Accuracy (%)	Precision (%)	% Deviation Lava 89OC115	% Deviation Lava 89OC123
Sc	1.5	12.3			**Ho**	5.8	4.8	2.6	0.9
V	0.9	1.8	8.8	3.5	**Er**	3.2	5.9	13.0	6.4
Cr	1.1	1.1	31.0	13.3	**Tm**	8.9	7.7	6.2	5.3
Co	4.0	3.1	1.8	10.1	**Yb**	4.2	5.7	3.3	4.5
Ni	6.4	1.7	54.7	64.1	**Lu**	6.1	8.1	3.5	11.0
Cu	8.3	5.1			**Hf**	1.9	5.1	22.0	15.0
Zn	1.8	8.7			**Ta**	2.0	10.5	13.5	1.4
Rb	5.7	3.3			**Pb**	5.0	4.7	73.1	85.2
Sr	1.8	1.8	12.4	23.1	**Th**	2.7	4.9		
Y	8.9	2.2	8.7	10.2	**U**	0.6	7.2	7.1	14.4
Zr	7.3	2.6	24.2	9.5					
					Element ratio				
Nb	9.7	2.0	16.0	5.8					
Mo	33.3	10.0			**Nb/Y**	0.8	2.4	8.0	4.9
Cs	10.3	9.9			**Th/Yb**	1.6	5.9		
Ba	4.4	2.8	76.1	212.5	**Nb/Yb**	5.7	4.7	13.2	1.4
La	3.1	2.0	14.7	6.3	**La/Sm**	0.7	4.4	16.9	8.7
Ce	4.3	2.0	6.2	17.0	**La/Yb**	1.2	6.3	11.9	1.9
Pr	5.7	1.9	7.7	8.4	**Gd/Yb**	1.9	10.8	16.0	12.8
Nd	2.8	3.1	5.3	2.3	**Dy/Yb**	0.2	7.0	3.0	4.7
Sm	2.4	4.0	2.6	2.5	**Eu***	3.4	9.0	9.4	6.4
Eu	5.8	7.3	2.8	1.6	**Dy***	0.2	5.4	7.1	5.4
Gd	2.4	6.5	12.2	7.8					
Tb	8.7	4.5	1.8	1.7					
Dy	4.1	4.1	0.4	0.0					

3.4 Major element mineral chemistry

3.4.1 Analytical Scanning Electron Microscope procedures

Mineral major element compositions were determined at Cardiff University using a Zeiss Sigma HD Field Emission Gun Analytical Scanning Electron Microscope (A-SEM) equipped with two Oxford Instruments 150 mm^2 EDS detectors. Quantitative analyses were conducted with a beam acceleration of 20 kV and an aperture of 60 µm, and a Co reference standard was used to monitor analytical drift at regular intervals. Acquisition time was 15 seconds for silicate minerals (plagioclase, clinopyroxene and olivine) and 20 seconds for Cr-spinels, and the process time was set to 3 seconds.

The EDS analyser was calibrated using ASTIMEX reference material and ASTIMEX olivine, Cr-diopside, plagioclase and chromite were used as secondary standards. Accuracy and precision for relevant elements was generally 1 – 2%. Silicate mineral analyses were rejected for totals of <98.5% and >101.5% and for cation : oxygen ratios that deviated more than 0.5% from a perfect stoichiometric ratio (3:4 for olivine, 4:6 for pyroxene, 5:8 for plagioclase). Cr-spinel analyses were rejected if totals, recalculated after having determined the iron-oxidation state (see next section), were <98.5% or >101.5%. Qualitative element maps were made of a selected number of gabbro samples and Cr-spinel grains using a 20 kV beam acceleration and a 120 µm aperture, with a set dwell-time of 5000 ms and a process time of 1 second.

3.4.2 Cr-spinels stoichiometry and iron oxidation state

Iron oxidation states in Cr-spinel were determined following a correction method developed by Wood and Virgo (1989, hereafter W&V89) and recently reviewed in detail by Davis et al. (2017). W&V89 based this correction on their observation of a systematic offset of the calculated $Fe^{3+}/\Sigma fe$ ratio (using mineral chemistry data and assuming perfect stoichiometry) from the true $Fe^{3+}/\Sigma fe$ ratio (determined by Mössbauer spectroscopy). This offset correlates linearly with spinel Cr#, making it possible to accurately and precisely determine iron oxidation states in spinel on a microprobe through calibration to secondary spinel standards with a known $Fe^{3+}/\Sigma fe$ ratio. For this purpose, four chemically homogenous Cr-spinel samples from the study of W&V89, with $Fe^{3+}/\Sigma fe$ ratios previously determined by Mössbauer spectroscopy, were used as calibration standards. These Fe^{3+}-calibration standards (KLB 8311, KLB 8315, KLB 8316 and MHP 79-1) span the compositional range of the Masirah Cr-spinels (Cr# 0.08 – 0.53, see Chapter 6) and were analysed at regular intervals.

During data reduction, the $Fe^{3+}/\Sigma fe$ correction was applied per session (defined as one workday). The $Fe^{3+}/\Sigma fe_{EMP}$ ratio of the Fe^{3+}-calibration standards was calculated assuming perfect stoichiometry (3 cations : 4 oxygen), assigning iron as Fe^{3+} to make up for any oxygen deficit. The difference between the calculated $Fe^{3+}/\Sigma fe_{EMP}$ and the true $Fe^{3+}/\Sigma fe_{Mössbauer}$ ($\Delta fe^{3+}/\Sigma fe$) was then regressed against Cr# resulting in the linear equation: $\Delta fe^{3+}/\Sigma fe = b + m * Cr\#$. The calculated slope (m) and intercept (b) were then used to correct the $Fe^{3+}/\Sigma fe_{EMP}$ of the samples measured during that session. The $Fe^{3+}/\Sigma fe$ correction for each session is based on ~35 – 50 analyses of the Fe^{3+}-calibration standards. Correlation factors (r^2) for the regressions varied between 0.24 – 0.69. Nevertheless, the W&V89 correction has been shown to improve accuracy even in the case of a poor correlation (Davis et al., 2017). Secondary spinel standards with a known $Fe^{3+}/\Sigma fe$ ratio were not available during this study, but when remeasuring the Fe^{3+}-calibration standards as unknowns during each session, the accuracy of the corrected $Fe^{3+}/\Sigma fe$ ratio is 1 – 3% and precision is 4 – 8%.

3.5 U-Pb ID-TIMS geochronology on zircons

3.5.1 Sample preparation and mineral separation

Nine samples were selected for high precision zircon U-Pb geochronology at the BGS NIGL facilities in Keyworth. Weathered surfaces were removed from the geochronology samples with a diamond bladed saw and rock material was cut into <40 mm pieces. Foreign material was removed using an ultrasonic bath. Mineral separation and subsequent zircon geochronology analysis was done at the NERC Isotope Geosciences Laboratories (NIGL) of the British Geological Survey (BGS), Keyworth. The rock material was processed by high-voltage electric pulse fragmentation in a Selfrag©, which splits rocks along planes of weakness, typically grain boundaries. The material was sieved and the <500 µm fraction was subsequently separated into a light and heavy fraction on a Rogers shaking table. The heavy fraction was further subjected to magnetic separation on a Frantz isodynamic barrier laboratory separator, followed by a heavy liquids density separation step using 3.27 g/cm^3 di-iodomethane. From the remaining material, zircon grains were picked under an optical microscope.

3.5.2 Chemical abrasion, chemical separation and ID-TIMS

Zircons selected for CA-ID-TIMS analysis were chemically abraded following a procedure modified after Mattinson (2005) to remove damaged parts of the crystal that were likely to have experienced open-system behaviour, minimising the effect of Pb-loss. First, the zircons were thermally annealed at 900°C for 60 hours in quartz crucibles before being individually selected, photographed and loaded into FEP Teflon beakers. Single zircon crystals, or fragments, were selected for dissolution using transmitted light microscopy based upon their external morphology and observation of internal feature (i.e., visible cores). Zircons were then refluxed in 4 M HNO_3 on a hotplate at 120°C for > 2 hours, followed by ultrasonic cleaning for at least 20 minutes. The zircon crystals were rinsed with acetone and 4 M HNO_3 and loaded into individual 300 µl FEP Teflon microcapsules and leached in 29 M HF inside a Parr vessel (a self-sealing stainless-steel jacket) for 12 hours at 180°C. The zircons were rinsed with 4 M HNO_3 and refluxed in 6 M HCl at 120°C for 2-5 hours, before a final rinsing with 4 M HNO_3 several times.

The leached zircons and all total procedural blanks were spiked with mixed ^{202}Pb-^{205}Pb–^{233}U–^{235}U (ET535) EARTHTIME tracer solution and dissolved in ~150 µl 29 M HF and trace HNO_3 in a Parr vessel at 220°C for at least 60 hours. Complete dissolution was checked by visual inspection of some larger crystals and assumed for smaller grains, following standard protocol for dissolution at BGS. The solutions were dried down as fluorides and re-dissolved in 3 M HCl in a Parr vessel overnight at 180°C. Uranium and Pb fractions were isolated by HCl-based anion exchange procedure using Bio-Rad AG-1 resin in Teflon columns. Lead and U fractions were then recombined and dried down with

~10 µl of H_3PO_4 and subsequently loaded onto zone-refined Re filaments in a silica gel matrix to enhance ionisation.

Isotope ratios were measured on a Thermo-Electron Triton TIMS. Lead was measured in dynamic mode on a MassCom secondary electron multiplier; Pb mass bias corrections were made using the measured $^{202}Pb/^{205}Pb$ for samples spiked using ET535. Dead-time and linearity of the secondary electron multiplier were monitored using repeated analyses of the standards NBS 982, NBS 981 and U 500. Uranium oxide (UO_2) was measured and corrected for isobaric interferences using a $^{18}O/^{16}O$ value of 0.00205 (IUPAC value and measured in-house at BGS, Condon et al., 2015). Uranium was measured in dynamic mode and a mass bias fractionation correction calculated in real-time using the ^{233}U-^{235}U ratio of the ET535 tracer solutions. Corrections for the addition of Pb and U during the procedure (i.e., laboratory contamination) were made using the long-term measured isotopic composition and variability of blanks using an amount that is based upon contemporary total procedural blanks. The U/Pb ratio for each analysis was determined via isotope dilution principles and the ET2535 mixed ^{202}Pb-^{205}Pb-^{233}U-^{235}U tracer relative to the calibration of that tracer (Condon et al., 2015; McLean et al., 2015). A $^{238}U/^{235}U$ value of 137.818 was assumed (Hiess et al., 2012) and used in the data reduction algorithm. Data reduction was carried out using Upb Redux (McLean et al., 2011), and plotted using IsoplotR (Vermeesch, 2018).

3.6 Dyke flow directions from Anisotropy of Magnetic Susceptibility (AMS)

3.6.1 Analytical procedures

Oriented block samples were taken of chilled dyke margins for the purpose of reconstructing melt flow lineations using the anisotropy of low-field magnetic susceptibility (AMS) as a proxy for the bulk petrofabric (e.g., Knight and Walker, 1988; Staudigel et al., 1992; Tauxe et al., 1998, Borradaile and Gauthier, 2003). The sampled dykes were generally 0.1 – 3 m thick and could be traced for metres to tens of metres in the field. Dyke margin orientations were determined in the field by averaging by multiple compass measurements. Oriented block samples were processed and analysed at the University of Plymouth. Mini-cores (~2.5 cm diameter) were drilled from the oriented block samples with diamond-tipped drill bits and split into standard ~11 cm^3 cylindrical specimens, producing between 1 and 15 specimens per sampled margin (6 on average, all <10 cm from the chilled margin surface). Several fractured and delicate rock samples were reinforced using set resin prior to drilling. The anisotropy of low-field magnetic susceptibility was measured with an Agico KLY-3S Kappabridge at the University of Plymouth and data was processed using Agico Anisoft 4.2 software (Chadima and Jelínek, 2009).

3.6.2 Data reduction and quality control

Two methods were used to derive a mean AMS tensor for each sample. The first is based on Jelinek statistics and is built into the Anisoft software (Jelínek, 1977, 1981; Chadima and Jelínek, 2009). This approach requires a minimum of 5 core analyses per sample and calculates (amongst other things) the orientation and magnitude of the three principal susceptibility axes of the mean AMS tensor (K_{max}, K_{int} and K_{min}), a confidence ellipse for the mean axes orientations, the corrected degree of anisotropy P_J (with $P_J = 0$ being isotropic and $P_J > 0$ indicating anisotropy) and the tensor shape T (where $0 < T < 1$ indicates an oblate shape and $-1 < T < 0$ indicates a prolate shape of the magnetic susceptibility ellipsoid). Since not all dyke margin samples had enough material for 5 or more core specimens (18 out of 51 dyke margins produced <5 cores), a second method using Bingham axial distribution statistics was applied to calculate the mean principal axis and eigenvalue for K_{max}, K_{int} and K_{min} of all samples in Stereonet v. 10.1.1 (Allmendinger et al., 2013; Cardozo and Allmendinger, 2013).

To determine a melt flow lineation from the magnetic fabric ellipsoid, the K_{max} axis of the AMS tensor was projected onto the dyke margin in Stereonet by finding the plane that contains both K_{max} and the pole to the dyke margin plane. The intersection of this 'projection plane' and the dyke margin plane defines the vector K'_{max}, i.e., K_{max} projected onto the dyke margin. Subsequently, the rake of K'_{max} is calculated as the angle between the strike of the dyke and K'_{max} using the dot product equation for these two vectors. The rake represents the plunge of the K'_{max} axis with respect to the dyke margin.

The magnetic fabric ellipsoid must meet several criteria for the plunge of K'_{max} to be interpreted as the steepness of melt flow. Firstly, K_{max} must be well clustered for the mean K_{max} to be meaningful. For this reason, samples were rejected if the tensor displayed an oblate girdle (as a result of susceptibility magnitudes $K_{max} \approx K_{int}$) or otherwise poor clustering of K_{max}. Samples for which Jelinek statistics were calculated were rejected if the long radius of the K_{max} confidence ellipse exceeded 15°, which was the case for four samples (18MM279, 18MM259, 18MM010 and 18MM176). All other samples were accepted or rejected based on a visual assessment of (a lack of) K_{max} clustering (3 samples rejected: 18MM019, 18MM319 and 18MM304). Samples with poor clustering of K_{int} and K_{min} (i.e., a prolate girdle) were not rejected if K_{max} was well clustered. Secondly, inverted magnetic fabrics, where K_{max} clusters around the pole of the dyke (i.e., perpendicular to the dyke), may form for a variety of reasons and cannot be interpreted as melt flow lineation (e.g., Tauxe et al., 1998). Thus, a total of 5 samples where the smallest angle between the mean K_{max} and the dyke margin (i.e., the angle between K_{max} and K'_{max}) exceeded 45° were rejected as well (18MM031, 18MM102, 18MM274, 18MM302 and 18MM344). Lastly, three samples had some uncertainties in the marking

of the orientated blocks (18MM343) or measurements of the dyke margin (18MM110 and 18MM111) and were also excluded for further interpretation.

The thirty-six remaining dyke margins met the outlined criteria for data quality and the rake of K'_{max} in these samples was interpreted as a melt flow lineation. The results for both the orientation of the mean K_{max} axis and the rake of K'_{max} derived with the Bingham statistics method agree well with those derived with the Jelinek statistics method, justifying the use of the former for dykes with less than five core specimens.

3.7 MasirahDB: a geochemical compilation for Masirah

3.7.1 Data sources

MasirahDB is a database of previously published data (Abbotts, 1979a; Peters et al., 1995; Meyer et al., 1996; Nägler and Frey, 1997; Peters and Mercolli, 1998, Mahoney et al., 1998) and some unpublished data (E. Gnos, pers comm) available for rocks of Masirah, intended to serve as a reference throughout this thesis. It was compiled and categorised according to sample type, location, setting and field relations, making no a priori assumptions about the geochemical characteristics of any particular suite or rock unit (more details of this classification are described in Chapter 4). Most of the major and trace element data was collected using XRF, whereas a smaller subset of trace elements was analysed by ICP-MS or Instrumental Neutron Activation Analysis (INAA, Table 3.4).

3.7.2 Compilation

MasirahDB is appended to this thesis as an excel file (Table XII). Data produced by Bern University was linked to a digital database with field notes and GPS coordinates from the Swiss mapping campaign (columns C-J "Swiss Field Data") and additional information from the published data tables (columns K-S "Published Data Swiss & Abbotts" and columns AE-AF "Swiss Geochem Metadata"). Using GPS coordinates for the Swiss data, and sketched sample location maps for the data of Abbotts (1979a), a location was deduced for each sample where enough information was available (columns T-W "Converted coordinates and deduced location"; obvious typing errors in the coordinates are identified in column V). Figure 3.1 shows the geographical extent of MasirahDB.

Some samples appear in multiple data tables across various publications, as well as the unpublished data tables. Data duplicates were identified based on sample name, or if no sample name was published, on the basis of identical data (columns AH-AI). Some samples were exclusively analysed for major or trace elements respectively, but in some cases it could be deduced from the field notes that they represent samples from the same feature in the same outcrop. Column AG contains information about how these data were combined into a single entry.

Table 3.4. MasirahDB data sources

Data Source	Publication type	Method major elements	Method trace elements	Method REE	Method Isotopes
Abbotts (1979a)	PhD Thesis	XRF (powdered pellets, some samples duplicated with fusion beads for quality control)	XRF (powdered pellets)	INAA	-
Peters et al. (1995)	Explanatory notes for Geological Map	XRF	XRF / ICP-MS	ICP-MS	-
Meyer et al. (1996)	Journal	XRF	XRF	ICP-MS	-
Nägler and Frey (1997)	Journal	XRF	XRF	-	Mass Spectrometry
Peters and Mercolli (1998)	Journal	XRF	XRF / ICP-MS	ICP-MS	-
Mahoney et al. (1998)	Journal	-	ICP-MS	ICP-MS	Mass Spectrometry
E. Gnos	Unpubl. Data.	XRF	XRF	-	-

Using the information available from the field notes, the coordinates and the geological map, every sample was assigned to a suite and sub-suite where possible (columns X-AA “Deduced rock suites”). An overview of this classification is given in Table 3.5. Lastly, in column AB entries for dykes and lavas were evaluated for whether they are likely to represent a melt (i.e., fine grained, aphyric, chilled margin etc.) or not (i.e., coarse grained, crystal rich etc.), or if this could not be determined (no specification in notes). Additional information on alteration and crosscutting relations is presented in columns AC-AD.

Table 3.5. MasirahDB lithological subdivisions

Main Group	Sub Group	Assigned suite
Dyke	Axial sequence Dyke	Axial Dyke – Sheeted dykes
		Axial Dyke – Gabbroic screens
		Axial Dyke
	Late Dyke	Late Dyke
	Mantle dyke	Mantle dyke
	Unknown	Melange Dyke
		Unknown dyke
Lava	Axial Lava sequence	Axial Lava sequence
	Later lavas (interbedded in Maghilah sediments)	Lava – Sediment
	Seamount lavas	Lava – Seamount
	Seamount subvolcanics	Dyke / subvolcanic – Seamount
	Out-of-sequence (on Mantle and Kalban sediments)	Lava – Mantle/Sediment
	Reworked in Fayah Unit	Lava – Reworked (?) in Fayah Unit Sediment
	Unknown	Alkaline Lava
		Unknown lava
Pluton	Axial Lower Crust	Axial Lower lower-crust gabbro
		Axial Lower lower-crust ultramafic
		Axial lower-crust gabbro
		Axial Upper lower-crust gabbro
		Axial Upper lower-crust plagiogranite
	Gb-Dol-Gr	Gb-Dol-Gr – Granite
		Gb-Dol-Gr – Gabbro
	Unknown – gabbro intrusion in mantle	Mantle pluton
	Unknown – plagiogranite dyke	Plagiogranite Dyke
	Unknown – gabbro	Unknown gabbro
Pluton/Dyke	Gb-Dol-Gr Dyke	Gb-Dol-Gr – Dolerite
Mantle	Mantle	Mantle
Other	Alteration / structural	Alteration vein – late
		Alteration vein – early
		Fault Breccia
		Alteration
	Sediments	Sediments – Tertiary
		Sediments – Mesozoic
	No description	No description

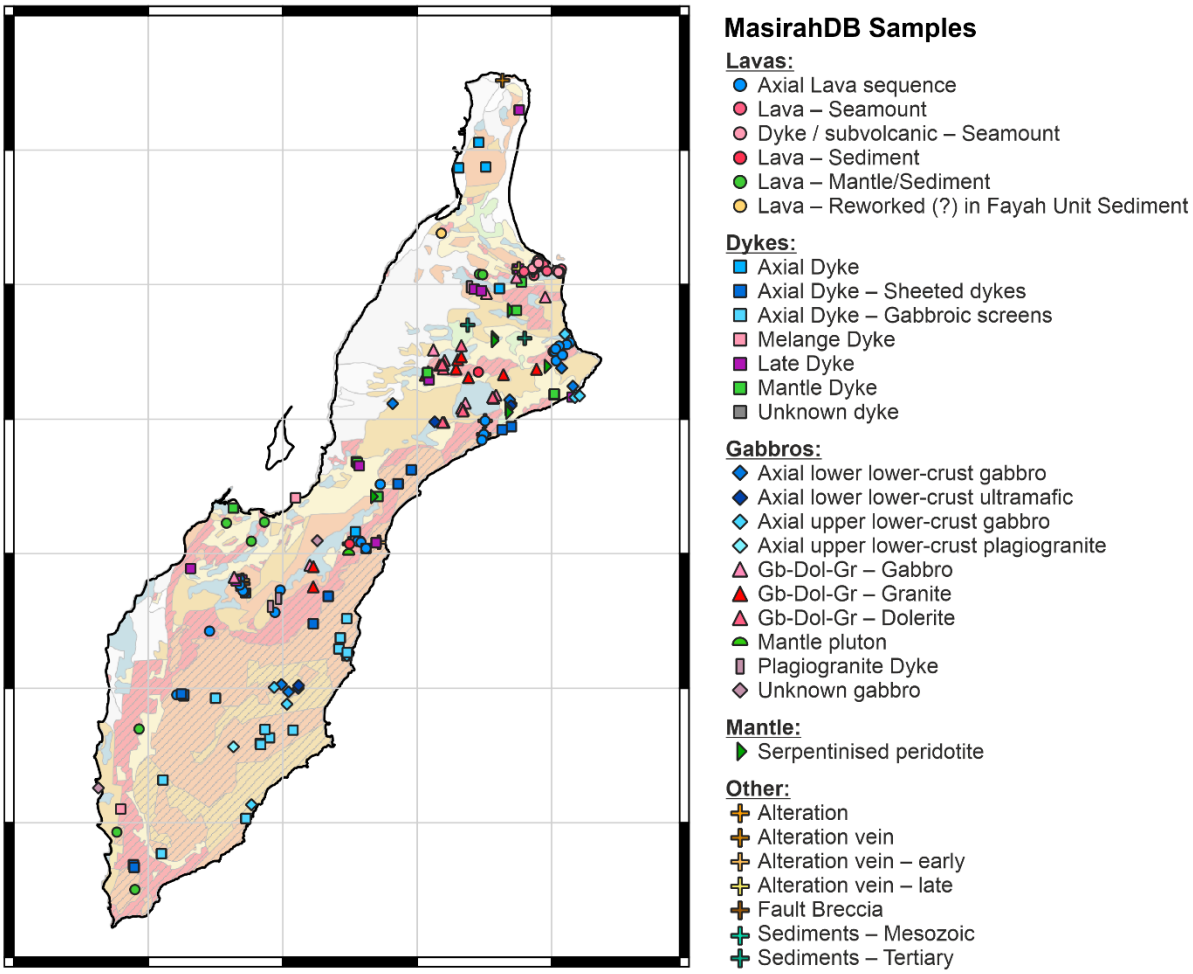

Figure 3.1: *Map showing the locations of the samples included in MasirahDB. The map background is the geological map of Figure 2.2 and grid spacing is 10 km.*

3.7.3 Data quality

The main strength of MasirahDB is to extract broad trends in geochemical parameters that are considered insensitive to alteration (i.e., immobile trace elements) from a large quantity of data, as is done in Chapter 4. As a result of the restricted detection limit of trace elements on the XRF, concentrations below several parts per million are less accurate than concentrations of tens to hundreds of parts per million. Amongst the XRF-analysed trace elements relevant to this study (i.e., Ti, V, Nb, Zr and Y), this issue is most pertinent to Nb, as other trace elements have concentrations >>10 ppm in the dykes and lavas. Of all the dykes and lavas with XRF Nb data in MasirahDB, 10% has a concentration of <3 ppm. As such, for this small group of samples, analytical scatter is expected to affect and obscure the low-Nb (i.e., most depleted, tholeiitic affinity) end of the compositional array on Masirah, described and discussed in Chapter 4. It is expected to have no significant effect on the main trends identified in Chapter 4, such as the transitional nature of the suites and the large variation in compositions regardless of field setting or geographic location.

4. Seafloor spreading and alkaline near-axis magmatism in the early Indian Ocean: the evolution of the Masirah Ophiolite

4.1 Introduction

This chapter investigates the formation and evolution of the Masirah ophiolite and re-evaluates the model proposed by the researchers of the University of Bern (see Chapter 2). In previous work, two magmatic suites were identified on Masirah: a MOR-type suite of purportedly Late Jurassic age and an alkaline suite determined to be Early to Mid-Cretaceous in age (Peters et al., 1995; Meyer et al., 1996; Peters and Mercoli, 1997, 1998; Peters, 2000). This classification, however, distinguishes the two suites based on both field relations as well as geochemical criteria, which introduces the risk of circular reasoning (e.g., all alkaline units are late and vice versa). This chapter sets out to describe the field characteristics of the various occurrences of lavas, dykes and gabbro on Masirah and proposes a new subdivision, which, in contrast to previous work, makes no a priori assumptions about geochemistry and is based purely on field relations. Following this, a geochemical characterisation of each of these newly defined groups is presented. This approach is designed to address and test two key aspects of the Swiss model: Firstly, that Masirah records two distinct magmatic events (on-axis and off-axis) with a distinct change in chemistry with time, from early N to E-MORB tholeiites to later enriched alkalic basalts; and secondly, that any lithological relations not expected for a classic layered magmatic crust, such as chilled dyke swarms intruding the mantle, are attributed to the later, off-axis event, and are therefore alkalic.

In the first section, the Masirah lavas, dykes and gabbros are grouped based on their field relationships and petrography. Subsequently, whole-rock geochemistry data is presented, as well as mineral chemistry for the gabbros, to characterise the previously defined groups and establish their similarities and/or differences. High-precision single zircon U-Pb ages for the axial lower crust are presented and provide the basis for a new geochronological model. Based on these data, constraints are placed on the timing, geographical extent and cause of both phases of magmatism. This chapter will show that the off-axis magmatism followed seafloor spreading much sooner than previously thought and has a compositional overlap with the axial suite, advancing the idea that, rather than two separate events, Masirah records the transition of on-axis seafloor-spreading to near off-axis ('near-axis') magmatism.

4.2 Field relations and petrography

4.2.1 Lavas

The lavas on Masirah occur in a variety of settings and for the purposes of this study were subdivided into four groups (Figure 4.2). The main exposures (by surface area) occur at the highest stratigraphical position of the contiguous magmatic crustal sequence and are subsequently referred

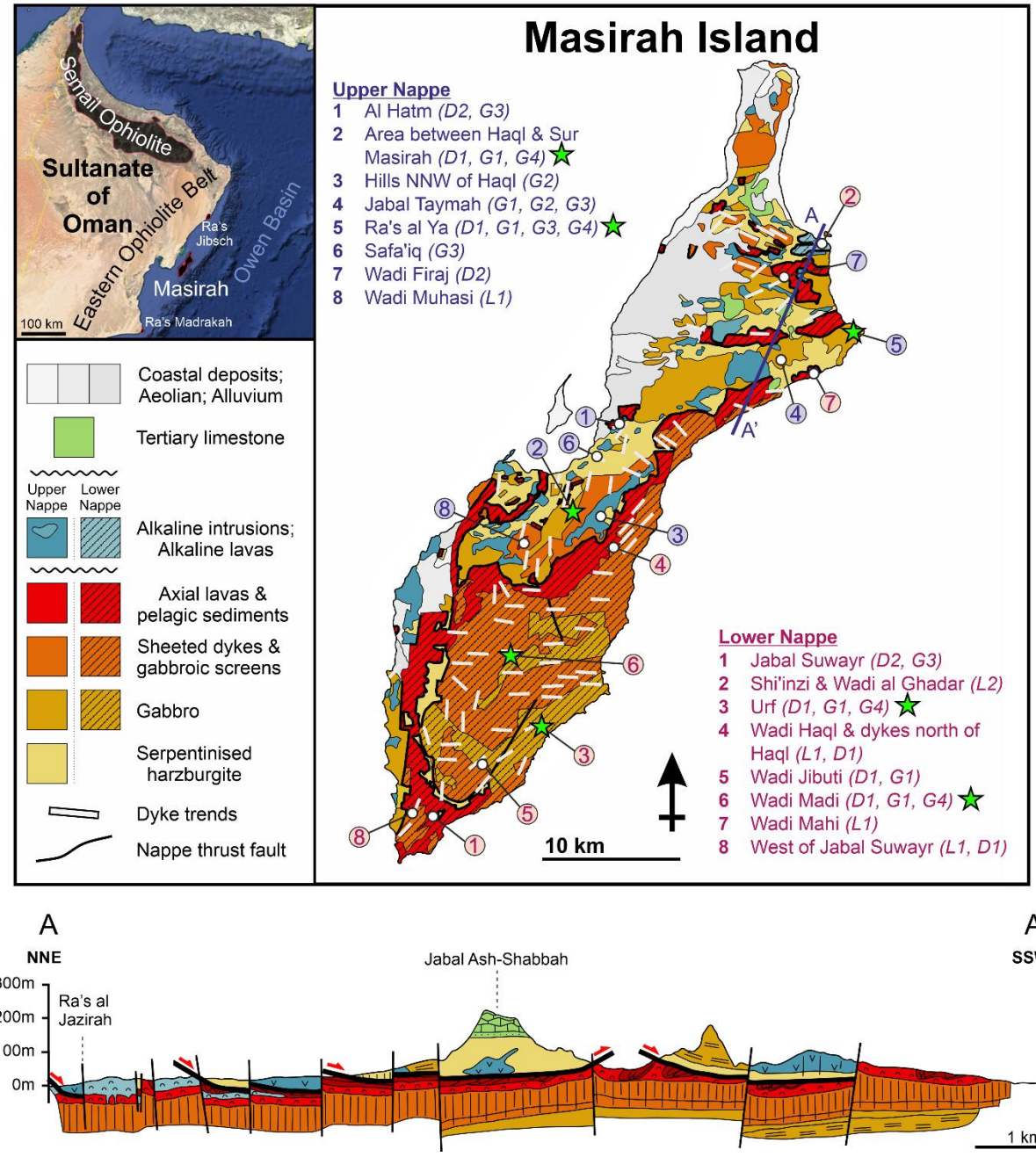

Figure 4.1: *Geological map of Masirah showing the sample locations for this chapter. L1, L2, D1 etc. refer to the various lava (L), dyke (D) and gabbro (G) units studied at each location (see Figure 4.2 and accompanying text for more information). Geochronology sample locations are marked with a green star. Figure adapted from Peters et al. (1995).*

to as ‘axial lavas’. They overly a sheeted dyke complex and are overlain by deep-marine sediments, and were sampled in four locations (Wadi Haql, Wadi Mahi and west of Jabal Suwayr in the Lower Nappe, Wadi Muhasi in the Upper Nappe; Figure 4.1). The second group of lavas comprise theextrusive rocks that occur as seamount structures near Shi’inzi in the north of the island, hereafter ‘seamount lavas’, sampled in Wadi al Ghadar (as described by Meyer et al., 1996; see also previous work on Masirah in Chapter 2). A third group comprises lavas and magmatic breccias interbedded with sediments that overly the axial lavas (‘post-axial lavas’). Lastly, a fourth group (‘out-of-sequence lavas’) is defined by lavas that overlie rock-units that are not expected to be exposed on the seafloor according to the classic model of a layered oceanic crust (primarily mantle as well as some gabbro). The seamount lavas, post-axial lavas and out-of-sequence lavas broadly

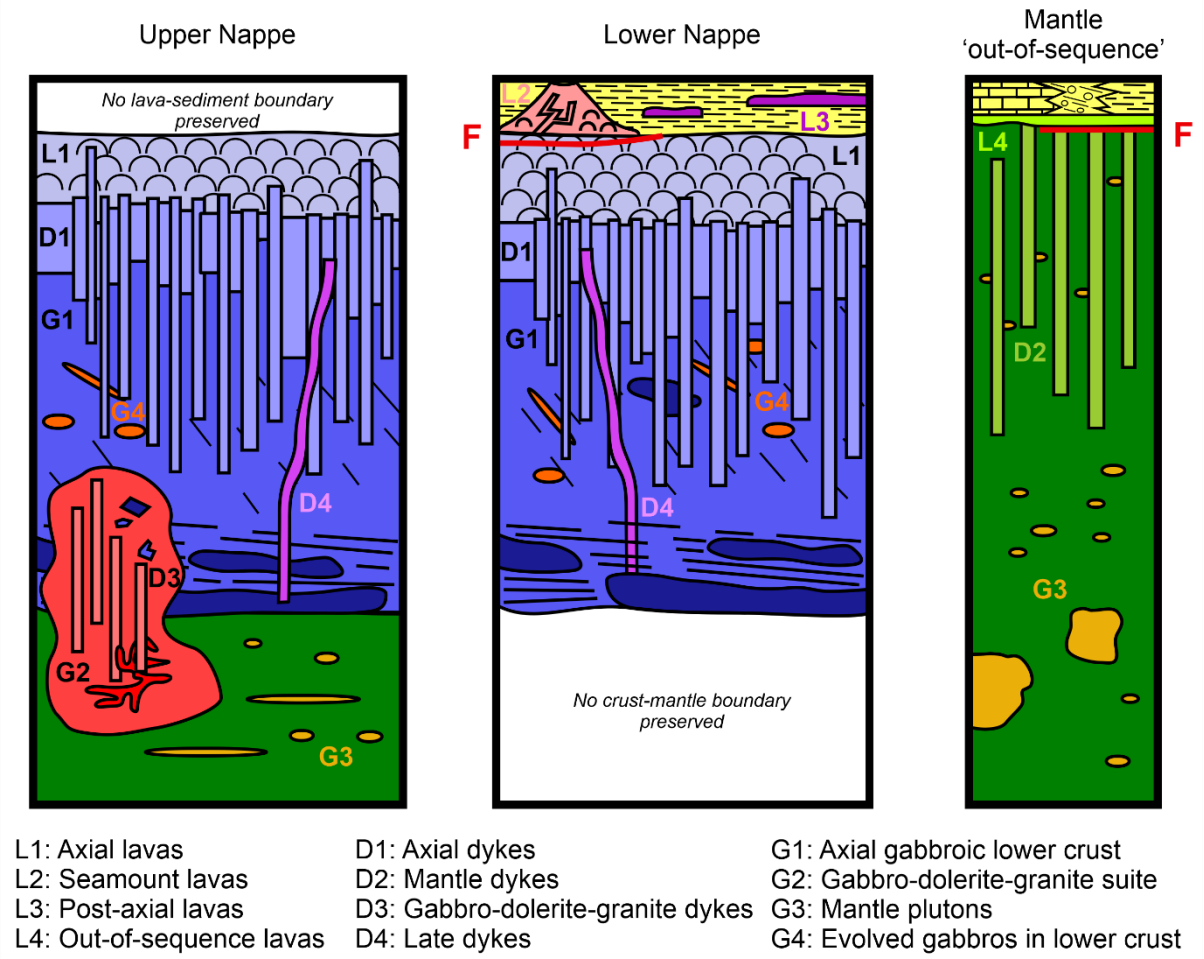

Figure 4.2: *Schematic cartoon (not to scale) illustrating the occurrence and relationships of the lava (L), dyke (D) and gabbro (G) units described in the text (based on field observations and Peters et al., 1995). Faults (F) marked in red to indicate that the seamount lavas are not observed overlying a full axial crustal sequence (except for some lavas) and that the out-of-sequence lavas are often in tectonic contact with the mantle and other units, except at Jabal Suwayr. Sediments overlying the Mantle ‘out-of-sequence’ are of the Kalban Unit, whereas the sediments covering the axial lavas of the Lower Nappe are of the Maghilah Unit.*

correspond to the mapped alkaline volcanic suite, contrasting the axial lavas of the MOR-suite, as defined by previous studies (Peters et al., 1995; Peters and Mercolli, 1997, 1998; Peters, 2000).

In Wadi Haql, the axial lava stratigraphy was studied in a transect from the sheeted dykes in the southeast to the overlying sediments of the Maghilah Unit in the northwest. Where preserved, pillow lavas (25 cm to 1.5 m, typically 50 – 100 cm) have a characteristic centimetre-thick pale green crust that often contains abundant plagioclase phenocrysts (Figure 4.3a and b). The pillow matrix is greyish-green, microcrystalline to doleritic and contains round olivine phenocrysts (1-20%, 0.5 – 2 mm) and less common plagioclase crystals (0-20%, 0.5 – 4 mm). Inter-pillow material consists of fine hyaloclastites and breccias. Outcrops that lack pillow morphologies are petrographically similar and may represent sheet flows or highly weathered pillow lavas. The pillow lavas are variably altered, with an average of 20 – 30% of secondary minerals and the most common alteration assemblage consisting of chlorite-sphene-albite-muscovite-celadonite-calcite-prehnite, although locally higher-temperature assemblages containing actinolite and clinozoisite/epidote occur (Peters et al., 1995). Generally, olivine is completely altered, plagioclase slightly to strongly, whereas clinopyroxene is mostly fresh (Peters et al., 1995). No glasses were observed, although it is not clear whether this is due to weathering or alteration. Higher up in the succession, the average size of pillow lavas decreases to 30 – 50 cm, although 1 – 1.5 m pillows still occur. Here, the pillow matrix and crust display a conspicuous red colour, and plagioclase phenocrysts and amygdules become more common, with subordinate amounts of olivine and pyroxene phenocrysts. The amygdules in the red pillow lavas are filled with zeolite-calcite-hematite/goethite and clay minerals and due to their occurrence in the vicinity of the Masirah nappe thrust fault throughout the island, this alteration assemblage has been interpreted as a late feature associated with the nappe thrusting and emplacement of the ophiolite (Peters et al., 1995). At Wadi Mahi, Wadi Muhasi and west of Jabal Suwayr, outcrops are very similar to Haql. At Wadi Muhasi the pillow lavas display well-developed varioles and west of Jabal Suwayr, near ancient copper working site, they display a distinct red colour.

The seamount lavas are exposed over ~2.5 km^2 near Shi'inzi in the north of the island in the Lower Nappe, where they are in tectonic contact with a mantle section of the Upper Nappe (Meyer et al., 1996). The lavas occur as structures interpreted as volcanic edifices, subvolcanic stock-like intrusions, vent agglomerates, pyro- to epiclastic deposits, and lavas intercalated with marine sediments (Meyer et al., 1996). Thought to represent the remnants of small submarine seamount volcanoes up to a few kilometres in diameter and a few hundred metres high, they are deposited on top of axial lavas of the Lower Nappe (Meyer et al., 1996). The volcanic and subvolcanic units range from basalts to differentiated trachytes and rhyolites and occur as pillow lavas, sheet flows,

pyroclastic and epiclastic breccias and subvolcanic dykes and sills (Meyer et al., 1996; Peters and Mercolli, 1997). The lavas tend to have a reddish-brown appearance and are rich (~25 vol%) in amygdules filled with calcite, zeolite, quartz, celadonite and Fe-hydroxides (Peters et al., 1995).

The post-axial lavas mainly occur as dark brown-green, unsorted volcanic breccias that are interbedded with the deep-marine sediments of the Maghilah Unit, which was deposited concordantly on the axial lavas and was interpreted to record sedimentation from the Late Tithonian to Upper Hauterivian – Lower Barremian age (~150 – 130/125 Ma; Peters et al., 1995; Immenhauser, 1996; Meyer et al., 1996). The Maghilah unit is subdivided into three sequences, with a basal Sequence 1 consisting of 7 – 15 m of micrites, overlain by Sequence 2 consisting of 12 – 15 m of ribbon cherts, in turn capped by Sequence 3, which is up to 20 m thick and consists of a sequence of interlayered volcanic breccia, turbidites of ophiolite material, shaley interbeds and nodular cherts. The post-axial lavas interfinger with the brick-red ribbon cherts of the top of Sequence 2 and mark the base of Sequence 3 (Immenhauser, 1996). These lavas are mainly pillow breccias with local occurrences of small lava flows, and have a similar mineralogy and amygdule content as the seamount lavas (Meyer et al., 1996). The Maghilah Unit is laterally variable, however, and the post-axial lavas do not occur everywhere (e.g., in Wadi Haql; Immenhauser, 1996).

The out-of-sequence lavas mainly occur as scattered outcrops along the western coastal Kalban plain as well as near Shi'inzi in the north and at Jabal Suwayr in the south. The lavas are commonly overlain by sediments of various facies of the Kalban Unit and are described as marking the base of this unit, the oldest microfossils of which were determined to be of Barremian age (~129.4 – 125 Ma; Immenhauser, 1995, 1996). In most of these localities, the primary relationships with the underlying rock-units have been obscured, but at and around Jabal Suwayr, horizontal lavas concordantly overlie harzburgite (Peters et al., 1995; Immenhauser, 1996; Meyer et al., 1996).

4.2.2 Dykes

Dykes were subdivided into four groups based on their field relationships (Figure 4.2). The 'axial dykes' occur at the stratigraphic level of the contiguous magmatic crustal sequence between the gabbros and lavas, either as a true sheeted dyke complex or as crustal dyke swarms intruding gabbro. These dykes were studied and sampled in a well-exposed sheeted dyke complex in the Lower Nappe (north of Haql) and in the gabbro-dyke transition of both nappes (Ra's al Ya and the area between Haql and Sur Masirah in the Upper Nappe; Wadi Madi/Urf and Wadi Jibuti in the Lower Nappe). The 'mantle dykes' consist of dyke swarms that intrude mantle harzburgite and were studied at Wadi Firaj (Upper Nappe) and Jabal Suwayr (nappe unclear but assigned to the Lower Nappe in reconstructions by Marquer et al., 1998). The third group of dykes, 'gabbro-dolerite-granite

dykes', are dykes that are clearly associated with the intrusive alkaline gabbro-dolerite-granite suite. Lastly, a group of 'late dykes' is defined as any dyke that either clearly crosscuts the main generation of axial dykes or dyke cutting a lithological unit where dykes are otherwise not expected, such as a single dyke occurring in the lower crust. Compared to the subdivision in previous work, the axial dykes as defined here broadly corresponds to the MOR suite, whereas the mantle dykes, gabbro-dolerite-granite dykes and late dykes broadly corresponds to the later alkaline suite (Peters et al., 1995; Peters and Mercolli, 1997, 1998; Marquer et al., 1998; Peters, 2000).

The axial sheeted dyke complex of Masirah consists, for a large part, of subparallel dyke swarms with common gabbroic screens (Figure 4.3d). The most common crosscutting relationships are dykes intruding gabbro with chilled margins developed to varying degrees, and rare occurrences of gabbro intruding into pre-existing dykes. Dyke-to-gabbro proportions vary from 0% to 100% over hundreds of metres of crustal stratigraphy and occurrences of 'true' sheeted dyke complex (i.e., 100% dyke-in-dyke intrusion, Figure 4.3c) are generally limited to the top of the sequence where the dykes are overlain by lavas (estimated several hundred metres thick, but thinner than the overall gabbro-dyke transition). These dykes have chilled margins on one or both sides, or occur as screens of dolerite or micro-gabbro that are crosscut by other dykes. Dykes are generally ~0.8 – 1.5 m wide, but can vary from a few centimetres to several metres, and can be crystal rich, containing plagioclase (up to 50%, 0.1 – 3 cm) and to a lesser extent pyroxene and olivine (~0 – 5%) phenocrysts and glomerocrysts (Figure 4.3e). Hydrothermal alteration of the dykes is pervasive with a middle greenschist facies assemblage typical for ophiolites and consisting of primarily chlorite and tremolite/actinolite, with additional albite, clinozoisite, sericite and very local areas of high-degree, epidote-dominated alteration (Peters et al., 1995). Some parts of the dyke complex are overprinted by prehnite mineralisation which itself is crosscut by late dykes, providing relative time constraints for this later alteration (Peters et al., 1995). In the studied locations, the oldest group of dykes are typically grey, aphyric to plagioclase- and pyroxene-phyric dolerites (30 – 50 vol.% of dykes in the outcrop), which is crosscut by black aphyric dolerite (30-70 vol.%) and pale green, aphyric to slightly plagioclase- and pyroxene-phyric dolerites (0 – 30 vol.%). In some instances, however, dyke crosscutting relationships are opposite to this generalised observation.

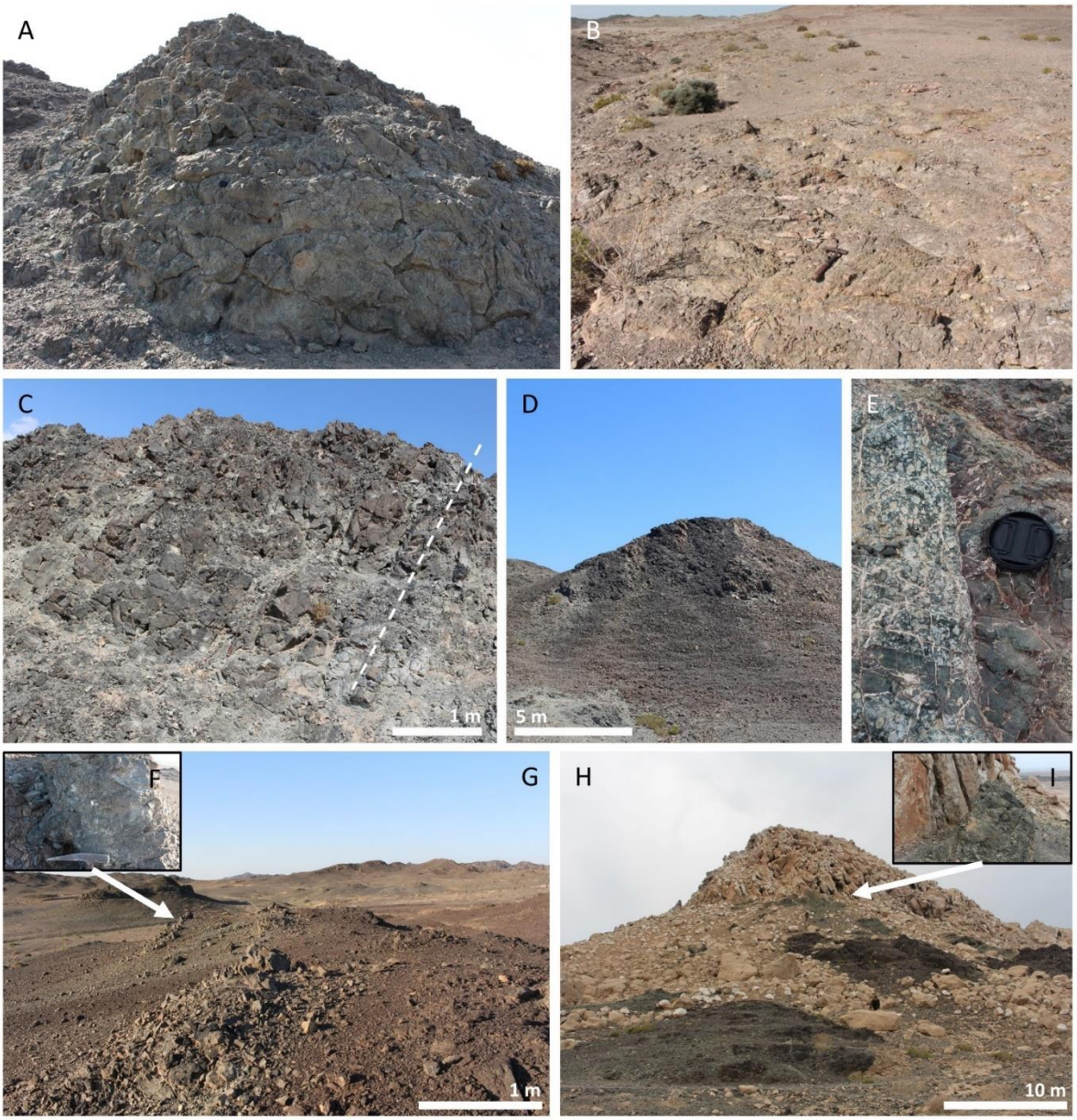

Figure 4.3: *(a) Axial pillow lavas at Wadi Haql (lens cap for scale). (b) Axial pillow lavas interbedded with pelagic sediments of the Maghilah Unit (hammer for scale). (c) Axial sheeted dykes north of Haql, dashed line indicates dyke trend. (d) Axial dykes swarm (dark grey) with gabbroic screens (light grey) in Wadi Madi. (e) Close-up of a plagioclase ultraphyric dyke in the axial sheeted dyke complex west of Jabal Suwayr. (f) & (g) Dyke swarm intruding the mantle near Jabal Suwayr, with a close-up of the chilled margin in the inset. (h) & (i) North slope of Jabal Suwayr, where carbonate platform sediments of the Kalban Unit overly mantle harzburgite (dark brown) intruded by dolerite dykes (pale green), with a close-up of the contact in the inset.*

Areas where dyke swarms intrude the mantle sections have a relatively small areal extent. The studied locations generally have patchy and discontinuous outcrops (~10% outcrop) and relationships between the various lithologies are often poorly exposed due to intense brecciation. Dyke trends are highly variable although they show more consistency on a <100 m scale, where they

are subparallel. In the more pristine outcrops, dykes display clear chilled margins and can be continuous for tens of metres (Figure 4.3f and g). Their field appearance is very comparable to the axial dykes. They are 0.1 – 2.5 m thick and mostly consist of dolerites with chilled margins. Crystal-bearing dykes are more common than aphyric dykes, with plagioclase as the most common phenocryst (generally <5%, occasionally up to 20%), sometimes accompanied by clinopyroxene (<5%), although some exclusively pyroxene-phyric dykes also occur. The mantle outcrops at Jabal Suwayr and Wadi Firaj also contain gabbroic plutons (described in more detail in the next section) that are crosscut by similar dykes and in rare instances the gabbro intrudes and stopes dolerite dykes. At Jabal Suwayr, carbonate platform sediments of the Kalban Unit rest on top of the mantle section (Figure 4.3h and i). The base of this succession is marked by a red breccia of variable thickness (tens of centimetres to metres) with clasts of basalt, dolerite, gabbro and epidosite and a clay-rich matrix. The carbonate sequence itself contains some beds with a high proportion of angular to subangular clasts (1-50 cm, 10 cm on average) of aphyric and plagioclase-phyric basalts and some gabbro.

The gabbro-dolerite-granite dykes are associated with the intrusive alkaline gabbro-dolerite-granite suite (see also next section). Some dykes crosscut the plutonic suite whereas others show intermingling structures and backveining with their host gabbros and granites, indicating contemporaneous emplacement (Peters and Mercolli, 1997). The mineralogy of the dykes has previously been reported to be dominated by brown hornblende with varying amounts of biotite and no clinopyroxene (Peters and Mercolli, 1997).

Late dykes can occur at all stratigraphic levels of the magmatic crust and are often aphyric. In most respects they are similar in field appearance to the axial and mantle dykes.

4.2.3 Gabbro occurrences

Gabbros on Masirah were divided into four groups (Figure 4.2): (1) the 'axial gabbroic lower crust' that underlies the axial lavas and sheeted dyke complex (studied in Jabal Taymah, Ra's al Ya, and the area between Haql and Sur Masirah in the Upper Nappe, and Wadi Madi/Urf and Wadi Jibuti in the Lower Nappe); (2) the alkaline gabbro-dolerite-granite suite (studied in the mountains west of Jabal Taymah and the low hills north-northwest of Haql, Upper Nappe); (3) isolated plutons in the mantle section (studied in the mantle sections between Jabal Taymah and Ra's al Ya, at Safa'iq and at Al Hatm in the Upper Nappe; and at Jabal Suwayr, nappe unclear, assigned to Lower Nappe by Marquer et al., 1998); and (4) evolved gabbros in the axial lower crust (studied at Ra's al Ya and the area between Haql and Sur Masirah in the Upper Nappe, and Wadi Madi/Urf in the Lower Nappe). On the geological map of Masirah and in associated papers, the axial gabbroic lower crust defined here

corresponds to the mapped units of layered and foliated gabbro and gabbroic screens in the sheeted dyke units and were interpreted as the MOR crustal sequence, whereas the gabbro-dolerite-granite suite, gabbro intrusions in the mantle, and evolved gabbros in the lower crust are mapped as isotropic gabbro, interpreted as late and alkaline (Peters et al., 1995; Peters and Mercolli, 1997, 1998; Marquer et al., 1998; Peters, 2000).

(1) The axial lower crustal sequence constitutes the main gabbro occurrence on Masirah and consists of a series of layered gabbro and dunite at its base, overlain by foliated gabbros that grade into the sheeted dyke complex (Figure 4.4a). A more detailed description of this suite will follow in Chapter 5, with relevant details highlighted here. The axial gabbros have an estimated thickness of ~500 m and are primarily made up of granular to ophitic gabbro (Figure 4.5a and b; a complete petrography is presented in Table II). At the base of the crust, gabbro is less common and olivine gabbro, troctolite, plagioclase-dunite and plagioclase wehrlite dominate instead, whereas in the upper part of the section some gabbros are more evolved, containing accessory brown amphibole, Fe-Ti oxides, titanite and apatite. The sampled lithologies are further subdivided as representing the main lithology in a section or a subordinate lithology.

(2) The alkalic gabbro-dolerite-granite suite forms 0.5 – 3.5 km sized plutons. These plutons are mainly located near the stratigraphic level of the crust-mantle boundary in the Upper Nappe and previous work has described locations where their intrusive nature is apparent from the presence of large xenoliths of the axial lower crust and mantle (Peters and Mercolli, 1997). Within the suite, the gabbros often display mutually crosscutting relationships with the dolerites and granites. In this section, two localities of this unit are described. To the west of Jabal Taymah, the gabbro-dolerite-granite suite is exposed over ~6 km^2 and forms mountains with a distinct jagged appearance that contrasts with the more rounded slopes of the adjacent exposures of the axial lower crust (Figure 4.4b). The dominant lithology is ‘varitextured’ hornblende-oxide gabbro, with a heterogeneous grain size, ranging from fine to pegmatoid over distances of tens of centimetres, containing plagioclase, clinopyroxene and magmatic amphibole crystals that reach up to 10 cm (Figure 4.4c). Coarse to pegmatoid grainsizes are most common. The pegmatoid gabbro segregates into veins and dykelets that back-intrude the microgabbro and forming irregular blocks (Figure 4.4d). Subordinate occurrences of felsic dykes intrude the gabbro (Figure 4.4e), and rare and discontinuous centimetre-scale bands of ductile deformation are marked by mylonitic fabrics in some of the gabbros. Marquer et al. (1998) report that ductile deformation is restricted to the gabbro-dolerite-granite suite and display a systematic sense of shear consistent with syn-emplacement bulk NW – SE extension. The area north-northwest of Haql exposes a ~4 km^2, NE-SW oriented elongate strip of gabbroic outcrops.

Figure 4.4: *The rounded ridge morphology of the axial lower crust at Jabal Taymah (a, ~200 m high) contrasts with the jagged ridges of the gabbro-dolerite-granite suite west of Jabal Taymah (b, ~150 m high). (c) - (e) Various outcrops of the gabbro-dolerite-granite suite west of Jabal Taymah illustrating the heterogeneous grainsize, pegmatitic veins and occurrence of felsic lenses (lens cap and hammer for scale). (f) Abundant pods of hornblende-gabbro pegmatite intruded into the mantle section at Safa'iq (lens cap for scale). (g) Sporadic gabbroic veins intruded into the mantle section west of Jabal Taymah (hammer for scale). (h) & (i): Varitextured gabbro in the upper gabbros of the axial lower crust in the area between Haql and Sur Masirah (h) and at Ra's al Ya (i) (lens cap for scale).*

In contrast to the outcrops near Jabal Taymah, in the Haql area the gabbro forms a plain with scattered outcrops in low-lying hills. Medium to fine-grained hornblende-oxide gabbro dominates, with subordinate coarser gabbro (present in patches or veins that back-intrude the host gabbro) and metre-sized felsic lenses, consisting of granite, tonalite and albitite. Brown amphibole is a major phase in all studied rocks of the suite, occurring as interstitial to poikilitic crystals in the finer-grained gabbro, enclosing plagioclase and clinopyroxene chadacrysts (Figure 4.5c) and often intergrown with subhedral to anhedral magnetite-ilmenite pairs (up to 5%). Brown amphibole also forms reaction rims around, and overgrowths on, clinopyroxene (Figure 4.5d), as well as anhedral blebs along cleavage planes. In some rocks clinopyroxene has been completely consumed by this reaction and replaced by brown amphibole oikocrysts with small plagioclase chadacrysts (Figure 4.5c). The occurrence of biotite, rare for oceanic gabbros, has been noted in this suite (Peters et al., 1995; Peters and Mercolli, 1997), but is not always present and was not observed in the samples obtained for this study.

(3) Gabbroic intrusions in the mantle section include dykelets, veins and metre-sized pods of pegmatoid to fine-grained gabbro, olivine gabbro and hornblende gabbro (Figure 4.4f and g), as well as less common metre-sized leucocratic and granitic dykes. Chilled margins are absent and some intrusions display ductile deformation in the form of isolated centimetre-scale mylonitic shear bands. Their occurrence is highly variable, ranging from virtually absent in the crust-mantle transition exposed in the foothills of Jabal Taymah, to highly abundant in the mantle near Safa'iq. In

Figure 4.5 (next page): *Microphotographs illustrating the petrographic relations of gabbros occurring on Masirah (left: plane-polarised light, PPL; right: cross-polarised light, XPL). (a) Olivine gabbro from the layered gabbros in the axial lower crustal sequence with a granular texture (Sample 18MM098, Ra's al Ya). (b) Olivine gabbro from the axial lower crustal sequence with an ophitic texture, containing clinopyroxene oikocrysts with plagioclase chadacrysts (Sample 18MM197, Ra's al Ya). (c) Hornblende-oxide gabbro from the gabbro-dolerite-granite suite, with oikocrystic hornblende enclosing small plagioclase grains (Sample 18MM373, from the mountains west of Jabal Taymah). (d) Hornblende-oxide gabbro from the gabbro-dolerite-granite suite, with arrow indicating hornblende rims around clinopyroxene grains. Hornblende and oxides are intergrown and interstitial (Sample 18MM168, from the area north-northwest of Haql). (e) Olivine gabbro with a granular texture from an 'axial affinity' mantle intrusion (Sample 18MM001, from the mantle section near Ra's al Ya). (f) Hornblende-oxide gabbro from an 'alkaline affinity' mantle intrusion, with clinopyroxene with hornblende around the rims and in blebs along the cleavage planes (Sample 18MM268, from the mantle section at Jabal Suwayr). G: Gabbro from a 'transitional affinity' mantle intrusion with small, interstitial hornblende and oxide grains (Sample 18MM242, Safa'iq). H: Varitextured gabbro with minor oxides and no hornblende (Sample 18MM189, Ra's al Ya). Pl = plagioclase; Cpx = clinopyroxene; Ol = olivine; Hbl = hornblende; Ox = oxides; Alt = altered.*

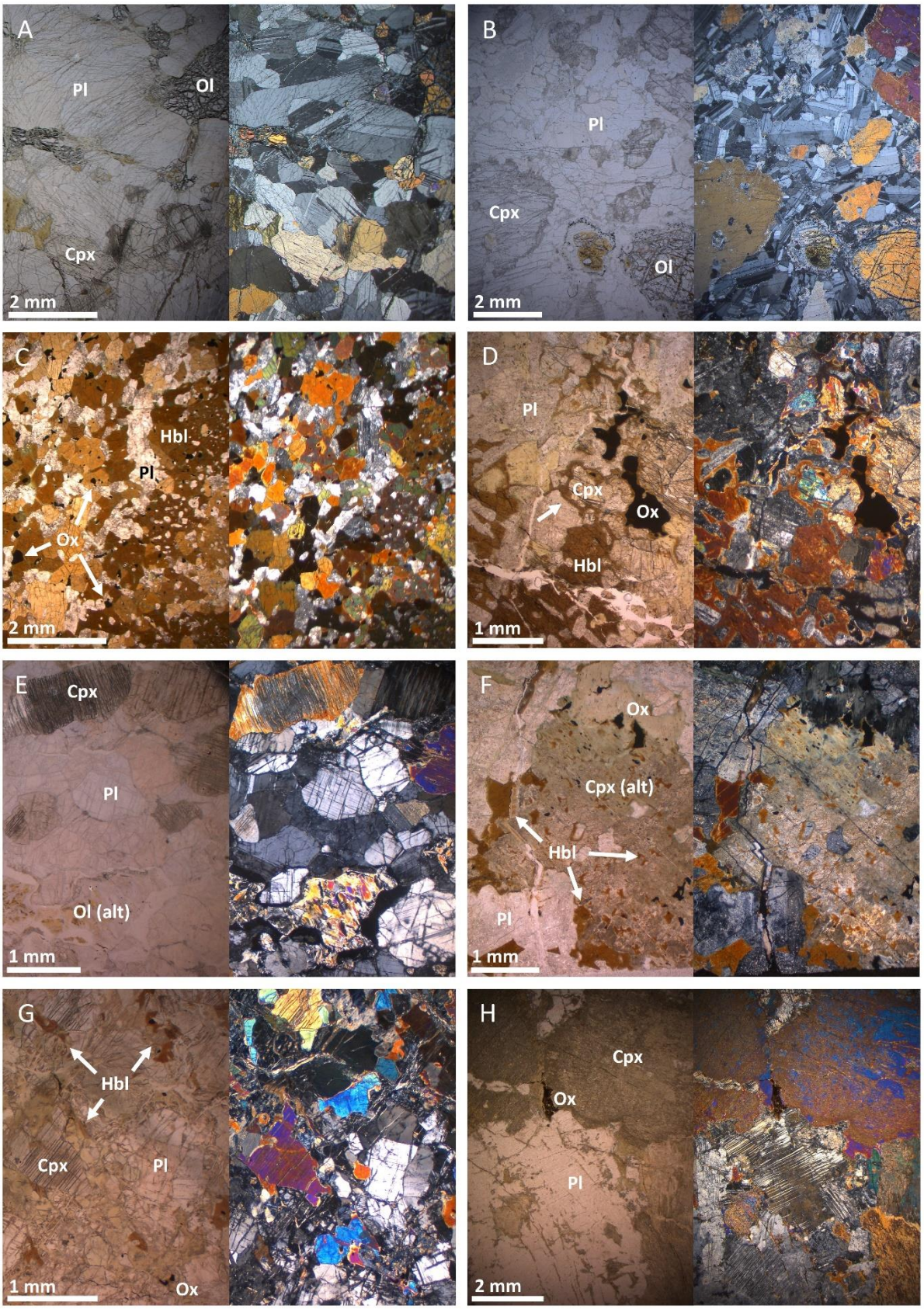
A
Pl
Ol
Cpx
2 mm
B
Pl
Cpx
Ol
2 mm
C
Hbl
Pl
Ox
2 mm
D
Pl
Cpx
Ox
Hbl
1 mm
E
Cpx
Pl
Ol (alt)
1 mm
F
Ox
Cpx (alt)
Hbl
Pl
1 mm
G
Hbl
Cpx
Pl
1 mm
Ox
H
Cpx
Ox
Pl
2 mm

the locations studied during this research, the abundance of intrusions appeared to be greater in mantle sections that lacked a spatially associated overlying igneous crust (e.g., Safa'iq, Jabal Suwayr). The gabbro intrusions were further grouped according to their apparent similarity to either the axial gabbros or the gabbro-dolerite-granite suite. The majority of the studied gabbro intrusions (at Safa'iq, Jabal Suwayr and between Jabal Taymah and Ra's al Ya) are pods of varitextured or pegmatoid hornblende-oxide gabbro comparable to the gabbro-dolerite-granite suite ('alkaline affinity'). They contain similar textures of brown amphibole replacing clinopyroxene, although the reaction has typically progressed to a lesser extent (Figure 4.5f). Pods are generally metre-sized but some plutons form larger bodies of gabbro (tens of metres) and at Jabal Suwayr they are crosscut by dykes similar to those intruding the mantle section. In rare instances, the varitextured gabbro intrudes and stopes the dolerite dykes. A small proportion of the studied mantle intrusions (several veins and a pod near Jabal Taymah, Ra's al Ya and Al Hatm) consist of olivine gabbro with similar granular to ophitic textures as gabbros from the axial lower crust ('axial affinity', Figure 4.5e). Some gabbroic plutons (at Safa'iq) are not easily assigned to either group, as they form metres-scale varitextured and pegmatoid pods, yet also consist of granular to ophitic gabbro and olivine gabbro containing only minor amounts of brown amphibole and oxides ('transitional affinity', Figure 4.5g).

(4) Evolved gabbros include varitextured and pegmatite isotropic gabbro that occur sporadically in the upper gabbros of the axial lower crust and often form sub-metre veins and segregations (Figure 4.4h and i). Typically, the host rock is a weakly-foliated gabbro comparable to those characteristic of the axial lower crust, and is crosscut by dyke swarms. These varitextured and pegmatite gabbro have a heterogeneous grainsize similar to the alkaline gabbro-dolerite-granite suite, but the replacement of clinopyroxene by brown amphibole is notably absent or present as a minor phase (Figure 4.5h), and Fe-Ti oxides are less abundant (contents vary from absent to an accessory phase). Metre-sized dykelets, pods and vein-segregations of leuco-gabbro, anorthosite, diorite and albitite, sometimes with accessory oxides, apatite, titanite and zircon, also occur sporadically in these outcrops.

4.3 Geochemistry

A total of 47 samples were selected for whole-rock (WR) geochemical analysis (12 lavas, 13 dyke margins crosscutting igneous crust, 16 dyke-margins crosscutting mantle peridotites, and 6 of the leucocratic lithologies that were also targeted for geochronology; results reported in Table IV). The first subsection below discusses the effects of alteration and crystal accumulation on the whole-rock compositions (Section 4.3.1), followed by an assessment of the extent to which major element variations can be explained by magmatic differentiation trends (Section 4.3.2). Subsequently, a whole-rock geochemical characterisation of the lavas (Section 4.3.3) and dykes (Section 4.3.4) is presented for each of the groups defined in the previous section based on field relations (Section

4.2). The geochemistry of the lava and dyke groups is compared to compositions in MasirahDB (Table XII) to demonstrate that the observed trends are representative for the whole ophiolite. In the last subsection, the gabbro groups are characterised according to their mineral chemistry (Section 4.3.5).

4.3.1 Effects of alteration and crystal accumulation in lavas and dykes

Sample for WR geochemistry were selected and processed to contain a minimum amount of amygdules and alteration veins. The relative abundance of alteration veins in the processed material of each sample was recorded using an arbitrary scale from 0 to 5, but this quantity was not found to correlate with any significant geochemical trend.

To investigate the potential effects of (background) alteration, the relation between major element variations and loss on ignition (L.O.I.) was examined, based on the assumption that rocks subjected to more intense alteration contain more hydrous minerals (e.g., chlorite, amphibole, serpentine and clays) resulting in elevated L.O.I. values. In Figure 4.6 major elements oxides recalculated to anhydrous compositions (i.e., totals excluding L.O.I. renormalised to 100 wt%) are plotted against zirconium (an incompatible and alteration immobile trace element; e.g., Pearce and Norry, 1979) and coloured by L.O.I. content. The Masirah lavas and dykes broadly follow the MORB differentiation trends defined by the MORB glass compositions compiled by Gale et al. (2013), although the trends of different elements are obscured to various degrees by scatter in the data. Generally speaking, samples with lower L.O.I. contents tend to mirror the MORB trends more closely. TiO_2 and P_2O_5 correlate well with Zr indicating these are immobile during hydrothermal alteration. Scatter in the trends of Al_2O_3, SiO_2, FeO^T, CaO and MgO indicates these elements are moderately mobile. Elevated L.O.I. values correlate with higher Al_2O_3 contents, which is consistent with results from previous geochemical studies on alteration of the upper oceanic crust (Staudigel, 2014) and is potentially related to a progressive increase in the modal proportion of chlorite during alteration. Higher L.O.I. is also weakly correlated to lower SiO_2 and FeO^T contents, whereas no clear relation exists between L.O.I. and CaO. For MgO, opposite trends are observed in the dykes and lavas, perhaps reflecting different geochemical fluxes due to contrasting alteration conditions in the lavas versus the dykes: elevated L.O.I. in the lavas correspond to lower MgO contents, whereas dykes with elevated L.O.I. tend to have higher MgO contents, compared to samples with low L.O.I. and MORB glasses. The alteration-sensitive alkali elements Na_2O and K_2O show the largest degree of scatter, with no

Figure 4.6 (next page): *Anhydrous major element trends for the Masirah lavas and dykes plotted against the immobile incompatible trace element Zr and coloured by L.O.I. content. Lavas and dykes from MasirahDB (dark grey) and fresh MORB glasses (light grey, from Gale et al., 2013) are shown for comparison.*

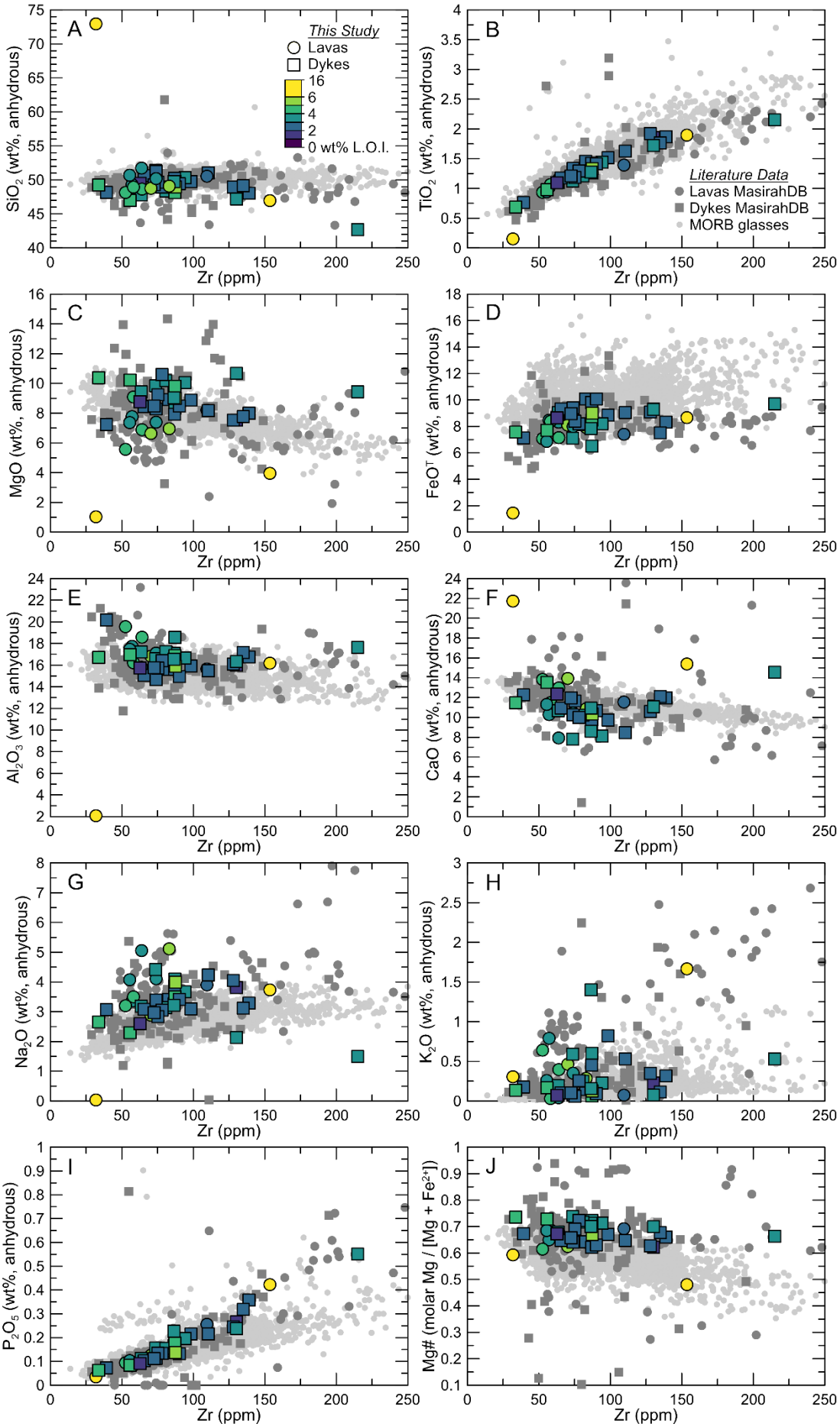
A
This Study
Lavas
Dykes
16
6
4
2
0 wt% L.O.I.
SiO2 (wt%, anhydrous)
B
Literature Data
Lavas MasirahDB
Dykes MasirahDB
MORB glasses
TiO2 (wt%, anhydrous)
C
MgO (wt%, anhydrous)
D
FeOT (wt%, anhydrous)
E
Al2O3 (wt%, anhydrous)
F
CaO (wt%, anhydrous)
G
Na2O (wt%, anhydrous)
H
K2O (wt%, anhydrous)
I
P2O5 (wt%, anhydrous)
J
Mg# (molar Mg / [Mg + Fe2+])
Zr (ppm)

systematic trends as L.O.I. increases.

Mobility of MgO and FeO^T has consequences for the calculation of Mg# (molar Mg / [molar Mg + Fe^{2+}] with Fe^{3+} / Fe_{total} = 0.12): higher L.O.I. contents correlate with an increase in Mg# in the dykes (0.026 per 1 wt% increase in L.O.I.), and a less pronounced decrease in Mg# in the lavas (0.012 per 1 wt% L.O.I.). Care must therefore be taken when interpreting the Mg# of samples with higher L.O.I. contents. Dykes with very primitive Mg# > 0.70, for example, all have L.O.I. > 3 wt%. Nevertheless, samples with low L.O.I. (< 2.5 wt%, n = 12) form relatively undisrupted differentiation trends for FeO and MgO and have Mg# values (Mg# = 0.62 – 0.69, average 0.65) that are similar to primitive MORB glasses and decrease with increasing Zr. Furthermore, the changes in MgO and FeO^T correlating with L.O.I. do not exceed ~2 wt%, and changes in Mg# do not exceed 0.10, indicating alteration cannot obscure trends with a magnitude greater than that. These observations lend some confidence to the interpretation of Mg# in terms of magmatic processes and the inference that the Masirah dykes and lavas were primitive.

Samples were prepared in such a way as to minimise the presence of crystal cargo, but nevertheless this was not possible for all samples. Before crushing, a rough visual estimate of the crystal content of the analysed material was made using an arbitrary scale from 0 to 5 (where 0 represents no crystals and 5 abundant crystals) for light crystals (plagioclase) and dark crystals (olivine, pyroxene etc.). This visual estimate was then compared to geochemical signatures deemed characteristic of crystal accumulation (Al_2O_3, Sr and Eu for plagioclase, MgO and Ni for olivine; and MgO, Cr and Yb for clinopyroxene; Figure 4.7). Al_2O_3 contents appear the most sensitive to plagioclase accumulation and samples with unusually high Al_2O_3 (>18 wt%) compared to MORB all have abundant plagioclase crystals. Strontium and Eu are less affected by plagioclase contents and are for the most part MORB-like. No significant patterns are observed for mafic crystal content and MgO, Ni, Cr or Yb contents. Instead of falling on a single liquid line of descent, variations in MgO at a constant Ni, Cr and Yb contents span the range observed in MORB and slightly exceed it, consistent with the earlier suggestion that alteration either removed small amounts of MgO from the lavas, added it to the dykes, or both.

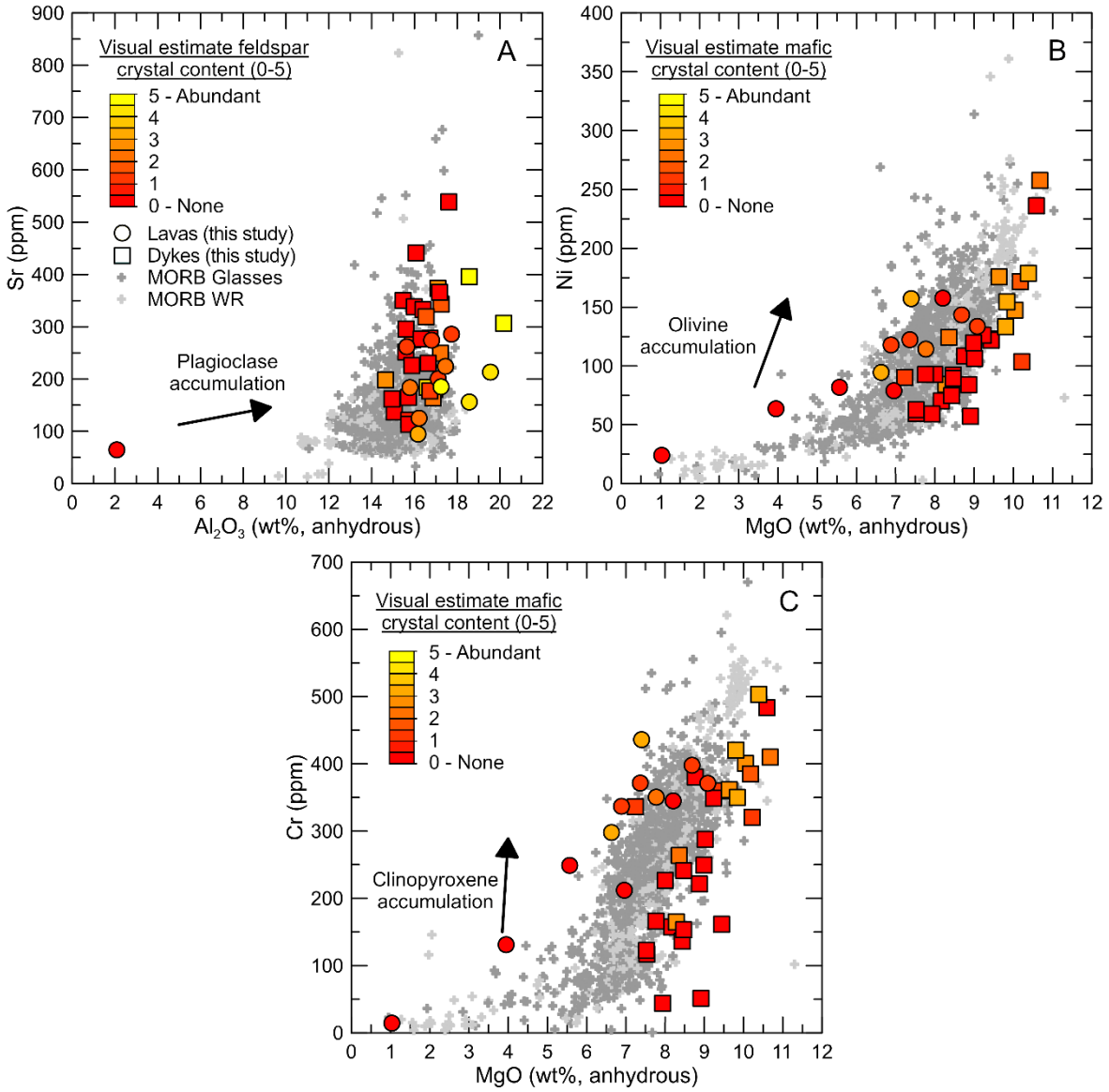

Figure 4.7: *Effect of crystal-accumulation of plagioclase (a), olivine (b) and clinopyroxene (c) on WR-compositions of the Masirah lavas and dykes. In each figure, a vector of arbitrary length shows the predicted geochemical trend that would be caused by crystal accumulation of plagioclase (with a composition of 32 wt% Al_2O_3; 300 ppm Sr), olivine (46 wt% MgO; 2350 ppm Ni) and clinopyroxene (16.7 wt% MgO; 10250 ppm Cr). Aluminium contents in some samples correlate with plagioclase accumulation, but neither MgO, Ni or Cr show any correlation with the visual estimate of mafic minerals in the crushed sample and variations in these elements are unlikely to be due to olivine or clinopyroxene accumulation. Analyses of MORB glasses and whole-rocks compiled by Gale et al. (2013) are shown in grey for comparison.*

4.3.2 Magmatic differentiation trends in lavas and dykes

Whole-rock major element compositions of the lavas and dykes, all recalculated to anhydrous compositions, broadly follow MORB differentiation trends but are disrupted to some extent due to crystal accumulation and subsequent alteration (Figure 4.8). The sampled axial lavas are primitive

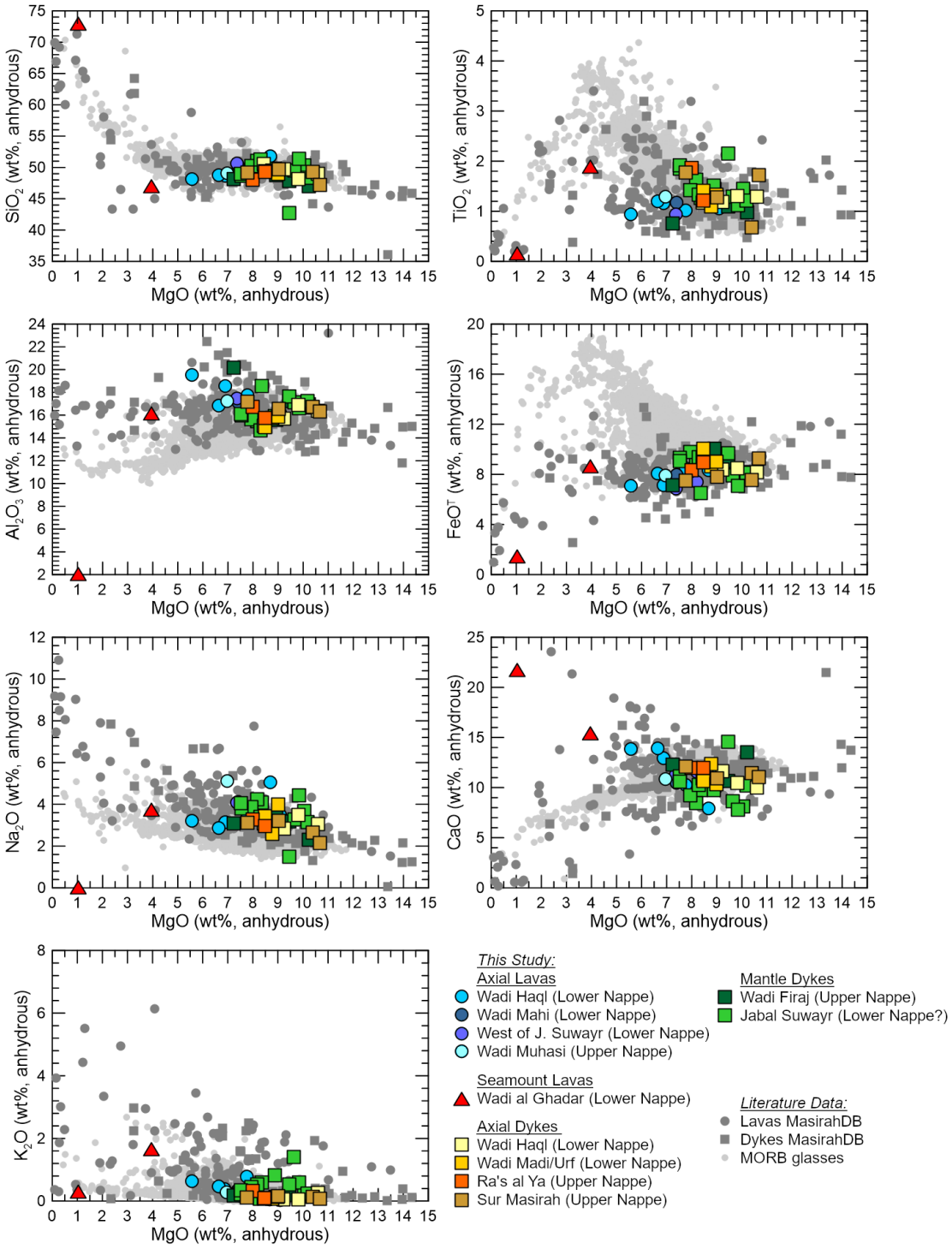

Figure 4.8: *Selected anhydrous major element trends of the Masirah lavas and dykes plotted against MgO. Compositions of lavas and dykes from MasirahDB (dark grey) and MORB glasses (light grey, Gale et al., 2013) are shown for comparison.*

(Mg# = 0.61 – 0.69, average 0.66 of n = 10) and have a L.O.I. of 2.2 – 5.9 wt% (average 4.0 wt%). Two seamount lava samples from Wadi al Ghadar just north of Shi'inzi have L.O.I. of 13.1 – 15.1 wt%. Of these, sample 18MM364 has a basaltic SiO_2 content (46.95 wt%) but is differentiated compared to the axial lavas, with 3.95 wt% MgO and Mg# = 0.48, whereas sample 18MM365 does not appear to reflect a melt composition (72.95 wt% SiO_2, 21.72 wt% CaO, all other major elements <2.1 wt%). The dyke compositions follow the same general major element trends as the axial lavas (Figure 4.8), with Mg# ranging 0.62 – 0.74 (average 0.68, n = 29), but with slightly lower L.O.I. (1.3 – 5.4 wt%, average 2.9 wt%) and higher MgO (7.2 – 10.7 wt% compared to 5.6 – 9.1 wt%) and FeO^T (6.5 – 10.1 wt% compared to 6.9 – 8.5 wt%).

Earlier work on the effect of the tectonic setting of ophiolites on the geochemical evolution of melts showed that small amounts of water introduced during subduction initiation affect the stabilisation of mineral phases and as a consequence the liquid lines of descent of a melt (MacLeod et al., 2013). Specifically, an earlier stabilisation of clinopyroxene with respect to plagioclase in a supra-subduction zone (SSZ) setting results in a less substantial increase in melt TiO_2 and less substantial decrease of Al_2O_3 with decreasing MgO, whereas Cr contents drop dramatically with increasing Zr (Figure 4.9). Some Masirah lavas plot away from the MORB field in TiO_2 and Al_2O_3 versus MgO diagrams and trend towards the field defined by back-arc basin basalts (BABB) with a SSZ origin. These trends can however be explained by a combination of plagioclase accumulation (increasing Al_2O_3 and diluting MgO and TiO_2) and up to 2 wt% MgO mobilisation during alteration, since the samples trending to the BABB field have higher plagioclase contents and/or higher L.O.I. contents (Figure 4.9). Other relations (Cr versus Zr) are also more consistent with dry (<0.5 wt% H_2O) MORB differentiation trends (Figure 4.9e). The Masirah lava and dyke major element compositions can therefore be interpreted to broadly represent fairly primitive, dry MORB-like differentiation trends that are disrupted to some degree by plagioclase accumulation and alteration.

Figure 4.9 (next page): *Differentiation trends the Masirah lavas and dykes compared to MORB and BABB differentiation trends for selected elements. Most Masirah lavas and dykes follow the MORB trends for TiO_2 versus MgO (a & b) and Al_2O_3 versus MgO (c & d). Deviations from MORB trends in several samples can be accounted for by either plagioclase accumulation, resulting in an increase in Al_2O_3 and a decrease (by dilution) of TiO_2 and MgO (a & c), or alteration trends, resulting in elevated Al_2O_3, a loss of MgO in the lavas and an increase of MgO in the dykes (b & d). Plagioclase accumulation vectors represent 10% crystal content (with a composition of 32 wt% Al_2O_3 and 0 wt% MgO and TiO_2) and alteration vectors for dykes and lavas represent the change in composition for an increase of 2 wt% L.O.I. (derived by a linear regression of major elements versus L.O.I.). The relations between immobile trace elements Cr and Zr (shown in e) are consistent with MORB rather than BAB. MORB and BABB data from Gale et al. (2013).*

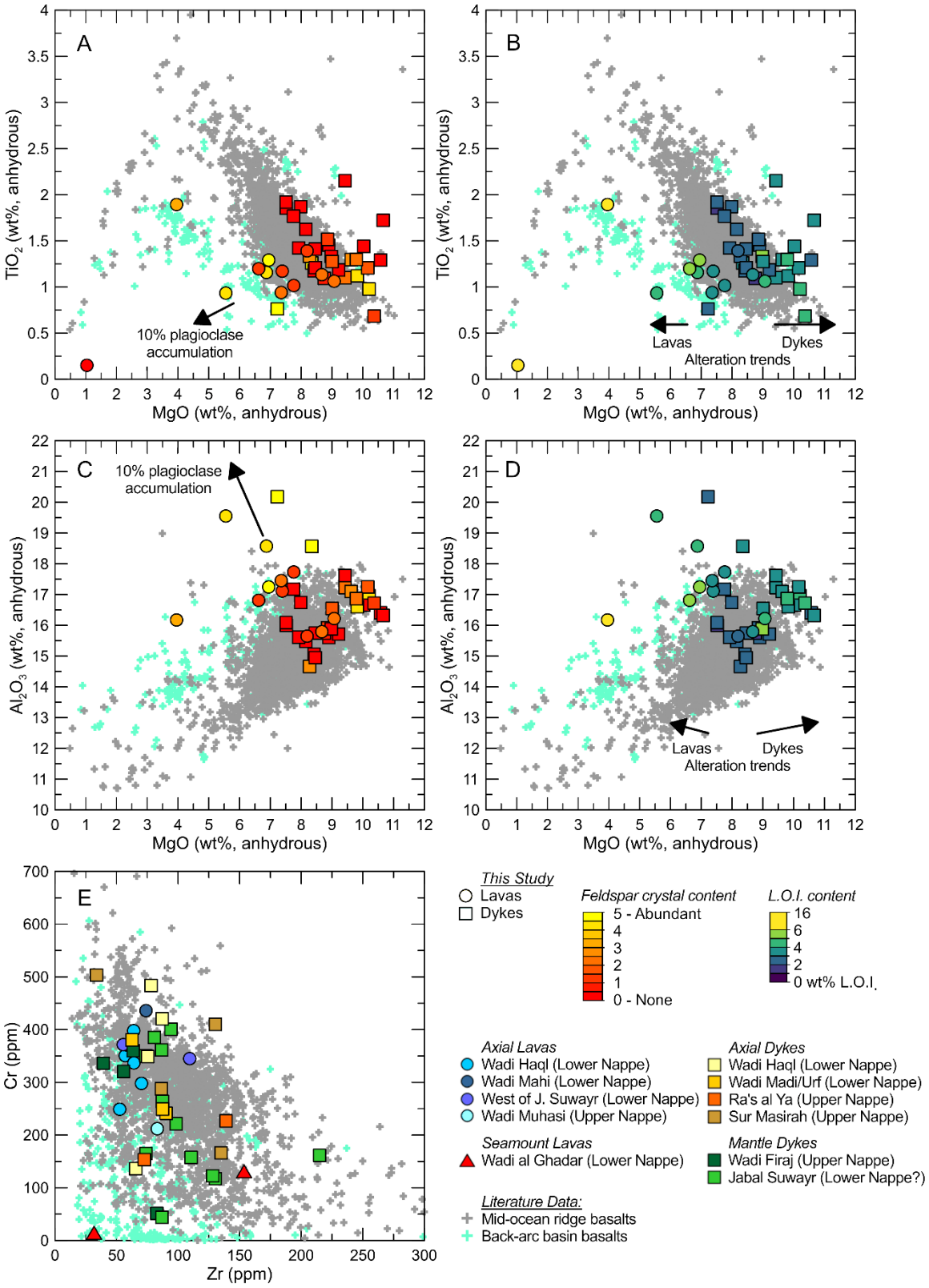

One of the geochemical parameters used by the Swiss researchers to distinguish the MOR-suite from the alkaline suite (as defined in their work) is the alkalinity of the lavas and dykes. They found that the former plotted in the subalkaline field in a total alkaline versus silica plot (TAS-diagram), whereas the latter plotted in the alkaline field (Meyer et al., 1996; Peters and Mercolli, 1997). The use of this

geochemical parameter as a discrimination criterium is undermined, however, by the observation that the major elements have been affected by alteration to various extents, especially the fluid-mobile elements Na_2O and K_2O, as indicated by the significant amount of scatter in the trends in Figure 4.6g & h. As an alternative, the following sections will focus on a geochemical characterisation of the lavas and dykes based on immobile trace elements (TiO_2, Zr, Y, Nb and the rare earth elements, REE). Floyd and Winchester (1977) used many volcanic rocks from a variety of tectonic settings to develop a TAS proxy diagram (later updated by Pearce, 1996) that helps discriminate between altered volcanic rocks using Zr/Ti and Nb/Y ratios, where the Nb/Y serves as an indication of magma alkalinity.

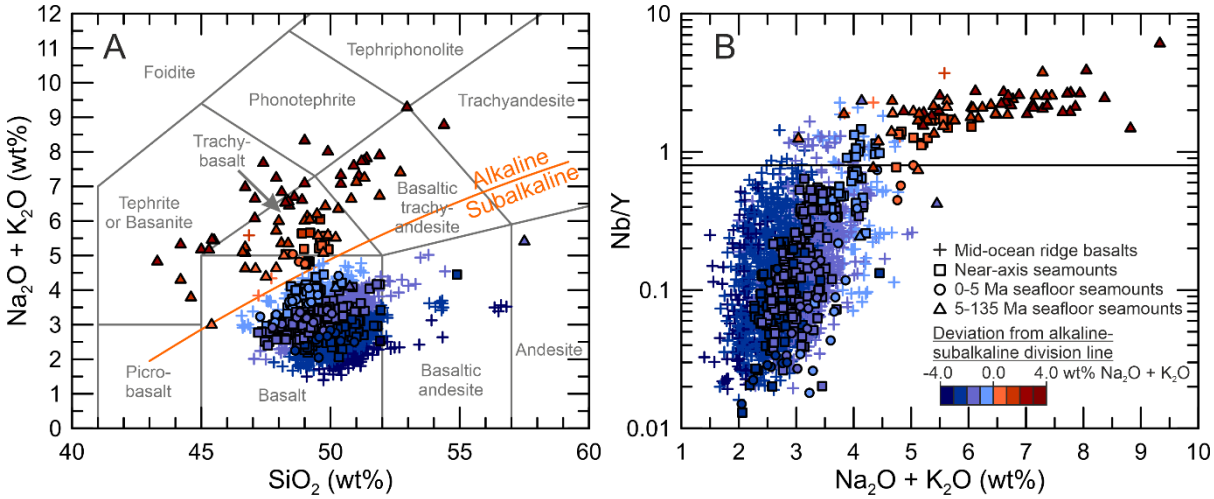

Figure 4.10: *(a) Oceanic lavas from various tectonic settings plotted on a total alkaline versus silica (TAS, Le Bas et al., 1986) diagram, coloured by their deviation from the alkaline-subalkaline division line of Irvine and Baragar (1971). Mid-ocean ridge basalts (compiled by Gale et al., 2013) are predominantly subalkaline (tholeiitic), whereas near-axis seamounts (data from Niu and Batiza, 1997; Geshi et al., 2007; and Anderson et al., 2021), off-axis seamounts erupted on 0 – 5 Ma seafloor (data from Janney et al., 2000; and Hall et al., 2006) and off-axis seamounts erupted on 5 – 135 Ma seafloor (data from Janney et al., 2000; Davis et al., 2002; and Hirano et al., 2006) are subalkaline to alkaline. (b) The alkalinity of oceanic lavas broadly correlates to Nb/Y, an immobile trace element ratio used by Pearce (1996) as a proxy for alkalinity. The division line at Nb/Y = 0.8 is the basalt/alkali basalt boundary proposed by Pearce (1996). Most subalkaline lavas have Nb/Y < 0.8 and most alkaline lavas have Nb/Y > 0.8, although both groups have several data that plot on the opposite side of the Nb/Y = 0.8 line.*

To show that this proxy holds for oceanic volcanic rocks that are not plume or arc related, Figure 4.10 shows a compilation of MORB and off-axis seamount lavas, with eruption sites that vary from young ocean lithosphere close to the ridge-axis ('near-ridge' seamounts) to old lithosphere far off-axis (data sources in figure caption). In the TAS diagram (Figure 4.10a), the vast majority of MORB plot in the subalkaline field on a tholeiitic differentiation trend. Near-axis seamounts and seamounts

erupted on <5 Ma ocean lithosphere span a range of subalkaline and alkaline compositions, with most rocks being subalkaline, whereas seamounts that erupted on older ocean lithosphere (5 – 135 Ma), including so-called 'petit-spot' intraplate volcanism (Hirano et al., 2006), tend to be dominantly alkaline. Figure 4.10b shows that Nb/Y compositions can be used to distinguish alkaline from subalkaline lavas accurately for most of the samples, using the division line at Nb/Y = 0.8 from Pearce (1996). Despite this broad correlation, there is a small amount of overlap between the two groups, indicating geochemistry cannot be solely relied upon: about 6.4% of the subalkaline rocks (defined using the TAS diagram) have a Nb/Y > 0.8, whereas about 1.7% of the alkaline rocks have Nb/Y < 0.8. Consequently, the Masirah lavas and dykes with Nb/Y < 0.8 will be described in the following sections as having a 'tholeiitic affinity', whereas lavas and dykes with Nb/Y > 0.8 will be referred to as having an 'alkaline affinity'.

4.3.3 Geochemical characterisation of the lavas

The axial lavas have TiO_2, Zr, Y and Nb contents similar to MORB, although one lava from Wadi Muhasi (18MM235) plots in the alkali-basalt field in the Zr/Ti versus Nb/Y immobile trace element diagram due to slightly elevated Nb contents, as do several axial lavas from MasirahDB (Figure 4.11a). Rare earth element (REE) compositions are variable and range from D-MORB to E-MORB (as defined by Gale et al., 2013), with La_N/Yb_N ratios of 0.64 – 1.51 (average 1.12, normalised to primitive mantle; McDonough and Sun, 1995) (Figure 4.12a). The aforementioned lava from Wadi Muhasi is more enriched in light REE (LREE, La_N/Yb_N=4.71). Using the lambda-parametrisation of REE-patterns of O'Neill (2016), in which subtle nuances in REE slope and curvature are more readily identifiable, the axial lavas of Masirah compare closely to the modern MORB array, with sample 18MM235 from Wadi Muhasi plotting at the most enriched extremity (Figure 4.13a). The lavas at Wadi Haql shows no clear geochemical stratigraphic trend, although the two most enriched samples (18MM143 and 18MM131) occur near the top of the sequence. The positive Sr anomaly present in nearly all samples (Figure 4.12) was noted previously by Peters and Mercolli (1997) and tentatively attributed to hydrothermal alteration processes.

The seamount lavas from this study (18MM364) and from MasirahDB have Zr and TiO_2 contents similar to enriched MORBs but they extend to higher Nb contents and tend to have lower Y for a given Zr content. Their compositions overlap to some degree with the more enriched axial lavas (Figure 4.11a). The more evolved lithologies extend to elevated Zr (~1200 ppm), Nb (~180 ppm) and Y (~120 ppm), and TiO_2 contents initially increase before dropping below 0.5 wt%, consistent with differentiation beyond Fe-Ti oxide saturation. Nb/Y ratios greater than 0.8 in nearly all rocks indicate their alkaline affinity (Figure 4.11a). They are LREE enriched compared to most MORBs (La_N/Yb_N of 4.85 – 11.84, average 8.45; Figure 4.12a and 4.13a).

Post-axial lavas and out-of-sequence lavas were not sampled for this study but geochemical compositions are obtained from MasirahDB. Only one post-axial lava appears in MasirahDB and its geochemistry is similar to the more primitive (i.e., basaltic) of the seamount lavas. The out-of-sequence lavas in MasirahDB span a wide range of major- and trace element compositions, overlapping with both the typical axial lava compositions as well as enriched seamount lava compositions (Figure 4.11a).

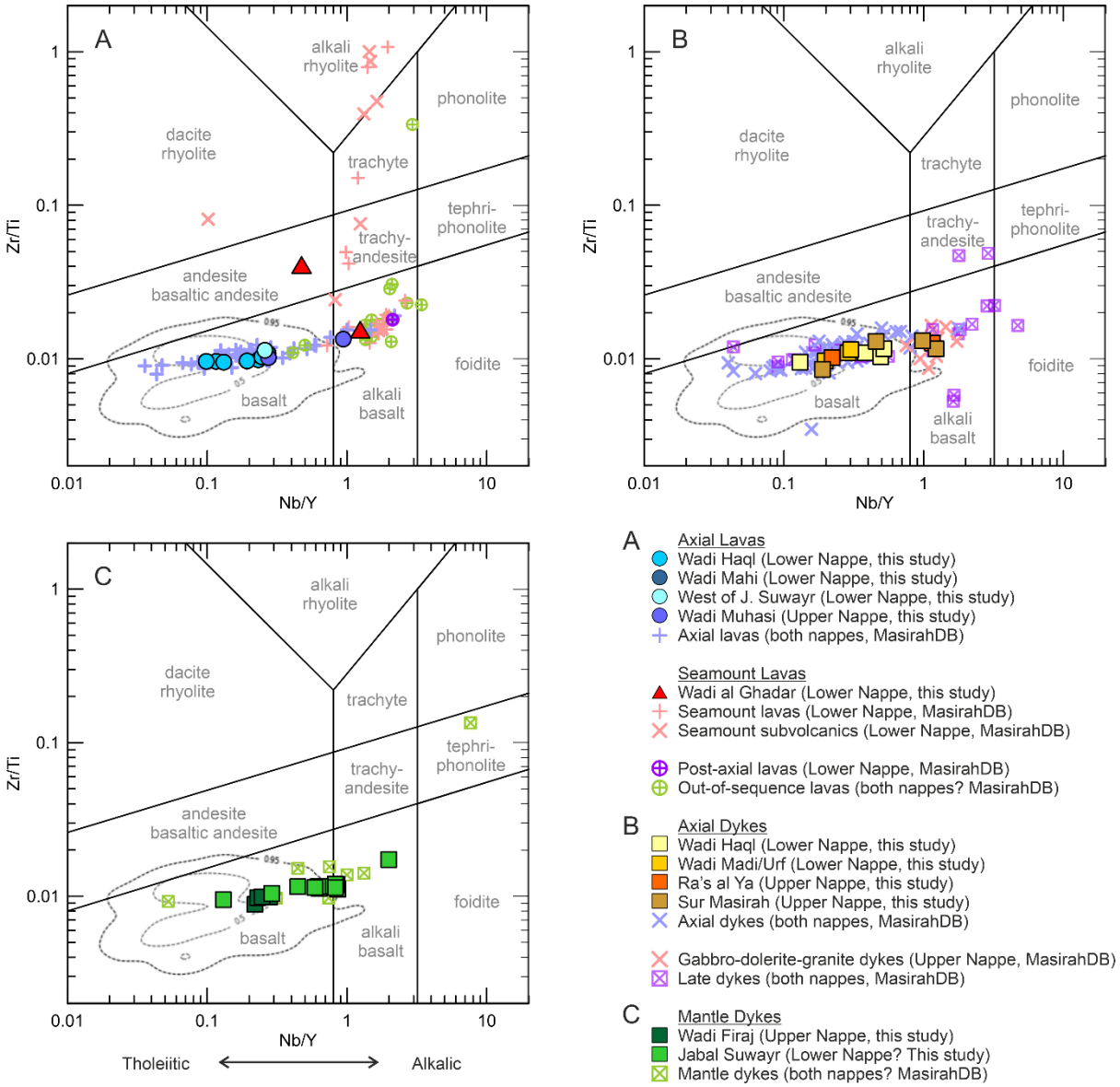

Figure 4.11: *Immobile trace element discrimination diagram (Zr/Ti vs. Nb/Y) after Pearce (1996) showing the variability in tholeiite and alkaline affinity the Masirah lavas (a), dykes in the crust (b) and dykes in the mantle (c). Note the significant amount of overlap between the ranges of the various defined groups (see text for discussion). The compositions of MORB are indicated by two contours (50% and 95%) of a kernel density estimate of the compilation by Gale et al. (2013), which was filtered for samples from mid-ocean ridges (as opposed to back-arc basins) that were >500 km from a hotspot.*

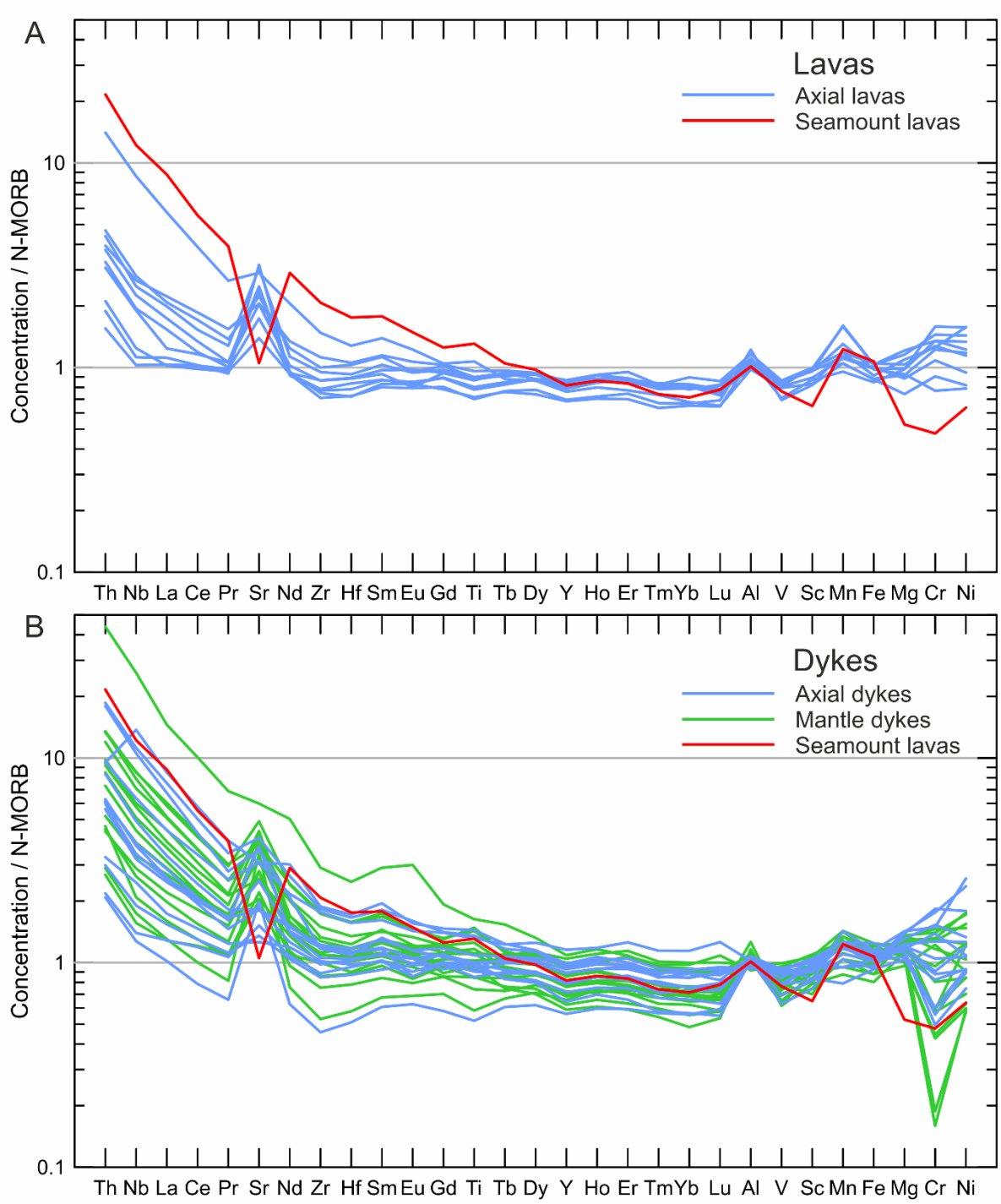

Figure 4.12: *N-MORB normalised trace element diagrams of the Masirah lavas (a) and dykes (b). Note the overlap of Axial dykes and Mantle dykes, as well as the overlap of the most enriched axial dykes and lavas with the seamount lavas (normalisation values from Pearce and Parkinson, 1993).*

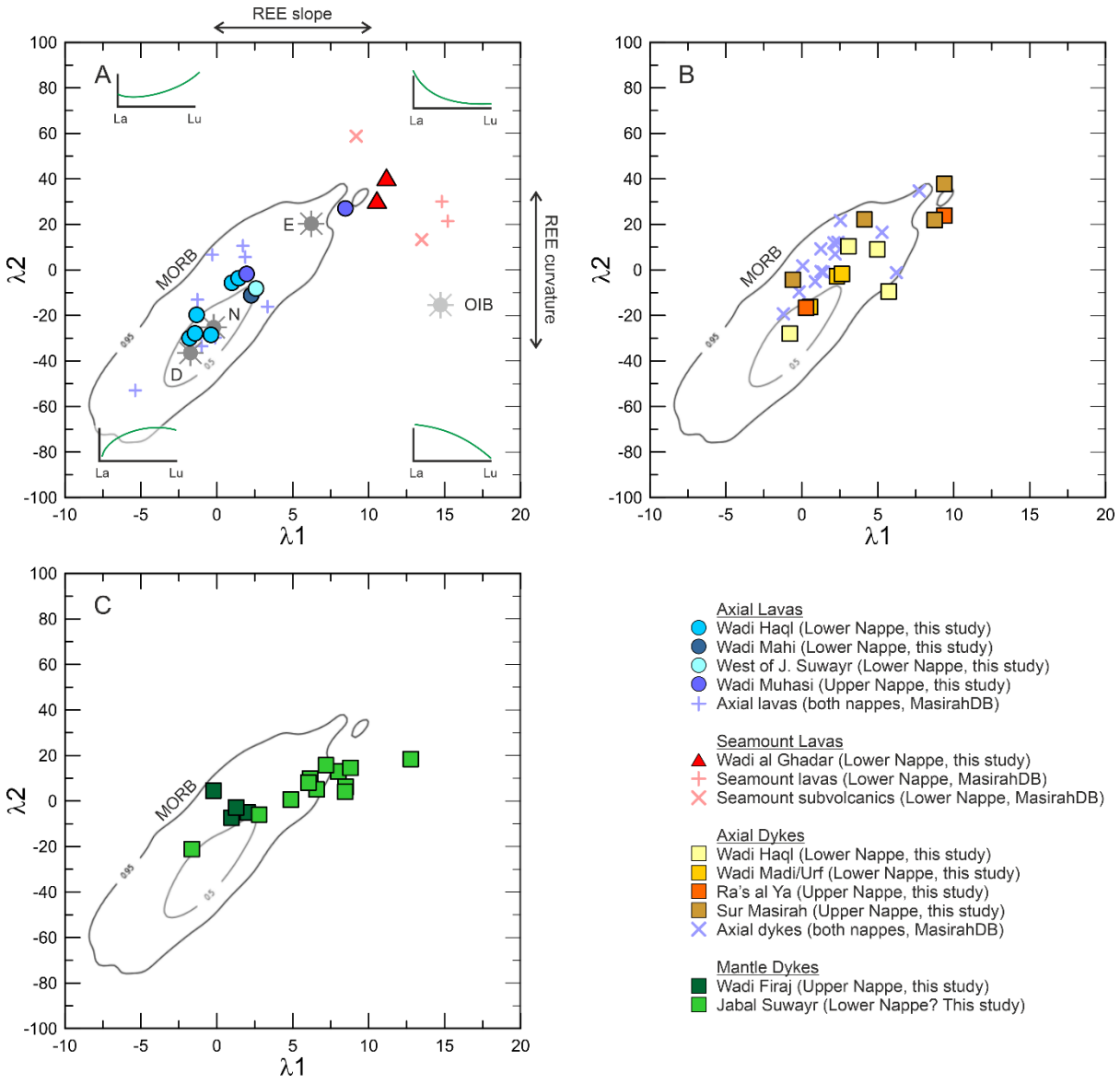

Figure 4.13: *REE shape-parameter plots ('Lambda plots') after O'Neill (2016) showing the variability in REE patterns for the Masirah lavas (a), dykes in the crust (b) and dykes in the mantle (c). Lambda 1 (x-axis) represents the slope of the REE pattern and Lambda 2 (y-axis) the curvature of the REE pattern (panel (a) contains four example REE patterns that illustrate the REE slopes and curvature for the λ1- λ2 coordinates they are positioned at). The compositions of MORB are indicated by two contours (50% and 95%) of a kernel density estimate of the compilation by Gale et al. (2013), which was filtered for samples from mid-ocean ridges (as opposed to back-arc basins) that were >500 km from a hotspot and had 10 or more REE analyses available. Grey sun symbols show where commonly used endmember compositions plot on a lambda plot and include D-MORB (labelled D), N-MORB (N) and E-MORB I as defined by Gale et al. (2013) and ocean island basalt (OIB) as defined by Sun and McDonough (1989). Lambda shape parameters were calculated using the web-applet of Anenburg (2020).*

4.3.4 Geochemical characterisation of the dykes

The sheeted dykes and dyke swarms from the gabbro-dyke transition (i.e., both occurrences of axial dykes) have similar trace element compositions, with MORB-like TiO_2, Zr, Nb and Y contents (Figure 4.11b). Their REE compositions range from D-MORB to E-MORB and most have La_N/Yb_N ratios of 0.85 – 2.83 (average 1.67), making them as a whole somewhat more enriched than the axial lavas (Figure 4.12b and 4.13b). Dykes 18MM152 and 18MM154 from Sur Masirah and dyke 18MM191 from Ra's al Ya have slightly elevated Nb, Zr and TiO_2, giving them an alkaline affinity. Furthermore, these dykes are also more strongly enriched in LREEs, plotting at the extremity of the MORB array and overlapping with the seamount lavas. The compositional range in axial dykes from MasirahDB broadly mirrors these results, displaying a range of D-MORB to E-MORB compositions and getting close to alkaline affinities.

Mantle dykes have Ti, Zr, Nb and Y compositions similar to the crustal dykes, with most falling in the tholeiite-basalt field, although slightly higher Nb contents brings some dykes close to the alkali-basalt field (Figure 4.11c). Substantially higher Nb contents in sample 18MM307 from Jabal Suwayr give this dyke an alkaline affinity. The mantle dykes have La_N/Yb_N of 0.73 – 8.66 (average 3.14), making them more enriched than the axial dykes on the whole, although the two groups still display a large amount of overlap (Figure 4.12b and 4.13c). Mantle dykes from MasirahDB cover a slightly larger range in trace element compositions, showing tholeiitic to alkaline affinities.

The gabbro-dolerite-granite dykes and late dykes were not sampled in this study and geochemical compositions were obtained from MasriahDB. The gabbro-dolerite-granite dykes mainly have elevated Ti, Nb and Y with respect to the axial dykes, with Zr/Ti and Nb/Y compositions that reflect an alkali basalt affinity, although some are tholeiitic (Figure 4.11b). The late dykes, in contrast, overlap with both the axial and the gabbro-dolerite-granite dykes, spanning the entire observed range of trace element compositions in these groups.

To establish the relation between the relative timing of dykes and their composition, and test the Swiss model involving early MORB-type and late alkaline-type dykes, it is necessary to combine crosscutting relationships with geochemical data. It was not practically possible during this study, however, to fully analyse all collected samples. Furthermore, for the bulk of the MasirahDB data, details on crosscutting relationships are not available. Nevertheless, despite analytical uncertainties in pXRF measurements, it was found that the pXRF data (collected as part of an initial characterisation of the dyke chemistry intended to guide sample selection, see Chapter 3 & Table V) was useful for determining whether to a first approximation the geochemical affinity of the remainder of the sampled dykes has a tholeiitic (MORB-like) or alkaline affinity. The subset of dyke

margins fully analysed for WR major and trace element compositions was compared to the trace element data obtained by pXRF. Figures 4.14a-c show that Zr and Y concentrations, as well as Zr/Y ratios, obtained by pXRF closely agree with LA-ICP-MS results. Figure 4.14d and e show that the Zr/Y ratio in the Masirah dykes and lavas correlates well with LREE enrichment, represented by the λ1 parameter following O'Neill (2016). This observation supports the use of Zr/Y as a LREE enrichment proxy for samples that lack more accurate LA-ICP-MS data. Dyke margin Zr and Zr/Y compositions measured by pXRF are shown sorted by location, cross-cutting relationships, crystal content and field appearance in Figure 4.15. Regardless of location or field-setting, a wide range of compositions is observed. The data span most of the compositional spectrum defined by modern MORBs (Gale et al., 2013), with some samples extending to more enriched compositions.

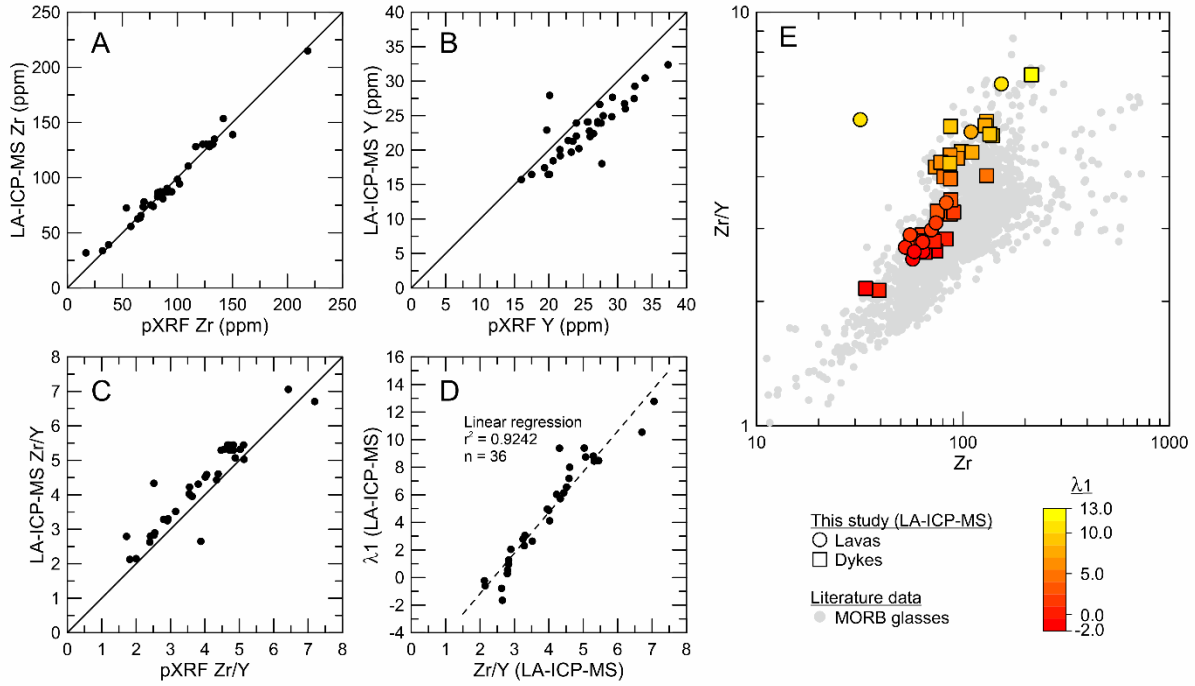

Figure 4.14: *Comparison of the Masirah dyke compositions measured by pXRF and LA-ICP-MS: (a) Zr, (b) Y and (c) Zr/Y. (d) A plot of Zr/Y versus REE shape parameter λ1, representing REE slope, shows there is a strong correlation between these two variables. (e) A plot of Zr versus Zr/Y shows this relation again for all dyke and lava LA-ICP-MS data (data are coloured by λ1).*

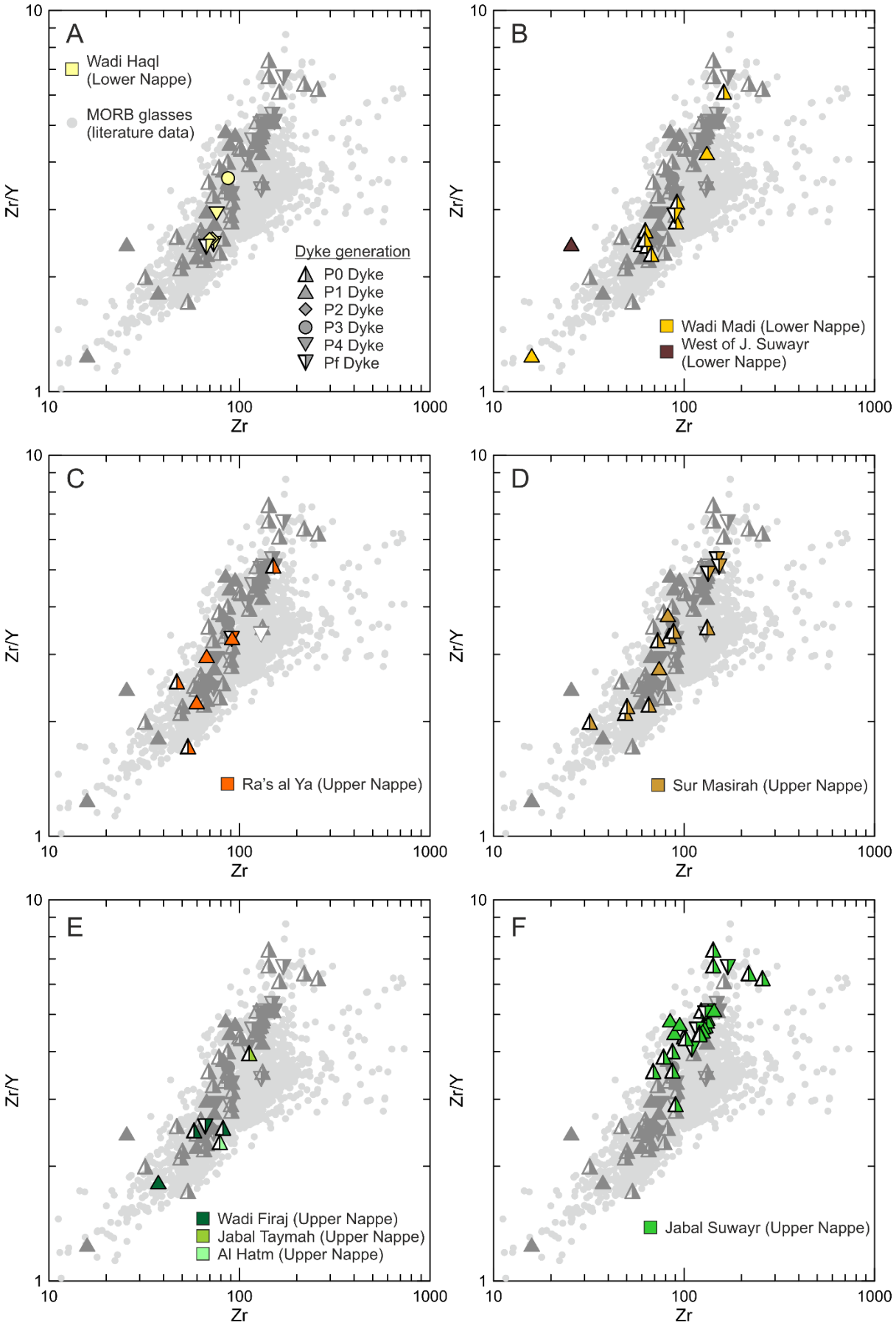
A
Wadi Haql
(Lower Nappe)
MORB glasses
(literature data)
Dyke generation
P0 Dyke
P1 Dyke
P2 Dyke
P3 Dyke
P4 Dyke
Pf Dyke
B
Wadi Madi (Lower Nappe)
West of J. Suwayr
(Lower Nappe)
C
Ra's al Ya (Upper Nappe)
D
Sur Masirah (Upper Nappe)
E
Wadi Firaj (Upper Nappe)
Jabal Taymah (Upper Nappe)
Al Hatm (Upper Nappe)
F
Jabal Suwayr (Upper Nappe)
Zr/Y
Zr
10
100
1000
1

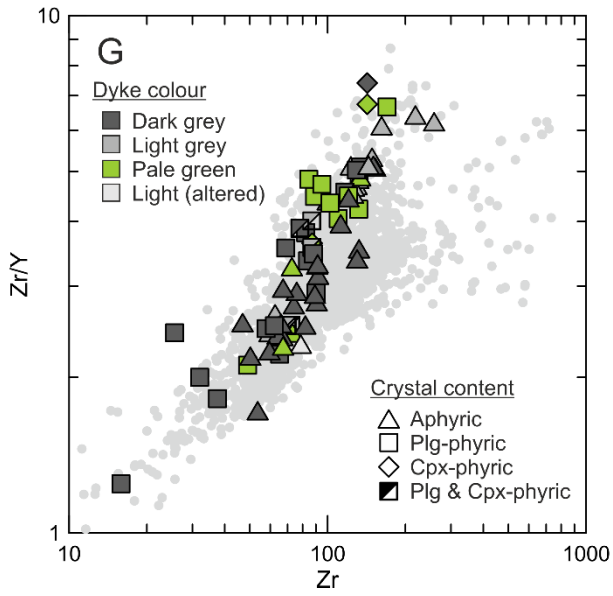

Figure 4.15 (this and previous page): *Zr/Y versus Zr plots of dykes analysed by pXRF. (a-f) Dykes from a single sampling location tend to span a large range in trace element composition. Dyke crosscutting relations were grouped as follows: P0: dyke is not observed crosscutting or being crosscut by another dyke; P1: dyke is not observed crosscutting an older dyke and is crosscut by a younger dyke; P2: dyke crosscuts an older P1 dyke and is crosscut by a younger dyke; P3: dyke crosscuts an older P2 dyke and is crosscut by a younger dyke; P4: dyke crosscuts an older P3 dyke and is crosscut by a younger dyke; Pf: dyke crosscuts an older dyke (P1-P4) but is not observed to be crosscut by a younger dyke. No systematic trends are observed in the crosscutting relationships of dykes: Early dykes range from depleted to enriched trace element compositions, although the most enriched dykes (top right of the plot) are never observed to be crosscut by younger dykes. (g) Dyke compositions grouped by their physical appearance (dyke colour and crystal content) also shows no systematic relationship.*

Examining a large number of crosscutting relationships reveals that there is no evidence in support of two distinct geochemical groups with a simple evolution of geochemistry through time, as implied by previous work (e.g., Meyer et al., 1996; Peters and Mercolli, 1997, 1998; Peters, 2000). Instead, the oldest generations of dykes span the entire N-MORB to E-MORB range (Figure 4.15). Dykes with an alkaline affinity are generally observed crosscutting older dykes, sometimes – but not always – with an anomalous orientation. Dyke compositions also lack a consistent correlation with their physical appearance (crystal content and colour), as implied by Peters et al. (1995), or sampling location, and each investigated subdivision spanned most of the range in trace element compositions (Figure 4.15g). Amongst the mantle dykes, there was likewise no systematic difference between dykes crosscutting mantle harzburgites and dykes crosscutting gabbroic plutons in the mantle.

4.3.5 Gabbro mineral chemistry

A total of 83 gabbro samples were analysed for their major element mineral chemistry at Cardiff University using a Zeiss Sigma HD EDS-SEM. These samples included 48 rocks from the axial gabbroic lower crust, 5 gabbro-dolerite-granite gabbros, 17 gabbroic plutons in the mantle and 13 evolved gabbros and felsic lithologies (Data reported in Table VI & VII). The mineral compositions of the four groups of gabbros show varying degrees of differentiation, but average core compositions nevertheless roughly form a single differentiation trend, comparable to gabbroic rocks from the Mid-Atlantic Rise and Southwest Indian Ridge (Figure 4.16a). In some samples, hand-sample scale textural heterogeneity (such as grainsize variation or a felsic vein segregating from an evolved gabbro) is correlated with variations in mineral chemistry, indicated by tie-lines in Figure 4.16a. The extremities of this differentiation trend are defined by the axial gabbroic lower crust on the primitive end and the gabbro-dolerite-granite suite at the evolved end, with some overlap between these two groups. Plagioclase compositions of the gabbro-dolerite-granite suite gabbros span a large range of anorthite content (An_4 – An_{69}, average An_{37}) but is generally more sodic than plagioclase from the axial gabbros (An_{37} – An_{95}, average An_{77}; Figure 4.16b). Clinopyroxene, when present, is also more evolved (Mg# = 55 – 78, average 68, where Mg# is calculated assuming all Fe is FeO) compared to the axial gabbros (70 – 95, average 87; Figure 4.16c).

The gabbroic plutons in the mantle with an axial affinity have primitive mineral compositions (plagioclase An_{76} – An_{88}, clinopyroxene Mg# = 84 – 91, and olivine Fo_{85} – Fo_{87}) that fall within the range found in the axial lower crust (Fo_{78} – Fo_{90}, average Fo_{85}). In contrast, the gabbroic mantle intrusions with an alkaline affinity have plagioclase and clinopyroxene compositions that overlap with the gabbro-dolerite-granite suite. The gabbros and olivine gabbros from Safa'iq, which have a transitional affinity, have clinopyroxene Mg# (78 – 86) and plagioclase An% (An_{59} – An_{77}) similar to the more evolved axial gabbros (which lack olivine). Their olivine compositions (Fo_{78} – Fo_{79}), however, are more evolved than those typically found in the axial lower crust.

The small-volume occurrences of evolved and varitextured gabbros in the axial lower crust are often more prone to alteration, making it difficult to obtain primary mineral compositions. Analyses in several samples nevertheless show clinopyroxene (Mg# 81 – 85) on the evolved end of the range for axial gabbros, and variable plagioclase compositions (An_{20} – An_{98}). High anorthite contents (>An_{85}) could result from elevated water contents in differentiated melts, which can also give rise to pegmatite textures. The large range in plagioclase anorthite content, often within single samples, can to a certain extent be explained by local (i.e., within-crystal), sodium mobilisation during hydrothermal albitisation. In varitextured gabbro 18MM106, a Ca-rich plagioclase crystal (An_{95}) is crosscut by sodic veins (An_{27}). The average compositions of several 100x100 µm areas are An_{76} –

An_{87}, and potentially reflect a more representative range of primary compositions. The sample that plots at a high anorthite content (>An_{90}) but nevertheless has a low clinopyroxene Mg# (~0.81) is interpreted to have had its composition shifted by alteration.

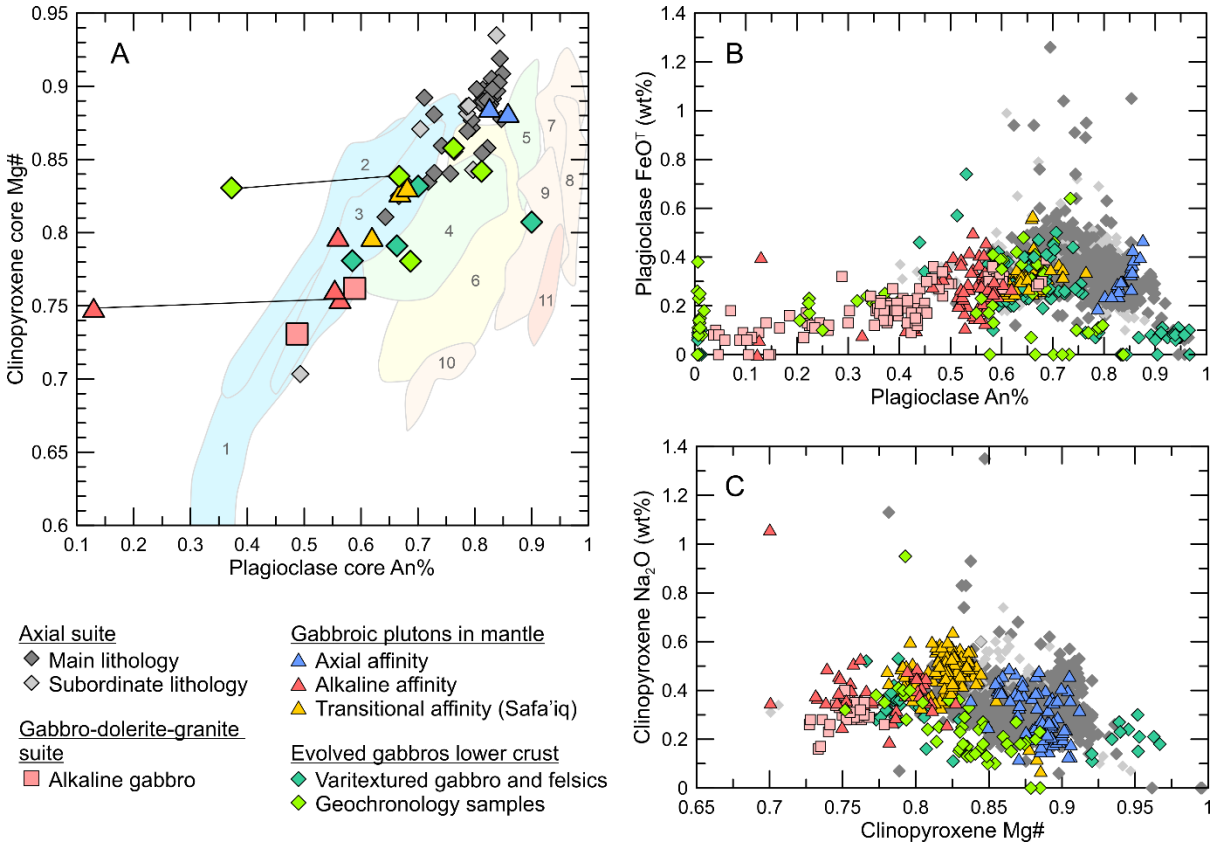

Figure 4.16: *(a) Plagioclase anorthite and clinopyroxene Mg# relations for crystal cores (averaged per hand-sample); tie-lines connect data points of heterogeneous samples (e.g., a gabbro with a felsic vein or pegmatite segregation). Fields indicate crystallisation trends for dry (mid-ocean ridge, blue), 'moist' (subduction initiation, green and yellow) and wet magmas (subduction zone proximal, light and dark orange) undergoing differentiation (1: Southwest Indian Ridge; 2: Cayman Rise; 3: Kane Fracture Zone; 4: Semail gabbros; 5: Semail crust-mantle transition; 6: Izu-Bonin Arc phenocrysts; 7: Troodos websterite; 8: Troodos lower gabbros; 9: Troodos upper gabbro; 10: Troodos granular dykes; 11: Lesser Antilles xenoliths; after Kvassnes et al. (2004) and references therein). (b) Plagioclase anorthite-Fe relations (individual analyses). (c) Clinopyroxene Mg#-Na relations (individual analyses).*

4.4 Geochronology

4.4.1 Sample selection, petrography and WR geochemistry

To establish the timing and duration of on-axis magmatism on Masirah, evolved lithologies from the axial gabbroic lower crust were identified in the field and sampled for high precision single zircon U-Pb geochronology. Eight leuco-gabbros, varitextured gabbros, diorites and anorthosites from various sites on Masirah (locations in Figure 4.1), as well as one felsic pluton from the mantle section at Ra's

Madrakah on the mainland, were selected for this purpose. The following section discusses their field relationships to establish their relative age with respect to the axial gabbro sequence (Table 4.1), and subsequently compares their petrography and whole-rock and mineral chemistry with the axial and gabbro-dolerite-granite gabbro occurrences.

Table 4.1. Field description of geochronology samples (continues on next page)

Sample	Nappe	Location	Lithology	Field relationship	Interpretation
18MM323	Lower	Urf	Varitextured leuco-gabbroic vein	Segregates from axial gabbros, which is elsewhere crosscut by dyke swarms of D-MORB to E-MORB affinities	Coeval with axial crustal sequence
18MM337	Lower	Wadi Madi	Varitextured leuco-gabbroic vein	Segregates from axial gabbros, which is elsewhere crosscut by dyke swarms of D-MORB to E-MORB affinities	Coeval with axial crustal sequence
18MM346	Lower	Wadi Madi	Anorthosite	Intrusive body several metres in size that crosscuts the axial gabbros and dyke swarms	Postdates axial crustal sequence
18MM032	Upper	Area between Haql and Sur Masirah	Altered evolved leucocratic dyke	Part of the north-south trending Sur Masirah dyke swarm (D-MORB to alkaline affinity) that intrudes the axial gabbroic lower crust. Elsewhere in the outcrop, the dolerite dykes and the felsic dykelets have mutually crosscutting relationships	Coeval with axial crustal sequence
18MM033	Upper	Area between Haql and Sur Masirah	Evolved oxide-diorite dyke	Part of the north-south trending Sur Masirah dyke swarm (D-MORB to alkaline affinity) that intrudes the axial gabbroic lower crust. Sampled dyke is crosscut by a dolerite dyke of the dyke swarm	Coeval with axial crustal sequence

18MM163	Upper	Area between Haql and Sur Masirah	Leuco-gabbroic vein	Crosscuts the axial lower crust, elsewhere in the area felsic lithologies display mutually crosscutting relationships with the axial gabbros	Coeval with axial crustal sequence
18MM170	Upper	Area between Haql and Sur Masirah	Anorthosite pod	Part of the axial lower crust, which is elsewhere crosscut by a dyke of E-MORB affinity	Coeval with axial crustal sequence
18MM189	Upper	Ra's al Ya	Varitextured gabbro	Segregating from the axial gabbros and crosscut by a dyke swarm of D-MORB to alkaline affinity	Coeval with axial crustal sequence
18MM368	N/A	Ra's Madrakah	albitite	Metre-sized lens intruded into the mantle section	Unknown

The field relations of seven of the samples from Masirah indicate they are coeval with the axial crustal sequence, whereas an eighth sample crosscuts the axial crust (Table 4.1). In the Lower Nappe, samples include two varitextured leuco-gabbroic veins from separate outcrops in the Wadi Madi/Urf area in the south of the island (18MM323 & 18MM337; Figure 4.17a-b & d-e). These samples segregate from their host gabbros of the axial lower crust and are therefore coeval with the axial gabbros. A third sample from the same area (separate outcrop) is an intrusive body of anorthosite several metres in size that crosscuts and postdates the axial gabbros and dyke swarms (18MM346; Figure 4.17j). In the Upper Nappe, four samples are from the area between Haql and Sur Masirah. Two evolved dykes from the same outcrop are part of (and therefore coeval with) the north-south oriented Sur Masirah axial dyke swarm, which intrudes the gabbroic lower crust and has mutually crosscutting relationships with the felsic dykelets (18MM032 & 18MM033; Figure 4.17h). A leuco-gabbroic vein (18MM163; Figure 4.17g) and an anorthosite pod (18MM170) occur in separate outcrops in the axial lower crust nearby. Elsewhere in the Sur Masirah area, felsic pods and veins are observed segregating from – and back-intruding into – the axial gabbro sequence, interpreted as the differentiated end-product of unerupted melts in a partially solidified axial magma mush. The fifth Upper Nappe sample is a varitextured gabbro segregating from (and therefore coeval with) the axial gabbros at Ra's al Ya (18MM189). The final sample is a metre-sized lens of albitite intruded into the

mantle section at Ra's Madrakah. Since no crust is exposed at Ra's Madrakah, the relative age of the Ra's Madrakah sample is unknown.

Most samples have mineral assemblages and textures comparable to the evolved gabbros in the axial gabbroic crust (Figure 4.17c & f and Figure 4.5h) and are distinct from the gabbro-dolerite-granite suite (Figure 4.5c & d). They often contain accessory titanite and occasionally zircon can be identified under the microscope. Brown amphibole and Fe-Ti oxides are generally absent or present as a minor phase (sample 18MM323 has accessory brown amphibole and samples 18MM170, 18MM337 and 18MM368 have accessory oxides). Dyke 18MM033 is an exception and has abundant Fe-Ti oxides (~5%) and brown amphibole blebs enclosed in green ophitic amphibole (Figure 4.17i). Both samples 18MM163 and 18MM189 have interstitial corrosive pockets containing euhedral to subhedral rutile and ilmenite and sometimes zircon, enclosed by titanite oikocrysts (Figure 4.17k). These textures are interpreted to have formed during hydrothermal alteration of Fe-Ti oxides, where iron was stripped from the rock by a fluid and hydrothermal rutile, ilmenite and titanite formed from the remaining, less mobile titanium. Plagioclase anorthite and clinopyroxene Mg# contents are variable and overlap with other varitextured gabbros and felsics, as well as the more evolved axial gabbros and the more primitive gabbro-dolerite-granite gabbros (Figure 4.16). The evolved plagioclase compositions in Figure 4.16 are from sample 18MM033, where plagioclase is albitic (An_1-An_2), and from the segregating veins in samples 18MM323 and 18MM337, where plagioclase is more evolved (An_{32}-An_{40} and An_{21}-An_{25} respectively) than plagioclase of the host rock (An_{66}-An_{69} and An_{55}-An_{60} respectively, see also tie-line in Figure 4.16a for 18MM323; no fresh clinopyroxene compositions were available for sample 18MM337).

Figure 4.17 (next page): *Field relations and petrography of geochronology samples (microphotographs panels are split in two, with plane-polarised light (PPL) images on the left and cross-polarised light (XPL) images on the right). (a) Varitextured leuco-gabbroic vein (18MM323) segregating from the axial gabbros near Urf, with a close-up of the contact in inset (b) and the petrographic relations in panel (c). (d) Varitextured leuco-gabbroic vein (18MM337) segregating from the axial gabbros in Wadi Madi, with a close-up of the contact in panel I and the petrographic relations in panel (f). (g) Leuco-gabbroic vein (18MM163) crosscutting the axial gabbros in the area between Haql and Sur Masirah. (h) Evolved oxide-diorite dyke (18MM033) within the Sur Masirah dyke swarm crosscutting the axial gabbros in the area between Haql and Sur Masirah, with the petrographic relations in panel (i). (j) Intrusive anorthosite body (18MM346) crosscutting the axial gabbros and dyke swarm in Wadi Madi. (k) Varitextured gabbro (18MM189) from Ra's al Ya containing a corrosive domain of euhedral to subhedral rutile and ilmenite crystals that are enclosed by titanite oikocrysts. Pl = plagioclase ; Cpx = clinopyroxene ; Amph = amphibole ; Ox = oxides ; Ilm = ilmenite ; Ru = rutile ; Tit = titanite ; alt. = altered.*

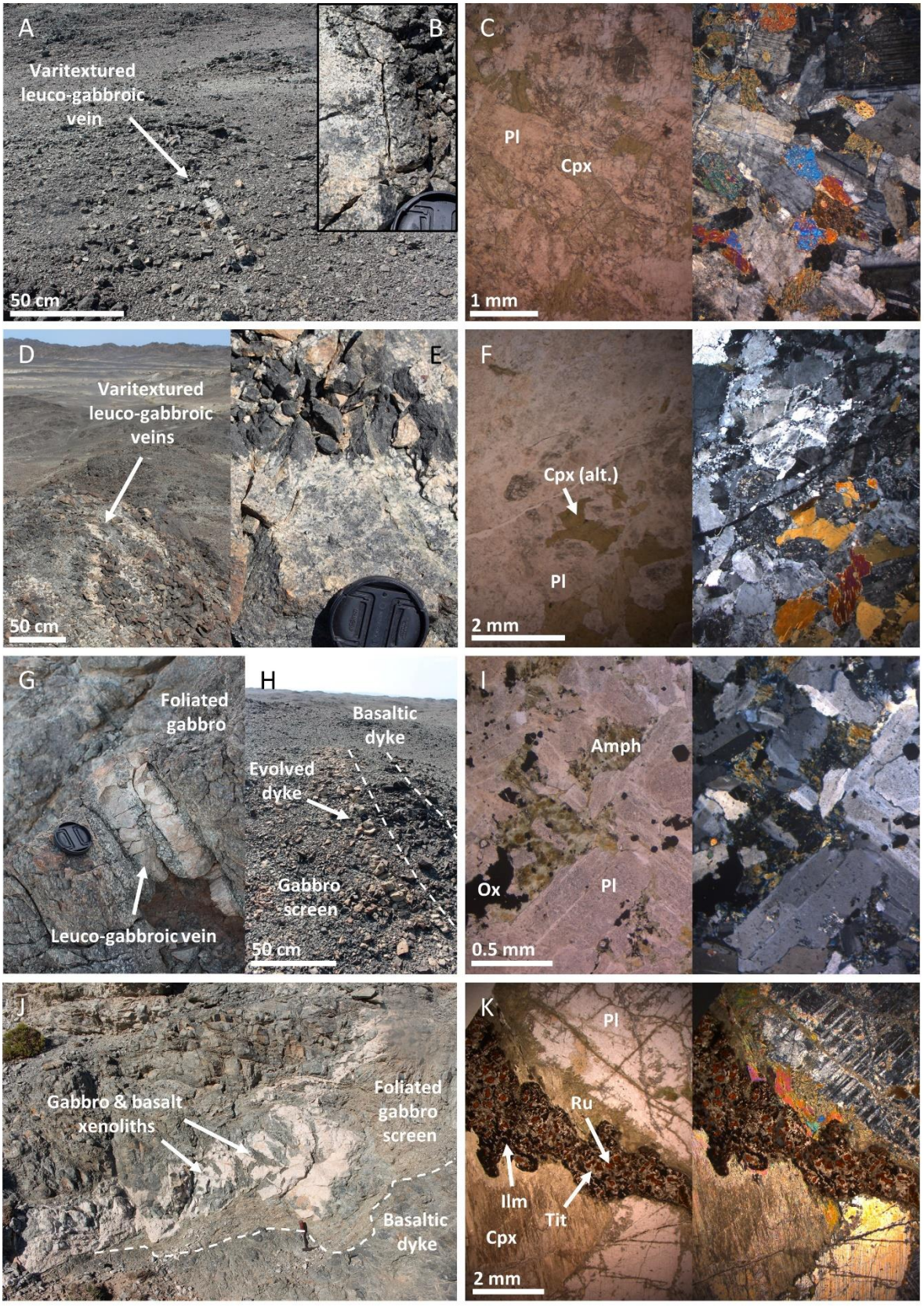
A
Varitextured leuco-gabbroic vein
B
50 cm
C
Pl
Cpx
1 mm
D
Varitextured leuco-gabbroic veins
50 cm
E
F
Cpx (alt.)
Pl
2 mm
G
Foliated gabbro
Leuco-gabbroic vein
H
Basaltic dyke
Evolved dyke
Gabbro screen
50 cm
I
Amph
Ox
Pl
0.5 mm
J
Gabbro & basalt xenoliths
Foliated gabbro screen
Basaltic dyke
K
Pl
Ru
Ilm
Tit
Cpx
2 mm

To test whether the geochronology samples represent cumulates or the crystallisation products of trapped melts, and in the case of the latter, whether the melts had a tholeiitic or alkaline affinity, the whole-rock compositions of six samples were examined and compared with melt and cumulate compositions from MasirahDB, as well as felsic plutonic rocks from modern oceanic crust (Figure 4.18). The varitextured gabbros 18MM189 and 18MM323 have whole-rock major element compositions that mostly overlap with the axial lavas and dykes (as well as the gabbro-dolerite-granite suite), although their FeO^T and MnO contents (and TiO_2 for 18MM323) are lower (Figure 4.18a & b). Their Nb/Y ratios are tholeiitic and Zr, Nb and Y contents are comparable to the axial lavas and dykes (Figure 4.18c). They have REE compositions comparable to the enriched axial dykes with La_N/Yb_N of 1.35 (18MM189) and 2.46 (18MM323), and pronounced to slight negative Eu* anomalies (0.5 and 0.9 respectively), indicating they likely formed from fractionated melts that (partially) segregated from the gabbroic mush (Figure 4.18d). Varitextured leuco-gabbro 18MM337 and anorthosite 18MM346, in contrast, both have positive Eu* anomalies (4.7 and 5.5 respectively) and major element and REE compositions consistent with plagioclase accumulation (Figure 4.18a & d), and hence a cumulate origin, with 18MM337 containing more sodic plagioclase than 18MM346. Dykes 18MM032 and 18MM033 both have lower MgO contents than the axial lavas and dykes and are relatively enriched in trace elements such as Zr (up to 1230 ppm), Nb (up to 52 ppm), Y (up to 101 ppm) and LREE (La_N/Yb_N of 4.35 and 1.95 respectively), with Nb/Y ratios on the enriched end of the tholeiite field and Zr/Ti ratios indicative of extensive differentiation (Figure 4.18c & d). These features give them a compositional affinity to the most enriched axial lavas and dykes and the seamount lavas. All six samples fall within the compositional range of major and trace elements defined by felsic plutonic rocks from modern oceanic crust, although 18MM032 and 18MM033 fall amongst the most enriched of that range and notably have higher Nb contents (Figure 4.18).

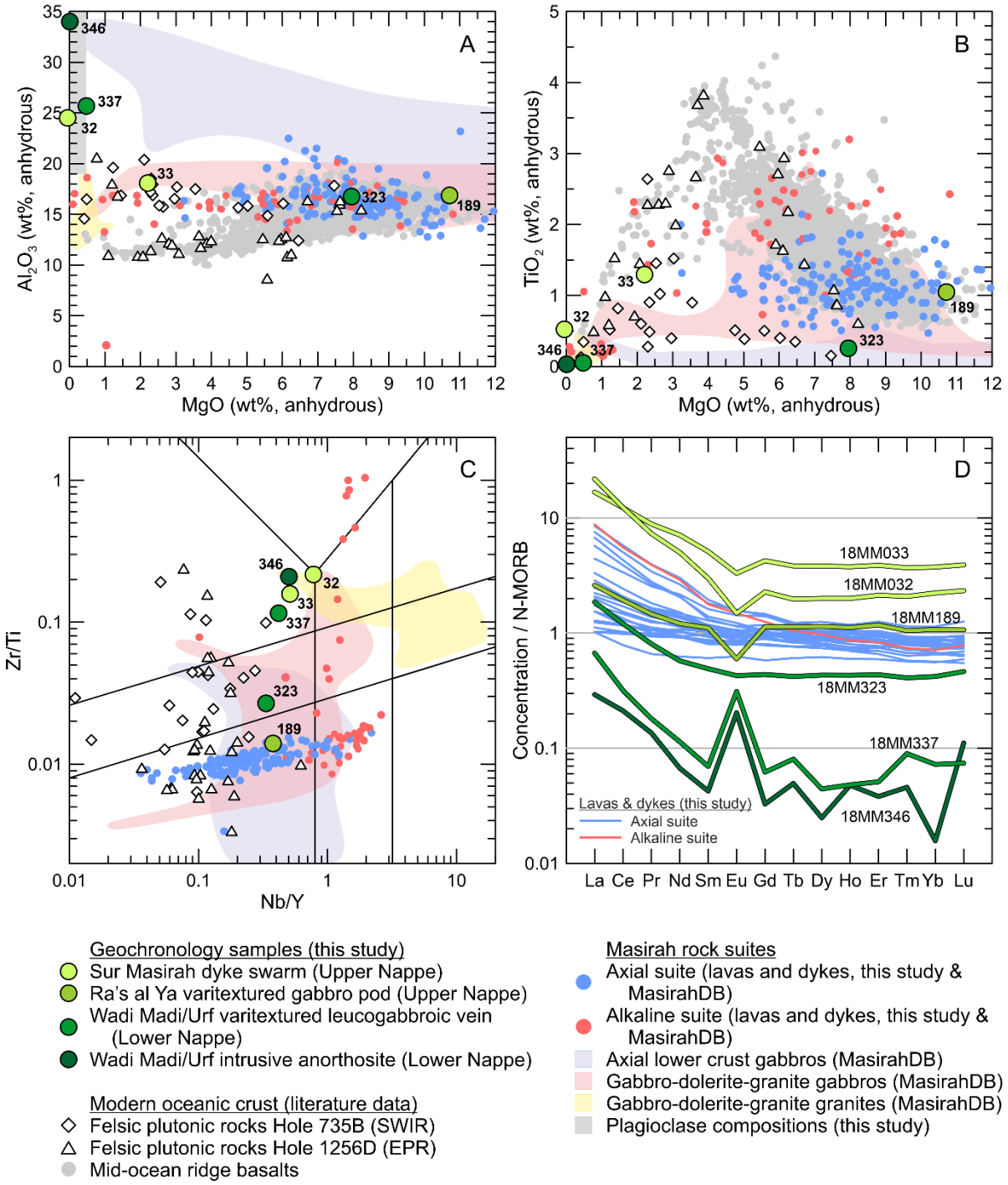

Figure 4.18: *Whole-rock compositions of geochronology samples compared to felsic plutonic rocks occurring in the modern oceanic crust formed at the slow-spreading Southwest Indian Ridge (SWIR, Hole 735B data from Niu et al., 2002 and Chen et al., 2019) and the fast-spreading East Pacific Rise (EPR, Hole 1256D data from Zhang et al., 2017), melt compositions (Masirah lavas and dykes and the global MORB compilation of Gale et al., 2013) and plutonic rocks occurring on Masirah (axial gabbros and the gabbro-dolerite-granite suite, WR data from MasirahDB). (a) & (b) Major element plots of Al_2O_3 and TiO_2 versus MgO. (c) Nb/Y versus Zr/Ti plot (after Pearce, 1996). (d) N-MORB normalised REE plot. See text for discussion.*

4.4.2 Results: high precision zircon ages

U-Pb zircon data are reported in Table IX and plotted in Figure 4.19. All dates discussed here are corrected for initial Th/U disequilibrium and reported uncertainties include propagated uncertainties on the tracer and blank compositions. The blank contribution was determined by monitoring ^{204}Pb and assuming all common Pb (Pb_c) was blank-derived. Seven zircon analyses with a significant blank contribution were not considered in further discussion of the data and the remaining 42 analyses had 0.2 – 1.1 pg Pb_c (0.42 pg on average) and a Pb^*/Pb_c ratio of 10 or greater (10 – 358, average = 53, with Pb* indicating radiogenic Pb). All dates plot on (or near) $^{207}Pb/^{235}U$-$^{206}Pb/^{238}U$ concordia. The $^{206}Pb/^{238}U$ ages of the seven samples from Upper and Lower Nappes span a range of 135.16 ± 0.11 to 130.47 ± 0.17 Ma (n = 38), whereas the two remaining samples (18MM346 intruding the Lower Nappe and 18MM368 from the mantle at Ra's Madrakah) have ages spanning 66.52 ± 0.04 to 65.80 ± 0.06 Ma (n = 4). For each sample the youngest zircon age and the weighted mean age with the mean square of the weighted deviates (MSWD) is reported (Table IX; Keller et al., 2018).

In the Lower Nappe, sample 18MM323 has a mean age of 135.07 ± 0.03 Ma (MSWD = 1.8, n = 8) and a youngest zircon age of 134.99 ± 0.10 Ma, with a total age range of 0.17 ± 0.21 Ma (calculated as the age difference between the youngest and oldest grains, with an uncertainty equal to the sum of their respective uncertainties). Sample 18MM337 has a mean age of 134.95 ± 0.05 Ma (MSWD = 8.7, n = 5; youngest zircon age = 134.73 ± 0.10 Ma) and an age range of 0.39 ± 0.19 Ma, and additionally yielded one grain with a much younger age of 131.22 ± 0.12 Ma, which was attributed to Pb-loss.

In the Upper Nappe, sample 18MM032 has a mean age of 131.36 ± 0.07 Ma (MSWD = 10.4, n = 3; youngest zircon age = 131.17 ± 0.11 Ma) and an age range of 0.39 ± 0.25 Ma. Sample 18MM033 has several zircon ages that cluster around a mean of 131.31 ± 0.05 Ma (MSWD = 0.2, n = 5; youngest zircon age = 131.26 ± 0.18 Ma) and a younger and older outlier, with respective ages of 130.94 ± 0.13 and 131.91 ± 0.08 Ma. The younger outlier was attributed to minor Pb-loss, whereas the older date may reflect a xenocryst or a zoned zircon with an inherited core derived from wall-rock assimilation. The total age range in this sample (excluding the zircon affected by Pb-loss) is 0.65 ± 0.26 Ma. Sample 18MM163 has a mean age of 130.63 ± 0.05 Ma (MSWD = 2.5, n = 5) and a youngest zircon age of 130.47 ± 0.17 Ma, with a total age range of 0.24 ± 0.26 Ma. Sample 18MM170 has a mean age of 130.62 ± 0.05 Ma (MSWD = 0.9, n = 4) and a youngest zircon age of 130.56 ± 0.12 Ma, with a total age range of 0.11 ± 0.21 Ma. Sample 18MM189 has an age cluster with a mean age of 131.03 ± 0.04 Ma (MSWD = 0.6, n = 4; youngest zircon age = 131.01 ± 0.08 Ma) and an older outlier (131.63 ± 0.07 Ma). The older zircon is interpreted to reflect wall-rock assimilation and the total age range in this sample is 0.62 ± 0.15 Ma.

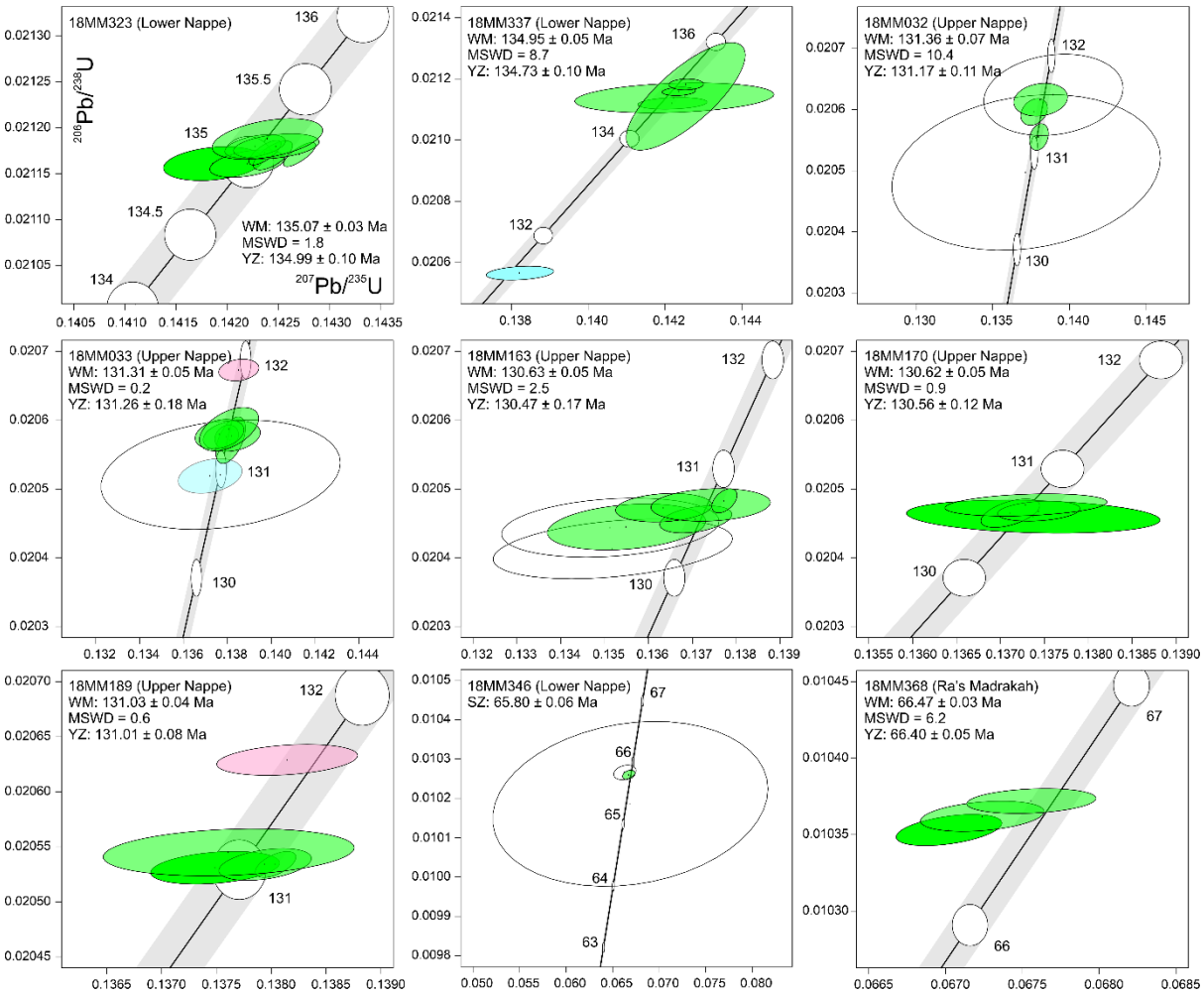

Figure 4.19: *Uranium-lead concordia diagrams of single-grain zircon ages. Open ellipses represent measurements rejected due to high common Pb, green ellipses are zircons interpreted as crystallisation ages, blue ellipses are data interpreted to be affected by Pb-loss, and pink ellipses are interpreted as inherited/assimilated zircons (see text). Zircon ages are corrected for initial Th/U disequilibrium using radiogenic ^{208}Pb and Th/U[magma] = 2.80000. Ages on concordia are in Ma and grey bands represent uncertainties on the decay constants and $^{238}U/^{235}U$-ratio (Jaffey et al., 1971). Axis labels are shown in the top-left panel. WM = weighted mean age; MSWD = mean square of the weighted deviates; YZ = youngest zircon age. For sample 18MM346 only a single zircon (SZ) age is displayed. Plots and MSWD of the weighted mean were generated using IsoplotR (Vermeesch, 2018).*

Of the two youngest samples, 18MM346 yielded one zircon with an age of 65.80 ± 0.06 Ma. Two additional zircons from this sample were rejected for not satisfying the blank criteria, but nevertheless reproduced the 65 Ma age. Sample 18MM368 (from Ra's Madrakah) has a mean age of 66.47 ± 0.03 Ma (MSWD = 6.2, n = 3; youngest zircon age = 66.40 ± 0.05 Ma) and an age range of 0.12 ± 0.10 Ma.

The degree of dispersion in $^{206}Pb/^{238}U$ ages within individual samples varies, with some samples showing age clusters whereas others do not. Samples 18MM323 and 18MM170 have single grain ages that are within analytical uncertainty and a MSWD consistent with the null hypothesis that the data represent repeated measurements of the same age (Wendt and Carl, 1991). Samples 18MM033 and 18MM189 have clusters of $^{206}Pb/^{238}U$ dates that are within analytical uncertainty as well as one or more outliers (outside of analytical uncertainty). These outliers can be attributed to either minor Pb-loss (resulting in younger ages) or inherited cores (resulting in older ages), whereas the age clusters of these samples statistically represent a single age. Lastly, samples 18MM032, 18MM163, 18MM337 and 18MM368 have single-grain ages that do not form age clusters and likely do not represent repeat measurements of the same age (MSWD>>1). The overdispersion of $^{206}Pb/^{238}U$ ages in these samples is greater than would be expected for a typical protracted crystallisation history for oceanic gabbros (up to 0.166 Ma, Lissenberg et al., 2009; Rioux et al., 2012b) and possibly reflect assimilation of zircons from adjacent wall rocks, multiple magma pulses in a crystal mush and/or varying degrees of minor Pb-loss. Nevertheless, the intrasample age range in these samples is relatively small (typically <0.4 Ma) and it is therefore not considered likely that the true crystallisation age of these samples is substantially different to the ages reported here.

4.5 Discussion: A new model for Masirah

4.5.1 Is there a meaningful field distinction between the 'mid-ocean ridge' and 'alkaline' suite?

Previous work on Masirah introduced a basic conceptual framework in which igneous units could be attributed to one of two separate magmatic events: a main crustal accretion event, which formed a thin Penrose-style crust at a mid-ocean ridge by seafloor spreading; and a later intraplate magmatic event, during which this pre-existing ocean crust was intruded by plutons and associated alkaline lavas erupted at small seamount volcanoes (Peters, 2000). On this basis, axial lavas are interpreted to have formed at the MOR, whereas the seamount lavas and post-axial lavas erupted during the later event. The out-of-sequence lavas were interpreted to have erupted following intra-oceanic rifting that accompanied the later event and exhumed gabbro and mantle rocks (Immenhauser, 1996; Meyer et al., 1996; Marquer et al., 1998). On a similar basis, sheeted dykes and dyke swarms in the lower crust, consisting of greyish-black micro-gabbroic dykes, porphyritic dykes and black aphyric dykes, were proposed to have formed at the MOR, whereas late, greenish-brown crosscutting dykes and mantle dykes were ascribed to the later 'intraplate' event (Peters et al., 1995; Peters and Mercolli, 1998). Gabbroic rocks were likewise grouped into a MOR gabbroic suite and a later gabbro-dolerite-granite suite (Peters et al., 1995; Peters and Mercolli, 1997).

The current study shows, however, that the classification scheme described above does not capture the full complexity present on Masirah. Based on Nb/Y ratios, a minority of the axial lavas have an

alkaline affinity, and a minority of out-of-sequence lavas are more tholeiitic. Likewise, axial dykes, the dyke swarms intruding the mantle, as well as late crustal dykes, span a large range with some having more tholeiitic affinity and others more alkaline. Furthermore, the field characteristics previously proposed for distinguishing between the dykes and lavas of the different suites do not always correlate with their chemical compositions (Peters et al., 1995; Peters and Mercolli, 1997): reddish-brown amygdule-rich pillow lavas were described to be diagnostic of the alkali-basalts, but during this study, lavas of this appearance were also encountered with a tholeiite affinity in the axial lavas at Wadi Haql (e.g., samples 18MM128 and 18MM143). Alkali-basalts were described as generally devoid of varioles, but lava 18MM235 with an alkaline affinity has well-developed varioles. For dykes it is likewise not possible to identify a reliable field characteristic (colour, crystal content, crosscutting relationship) to predict chemical composition. Instead, this study finds that the trace element geochemistry of the lavas and dykes on Masirah show a continuum of compositions rather than the existence of distinct MORB versus alkaline suites. In terms of alkalinity proxy index (Figure 4.11) and REE patterns (Figure 4.12 and 4.13) , nearly all subdivisions of lavas and dykes display a spectrum of compositions with considerable overlap. Despite this large and seemingly random variation within each defined subgroup, there appears to be a general overall trend of dyke and lava compositions on average becoming progressively more Nb/Y and LREE-enriched over time.

The subdivision for gabbros is also not straightforward. The intrusive nature of the gabbro-dolerite-granite suite is indicated by the presence in several locations of large xenoliths of various units of the axial lower crust and mantle lithosphere (Peters et al., 1995; Peters and Mercolli, 1997). Based on petrography (the presence of brown amphibole replacing clinopyroxene and the presence of Fe-Ti oxides) and mineral chemistry (overall more evolved compositions), gabbros of the gabbro-dolerite-granite suite can generally be distinguished from gabbros of the axial lower crust. These characteristics of the gabbro-dolerite-granite suite are best developed at the studied kilometre-sized type-locality plutons and to a lesser extent in the smaller gabbroic mantle intrusions. Most gabbroic plutons in the mantle have mineral assemblages, textures and compositions that resemble the gabbro-dolerite-granite suite, whereas some of the smaller dykes, sheets and pods derived from mantle sections underneath a ‘normal’ crust-mantle boundary are similar to the more primitive axial gabbros. Some mantle plutons (e.g., at Safa’iq), however, have mineral assemblages, textures and mineral compositions that sit in between these two groups. Outcrops of evolved and varitextured gabbro that sporadically occur near the top of the lower crustal sequence are sometimes assigned to the same map unit as the gabbro-dolerite-granite suite (isotropic gabbro, Peters et al., 1995). Although similar in field appearance (pegmatites and heterogeneous grainsizes), these rocks contain significantly less amphibole and Fe-Ti oxides and often have field relationships that show they are

cogenetic with the axial lower crust and likely analogous to the ~150 m thick 'varitextured gabbro' unit located at the top of the lower crust in the Semail Ophiolite, thought to represent a fossil melt lens (e.g., MacLeod and Yaouancq, 2000). Despite the potential use of the Swiss classification scheme, core compositions of coexisting clinopyroxene and plagioclase in all the gabbros roughly form a single differentiation trend, implying that a common origin cannot be ruled out for the gabbroic plutons (Figure 4.16a).

4.5.2 Is there an age difference between the 'mid-ocean ridge' and 'alkaline' suites?

Previous work proposed that seafloor spreading and the accretion of ocean lithosphere occurred in the Late Jurassic at ~150 Ma (Upper Tithonian), followed by a second, distinct alkaline magmatic event ~20 Ma later (Peters et al., 1995; Immenhauser, 1996; Peters, 2000). The results from this study, however, were unable to reproduce the previously determined, and widely cited, ~150 Ma age of Masirah. The weighted means of the high-precision single grain zircon ages presented in this study suggest a formation age of 135.1 – 135.0 Ma for samples from the Lower Nappe and 131.4 – 130.6 Ma for samples from the Upper Nappe. Field relations, petrography and whole rock chemistry indicate that these geochronology samples form part of the axial crustal sequence and are not part of a later crosscutting suite. Additionally, two intrusive plutons (an anorthosite crosscutting the Masirah Lower Nappe and an albitite in the mantle section at Ra's Madrakah on the mainland) indicate magmatic activity occurred 66.5 – 65.8 Ma. The robustness of the chemical abrasion method, as well as the concordance and reproducibility of the age results, suggest it is unlikely that Pb-loss is responsible for our younger ages for the Masirah axial crust. In the remainder of this section, previous work supporting the contradictory Upper Tithonian age is critically evaluated and a revised geochronological model is proposed.

Previous radiometric dating studies placed the formation of the Masirah ophiolite in the Late Jurassic to Early Cretaceous (Figure 4.20). Smewing et al., (1991) used K-Ar techniques to date hornblende mineral separates from gabbros and biotite mineral separates from granites from the area south of Jabal Humr (Upper Nappe). Their results suggest a formation age around 126 – 158 Ma for both the gabbros and the granites, though the ages have low precision. Peters et al. (1995) provided preliminary data for Ar-Ar and U-Pb ages of various lithologies (gabbroic plutons in the mantle, hornblende gabbros, potassium granites and the seamount structures) obtained from both nappes as part of their mapping campaign, although the quality of these data cannot be assessed since they were never published in full. These ages cover a large range and, apart from a few of the younger Ar-Ar dates, have considerable (>>1 Ma) uncertainties (Figure 4.20). Nevertheless, they were interpreted to roughly fall into an older group (two U-Pb samples of 156 – 150 Ma and two Ar-Ar samples giving poor age estimates around 150 Ma) and a younger group (five U-Pb samples of

125 – 108 Ma and ten Ar-Ar samples of 133 – 120 Ma). The authors note that it is difficult to explain that in the U-Pb ages on zircons in this second group tend to be younger than the Ar-Ar ages on hornblendes and biotites, and although age uncertainites are not discussed, a Pb concordia diagram for one sample included in the publication suggests complex discordance patterns (Peters et al., 1995).

Further age constraints were derived from biostratigraphical markers in the autochthonous sediments overlying the ophiolite sequence, which according to previous work span the Tithonian (~152.1 – 145 Ma, after the ICS geological timescale; Cohen et al., 2013), Berriasian (~145 – 139.8 Ma), Valanginian (~139.8 – 132.9 Ma), Hauterivian (~132.9 – 129.4 Ma), Barremian (~129.4 – 125 Ma), as well as younger Cretaceous ages. Beurrier (1987) reported an Upper Tithonian-Hauterivian age and Moseley (1990) a Tithonian age based on radiolarian faunal assemblages in the earliest sedimentary unit, but neither carried out a systematic study. Immenhauser (1995, 1996) described the autochthonous sediments in detail and constructed a geochronological and stratigraphical framework for the post-formation history of Masirah. Based on radiolarians recovered from the oldest sediments of the Maghilah Unit overlying the axial lavas (UA 6-7, *Artocapsa* (?) *amphorella*, *Sethocapsa uterculus* and *Canoptum banale* n. sp.), the Masirah Ophiolite was assigned a Tithonian/Berriasian age, corroborating the ~150 Ma radiometric ages. A later, more detailed study on the radiolarian biostratigraphy on Masirah by the same research group, however, noted that a well-defined *in situ* Tithonian or Berriasian assemblage was not found in the samples (Dumitrica et al., 1997). According to this study, radiolarians from the two stratigraphically oldest samples were moderately to very poorly preserved, and yielded a relatively large range of possible ages: Upper Tithonian to Hauterivian for a sample from Wadi Maghilah and Upper Berriasian to Lower Valanginian for a sample from Wadi Thoumi. A recent review on radiolarian biostratigraphy furthermore notes that the current calibration of the Jurassic and Early Cretaceous zones is still relatively poorly constrained, whereas the calibration for the Barremian onwards is non-problematic in comparison (Goričan et al., 2018). Calcareous nannofossils from the Maghilah Unit yielded two samples that were tentatively assigned an approximate Berriasian age, but due to poor preservation of the specimens, it was not possible to provide precise age constraints for those lowest stratigraphic levels (Von Salis and Immenhauser, 1997).

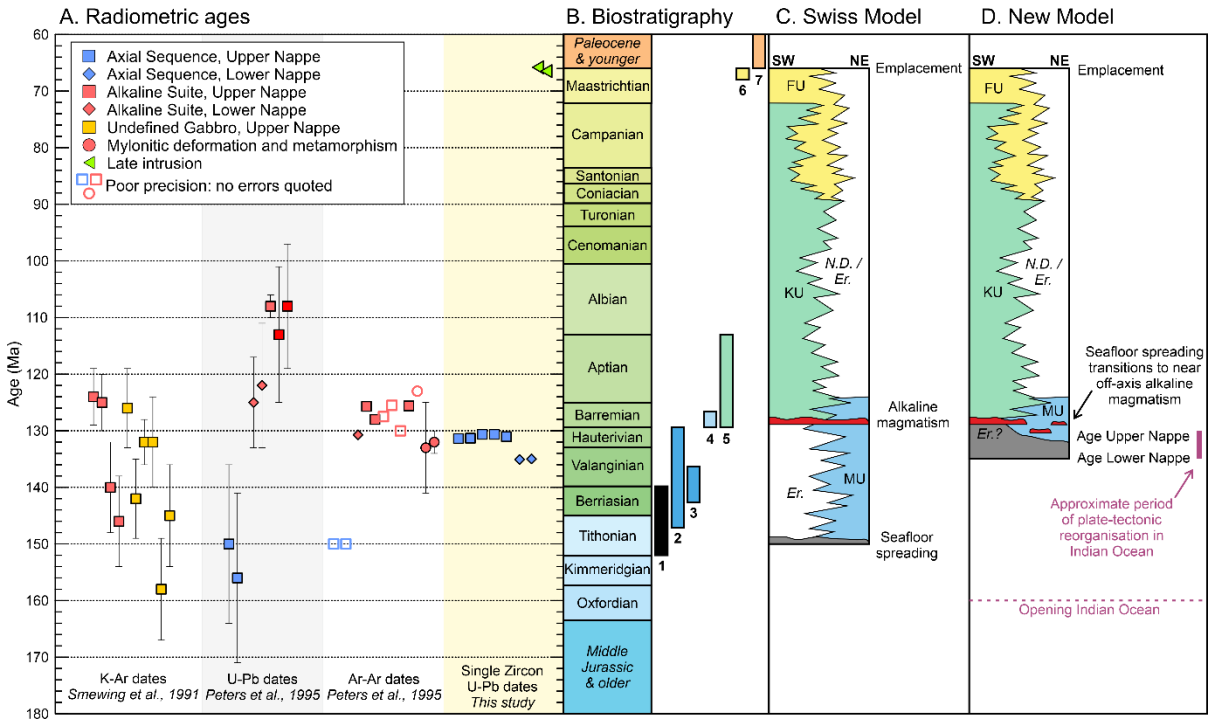

Figure 4.20: *(a) Previous radiometric ages for Masirah compiled and compared to the weighted means of single zircon U-Pb ages from this study (yellow shaded area). Note the large uncertainty and unreported uncertainty (open symbols) for data from previous work. Uncertainty for the single zircon U-Pb ages and several Ar-Ar ages (filled symbols) is smaller than the symbol size. Stratigraphic geological timescale from the International Commission on Stratigraphy (Cohen et al., 2013). (b) Relevant biostratigraphical age constraints from previous studies: 1: Tithonian/Berriasian radiolarian age for the oldest Maghilah Unit sediments, sampling location not published (Peters et al., 1995; Immenhauser, 1996), 2: Upper Tithonian – Hauterivian radiolarian age for the oldest Maghilah Unit sample from the Wadi Maghilah section, 3: Upper Berriasian – Lower Valanginian radiolarian age for the oldest Maghilah Unit sample from the Wadi Thoumi section, 4: Lower Barremian – lower part of the Upper Barremian radiolarian age for Maghilah Unit sediments interfingering with post-axial lavas in the Wadi Maghilah section (2-4 from Dumitrica et al., 1997), 5: Barremian – Aptian age range of foraminifera from the platform carbonates of the Kalban Unit at Jabal Suwayr (Immenhauser, 1996), 6: Late Maastrichtian calcareous nannofossil age for the latest Fayah Unit sediments from Wadi al Firay (Von Salis and Immenhauser, 1997), 7: Sediments of Palaeocene age are the earliest post-emplacement sediments covering the Batain Nappes on the mainland (Schreurs and Immenhauser, 1999; Immenhauser et al., 2000). (c) Geochronological model for Masirah after Peters et al. (1995), with a stratigraphic chart indicating the sedimentary units along a rough southwest-northeast transect across the Masirah Lower Nappe on the left (after Immenhauser, 1996) and important events on the right. (d) Update of the geochronological proposed in this study, with stratigraphy on the left and important events on the right as in panel (c). Events relating to the plate-tectonic geology of the Indian Ocean in purple (Gaina et al., 2007, 2015). MU = Maghilah Unit, KU = Kalban Unit, FU = Fayah Unit, N.D. = non-deposition, Er. = Erosion.*

Based on the high-precision geochronology results in this study, it is proposed that the crustal accretion of the preserved portion of the Masirah ophiolite took place in the interval 135 – 130 Ma (Early Cretaceous). This is ~15 – 20 Ma younger than the previously accepted 150 Ma (Late Jurassic) age of formation, but does not necessarily contradict earlier work, given the large uncertainties on previous radiometric ages and the age ranges of the oldest radiolarians according to Dumitrica et al. (1997). An important implication is that the new formation age for Masirah is very close to the age of the alkaline magmatic suite. Field observations of gabbro-dolerite-granite plutons crosscutting the main ophiolite sequence (Peters et al., 1995; Peters and Mercolli, 1997), as well as post-axial lavas interbedded with the autochthonous sedimentary cover (Immenhauser, 1996), indicate that later melts were added to the Masirah crust off-axis, but their absolute ages are not precisely known. The radiometric dates of this suite from Peters et al. (1995) indicate they could either have formed coevally with the Masirah crust or several (possibly up to tens of) million years afterwards, taking into account that the uncertainties on these ages are not well constrained (Figure 4.20).

The sedimentary record offers little firm constraints. Post-axial lavas interbedded in the upper member of the Maghilah Unit overlie ~19 – 30 m of pelagic sediments covering the axial lavas in Wadi Zamir/Thoumi, Wadi Maghilah and Wadi Rasiyah, but are absent in Wadi Haql (Immenhauser, 1996). In Wadi Maghilah the interfingering sediments yielded moderate to well preserved radiolarian fauna of Barremian age (~129.4 – 125 Ma; Dumitrica et al., 1997), which combined with a Lower Nappe age of 135 Ma would imply maximum sedimentation rates of ~3.8 – 6.0 m/Ma, consistent with the pelagic realm (~1 – 10 m/Ma, Molinie and Ogg, 1992; Hori et al., 1993). The post-axial lavas in the other sections of the Maghilah Unit have no firm biostratigraphical age constraints. In the south and southwest of Masirah Island, alkaline pillow lavas and volcanic breccias (i.e., the out-of-sequence lavas) are overlain by sediments of the Kalban Unit in Wadi Zabil, Wadi Shi'bat Halit, the Northern Kalban Plain and at Jabal Suwayr (Peters et al., 1995; Immenhauser, 1996). The oldest of these sediments are also considered to be of Barremian age, on the basis of multiple independent biomarkers from Wadi Zabil (foraminifera, radiolarians and calcareous nannofossils) and from the platform carbonates of Jabal Suwayr (foraminifera; Immenhauser 1995, 1996; Dumitrica et al., 1997; Von Salis and Immenhauser, 1997).

Whilst these observations constrain the latest magmatism to postdate the axial sequence by a maximum of ~5 Ma, the overlap in field characteristics, petrography and geochemistry of the 'axial' and 'later' suites is instead more consistent with a single, transitional magmatic event than with two separate events at distinct times. During this transitional magmatic event, on-axis magmatism, responsible for ocean lithosphere accretion, progressed into off-axis magmatism close to the ridge axis ('near-axis'). In the revised geochronological model, the deposition of the Maghilah and Kalban

Units are interpreted to overlap in time, whereas the Kalban Unit was previously interpreted to largely postdate the Maghilah Unit (Immenhauser, 1996). Several observations from Immenhauser (1996) are permissive of this reinterpretation: (1) the Kalban Unit is not observed directly overlying the Maghilah Unit in any outcrop, since the Maghilah Unit mainly occurs in the northern and eastern half of the island part of the island whereas the Kalban Unit is primarily found in the southern and western parts of the island; (2) some turbidites at the top of the Maghilah Unit contain carbonate clasts of the Kalban Unit, indicating there was at least some overlap; and (3) the Kalban Unit is laterally variable with facies ranging from slope proximal to distal, suggesting the pelagic Maghilah Unit can also be interpreted as the most distal facies of the sedimentary system. The presence of 'out-of-sequence' lavas erupted onto mantle peridotites and the subsequent deposition of rudist- and coral bearing platform carbonates at Jabal Suwayr, and platform detritus and ophiolite clasts in other sections of the Kalban Unit, indicate that rapid (local) uplift, accompanied by exhumation and erosion, took place (Immenhauser, 1996). Consequently, the new geochronological model presented here suggests this occurred (relatively close to the ridge axis?) at the same time as pelagic sedimentation continued in what is now the northern and eastern part of Masirah.

Notably, the two younger plutons (66.5 – 65.8 Ma) crosscutting the Masirah Lower Nappe and the mantle at Ra's Madrakah respectively, have ages that closely agree with the proposed obduction age of the Eastern Oman Ophiolites (Gnos et al., 1997). Studies on the Batain coast on the mainland showed that the youngest sediments involved in the emplacement-related thrusting are late Maastrichtian whereas the oldest post-emplacement sediments are early Palaeogene (Schreurs and Immenhauser, 1999; Immenhauser et al., 2000). This temporal correlation suggests that emplacement was accompanied by small-scale melting that resulted in the intrusions. Frictional heating in shear zones provides a potential melting mechanism, and carbonate and clay-rich sediments a possible source for a CaO and Al_2O_3-rich melt that could conceivably form an anorthosite. These possibilities require further investigation, however, before any conclusive statement can be made.

4.5.3 Origin of the transitional nature of the magmatism that fed dykes and lavas

Whole-rock major and trace element compositions of the dykes and lavas are consistent with a dry mid-ocean ridge setting for Masirah, without the influence of subduction. Immobile trace element data show that Masirah plots on the MORB-OIB array and does not display Th enrichment characteristic of subduction zone lavas (Figure 4.21; Pearce, 2008, 2014). High Ti/V ratios similarly indicate that the oxidation state of the melting regime was slab-distal and MORB-like (Shervais, 1982; Pearce, 2014). The increase in TiO_2 and decrease in Al_2O_3 with increased melt differentiation is consistent with early saturation of plagioclase relative to clinopyroxene at low pressures (≤2 kbar),

similar to dry MORB (MacLeod et al., 2013). A subset of the Masirah samples that plot away from the MORB trends is explained by a combination of plagioclase crystal accumulation and alteration.

To investigate the magmatic processes that could be responsible for the trace element variability on Masirah, the effects of fractional crystallisation, mantle melting and mantle source are considered. The primitive nature of the dykes and lavas (in terms of MgO, Cr, Ni and Mg#), combined with the limited thickness of the gabbroic lower crust, argues for a subordinate role for fractional crystallisation in modifying trace element compositions and ratios. The trace element compositions observed in the most enriched lavas and dykes can be produced by both a reduced degree of melting and variability in the composition of the mantle source. Figure 4.21 shows that the shape of the lava and dyke REE patterns can be modelled by various degrees of shallow melting (spinel stability field, 10 kbar) of a variably enriched source (melting model from O'Neill, 2016 and references therein). Notably, the LREE enriched Masirah lavas and dykes lack a corresponding relative depletion in heavy REE (HREE), expressed in Figure 4.21 by relatively high λ2 values. Their origin is therefore inconsistent with a plume-fed ocean island basalt (OIB), as suggested by Meyer et al. (1996), where deeper melting in the garnet stability field typically depletes the HREE.

By examining co-variations between Nb/Y and Zr/Y it is possible to distinguish between variations caused by the extent of fractional melting and trace element variations in the mantle source (Fitton et al., 1997). Low pressure fractional crystallisation has no significant effect on these ratios for MgO > 5 wt% and varying degrees of melting result in covariation along linear arrays parallel to the Iceland array (Figure 4.21d). Any vertical offset from this array, expressed as excess or deficit in log units of Nb (ΔNb) from the reference line marking the lower bound of the Iceland array, arises from source heterogeneity (Fitton et al., 1997). Trends oblique to the melting and source variation vectors indicate mixing of magmas derived from different degrees of melting of different sources. The Nb/Y versus Zr/Y diagram was originally developed to differentiate between the mantle source of North Atlantic MORB and Icelandic mantle-plume basalts (Fitton et al., 1997), but Fitton (2007) showed that the Iceland array and ΔNb reference line on the diagram have a global significance and can be used to identify enriched, OIB-like mantle sources in MORB (E-MORB), plume-fed oceanic islands, and off-axis seamounts. The Masirah axial dykes and lavas form a trend which starts oblique to the ΔNb reference line, spanning the depleted (ΔNb < 0) and enriched (ΔNb > 0) mantle source fields, and continues along a trend parallel to the Iceland array in the enriched mantle source field, where they overlap with seamount lavas and gabbro-dolerite-granite dykes. Compared to global MORB, the Masirah lavas and dykes overlap with much of the compositional range spanned by MORB but extend to more enriched compositions than found in MORB.

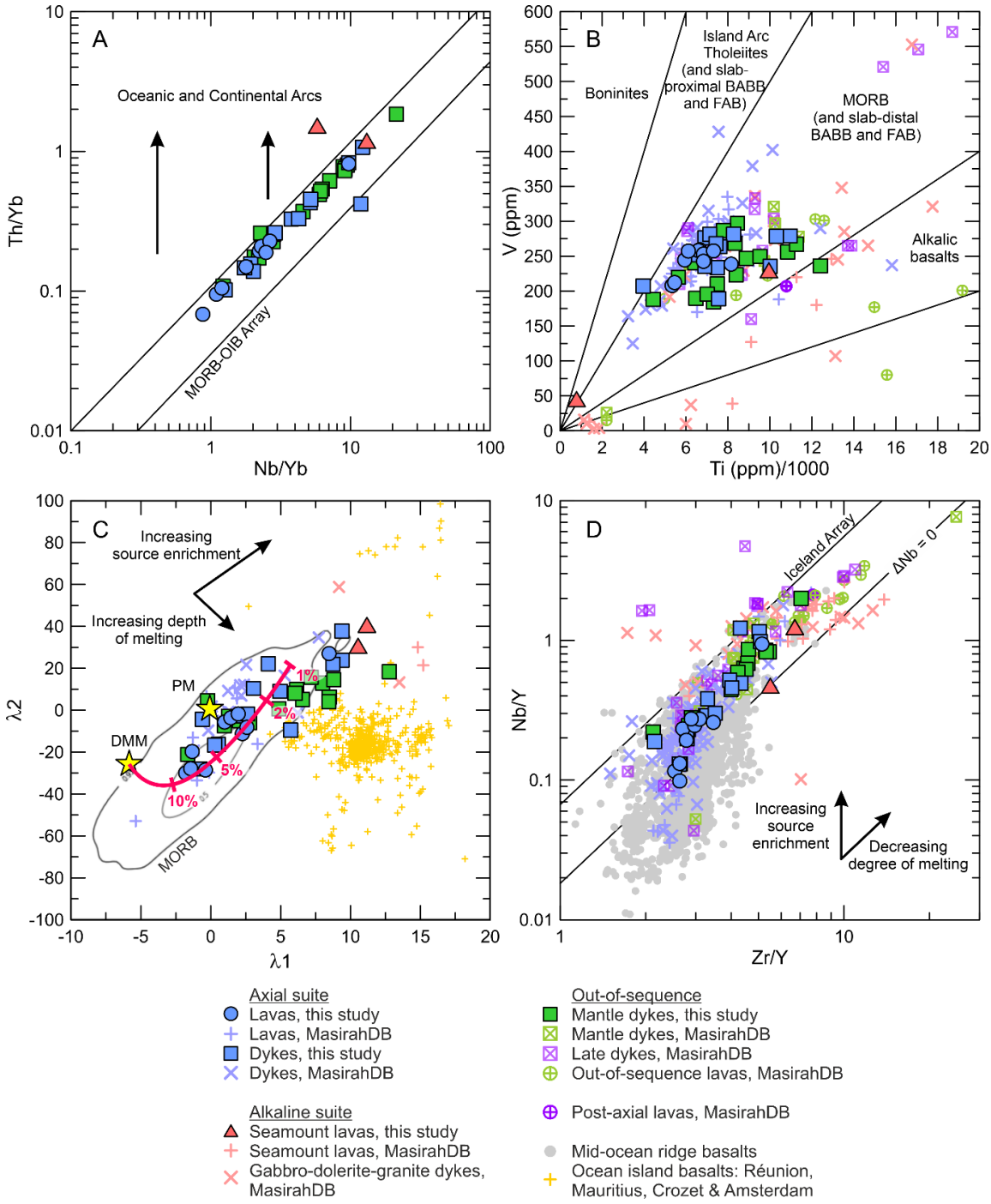

Figure 4.21: *(a) Immobile trace element diagram after Pearce (2008) with Masirah dykes and lavas plotting on the MORB-OIB array. The sample elevated above the array is seamount lava 18MM365, which does not represent a melt composition. (b) Titanium versus vanadium diagram after Shervais (1982). (c) Lamda-plot for REE shape patterns after O'Neill (2016). Ocean island basalts (OIB) data from Reunion, Mauritius, Crozet and Amsterdam Island are from the GEOROC Geochemical Database (https://georoc.eu/; Lehnert et al., 2000, individual references in Supplementary Material). Melting trend is an accumulated fractional melting model of spinel lherzolite at 10 kbars (from O'Neill, 2016). Depleted MORB Mantle (DMM) from Workman and Hart (2005) and Primitive Mantle (PM) from McDonough and Sun (1995). Kernel density contours represent the MORB dataset of Gale et al. (2013). (d) Nb/Y versus Zr/Y trace element diagram after Fitton et al. (1997).*

Based on these trends, it is concluded that the magmatism in the main seafloor-spreading phase was derived from the mixing of magmas derived from variable degrees of melting of a heterogeneous source, followed by episodic, reduced melting of the more enriched mantle component. This is consistent with previous Nd-Sr-Pb isotope analyses which showed that Masirah melts were derived from a heterogeneous mantle containing a MORB mantle source and an enriched Indian Ocean source similar to that of Réunion, Mauritius, Crozet and Amsterdam (Mahoney et al., 1998; Zhang et al., 2005).

4.5.4 Petrogenesis of the alkaline gabbroic plutons

The differences in mineral assemblage and composition between the axial gabbros and the gabbroic plutons of the gabbro-dolerite-granite suite can be related to differences in either parental melt composition or degrees of melt differentiation and extraction, or both. Parental melts derived from a smaller degree of melting of an enriched mantle component in some cases have higher FeO, Na_2O, K_2O and TiO_2 contents (Lambart et al., 2009), conceivably leading to crystallisation of more iron-rich clinopyroxene and olivine, more sodic plagioclase, and earlier stabilisation of amphibole and Fe-Ti oxides. Alternatively, differences in the extraction and retention of melts within crystallising bodies can affect the final degree of differentiation of the plutons. Efficient melt-crystal separation will form primitive cumulates (such as found in the axial lower crust), whereas melt that remains trapped will continue reacting with the cumulates as it cools, resulting in a more evolved end-product (e.g., Bowen, 1922). Whole-rock major element compositions of the hornblende-oxide gabbros and associated dolerites, compiled in MasirahDB, are consistent with either process, as they can be interpreted to reflect mixtures of varying proportions of cumulate plagioclase and amphibole (± clinopyroxene and oxides); alternatively they may represent the crystallisation product of stalled melts, as they also overlap with the range of dyke and lava whole-rock compositions (Figure 4.18a & b). While it is beyond the scope of this study to assess the relative contribution of each process, both were likely important in the petrogenesis of the hornblende-oxide gabbros. The temporal increase in enrichment of the parental magmas observed in the dykes and lavas argues for a similar evolution in the intrusive suite, while the textural evidence (poikilitic amphibole and oxides, resorption of plagioclase, replacement of clinopyroxene by amphibole) indicates that melt-crystal reactions, and hence inefficient extraction of evolved melts, also played an important role.

The progressive replacement of clinopyroxene by (magmatic) brown amphibole is indicative of a peritectic reaction that has previously been described in arc cumulates, where this so-called 'amphibole-sponge' is known to drastically increase melt SiO_2 over a relatively short crystallisation interval (Davidson et al., 2007; Smith, 2014). The occurrence of 'true' K-feldspar bearing granites on Masirah was not investigated in this study but its main exposure, concentrated on the jagged ridges

south of Jabal Humr, has been described previously (Abbotts, 1978; Peters et al., 1995; Nägler and Frey, 1997). Here, the granites mutually crosscut and intermingle with the gabbro-dolerite-diorite suite and are plausibly related to the amphibole-forming reaction (Peters and Mercolli, 1997). In arcs, rhyodacitic melts derived from the amphibole-forming reactions are thought to ascend to shallow crustal levels where they mix with basalts to form andesites (e.g., Annen et al., 2006; Klaver et al., 2018), but in Masirah the felsic melts appear to have remained trapped and crystallised as granites. The high concentration of potassium required to stabilise K-feldspar in the granites is uncommon for oceanic systems, but is likely related to the enriched nature of the parental melts and extensive differentiation recorded in the gabbro-dolerite-granite suite.

The stabilisation of amphibole as a major phase on Masirah at shallow pressures (i.e., around crust-mantle boundary) is noteworthy. Oceanic gabbros with brown amphibole and Fe-Ti oxides commonly occur at both fast- and slow-spreading ridges and are believed to crystalise from late evolved melts in the gabbroic mush (e.g., Dick et al., 2000; Gillis, 1996). The hornblende-oxide gabbros from Masirah, however, have considerably higher modal mineral proportions for amphibole and oxides, and occur in larger volumes, than gabbros so far recovered from mid-ocean ridges and may be more comparable to some cumulates formed during intraplate alkaline magmatism (e.g., Mattioli et al., 1997; Neumann et al., 2000). Amphibole stability increases with increasing pressure, although increased Na_2O contents in the melt allows amphibole to form in the shallow crust as well (Sisson and Grove, 1992; Smith, 2014). Relatively high Na_2O contents in Masirah melts, especially in the later more alkaline melts, likely helped to increase the stability of amphibole ($Na_{8.0}$ = 2.0 – 5.3 wt% for Masirah dykes and lavas in this study, compared to ~1.5 – 3.5 wt% for global MORB; Klein and Langmuir, 1987). Water is also required for the crystallisation of amphibole and in the Semail Ophiolite, textural and geochemical evidence for amphibole-forming reactions in late-stage intrusions has been attributed to subduction-influenced hydrous melting (De Graaff et al., 2019). In contrast to Semail, however, subduction is an unlikely source for water in the magmas at Masirah since lava and dyke major- and trace element chemistry (Figure 4.9 and 4.21), as well as gabbro mineral compositions (Figure 4.16a), are consistent with dry liquid lines of descent. Furthermore, brown amphibole and Fe-Ti oxides are typically present as late, poikilitic phases, in contrast to arc cumulates where they tend to occur earlier with euhedral to subhedral habits (e.g., Cooper et al., 2016). Instead, low degrees of melting combined with extensive differentiation likely enriched water contents in the trapped melts to the point of amphibole saturation. Since water behaves as an incompatible element during crystallisation of all phases, including amphibole, the amphibole-forming reaction can progress to a considerable extent without depleting melt H_2O once the phase is stabilised. A heterogeneous distribution of these trapped melts would result in spatially variable

amphibole contents and late hydrous pegmatite veins crosscutting their host-rocks, as observed on Masirah.

4.5.5 A revised geochronological and tectonic model for Masirah

The new geochronological constraints presented in this study show that the age of the main seafloor-spreading phase (135 – 130 Ma, Valanginian to Hauterivian) is within error of the age estimates for the later lavas and the crosscutting igneous suite. The significant overlap in trace element composition between axial lavas, the seamount lavas, the crustal dykes, the gabbro-dolerite-granite dykes and the mantle dykes, strongly suggests that these magmatic suites are transitional and derived from a heterogeneous mantle source that underwent a progressively decreasing degree of melting in the spinel-stability field. Small volumes of alkaline magmas erupted during the main phase of seafloor-spreading and alkaline melts were episodically added to the Masirah lithosphere off-axis, where they stalled as plutons, intruded as dykes and erupted as lavas. Lava eruption on the Lower Nappe had ceased by Barremian times (~129.4 – 125 Ma) and was accompanied by significant uplift as indicated by the shallow water carbonates and the ophiolite-erosion products present in the Kalban Unit (Immenhauser 1996; Meyer et al., 1996). Additionally, the occurrence of some tholeiitic lavas erupted onto serpentinised peridotite indicate that mantle lithologies must have been partially exposed at the seafloor during or soon after the main phase of seafloor-spreading (the extent to which this was the case, and the implications this has for seafloor spreading, are further discussed in Chapter 5).

Any model for Masirah must be able to explain the continuation of magmatism off-axis, as well as the increasing contribution of a more enriched mantle source through time. This latter point is not straightforward, since such enriched, fusible components would have been exhausted rapidly during the initial melting phase underneath the ridge-axis. Importantly, the enriched mantle source of off-axis magmatism is not necessarily an indication of a plume-fed hotspot (e.g., Fitton, 2007) and shallow and low volume melting in Masirah are inconsistent with a hotspot source for the off-axis magmatism. Furthermore, the enriched component from which the Masirah melts were derived appears to have been present throughout the Indian/Tethyan Ocean mantle in Jurassic and Cretaceous times, precluding the need for a point-source hotspot (Zhang et al., 2005). Instead, two models that could account for the transitional style of magmatism observed at Masirah are advanced (Figure 4.22).

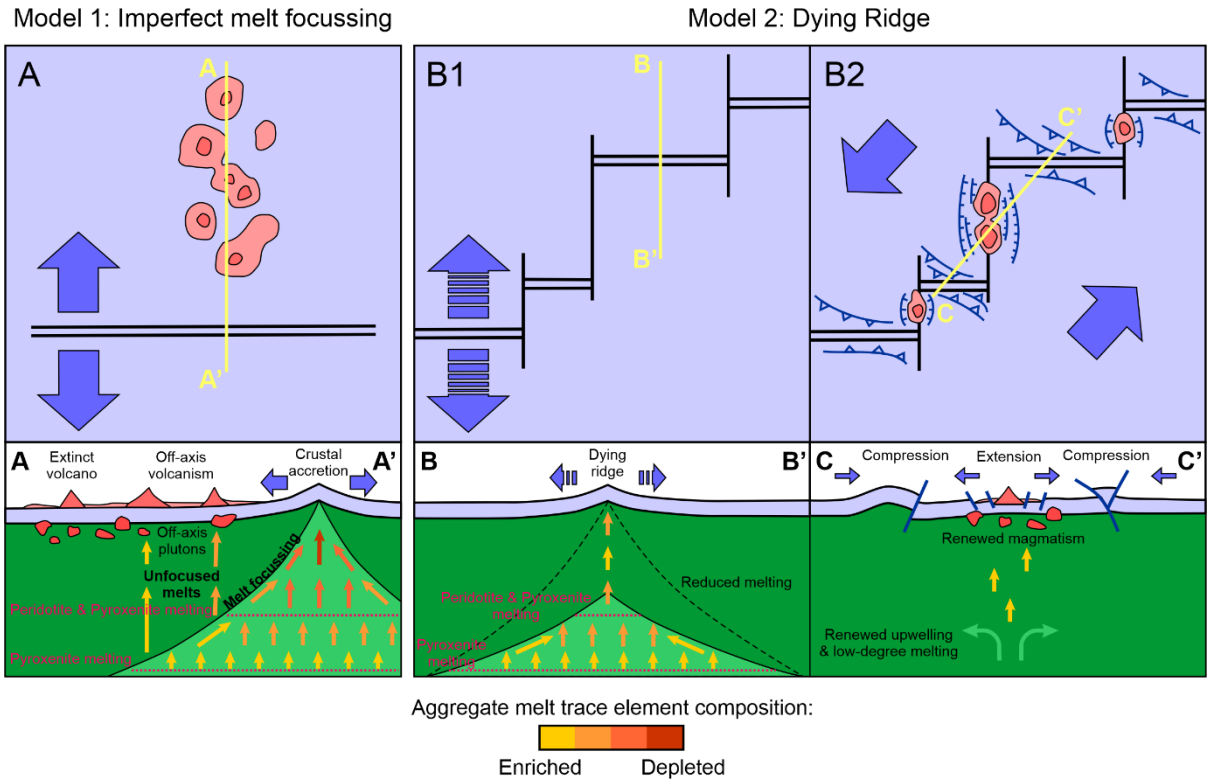

Figure 4.22: *Sketch diagrams illustrating the two models that can explain the transitional magmatic event at Masirah: (a) imperfect melt focussing and (b) a dying spreading ridge. Top panels show map views and bottom panels show cross-sections along the lines indicated on the maps. See text for discussion.*

(1) The first proposes that near off-axis magmatism occurred as an intrinsic part of crustal accretion at Masirah. Imperfect focusing of melts towards the ridge-axis can result in low-volume off-axis magmatism (e.g., Lundstrom et al., 1999), equivalent to the near-axis seamount volcanoes that have been described in a variety of settings and can have a range of compositions from depleted to enriched MORB (e.g., Allan et al., 1989; Niu and Batiza, 1997; Geshi et al., 2007; Anderson et al., 2021). Because of the triangular shape of the axial melting zone, the height of the melting column, and therefore degree of melting, reduces with increasing distance off-axis. As such, melts generated off-axis would preferentially sample enriched, fusible components and imperfect focusing would lead to the addition of these melts to the off-axis lithosphere (Figure 4.22a).

(2) The second model proposes an external control on the near off-axis magmatism, where a change in tectonic plate motion caused cessation of seafloor spreading, followed by renewed tectonic plate motions accommodated along the former ridge-axis. As seafloor spreading slows down, asthenospheric upwelling and associated melting decreases, leading to increasingly lower degree melting of enriched components (panel 1 in Figure 4.22b). When the spreading ridge becomes extinct, asthenospheric upwelling ceases and the incompletely molten mantle underneath the ocean lithosphere is essentially frozen. A subsequent reorientation of plate tectonic stresses would result

in plate motion in a new direction along the irregular geometry of the segmented ridge axis, creating localised regions of transpression and transtension, where the former is associated with uplift and the latter may lead to small amounts of asthenospheric upwelling and renewed, low-degree melting (panel 2 in Figure 4.22b). A present-day example of the dying ridge model can be found on Macquarie Island (south-west of New Zealand). Macquarie Island is a fragment of oceanic lithosphere that formed at a highly segmented, dying spreading ridge and was uplifted to sea level when the plate boundary became obliquely convergent (Varne et al., 2000). Basalts from Macquarie Island and other parts of the Macquarie ridge are notable for their trace element enrichments and distinct isotopic signatures (Griffin and Varne, 1980; Kamenetsky et al., 2000; Kamenetsky and Maas, 2002; Jiang et al., 2021).

Both models have several merits as well as shortcomings. Figure 4.23 shows that near-axis seamounts along the East Pacific Rise (EPR) as well as basalts from Macquarie ridge share geochemical characteristics with Masirah: a transitional trend from tholeiitic to slightly alkaline melts, LREE and Nb enrichments without relative HREE depletion, and ΔNb offsets indicative of reduced melting of a heterogeneous source (see section 4.5.3 above). The first model, proposing imperfect melt focussing to the ridge axis, involves a continuous process and therefore predicts that alkaline magmatism on Masirah is not geographically restricted but occurs throughout the Upper and Lower Nappes (formed ~130 Ma and ~135 Ma respectively). In the dying ridge model, the geochemical signature of waning magmatism is expected to be stronger near the extinct ridge axis, and off-axis magmatism would similarly be restricted to deformation zones along or nearby the extinct ridge axis, thus predicting alkaline magmatism to be more prominent in the younger Upper Nappe. Alkaline lavas and dykes occur throughout the Upper Nappe (e.g., lavas at Wadi Muhasi and dykes at Sur Masirah & Ra's al Ya) and Lower Nappe (e.g., post-axial lavas interbedded with Maghilah Unit sediments and the seamounts at Shi'inzi), favouring the imperfect melt focussing model. The alkaline plutons, in contrast, are mainly situated in the Upper Nappe, suggesting alkaline magmatism was most voluminous there (e.g., Marquer et al., 1998) and favouring the dying ridge model.

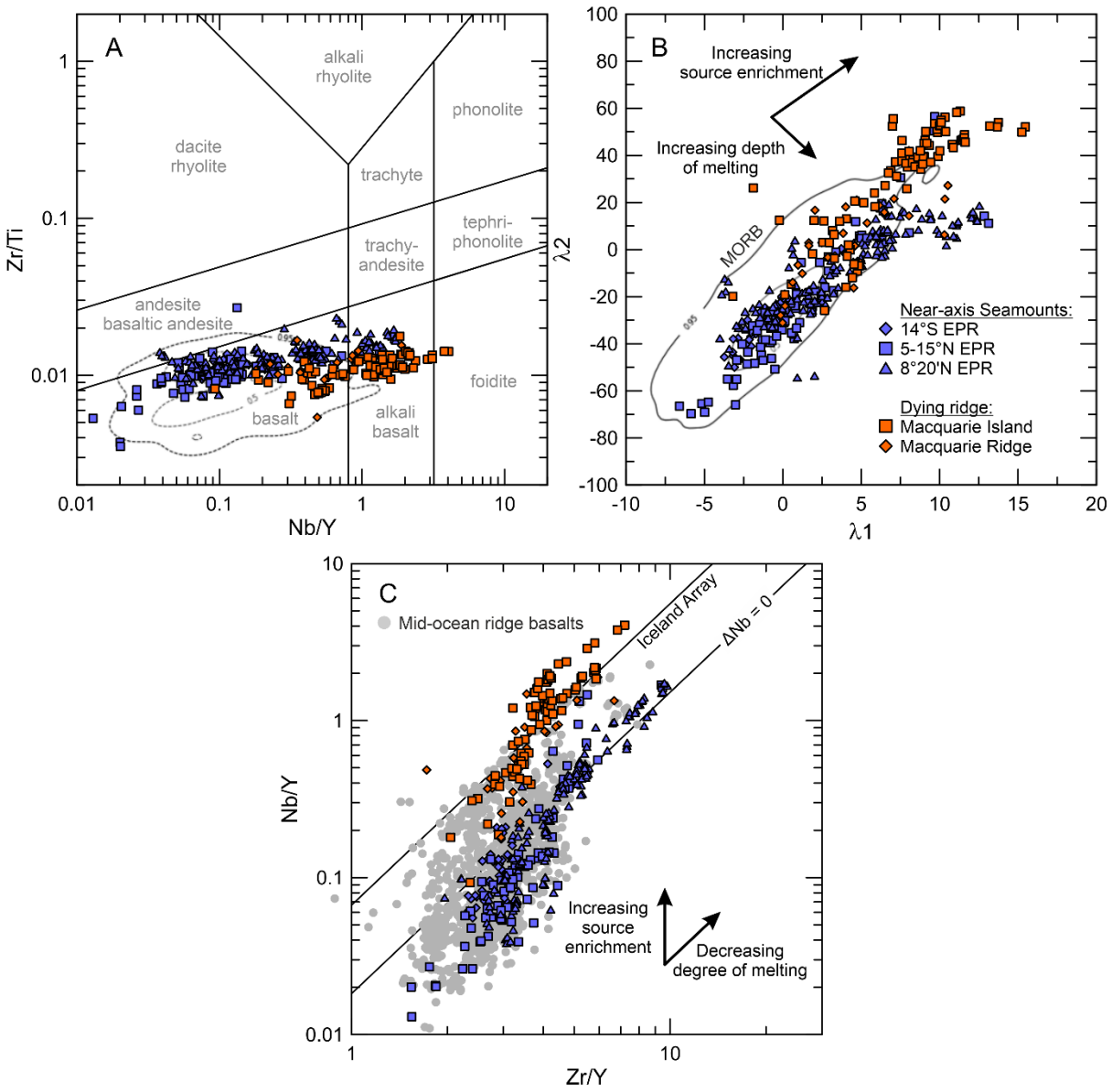

Figure 4.23: *A comparison of basalt from near-axis seamounts along the East Pacific Rise (EPR) and from a dying ridge along Macquarie ridge. Both groups extend from a tholeiitic affinity to an alkaline affinity (a), have LREE enrichments extending beyond the MORB array without HREE depletion (b), and show trends consistent with a combination of source heterogeneity and variable degrees of melting (c). Near-axis seamount data from Niu and Batiza (1997), Geshi et al. (2007) and Anderson et al. (2021). Macquarie island and ridge data are from a compilation by Jiang et al. (2021). Kernel density contours in (a) and (b) represent the MORB dataset of Gale et al. (2013) filtered for samples from mid-ocean ridges that were >500 km from a hotspot. Iceland array in (c) from Fitton et al. (1997) and MORB data from Gale et al. (2013).*

4.5.6 Paleo-spreading rates for the formation of Masirah

The high resolution obtained on the weighted means of single zircon U-Pb ages of this study (~30 – 70 ka) allow for an examination of the age variations within the Upper and Lower Nappes for the purpose of providing constraints on the paleo-spreading rate. The two samples from the lower

nappe (18MM323: 135.07 ± 0.03 Ma and 18MM337: 134.95 ± 0.05 Ma) differ 110 ka in age (40 – 190 ka when taking the full age range defined by the uncertainties into account). The sample locations are ~5 km apart, corresponding to ~4.5 km of distance perpendicular to the local east-west strike of the sheeted dyke complex. Assuming the strike of the dyke complex represents the strike of the paleo-ridge-axis (i.e., E-W), this translates to a paleo-half spreading rate estimate (HSR) of ~24 - 122 mm/yr, when displacement by post-axial tectonism is disregarded. This range is large and spans fast- (HSR > 40 mm/yr) and intermediate spreading rates (HSR = 20 – 40 mm/yr) as well as the faster end of the slow-spreading spectrum (HSR = ~20 mm/yr), but is nevertheless not consistent with slow (HSR = 10 – 20 mm/yr) and ultraslow (HSR < 10 mm/yr) spreading rates for the Lower Nappe. As the youngest sample (18MM337) is located the furthest north, this would suggest the Lower Nappe accreted south of an E-W oriented spreading ridge.

The age patterns within the Upper Nappe are more complex. In the Sur Masirah area, the two evolved dykes from the Sur Masirah dyke swarm have overlapping ages (18MM032: 131.36 ± 0.07 Ma and 18MM033: 131.31 ± 0.05 Ma, same outcrop). The leucocratic vein (18MM163: 130.63 ± 0.05) and pod (18MM170: 130.62 ± 0.05) from the nearby gabboic lower crust (~700 m to the west of the evolved dykes; 18MM163 and 18MM170 are ~400 m apart), however, have an overlapping age that is ~0.6 – 0.8 Ma younger than the evolved dykes. The Sur Masirah section is disrupted by faults although dyke orientations are fairly consistent with moderate to steep dips and a N-S trend (variable from NE-SW to WNW-ESE). The estimate for a paleo-half spreading rate based on these samples is unrealistically slow (~1 mm/yr). Alternatively, the age difference could indicate that crustal accretion was protracted over ~0.6 – 0.8 Ma, or that complex post-ridge tectonism resulted in a juxtaposition of older and younger rocks in the same section. The fifth Upper Nappe sample has an age that is younger than the evolved dykes but older than the leucocratic gabbros at Sur Masirah (18MM189: 131.03 ± 0.04 Ma). This varitextured gabbro is from Ra's al Ya, ~24 km northeast of Sur Masirah, and is 0.2 – 0.4 Ma younger than the oldest Sur Masirah samples. The sheeted dyke complex, however, has contrasting orientations (N-S at Sur Masirah and E-W at Ra's al Ya) and is not continuously exposed over the area between these two locations, preventing an estimation of the paleo-spreading rate.

Previous estimates of the paleo-spreading rate of the MOR at which Masirah formed are based on plate tectonic models. An apparent polar wander path for the Lower Nappe, determined in the paleomagnetic study by Gnos and Perrin (1996), suggests that Masirah formed south of a spreading ridge at a paleolatitude close to the present-day Somali basins. These basins are also aged Late Jurassic to Early Cretaceous and formed during the early stages of the opening of the Indian Ocean at half spreading-rates of 10 – 20 mm/yr (Rabinowitz et al., 1983; Cochran, 1988; Gaina et al., 2015).

Based on this analogy to the North and West Somali Basins, Peters and Mercolli (1998) previously proposed a paleo-half spreading rate of ~18 – 20 mm/yr for the formation of Masirah.

The spatial age distribution in the Lower Nappe determined in this study, with the youngest sample in the north, is consistent with accretion on the southern flank of a spreading ridge, but the half-spreading rate estimate for the Lower Nappe calculated here (~24 – 122 mm/yr) suggests the paleo-ridge may have been faster spreading. It is noted, however, that this estimate is based on just two samples. Analysis of a greater number of samples in the Upper Nappe, yielding a large age range in a small region, shows that spatial age distributions can be more complex. Further constraints on post-ridge tectonic displacements and on the original orientation of the sheeted-dyke complex, as well as a more systematic sampling approach, are therefore required to provide more accurate constraints on the paleo-spreading rate.

4.5.7 The link to the tectonic evolution of the Indian Ocean

Plate-tectonic models for the North and West Somali basins (west Indian Ocean) indicate a cessation of seafloor spreading during the early history of the opening of the Indian Ocean, which may be analogous to the dying ridge model proposed for Masirah in the previous section (4.5.5). Initial seafloor spreading was accommodated along east-west trending ridges offset by north-south oriented fracture zones, as a consequence of the breakup of East (India, Madagascar, Australia and Antarctica) and West (Africa, Arabia and South America) Gondwana in the Late Jurassic (Cochran, 1988; Gaina et al., 2015; Davis et al., 2016; Reeves et al., 2016). Further breakup of East Gondwana, starting ~135 – 130 Ma (Gaina et al., 2007, 2015; Davis et al., 2016), resulted in a change of motion of the Indian Plate and consequently a cessation of spreading in the North Somali Basin and reduced spreading along a slightly changed direction in the West Somali Basin (Gaina et al., 2015; Phethean et al., 2016). The West Somali Basin records deformation of the ocean crust that initiated before Hauterivian times (i.e., before 132.9 – 129.4 Ma), shortly after crustal accretion, and ceased in the Aptian (125 – 113 Ma; Sauter et al., 2018). Plate tectonic models suggest that during this time, the highly segmented spreading ridge west of Madagascar started accommodating strike-slip motion, facilitated by the coalescing of ridge-discontinuity fracture-zones into what would become the Davies Fracture Zone (Phethean et al., 2016). Seismic reflection sections indicate that this event was accompanied by steep thrust faults and 20 – 30 km wavelength folds, both on crustal scales, as well as the emplacement of off-axis volcanic edifices and plutons stalled in melt feeder-channels along deformation zones (Sauter et al., 2018).

The proposed origin of Masirah in the western Indian Ocean somewhere between Madagascar and Arabia (Gnos and Perrin, 1996; Peters and Mercolli, 1998) places it in close spatial and temporal

vicinity of the ~135 – 130 Ma reorganisation of plate motions that affected the Western Somali basin (Figure 4.20d). A similar cessation in seafloor spreading and lithosphere-scale deformation in other parts of the young Indian Ocean (i.e., the North Somali Basin and proto-Owen Basin) is plausible and would be consistent with the timing of off-axis magmatism, deformation and uplift on Masirah, as well as the geochemical constraints. A link between a change in plate motions and the late-stage magmatism in Masirah was proposed by previous studies (Meyer et al., 1996; Marquer et al., 1998; Peters, 2000), but new data from this study suggest that the main phase of crustal accretion only slightly predates this event. Furthermore, a reorganisation of plate motions may have had ramifications beyond generating off-axis magmatism, since crustal-scale thrust faults as described by Sauter et al. (2018) could have potentially been reactivated and utilised to initiate the nappe-thrusting observed on Masirah, and subsequent obduction, during the proposed (much later) transpressive strike-slip plate motions (e.g., Rodriguez et al., 2020).

4.5.8 Further work

Important uncertainties relating to the distribution of the alkaline magmatism (and therefore the criteria to distinguish between the 'imperfect melt focussing' versus 'dying ridge' models, section 4.5.5) remain, however, since the Upper Nappe – Lower Nappe distinction is not demonstrated conclusively for some parts of the island. The mantle section near Jabal Suwayr in the south of Masirah, which is intruded by alkaline plutons and dykes ranging from tholeiitic to alkaline basalts, could for example represent part of the Upper Nappe (as mapped by Peters et al., 1995) or Lower Nappe (as in reconstructions of Immenhauser, 1996 and Marquer et al., 1998), with important implications for the extent of alkaline magmatism within each nappe. Likewise, the seamounts near Shi'inzi overlie MORB-like lavas but are otherwise tectonically dismembered from an axial crustal sequence (Meyer et al., 1996), suggesting the proposed Lower Nappe origin (Peters et al., 1995; Meyer et al., 1996) carries some uncertainty. Furthermore, the precise nature of the tectonic relationship between the Upper and Lower Nappes remains to be investigated, as this has implications for the proximity of the nappes to proposed dying ridge. It is unclear for instance whether the nappes formed sequentially at the same spreading segment (implying the older Lower Nappe is more distal to the dying ridge than the younger Upper Nappe) or whether they formed at different spreading segments and/or on opposite tectonic plates (allowing for the juxtaposition of older and younger lithosphere in the proximity of the dying ridge). To conclusively differentiate between the two models for the transition from on to off-axis magmatism, further high-precision geochronological work is required to constrain the timing of the off-axis plutons, dykes and lavas relative to the axial sequence in both the Upper and Lower nappes. By establishing a precise age for both nappes, this study provides a geochronological framework for future work.

4.6 Conclusions

1. New high-precision U-Pb dating of single zircons indicate that the Masirah ocean crust was accreted at 135 – 130 Ma instead of 150 Ma. Two crosscutting plutons yielded a ~66 Ma age, coinciding with the proposed emplacement age of the Eastern Oman Ophiolites and suggesting obduction was accompanied by small amounts of melting.
2. Field relations and geochemistry of the dykes and lavas record a transitional event where the main phase of crustal accretion was followed by episodic off-axis magmatism. The bulk of the igneous crust was formed from parental melts with variable trace element compositions that were derived from a heterogeneous mantle, while later melts are increasingly derived from a smaller degree of melting of the enriched, more fusible mantle component. Off-axis volcanism ceased by Barremian times (129.4 – 125 Ma).
3. The gabbros of the axial lower crust and the gabbro-dolerite-granite suite are distinct in petrography and mineral compositions, although their mineral compositions fall on a single differentiation trend and some mantle intrusions share characteristics with both suites. The distinctive mineral assemblage and evolved character of the gabbro-dolerite-granite suite may be a result of crystallisation from melts derived from the more enriched mantle component and/or less efficient melt extraction from the crystallising bodies.
4. The transitional nature of the magmatic suites and the occurrence of episodic off-axis magmatism on Masirah are inconsistent with a plume-fed hotspot origin. They can instead be accounted for by (1) imperfect focusing of melts to the ridge axis or (2) a cessation of seafloor spreading and mantle upwelling and melting, followed by episodic melting during renewed (local) extension. A mechanism for the second alternative is potentially provided by the reorganisation of plate motions that occurred in the Indian Ocean around ~135 – 130 Ma, plausibly resulting in local transtensional settings as the former spreading-ridge and ridge-discontinuities began to accommodate the new direction of plate motion. The second model is also consistent with the localised uplift to near sea-level recorded in the autochthonous sedimentary cover of the ophiolite, but further geochronological constraints on the alkaline magmatism are needed to definitively differentiate between the two alternatives.

5. Penrose on a diet: the architecture of the Masirah Ophiolite, a remnant of slow-spreading oceanic lithosphere

5.1 Introduction

The largest volumes of magma on the present-day Earth erupt at mid-ocean ridges (MOR) as a fundamental component of plate tectonics in the process of seafloor spreading. As tectonic plates are pulled apart and the upper mantle melts during adiabatic upwelling, the resulting magmas accumulate at the spreading ridge and form an igneous oceanic crust, continuously repaving the ocean basins on timescales of approximately 200 million years. Constraining the process of crustal accretion and the resulting architecture of the oceanic lithosphere is a first order problem in geology and has important consequences for global geochemical cycles, crustal rheology and chemical fluxes between the Earth's interior and the oceans and atmosphere. Spreading-rate is a key variable: at the fast (>80 mm/yr) end of the spectrum, mantle melting is extensive, resulting in a continuous, 6 - 7 km thick igneous layer-cake 'Penrose' crust (Anonymous, 1972; Cann, 1974; Sinton and Detrick, 1992). In contrast, at ridges where spreading is slow (20 - 40 mm/yr) or ultraslow (<20 mm/yr), magmatism is sparser and more intermittent, and plate separation is consequently required to be partly accommodated by faulting, resulting in a highly heterogeneous lithosphere (e.g., Cannat, 1996; Dick et al., 2003).

Current models for slow-spreading ridges hold that, as melt supply varies in space and time, the mode of crustal accretion alternates between two styles (Figure 5.1). At magmatically robust segments along the spreading ridge, it is thought a 'classic' 6 – 7 km thick, layered igneous crust is generated through 'magmatic spreading', which thins towards ridge discontinuities (e.g., Lin et al., 1990; Cannat, 1993, 1996). At magma starved portions of the ridge, in contrast, a significant proportion of plate separation is accommodated by 'tectonic spreading' on large detachment faults whose uplifted footwalls exhume the deep crust and shallow mantle onto the seafloor in oceanic core complexes (e.g., Cann et al., 1997; Blackman et al., 1998; Tucholke et al., 1998; Ildefonse et al., 2007). Due to a thicker lithosphere, a continuous layered igneous crust is absent in such settings and instead a plum-pudding type lithosphere is formed (Cannat, 1993, 1996). Furthermore, as spreading rates transition from slow to ultraslow, amagmatic ridges may occur (e.g., Dick et al., 2003).

Reconstructing the architecture of the oceanic lithosphere remains challenging, however: observations are largely limited to the seafloor, supplemented by 1D drill core obtained by scientific drilling. This places severe limitations on our understanding of the lower crust in particular. Studies of the plutonic slow-spreading crust have so far largely been limited to oceanic core complexes, which may not be representative for large sections of mid-ocean ridge crust, as it is unclear whether

they represent a section dismembered from a full layer-cake crust (e.g., Dick et al., 2000, 2008, 2019b) or lithosphere where an overlying upper crust did not develop and instead formed a gabbroic batholith as melts intruded the footwall and differentiated *in situ* without being extracted (e.g., Godard et al., 2009; MacLeod et al., 2009; Boulanger et al., 2020). Conversely, magmatically robust ridge segments have only been sampled in the upper basaltic layer at the seafloor, with the thickness of the igneous crust primarily inferred from geophysical data (e.g., Lin et al., 1990; Cannat, 1993). Due to the restricted nature of direct observations, our understanding of the architecture of slow-spreading oceanic lithosphere remains relatively poor.

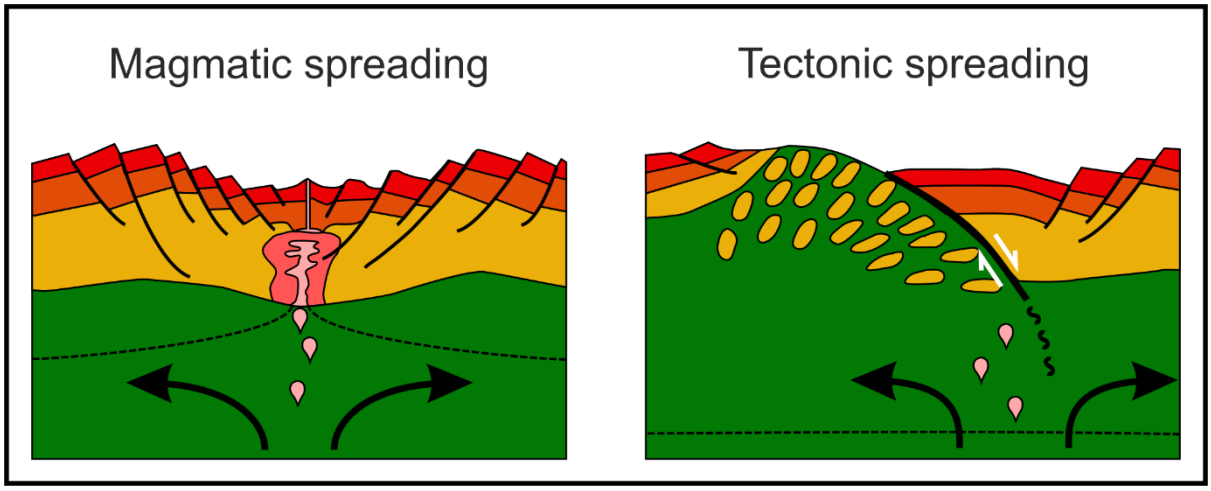

Figure 5.1: *Schematic diagrams of across-axis cross-sections illustrating the two main modes of ocean spreading and the lithosphere they produce at slow-spreading ridges. Dashed line represents the lithosphere-asthenosphere boundary. The detachment fault in the righthand panel cuts through the brittle lithosphere and extension in deeper parts of the lithosphere is accommodated by plastic deformation, shown as wavey lines (~).*

Ophiolites expose often complete sections of oceanic lithosphere in 3D, and thus have the potential to provide critical insights into lithospheric architecture. However, many originate at non-typical spreading ridges in marginal basins near subduction zones, complicating direct comparisons with MORs. Notably, the presence of water derived from subduction processes has a significant effect on the degree of mantle melting and crustal-level magma differentiation, in turn affecting melt chemistry, viscosity and density (e.g., MacLeod et al., 2013). An important exception is the Masirah ophiolite, exposed over ~650 km^2 on Masirah Island off the southeast coast of Oman (Peters, 2000). Masirah is regarded as a rare, exhumed fragment of true 'open-ocean' lithosphere that formed at a slow-spreading ridge during the opening of the early Indian Ocean (~135 - 130 Ma, Peters and Mercolli, 1998; Chapter 4). It thus offers a unique opportunity to study a fragment of slow-spreading ocean lithosphere and test the current models of seafloor spreading.

This chapter presents detailed field observations to obtain a reconstruction of the axial lithosphere and describe the architecture of the Masirah ophiolite, which is different from what has been observed for slow-spreading ridges so far. Subsequently, the mineral chemistry of the gabbroic lower crust, as well as the bulk whole-rock composition of the igneous crust, are investigated to see if the magmatic differentiation processes they record are consistent with the crustal configuration observed and whether the bulk igneous crustal composition resembles a parental MORB melt. Additionally, melt flow lineations in dykes, obtained from the anisotropy of magnetic susceptibility (AMS), are analysed to assess the extent of vertical versus lateral (along-axis) melt transport and determine whether the dyke complex on Masirah was sourced from the gabbroic lower crust. The main conclusion is that the Masirah ophiolite was accreted magmatically rather than tectonically, but has a total igneous crustal thickness that is a lot thinner (~2 km) than predicted by current models for magmatic spreading (~6 – 7 km). These findings suggest that a reduced melt supply does not necessarily result in detachment faulting and show that variations in crustal architecture at slow-spreading mid-ocean ridges may be greater than previously thought.

5.2 Field observations and petrography

The complex internal structure and disposition of outcrop of the ophiolite is the result of several generations of emplacement- and post-emplacement-related faulting (Marquer et al., 1995), resulting in many tectonic contacts that obscure the primary relationships between the various lithological units. Ophiolite emplacement was accompanied by nappe-thrusting, forming an Upper and Lower Nappe on Masirah. Post-emplacement extensional tectonics in the Tertiary subsequently resulted in orthogonal N-S and E-W block faulting, spaced 200 – 500 m with vertical offsets of metres to 200 m (Marquer et al., 1995). As a result of interference of these normal faults with the near-horizontal nappe thrust, the geology of Masirah is complex and many field contacts between lithological units are poorly exposed and structural rather than primary (Marquer et al., 1995). This is particularly true for western coastal plains along the centre and south of Masirah. Nevertheless, a more contiguous magmatic crust is preserved in the north of Masirah (Jabal Taymah and Ra's al Ya, Upper Nappe, exposing the mantle, lower crust and gabbro-dyke transition), in the centre (Sur Masirah and Wadi Muhasi, Upper Nappe, exposing the lower crust, gabbro-dyke transition and sheeted dyke complex), and large parts of the island's interior in the south (Haql, Wadi Madi, Urf, Wadi Jibuti, Lower Nappe, exposing the lower crust, gabbro-dyke transition, sheeted dykes and lavas)(Peters et al., 1995; Figure 5.2).

The primary relationships between the various lithological units can be studied in carefully selected sections through various levels of the crust, which allowed Marquer et al. (1998) to reconstruct the geometry of the oceanic crust. Based on the previous characterisation of the axial suite and the

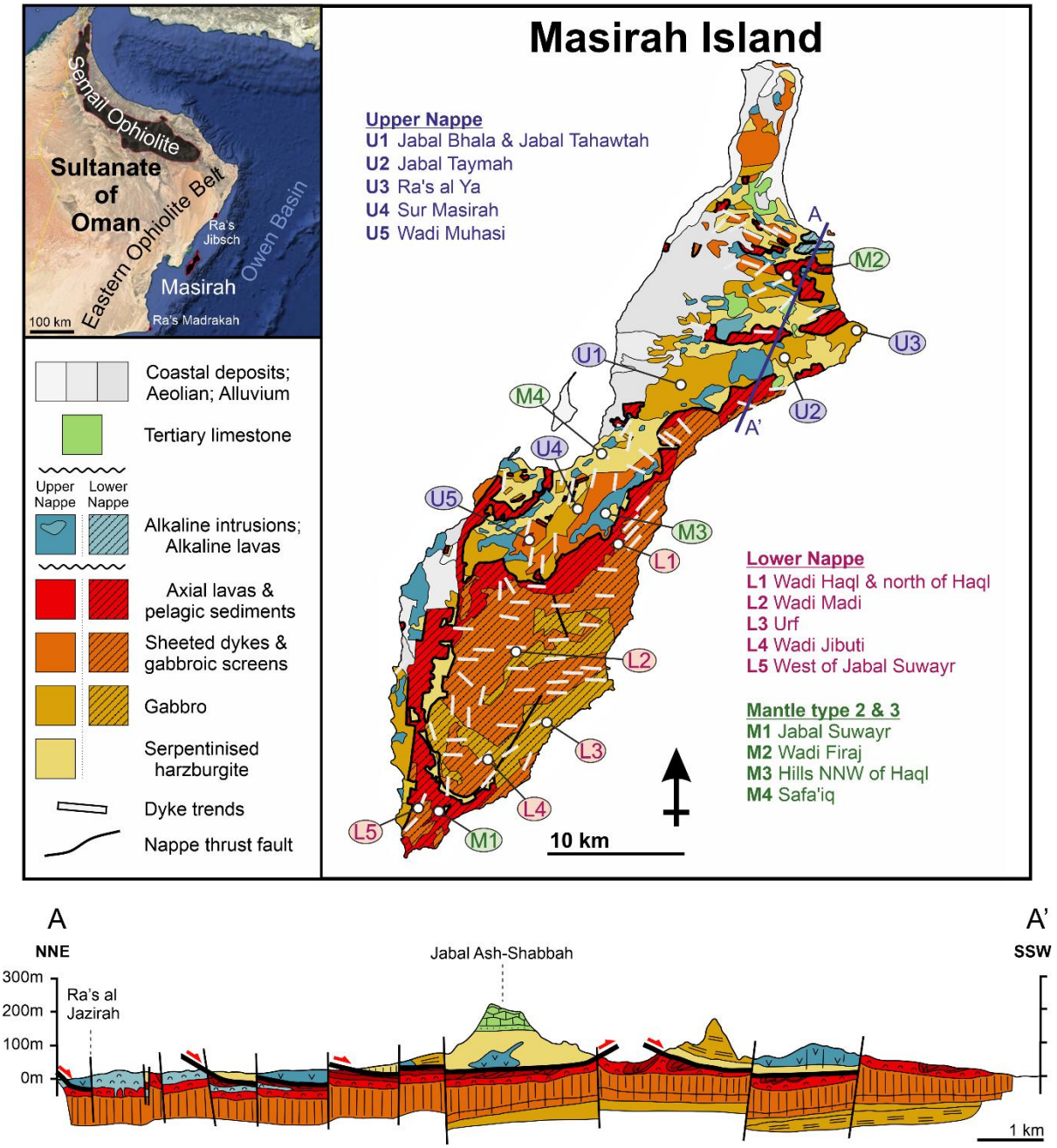

Figure 5.2: *Geological map of Masirah showing the sample locations for this chapter. U1, U2, L1 etc. refer to the various localities containing partial sections through the crust (see Figure 5.3 and accompanying text for more information). Figure adapted from Peters et al. (1995).*

alkaline near off-axis suite on Masirah (Chapter 4), sections thought to represent the axial lithosphere were identified using the geological map by Peters et al. (1:50,000; 1995) and cross-sections by Marquer et al. (1998). Google Satellite images were studied in QGIS (v. 3.8) and augmented with field observations to identify topographic expressions of major faults disrupting the sections. Many such sections were combined, noting their similarities, differences, consistencies in relationships and inferred stratigraphical overlap, with the aim of investigating the relations of the main lithological units from a mid-ocean ridge perspective and updating the reconstructed

composite section of the oceanic lithosphere pseudo-stratigraphy at Masirah of Marquer et al. (1998). Paleo- vertical or paleo-horizontal markers were used to reconstruct the stratigraphical heights of samples where this was possible. For sections near the crust-mantle boundary, the orientations of gabbroic lenses in the mantle, modal layering in the gabbros, and dunite-gabbro layering in the lower crust were averaged and interpreted as a paleo horizontal. Using this orientation, the crust-mantle boundary plane could be reconstructed, as well as the height of samples with respect to this boundary. When faults with an unknown displacement interrupt the section, or when paleo-horizontal and vertical markers are ambiguous or result in non-unique interpretations, samples were not assigned an absolute height. In figures that occur later on in this chapter (e.g., the mineral chemistry stratigraphy in Figure 5.9), these samples are plotted at a rough relative height based on the succession of lithological units present in the sections.

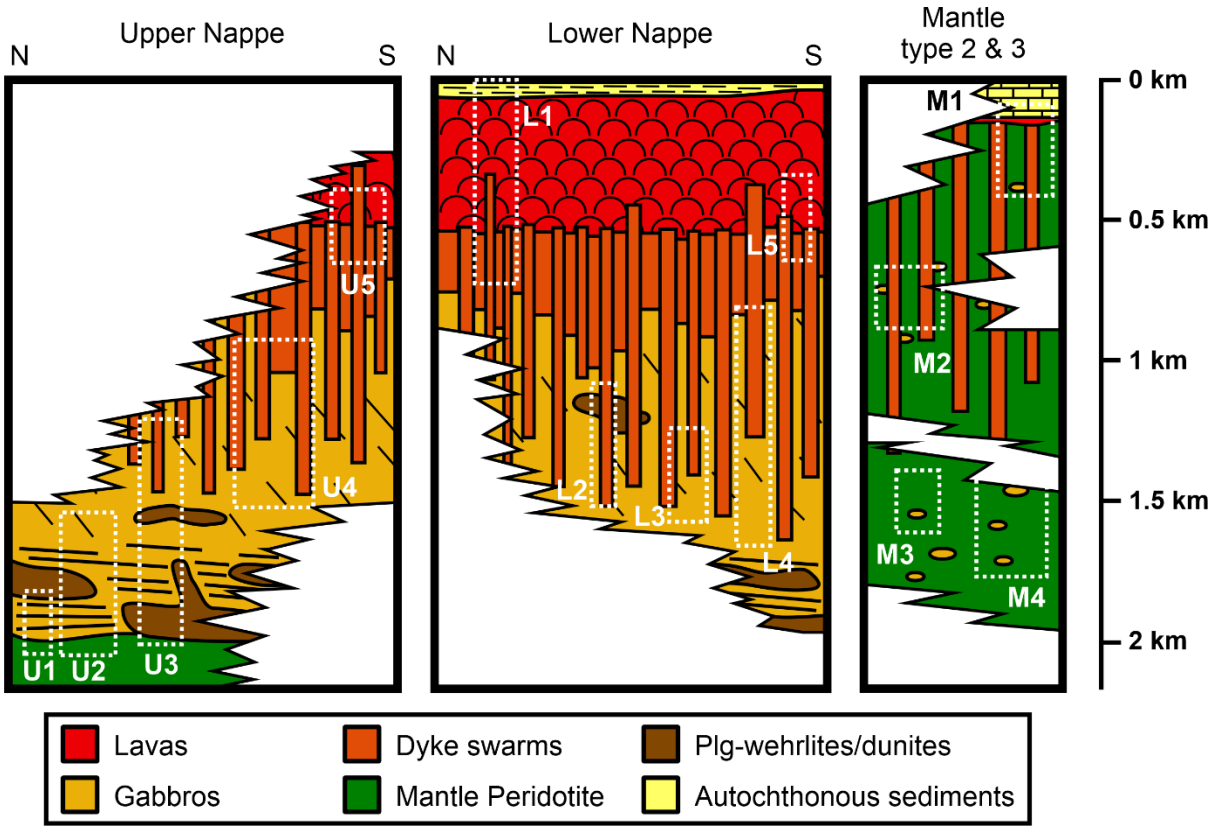

Figure 5.3: *Overview of the lithological relations in the Upper Nappe and Lower Nappe along roughly north-south transects, as well as the mantle types 2 & 3 (mapped as Upper and Lower Nappe). White boxes illustrate which portion of the crust was studied in which section. U1 = Jabal Bhala/Jabal Tahawtah, U2 = Jabal Taymah, U3 = Ra's al Ya, U4 = Sur Masirah, U5 = Wadi Muhasi, L1 = Wadi Haql & north of Haql, L2 = Wadi Madi, L3 = Urf, L4 = Wadi Jibuti, L5 = West of Jabal Suwayr, M1 = Jabal Suwayr, M2 = Wadi Firaj, M3 = hills north-north-west of Hawl, M4 = Safa'iq.*

The following subsections describe the main lithological units. To avoid repetition, the reader is referred to Chapter 4 for additional descriptions of the gabbroic plutons in the mantle, as well as the dykes and lavas.

5.2.1 Relationship between the Upper and Lower Masirah Nappe

The Lower Masirah Nappe, mainly exposed in the south and south-east of Masirah, formed ~5 Ma before the Upper Nappe, exposed in the north and north-west of the island (Chapter 4). A main difference between the nappes is the stratigraphic level which is exposed. The Upper Nappe has extensive outcrops of mantle, crust-mantle boundary, base of the lower crust and upper gabbros (e.g., at Jabal Taymah and Ra's al Ya) and upper gabbros intruded by dykes (at Sur Masirah). The higher stratigraphical levels of the sheeted dykes and lavas are present but limited in extent (e.g., at Wadi Muhasi). The Lower Nappe, in contrast, has extensive exposures of lavas, sheeted dykes and the gabbro-dyke transition, but limited occurrences of the lower layered gabbros. Despite these differences, the similarities of identical units and their relations between the nappes, as well as the significant overlap of the stratigraphy occurring in both nappes, argue for a broadly similar crustal architecture for both.

5.2.2 Mantle

The mantle of the Masirah ophiolite is extensively to completely serpentinised (generally >95%) and mainly consists of spinel-harzbugite and some spinel-dunite, with minor amounts of clinopyroxene (up to 5%) sometimes present. The studied mantle sections are spatially variable and are here divided into three categories according to their field appearance and relationships to other lithologies.

Mantle type 1 ('sub-crustal mantle') occurs on the distinctive orange-brown slopes of the mountain range spanning between Ra's al Ya and Jabal Tahawtah in the north of the island (Upper Nappe; Figure 5.2), where ~50 – 100 m of mantle is exposed beneath the igneous lower crust (Figure 5.4a). Varying modal proportions of olivine and orthopyroxene commonly give rise to parallel layering on scales of tens of centimetres to tens of metres, which is often steeply oriented with respect to the sub-horizontal crust-mantle boundary (Figure 5.4b). A high-temperature foliation was difficult to identify in the field, but has been described previously (Peters et al., 1995; Peters and Mercolli, 1998) and deformation is recorded by kinkbands in olivine and minor undulose extinction in orthopyroxene (see Chapter 6 for a detailed description of the peridotite petrography). Metre-sized lenses of pure dunite also occur; plagioclase peridotites are absent. Gabbroic intrusions are generally rare to absent in these sections (generally <1% of the outcrop) and occur as metre-sized pods or as veins, sheets or dykes (from several to tens of centimetres thick, tens of metres long, Figure 5.4c).

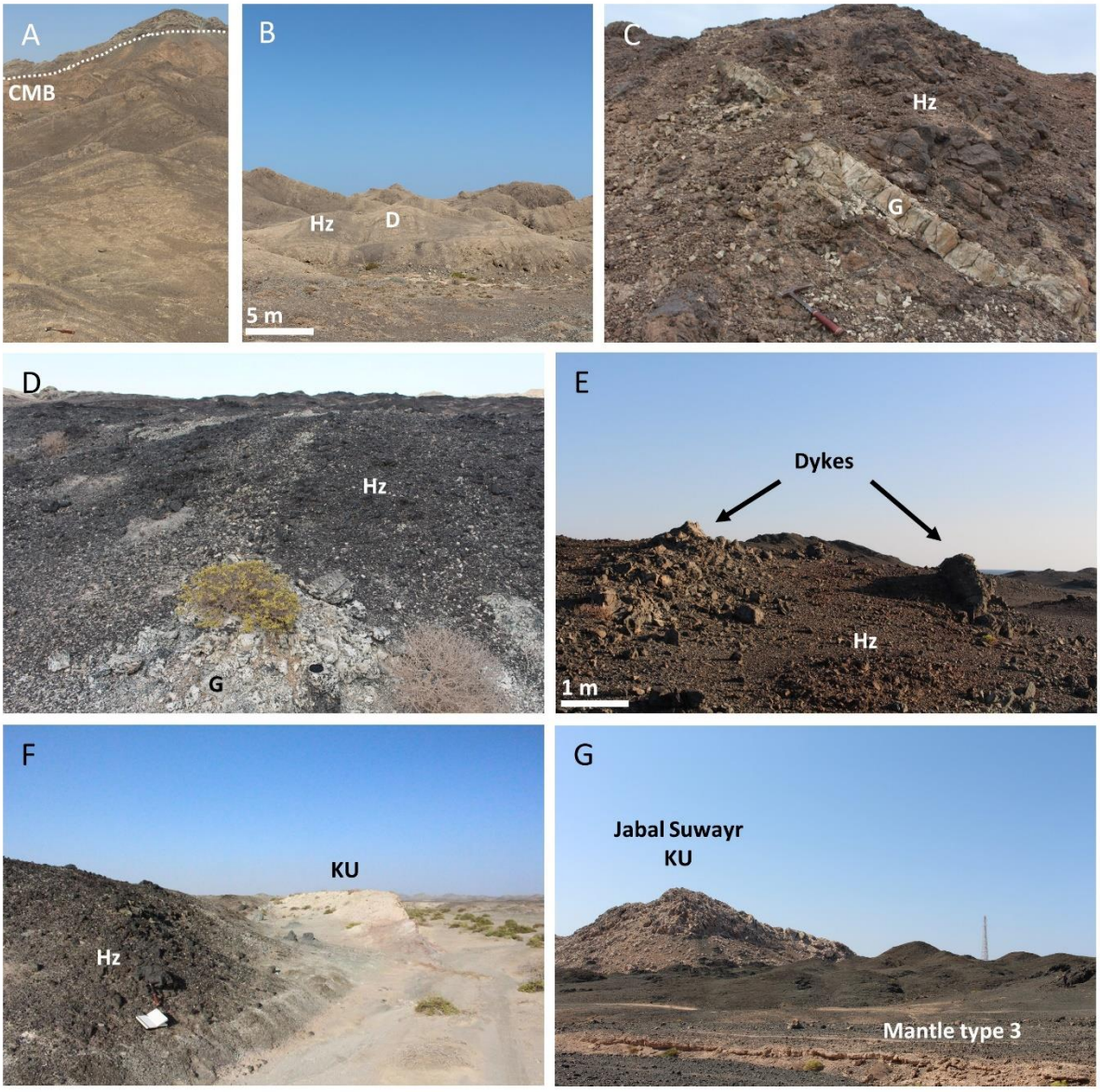

Figure 5.4: *(a) A section of type 1 mantle exposed in the ridge east of Jabal Taymah, with the crust-mantle boundary and base of the lower crust exposed at the top of the hill (hammer in foreground for scale). (b) Steep modal layering in type 1 mantle (ridge east of Jabal Taymah). (c) Rare gabbroic sill in type 1 mantle in the southwestern part of Wadi Thoumi/Wadi Zamir (hammer for scale). (d) More abundant gabbroic intrusions in type 2 mantle in the hills north-northwest of Haql (lens cap in foreground for scale). (e) Dyke swarm intruding type 3 mantle near Jabal Suwayr. (f) Abrupt contact between type 2 mantle harzburgites and sediments of the Kalban Unit separated by a fault running through the gully (Al Hatm, fieldbook in foreground for scale). (g) Platform carbonate sediments of the Kalban Unit deposited on mantle type 3, forming Jabal Suwayr (approximately 70 m high). CMB = crust-mantle boundary; Hz = harzburgite; D = dunite; G = gabbro; KU = Kalban Unit (sedimentary cover).*

Mantle types 2 and 3 tend to occur in parts of the island where the relationship with the overlying crust (if any?) has been tectonically disrupted, such as at Safa'iq, Wadi Firaj and in the area north-

northwest of Haql (Upper Nappe; Figure 5.2) and at Jabal Suwayr (nappe unclear but assigned to the Lower Nappe in reconstructions by Marquer et al., 1998). Occasionally they are spatially associated with sediments of the Early Cretaceous Kalban Unit (Figure 5.4f), and at Jabal Suwayr the contact is preserved, showing these Barremian age (~129.4 – 125 Ma) platform carbonates were deposited directly onto the mantle (Figure 5.4g; Immenhauser, 1996). Gabbroic intrusions are (locally) more abundant in these locations (ranging from 5% up to 70% of the outcrop) and are often pegmatitic and 'varitextured', lacking chilled margins (Figure 5.4d, see also Chapter 4). Modal orthopyroxene-olivine layering and dunite lenses, common in sub-crustal mantle, were not encountered in the tectonically dismembered mantle sections and their field appearance tends to be distinctively more waxy and dark-brown to green and red, corresponding to a coarser serpentine mesh and a greater abundance of magnetite veins (further described in Chapter 6). Rare plagioclase peridotites also occur and likely represent high-temperature impregnation by a melt, with plagioclase and clinopyroxene interstitial to olivine and locally grading into olivine-rich gabbros where the interstitial minerals are more abundant. Besides these comparable features, type 3 mantle stands out from type 2 mantle by the presence of swarms of cross-cutting dolerite dykes with chilled margins ('dyke-intruded mantle', studied at Jabal Suwayr and Wadi Firaj; Figure 5.4e). These outcrops are described in further detail in the section on the sheeted dyke complex.

5.2.3 Igneous lower crust

The igneous lower crust has a vertical extent of about 500 m from the crust-mantle boundary to the base of the gabbro-dyke transition. It is here subdivided into the base of the lower crust, consisting of layered gabbros and ultramafics in the lower 150 – 200 m above the crust-mantle boundary, and the upper gabbros, consisting of several hundred metres of foliated and isotropic gabbros. Throughout the gabbroic lower crust, subsolidus high-temperature deformation structures such as mylonites are rare and locally occur in the upper gabbros as centimetre-scale shear zones with pophyroclasts and mineral stretching. The petrography of the various lithologies of the lower crust will be described in detail in section 5.2.6 below.

5.2.3.1 Crust-mantle boundary and base of lower crust

The crust-mantle boundary and the base of the lower crust, overlying mantle type 1, was studied around Jabal Taymah and Ra's al Ya (north Masirah, Upper Nappe), where it is well exposed. The crust-mantle boundary itself is relatively abrupt: orthopyroxene-bearing harzburgites disappear over several metres vertically at the base of the lower crust, with little obvious change in their appearance in the metres beneath this boundary (Figure 5.5a). The disappearance of harzburgites is concomitant with an upward change over a few metres to massive dunite with local transitions to troctolite ± plagioclase-wehrlite. The first ~150 – 200 m above this boundary at the Jabal Taymah

and Ra's al Ya sections, hereafter the 'base of the lower crust', is comprised of sequences (up to tens of metres thick) of modally layered olivine-gabbro, interlayered dunite and olivine-gabbro, and plagioclase dunites and plagioclase wehrlites. The sequences alternate and repeat vertically in a random order, orientated as layers (metres to tens of metres) sub-parallel to the crust-mantle boundary (Figure 5.5a-c), and can thin and pinch out laterally over hundreds of metres. They sometimes truncate each other, most clearly indicated by bodies of plagioclase-dunite that crosscut the modal layering in the gabbros (details below, Figure 5.5d & h-i). Although there is no uniform stratigraphy, there is a general trend of an upwards decrease in interlayered dunite and gabbro and plagioclase-dunites and plagioclase-wehrlites (collectively referred to as the 'ultramafic suite'), and an increase in modally layered gabbros (the 'layered gabbro' unit). Layered gabbro begins to dominate around ~100 m above the crust-mantle boundary, but rare isolated, elongate bodies of ultramafic units (metres to tens of metres in size) continue to occur higher up in the section.

The mafic and ultramafic units display complex, mutually cross-cutting relationships in the base of the lower crust. Dunites, plagioclase dunites, plagioclase wehrlites and melanotroctolites are interlayered with olivine-gabbros and gabbros at scales of several centimetres to several metres and contacts can be diffuse over tens of centimetres or sharp and serrated along crystal grain boundaries (Figure 5.5c & d). The plagioclase dunites and plagioclase-wehrlites consist of conspicuous rounded olivine grains with interstitial plagioclase and clinopyroxene oikocrysts (1 – 5 cm; Figure 5.5e).

Figure 5.5 (next page)*: (a) Jabal Taymah (~200 m tall) exposes the base of the lower crust overlying type 1 mantle, showing the abrupt transition from mantle (orange-brown) to crust (gabbros are grey and ultramafic suite is dark brown), as well as the layered structure of the base of the crust (arrow indicates the lateral pinching out of a gabbroic layer). (b) View from the top of Jabal Taymah to the northwest, showing the layered structure of the base of the lower crust, overlying type 1 mantle. Jabal Humr (in the background, ~200 m tall) consists of Tertiary post-emplacement sediments deposited on the ophiolite nappes. (c) Close-up of the layered structure (layered gabbro and plagioclase dunite) of the base of the lower crust in the Jabal Taymah section. (d) Layered structure of the base of the lower crust on a sub-metre scale, where an isomodally layered gabbro pinches out and alternates with homogenous gabbro (Ra's al Ya section, lens cap for scale). (e) Characteristic texture of plagioclase dunite: rounded olivine with oikocrystic clinopyroxene and interstitial, amoeboid plagioclase, which sporadically concentrates in leucocratic veins. (f) Plagioclase-rich vein crosscutting plagioclase dunite grades into the host rock with varying proportions of plagioclase (hammer for scale). (g) Blocks of plagioclase dunite in a matrix of gabbroic veins and pods. (h) & (i) A vertical body of plagioclase dunite, tens of metres in size, intrudes and crosscuts the layered gabbro unit, truncating the modal layering. Photos (e) – (i) are from the Western ridge of Jabal Taymah section. CMB = crust-mantle boundary; LG = layered gabbro; PD = plagioclase dunite; G = gabbro.*

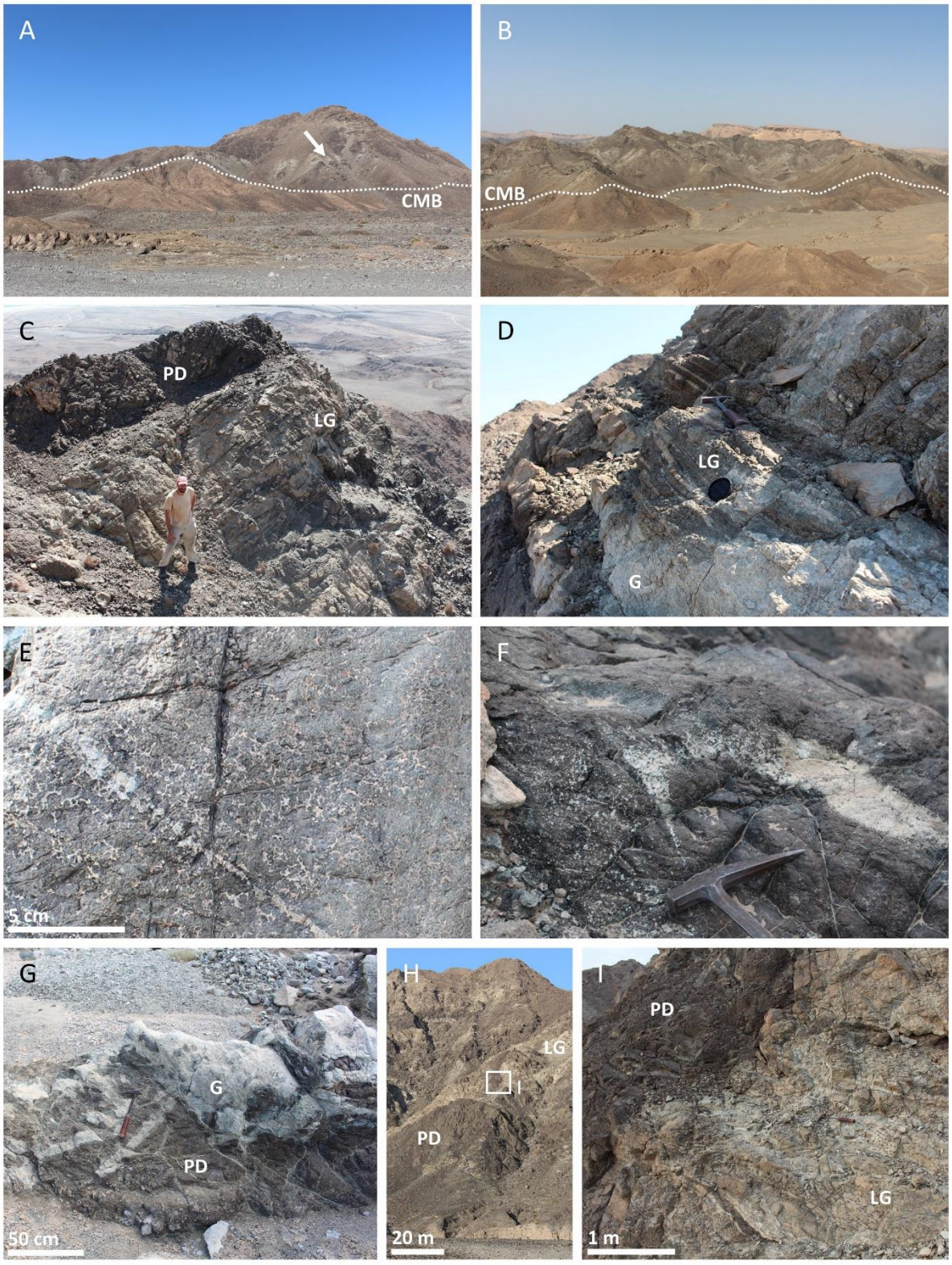

Importantly, the rocks classified as plagioclase-wehrlites do not contain cumulus clinopyroxene or textures indicating clinopyroxene crystallisation preceded plagioclase. Instead, they are part of a suite of olivine-rich lithologies with variable propositions of interstitial plagioclase and clinopyroxene that are locally wehrlitic, and therefore different from wehrlites described in supra-subduction zone

ophiolites such as Troodos. Plagioclase contents are variable throughout the rocks and sporadically concentrate into pockets of melanotroctolite, which can grade into plagioclase-rich gabbroic dykes (± olivine) that crosscut the ultramafic host-rock (Figure 5.5f). Where abundant, these gabbroic dykes form stockworks that fragment the ultramafic host into blocks (Figure 5.5g). Ultramafic layers are sometimes ductilely folded or can occur as magmatic partially disaggregated xenoliths and schlieren within the gabbroic units. Conversely, the plagioclase-dunite units crosscut layered gabbros at steep angles and sometimes contain gabbroic xenoliths resorbed to various degrees (Figure 5.5h & i). Where layered gabbro is cross-cut, the layering is warped but devoid of shear strain, suggesting the deformation was magmatic and modal layering formed relatively early during the accretion of the lower crust.

The layered gabbros consist of olivine gabbros and gabbros and often exhibit modal layering sub-parallel to the crust-mantle boundary. Layering is developed to various degrees and accompanied by a magmatic foliation and lineation (further described in the petrography section). Layering arises from variations in modal mineral proportions of olivine, clinopyroxene and plagioclase, resulting in centimetre to metre thick modal layers that may be laterally continuous for tens of metres. Layer boundaries can be sharp or diffuse, and layer morphology varies between graded layering, with olivine-rich base and plagioclase-rich tops, and isomodal layering, with alternating levels of internally homogeneous melanogabbro and leucogabbro (Figure 5.5c-d & i). In some cases, thin leucogabbroic veins (~0.5 – 1 cm) in plagioclase-dunite and elongate dunite lenses (~1 x 10 cm) in gabbroic bodies can resemble a type of 'proto-layering'. Some layers are clearly intrusive and cross-cut other layers at high angles, whereas other layers may thin out and terminate laterally. The orientation of modal layering is variable, although within continuous sections it is sub-parallel to the crust-mantle boundary, as are the gabbroic intrusions in the underlying mantle (with axial affinity, Chapter 4), the dunite/gabbro layers in the base of the lower crust and the foliation fabrics in homogenous gabbros.

5.2.3.2 Upper gabbros

From ~150 – 200 m above the crust-mantle boundary at Jabal Taymah and Ra's al Ya (Upper Nappe), modal layering generally disappears and ultramafic bodies become rare to absent (Figure 5.6a). Sections of the lower crust studied at Sur Masirah (Upper Nappe) and Wadi Madi, Wadi Jibuti and Urf (Lower Nappe; Figure 5.2) do not expose the base of the lower crust but are similar to the gabbros at the top of the sections at Jabal Taymah and Ra's al Ya, and pas upwards into the gabbro-dyke transition and sheeted dykes. Gabbro (*sensu stricto*) is the most common lithology, with subordinate occurrences of olivine-gabbro, leucogabbro and melanogabbro. The two dominant textures are 'foliated gabbro', which has a prominent magmatic lineation (sometimes accompanied by a foliation), and coarse, isotropic 'spotty' gabbro, which contains centimetre-sized spots formed

by clinopyroxene oikocrysts (more details in the petrography section). The two types of gabbro can occur side-by-side in the same outcrop, with gradational contacts rather than clear crosscutting boundaries (Figure 5.6b). The fabric in the gabbro is never pervasive, but forms vague traces within outcrops, generally with a consistent orientation. Due to the structural complexities, it is however difficult to assess whether variations between the studied sections are primary or due to later faulting. There are rare occurrences of discontinuous, 'wispy' layering in the gabbro, where modal variations in plagioclase and clinopyroxene result in alternating centimetre-thick layers of leucogabbro and melanogabbro. Occasional bodies of ultramafic rock occur in the upper gabbros in the sections at Ra's al Ya and Wadi Madi (Figure 5.6a). They form elongate or irregular bodies up to tens of metres in size and consist of plagioclase-dunites and plagioclase-wehrlites with similar textures to those at the base of the crust. The contacts of these ultramafic bodies are often gradational over centimetres to metres. Some plagioclase-dunites, plagioclase-wehlites and olivine gabbros occur in the upper gabbros as partially disaggregated bodies or mafic schlieren in the gabbroic host.

Near the top of the Ra's al Ya section, and throughout the sections at Sur Masirah, Wadi Madi, Wadi Jibuti and Urf, the gabbros are intruded by variable proportions of basaltic and doleritic dykes (Figure 5.6c). Magmatic fabrics in the gabbroic screens are often sub-parallel or slightly oblique to the trends of the crosscutting dykes (Figure 5.6d). Isotropic, varitextured gabbros and pegmatites occur commonly, sometimes bearing hornblende and Fe-Ti oxides, scattered throughout the upper levels of the lower crust as isolated intrusive pods and crosscutting veins, or as segregations that grade into spotty or weakly foliated gabbro (Figure 5.6e). Their lithology is similar to the varitextured

Figure 5.6 (next page): *(a) Section of upper gabbros with sporadic occurrences of ultramafic bodies in the section at Ra's al Ya (mountains approximately 150 m high). (b) Foliated gabbro grades into spotty gabbro over less than a centimetre distance (Sur Masirah area, pen for scale aligned with foliation). (c) Dyke swarm crosscutting the upper gabbros in the gradual gabbro-dyke transition at Wadi Madi. (d) Two dykes and a screen of foliated gabbro in the gabbro-dyke transition at Wadi Jibuti. Dykes are intruded subparallel to the foliation in the gabbros (indicated with the dashed line, lens cap for scale). (e) A pod of varitextured gabbro segregating from the upper foliated gabbros at Wadi Jibuti. (f) Pods of differentiated rocks in the upper foliated gabbros at Sur Masirah (hammer for scale). (g) Outcrop of porphyritic gabbro at Sur Masirah, with plagioclase megacrysts within a fine-grained matrix that locally grades into patches of varitextured gabbro (lens cap for scale). (h) Sheeted dykes with 100% dyke-in-dyke intrusion (north of Haql). (i) Pillow lavas interbedded with sediments of the Maghilah Unit at the top of the section in Wadi Haql (hammer for scale). UM = ultramafic body; VTG = varitextured gabbro; PL = pillow lava; MU = sediments of the Maghilah Unit.*

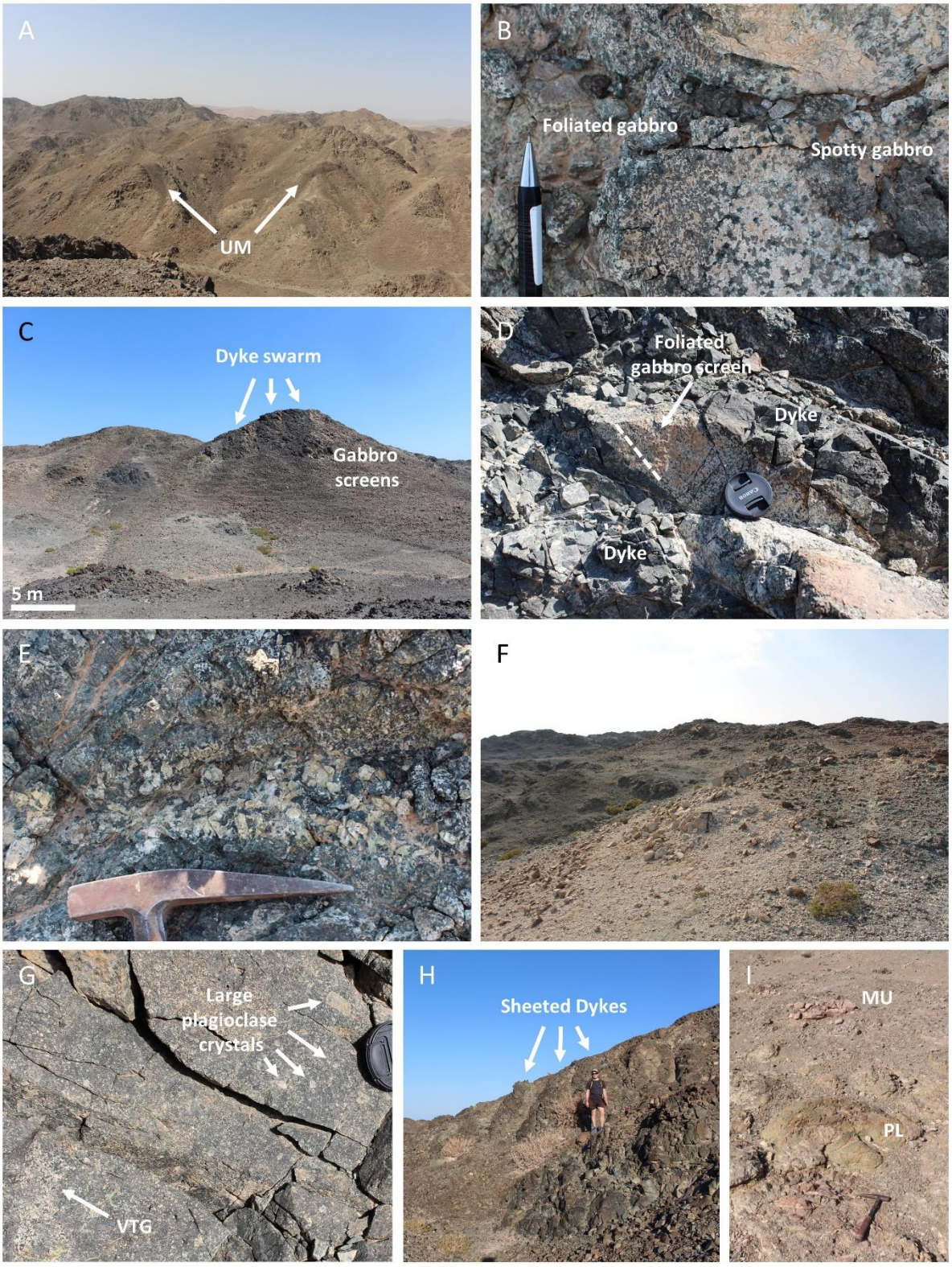

unit described in the Semail ophiolite (Oman) by MacLeod and Yaouancq (2000), from which the term 'varitextured' was borrowed, but in contrast to the Semail Ophiolite, on Masirah they don't constitute a continuous layer at a consistent pseudo-stratigraphic level. Instead, their occurrence is irregular, although they are especially prevalent in the Sur Masirah section. At Sur Masirah, and to a

lesser extent at Wadi Madi and Urf, small volumes of differentiated rocks, such as diorites, tonalities and trondhjemites, occur as centimetre to metre-scale intrusive dykes and pods, as well as veins segregating from their host gabbro (Figure 5.6f). These felsic dykes and veins are generally oriented subparallel to the regional trend of the dyke complex and they often have mutual crosscutting relationship with the gabbroic crust and dyke swarms. At Sur Masirah and Wadi Madi, there are rare, metre-sized outcrops of porphyritic gabbro and dolerite that texturally resemble the cores of porphyritic dolerite dykes of the dyke complex, but do not display chilled margins (figure 5.6g). Centimetre-sized plagioclase crystals sit in a finer-grained groundmass that locally grades into coarser patches and varitextured gabbro (detailed petrographic description in section 5.2.6). The outcrops are crosscut by the dyke swarms and rare basaltic xenoliths indicate that these lithologies themselves are also intrusive.

5.2.4 Sheeted dyke complex

5.2.4.1 Sheeted dykes and dyke swarms in crust

The total vertical extent of the sheeted dyke complex was previously estimated to be ~1 km (e.g., Marquer et al., 1998). There is no well-defined boundary between the upper gabbros of the lower crust and the sheeted dykes of the upper crust: rather, a gradual gabbro-dyke transition, is observed, where dykes become more abundant upwards. A considerable part of the "sheeted dyke complex" on Masirah therefore consists of subparallel dyke swarms with gabbroic screens, with dyke-proportions varying from 0% to 100% over several hundred metres up-section (Figure 5.6c). This contrasts with the abrupt gabbro-dyke transition at the fast-spreading Semail ophiolite (where it takes place over tens of metres, e.g., MacLeod and Rothery, 1992), and is more similar to the dyke-complexes of slower spreading ophiolites such as Troodos in Cyprus (where the transition can be hundreds of metres, e.g., Moores and Vine, 1971) and the Lizard in the United Kingdom (where dyke swarms with gabbroic screens are dominant, e.g., Kirby, 1979). The main exposure of the sheeted dyke complex occurs in the southern part of the island, where it was studied in the sections at Wadi Jibuti, Wadi Madi, Urf and north of Haql (all Lower Nappe, with 100% dykes exposed at Haql). Additional observations were made at the top of the section at Ra's al Ya, at Sur Masirah (both Upper Nappe), and west of Jabal Suwayr (considered Lower Nappe).

From field observation the predominant relationship by far is that of dykes intruding the upper gabbros, with chilled margins that are either basaltic or fine-gained doleritic, or cross-cutting dykes that are wholly-chilled. Dykes are generally 80 – 150 cm wide, although dykes of a few centimetres to several metres also occur, and range from aphyric to ultraphyric, with plagioclase (up to 50%, 0.1 – 3 cm) and to a lesser extent pyroxene phenocrysts and glomerocrysts. In rare instances in the Sur Masirah section, varitextured gabbro and differentiated rocks can be observed crosscutting or

stoping dykes. The proportion of dykes is variable and, because abundant faults disrupt sections, it is difficult to determine whether dyke abundance increases up-stratigraphy or also varies laterally. Nevertheless, a 'true' sheeted dyke complex, with 100% dyke-in-dyke intrusions, is always developed where the dykes are overlain by lava units (at Wadi Haql, Sur Masirah and West of Jabal Suwayr; Figure 5.6h). Furthermore, despite disruption by faults, dyke trends are generally consistent within single studied transects and regions of several km^2 to tens of km^2, suggesting the bulk of tectonic deformation resulted in rotation of km-sized blocks with a large degree of internal coherence preserved. Within coherent outcrops, dykes are orientated subparallel, although most sections contain a small number of anomalously oriented dykes, which tend to be late and have an alkaline affinity (see Chapter 4).

The most complete gabbro-dyke transition was studied in the Wadi Jibuti section, where a mainly ENE-WSW trending dyke swarm intrudes the upper gabbros and dyke proportions increase towards the southeast over a geographic area of ~1.5 km from 20% to 80% of the outcrop. The presence of several faults with unknown kinematics and displacement complicates a reliable estimate of the vertical thickness of this transition. Steeply dipping dykes in a ~1 km^2 area at Urf trend NE-SW and make up ~10% of the outcrop, whereas at Wadi Madi they mainly trend E-W to NE-SW, making up ~25% – 40% of the outcrop over a ~1 km^2 area. The top ~200 m of the lower crustal section at Ra's al Ya is intruded by dykes that mainly trend E-W and make up roughly 10% of the outcrop. Due to the presence of several faults in the section, the total thickness of the Ra's al Ya cannot be reliably estimated and the primary relationship between the orientation of dykes near the top and the layering of the gabbros near the base of the section has been disrupted. At Sur Masirah, most dykes have moderate to steep dips and trend N-S (variable from NE-SW to WNW-ESE) and proportions vary from ~10% – 100% in a ~1 km^2 area. Further to the south, in Wadi Muhasi, scattered outcrops of pillow lavas occur in a 500 m area of sub-parallel dyke-in-dyke intrusions, although the contact between the two units is not clearly exposed. Sections with 100% dykes were studied north of Haql (trending NE-SW and stepply dipping, over a ~1 km^2 area) and west of Jabal Suwayr (trending NE-SW, over a 400 m area) as well. Gabbroic xenoliths (centimetre-sized) are common in the dyke swarms cutting the upper gabbros, but were also encountered in rare dykes in the sheeted dykes north of Haql.

5.2.4.2 Dykes swarms in mantle

Mantle type 3, the dyke-intruded mantle, has a relatively small aerial extent on Masirah compared to the sheeted dykes and dyke-intruded upper gabbros (< ~1% of the island; < ~10% of the mantle exposures). These dyke swarms were studied in two sections, a 1 km transect east of Jabal Suwayr and a 300 m transect at Wadi Firaj (see also Chapter 4). Despite the low abundance of exposure

(~10%) and intense brecciation, dykes are observed intruding the mantle as well as gabbroic plutons and display clear chilled margins (Figure 5.4e). They are similar in appearance to crustal dykes, with thicknesses of 0.1 – 2.5 m and are commonly porphyritic (often with plagioclase crystals and less often with pyroxene and olivine). The harzburgite screens are metres to tens of metres thick and make up most of the outcrops. Peridotite xenoliths in dykes were not observed. Due to poor outcrop quality most dyke trends could only be roughly estimated, but limited measurements show that they are highly variable (trends ranging from E-W, ESE-WNW, NE-SW to N-S at Jabal Suwayr and from E-W, NE-SW to NW-SE at Wadi Firaj), although at Jabal Suwayr dyke orientations are relatively consistent over small distances (<100 metres).

5.2.5 Lavas

The main lava exposures on Masirah overlie the sheeted dyke complex and were previously estimated to be ~500 m thick (Marquer et al., 1998), although small volumes of lava also occur in the seamount structures at Shi'inzi (Figure 5.2), out-of-sequence or interbedded with sediments (see Chapter 4). Similar to the dykes, lavas tend to be porphyritic with olivine (0 – 20%, 0.5 – 2 mm) and plagioclase (0 – 20%, 0.5 – 4 mm) crystals, although in general crystal sizes are smaller than those in the dykes, which are often centimetre-sized. The dyke-lava transition was studied in the sections at Wadi Haql, Wadi Muhasi and west of Jabal Suwayr, where it is poorly exposed and occurs over tens of metres.

A full section of lava stratigraphy is exposed over several km^2 in Wadi Haql, from the sheeted dykes in the southeast to the overlying sediments of the Maghilah Unit in the northwest (Figure 5.6i). At the dyke-lava boundary, which may represent a fault, many outcrops of dolerite lack either clear chilled margins or clear lava morphologies ('massive dolerites'). Overlying lavas occur either as stacks of pillow lavas or as sheet flows, and at the top of the sequence they are intercalated with deep-marine sediments. Accurate paleo-horizontal and paleo-vertical markers within the lava succession are rare, complicating estimates for the thickness of the unit. The lateral extent of the lavas between the dykes and the sediments varies between 0.8 and 2.2 km, and the overlying sediments dip ~40 – 60° NW, whereas the lavas overlying the near-vertical sheeted dykes towards the southeast are sub-horizontal, as estimated from 'pillow-lava tails'. Assuming the Wadi Haql lavas dip 25° to the northwest on average, and disregarding potential disruptions by faults, the lavas exposed at Wadi Haql are estimated to be roughly 300 - 900 m thick.

5.2.6 Petrography of lower crust and dykes

A systematic petrography of the sampled lower crust and dykes is reported in Table II. Gabbros and olivine gabbros from the base of the lower crust (layered gabbros, Figure 5.7a) have plagioclase

crystals that tend to have a stubby to tabular aspect ratio and have grainsizes that are 2 – 3 mm on average, although outcrops with coarser (10 mm) lithologies occur as well. Olivine occurs as anhedral oval-shaped clusters and elongate trains parallel to the magmatic foliation and are subdivided into subgrains. Clinopyroxene is granular to poikilitic, indicating crystallisation after plagioclase, consistent with dry, low-pressure magmatic differentiation typical of mid-ocean ridges. The rocks generally have moderately to well equilibrated grain boundaries, expressed by ~120° angles at triple grain boundaries. Crystal shape alignment of plagioclase and clinopyroxene form a moderate to well defined magmatic foliation and lineation in most samples. The dunites, troctolites, plagioclase dunites and plagioclase wehrlites (ultramafic suite) contain round olivine grains (2 – 5 mm) and euhedral to subhedral Cr-spinel enclosed in centimetre-sized clinopyroxene oikocrysts and/or interstitial amoeboid plagioclase, and lack a magmatic fabric (Figure 5.7b).

The upper gabbros consist of plagioclase and clinopyroxene, and generally lack olivine. The crystal-shape defined magmatic fabric in the upper gabbros is variable, ranging from well developed to absent, but generally less prominent compared to the layered gabbros. The strength of the magmatic fabric arises from the variable occurrence of granular and oikocryst clinopyroxene and roughly corresponds to the foliated and isotropic spotty gabbros identified in the field and, but detailed observations show that there is a spectrum between the prominence of a foliation and the presence of clinopyroxene oikocrysts (Figure 5.7c-e). In some rocks the poikilitic textures of clinopyroxene are due to late crystallisation, whereas other samples show clear resorption textures in plagioclase chadacrysts enclosed by large clinopyroxene oikocrysts (Figure 5.7e). Olivine sporadically occurs as a minor phase (1 – 10 modal %), both as anhedral oval-shaped grains as well

Figure 5.7 (next page): *Microphotographs illustrating the petrographic relations of the Masirah axial lower crustal sequence (cross-polarised light, XPL). (a) Olivine gabbro from the layered gabbros in the axial lower crustal sequence with a granular texture and strong magmatic foliation defined by the preferred crystal shape alignment of plagioclase and clinopyroxene (Sample 18MM245, Western ridge of Jabal Taymah). (b) Plagioclase dunite from the ultramafic suite at the base of the lower crust with rounded olivine enclosed by clinopyroxene oikocrysts and interstitial plagioclase (Sample 18MM253, Western ridge of Jabal Taymah). (c) Moderately foliated gabbro from the upper gabbros (Sample 18MM099, Ra's al Ya). (d) Strongly foliated and lineated gabbro from the upper gabbros (Sample 18MM165, Sur Masirah). (e) Spotty gabbro with large clinopyroxene oikocrysts enclosing elongated and resorbed plagioclase crystals and no magmatic foliation (Sample 18MM196, Ra's al Ya). (f) Varitextured gabbro with highly heterogeneous grainsizes (Sample 18MM158, Sur Masirah). (g) Porphyritic gabbro with plagioclase megacrysts within a fine-grained matrix (Sample 18MM161, Sur Masirah). (h) Plagioclase ultraphyric dyke with abundant plagioclase and some clinopyroxene crystals and glomerocrysts (Sample 18MM262, west of Jabal Suwayr). Pl = plagioclase; Cpx = clinopyroxene; Ol = olivine; Hbl = hornblende; Ox = Fe/Ti oxides; alt = altered.*


A
Pl
Cpx
Ol (alt)
2 mm
B
Pl
Cpx
Ol
2 mm
C
Pl
Cpx
2 mm
D
Cpx
Pl
2 mm
E
Cpx
Pl
Ol (alt)
2 mm
F
Cpx (alt)
Pl
5 mm
G
Ox
Pl
Hbl
Cpx (alt)
2 mm
H
Pl
Cpx
2 mm

as an interstitial phase around plagioclase and clinopyroxene indicating late crystallisation (Figure 5.7e). Plagioclase crystals commonly display optical zoning and their grain boundaries are generally less well equilibrated than in the layered gabbros, especially in the more poikilitic samples. Although grainsizes are variable, on average the upper gabbros are slightly finer grained (1 - 3 mm) and plagioclase laths are more elongate compared to the tabular grains in the layered gabbros. Minor crystal plastic deformation is present in the form of undulose extinction and tapered plagioclase twins. Fe-Ti oxides, hornblende, apatite, and titanite occur as minor, predominantly interstitial phases, although they are not ubiquitous in these rocks. The ultramafic bodies in the upper gabbros consist of dunites and olivine-rich gabbros and troctolites, and are texturally similar to the ultramafic suite in the base of the lower crust: rounded olivine with interstitial and poikilitic plagioclase and clinopyroxenes.

Varitextured gabbros and porphyritic gabbros have heterogeneous grainsizes (0.5 – 20 mm in thin-section, up to centimetre-sized crystals in outcrop; Figure 5.7f) and often contain brown hornblende and Fe-Ti oxides as a minor phase, as well as accessory titanite, apatite and zircon. Some samples are granular with subhedral grains, whereas others have better developed poikilitic textures, with plagioclase enclosed by clinopyroxene and/or hornblende. The term porphyritic gabbro is here used to describe heterogeneous, fine to medium grained, ophitic to subophitic gabbros with cm-scale plagioclase megacrysts (Figure 5.7g). The megacrysts are subhedral to euhedral with an equant to stubby habit and have thin overgrowths on the rims that are intergrown with adjacent grains of the groundmass. Felsic segregations and crosscutting veins in the upper gabbros are typically more fine-grained (~1 mm) than their hosts and more plagioclase rich (leucocratic gabbros). Quartz is absent in all of the studied evolved lithologies.

Dykes are often porphyritic and crystal content ranges from single crystals to glomerocrysts (Figure 5.7h). Plagioclase is the most common phase and forms euhedral to subhedral stubby to equant crystals up to 2 cm, although some glomerocrysts also contain clinopyroxene. Dykes with coarser, doleritic cores have textures that resemble the porphyritic gabbros, with stubby to equant euhedral and subhedral plagioclase megacrysts, as well as anhedral clinopyroxene, with small overgrowth rims that are intergrown with the crystals of the matrix. The matrix typically consists of elongate plagioclase laths enclosed by ophitic clinopyroxene and hornblende, accompanied by minor oxides and titanite.

5.3 The lithospheric architecture of the Masirah Ophiolite: 'Penrose on a diet'

The following subsections synthesise the field and petrographic observations and demonstrate that the oceanic lithosphere at Masirah has an architecture that departs significantly from the existing models. This new type of architecture is referred to here as 'Penrose on a diet' (Figure 5.8).

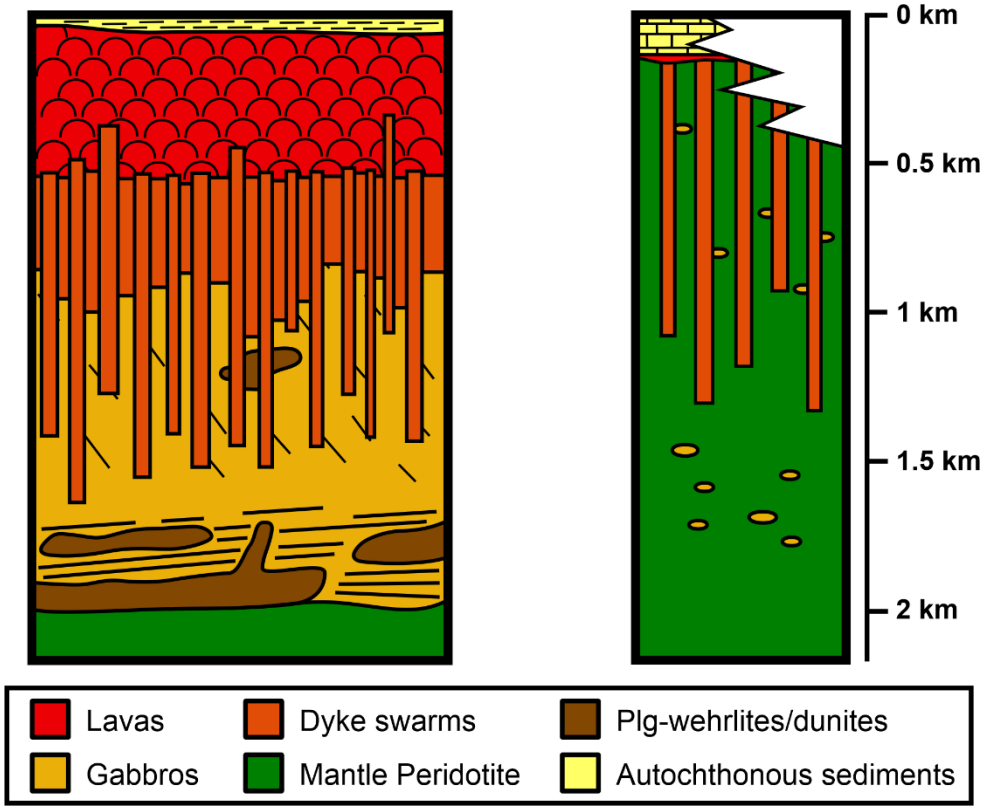

Figure 5.8: *Reconstruction of the crustal architecture at Masirah. See text for discussion.*

5.3.1 The igneous crust is remarkably thin

Compared to the conventionally assumed ~6.5 km thickness of 'typical' igneous oceanic crust (e.g., White et al., 1992), the maximum reconstructed crustal thickness of ~2.0 km at Masirah is very thin (Marquer et al., 1998). This reduced thickness is mainly the result of a thin lower crust, as expressed in the sections at Jabal Taymah and Ra's al Ya, where the layered gabbros do not exceed a thickness of ~200 m, compared to an average equivalent of ~2.3 km in the Semail Ophiolite (Lippard, 1986). The thickness of the overlying foliated and isotropic gabbros is more difficult to estimate due to a lack of reliable paleo-horizontal or vertical markers and emplacement related disruptions to the sections. The presence of dyke swarms near the top of the Ra's al Ya section, and throughout most of the sections at Sur Masirah, Wadi Jibuti, Wadi Madi and Urf, however, are consistent with a thickness of no more than several hundred metres, as was suggested based on the structural reconstruction of Marquer et al. (1998). It should be noted that in their reconstruction, Marquer et al. (1998) consider the volumetrically significant dyke swarms with gabbroic screens (the gabbro-

dyke transition, marking the transition between the lower and upper crust) to be part of the upper crustal sheeted dyke complex. Consequently, when the lower crustal thickness is defined as the total (maximum) thickness of the plutonic suite, a thickness of ~750 – 1000 m is more accurate than the ~500 m determined by Marquer et al. (1998). Similarly, sections at Wadi Haql, Sur Masirah and West of Jabal Suwayr show that the 'true' sheeted dyke complex is estimated to be ~500 m thick at most, compared to a ~1 km thickness of the complete 'dyke complex' (Marquer et al., 1998). The thickness estimates of the lava section at Wadi Haql (~300 – 900 m) are consistent with the ~500 m determined by Marquer et al. (1998).

Furthermore, field evidence for melts stalling in the mantle is lacking (at least to the extent that the mantle is exposed on Masirah). Plagioclase peridotites, commonly interpreted as melt-impregnated mantle (e.g., Dick, 1989), are rare and were only found in type 2 and 3 mantle, i.e., without a preserved overlying igneous crust. Additionally, the greatest proportion of gabbroic intrusions present in the type 2 and 3 mantle sections at Masirah were shown to be of an alkaline nature, associated with the near off-axis continuation of magmatism (see Chapter 4).

5.3.2 The presence of a pseudo-stratigraphy and a sheeted dyke complex indicates spreading was accommodated magmatically

Whenever primary contacts between units are intact, they conform to a general layered structure of a mafic-ultramafic base of the lower crust, overlain by layered gabbros, foliated and isotropic gabbros, dyke swarms, sheeted dykes and lavas. The consistency of these primary relationships in the studied crustal sections suggest that, despite the igneous crust being very thin, for the most part a 'classic' pseudo-stratigraphy is present in the sections at Masirah.

The main structural features in this sequence are magmatic. The main fabrics in the gabbroic lower crust are magmatic foliations and lineations. These fabrics arise from crystal alignment during magmatic flow through a critical temperature interval (e.g., Nicolas et al., 1988b) and are common in the layered gabbros and occur sporadically in the upper foliated and isotropic gabbros. The upper crust is dominated by brittle magmatic extension in the form of a sheeted dyke complex (i.e., 100% dyke-in-dyke intrusion), strongly suggestive of magmatic spreading (e.g., Gass, 1968; Cann, 1970). The boundary between the lower and upper crust is a gradual transition from gabbro to dykes where the proportions of dykes increase, and gabbroic screens decrease, upwards, indicating a primary relationship between the two units, rather than tectonic juxtaposition. The formation of a sheeted dyke complex is generally thought to require a narrow (~50 m) zone of dyke intrusion, resulting in abrupt gabbro-dyke and dyke-lava transitions (e.g., Kidd, 1977). Although the dyke-lava transition, albeit poorly exposed, is abrupt (see also Peters, 2000; Abbotts, 1979b), the gabbro-dyke transition

is more gradual and no continuous horizon of isotropic varitextured gabbros is present (e.g., MacLeod and Yaouancq, 2000). This could be the result of 'dyke penetration zones' formed due to laterally discontinuous melt lenses (e.g., Rothery, 1983; MacLeod and Rothery, 1992) and a significant component of along-axis dyke propagation (e.g., Dziak et al., 1995), and/or the vertical migration of the top of the crystal mush (and hence the zone of dyke intrusion) caused by the waxing and waning of melt supply (e.g., Hooft et al., 1997). Both hypotheses are consistent with the sporadic occurrence of varitextured gabbros throughout the upper gabbro unit.

5.3.3 There is no evidence for a major role for tectonic spreading in the igneous crust

Although faulting is known to play a significant role during seafloor spreading at slow-spreading ridges (e.g., Buck et al., 2005), several observations argue that tectonism at Masirah was not the dominant spreading mechanism during the accretion of the main igneous sequence:

- Previous studies have described the intensive degree of faulting throughout the ophiolite and demonstrated the axial origin of some of these faults, evidenced by their hydrothermal mineralogy as well as some faults being crosscut by late dykes (Peters, 2000). Although numerous, the displacement along these faults that can be attributed to on-axis kinematics appear to have been relatively minor relative to the thickness of the ophiolitic units, with larger displacements resulting from reactivation of faults during emplacement (Peters, 2000). In the studied sections through the igneous crust, a sheeted dyke complex consistently separates the lava unit from the lower crustal plutonic sequence. As noted by Peters and Mercolli (1998), as well as this study, both the harzburgite to layered gabbro boundary and gabbro to sheeted dyke transition appear to be intact and not disrupted by detachment faults.
- Tectonic spreading accommodated by rotational normal faults (as in the Lizard Ophiolite, United Kingdom, e.g., Roberts et al., 1993) or low-angle detachment faults (as in oceanic core complexes e.g., MacLeod et al., 2011) results in syn-magmatic rotations in the footwall along a ridge-parallel axis. The effect of such on-axis rotations is that originally vertical dykes are rotated to shallower dips while being intruded by new, vertical dykes, resulting in variable dyke dips. Instead, insofar primary relationships can be reconstructed, the dykes on Masirah are sub-parallel (both in outcrop as well as regionally, Abbotts, 1979b, Peters et al., 1995), and perpendicular to the axial lavas (e.g., at Haql), suggesting that rotation taking place during on-axis magmatic accretion was minor. Occasional occurrences of late crosscutting dykes with anomalous orientations are exclusively alkaline and indicate more significant tectonic-related rotations took place near off-axis, but largely post-date the main crustal accretion.

- Tectonic thinning of the oceanic lower crust is typically accommodated along high-temperature ductile shear zones with sub-solidus strain indicators such as porphyroclasts, deformed and stretched crystals with tapered tails and grain size reduction in mylonites, as observed in slow-spreading oceanic crust (at Atlantis Bank, Southwest Indian Ridge, e.g., Mehl and Hirth, 2008; Atlantis Massif, Mid-Atlantic Ridge, e.g., Schroeder and John, 2004; Kane area, Mid-Atlantic Ridge, e.g., Hansen et al., 2013) and in ophiolites (e.g., the Lizard, UK, Gibbons and Thompson, 1991; the Ligurian ophiolites, Italy, e.g., Molli, 1995). Observations from Masirah do not show consistent and recurring evidence for shear zones and crystal plastic deformation that could be related to large scale on-axis deformation, arguing against tectonic thinning of the lower crust. The near off-axis alkaline plutons do record such features, suggesting syn-magmatic extensional deformation during their emplacement (Marquer et al., 1998).
- A main tectonic feature on Masirah is the 'Main Masirah Thrust' fault, which juxtaposes the two Masirah Nappes that have a ~5 Ma age difference (Peters et al., 1995; Marquer et al., 1995; Chapter 4). The sub-horizontal top-to-south stretching lineations and zeolite facies mineralogy of this sub-horizontal thrust fault records low P-T conditions and was previously interpreted to be a late structure (Latest Cretaceous – Palaeocene) related to ophiolite emplacement (Marquer et al., 1995). It could be argued, however, that the thrust represents a low temperature overprint acquired during the re-activation and inversion of a major detachment fault that initially formed at higher P-T conditions on-axis. The inversion of extensional oceanic detachment faults as thrust faults during compression has previously been proposed by Maffione et al. (2015) and with strain localised along the weak extensional fault, the hanging wall and footwall blocks would not necessarily record any pervasive internal deformation. Whereas this hypothesis remains to be investigated, it is noteworthy that the deformation associated with the Main Masirah Thrust is limited to the harzburgite mantle of the Upper Nappe (hanging wall) and sediments of the Lower Nappe (foot wall) and is not observed cutting through the igneous pseudo-stratigraphy (Marquer et al., 1995). As such, regardless of a hypothetical on-axis origin of this feature, it did not dismember the igneous crust or exhume the gabbro and harzburgite units present on Masirah, as is characteristic of tectonic spreading.

5.3.4 Exceptions to the Penrose on a diet architecture

The mantle sections with abundant gabbroic intrusions and dolerite dyke swarms (mantle type 2 and 3 respectively) do not cover a large areal extent on Masirah compared to mantle type 1 and the igneous crustal sequence, but their occurrences contrast with respect to the 'Penrose on a diet'

lithosphere described above. Their relationship with the rest of the ophiolite is difficult to reconstruct, as primary relationships with the igneous crust have been disrupted. Magmatism is recorded by gabbroic intrusions (mainly near off-axis varitextured alkaline gabbros, Chapter 4), dyke intrusions (D-MORB tholeiites to alkaline basalts, Chapter 4) and (rare) plagioclase-peridotites. Dyke orientations are more chaotic than those of dykes in the igneous crust, but locally parallel sets of dykes suggest they intruded as parallel swarms, the trends of which were later tectonically disrupted on a <100 m scale. The presence of lavas and Barremian (~129.4 – 125 Ma) sediments covering the dyke-intruded mantle at Jabal Suwayr indicate that the peridotites must have been exposed at the seafloor, either on-axis or shortly afterwards. The localised and tectonically dismembered nature of these mantle exposures, as well as the absence of evidence for tectonic exhumation in the rest of the ophiolite, argue for a limited significance of this second type of lithosphere (see also discussion in section 5.6.2 below).

5.4 Mineral and bulk chemistry

To test whether the unusual architecture of the Masirah Ophiolite, particularly the thin plutonic sequence with respect to the upper crust (i.e., dykes and lavas), is consistent with the magmatic differentiation recorded in the igneous suite, this next section presents mineral chemistry data for the gabbroic lower crust as well as an estimate for the bulk crustal composition. Subsequently, the bulk crust composition is examined to see whether the estimated thicknesses of the crustal units reflect a parental MORB melt. In the discussion of the magmatic plumbing system (section 5.6.1 below) these data will be used to evaluate whether the low amounts of plutonic crystallisation observed in the field (i.e., relatively thin lower crust) are reflected in the mineral and bulk chemistry and whether the melts in equilibrium with the gabbros resemble the composition of the erupted dykes and lavas.

5.4.1 Gabbro mineral chemistry

Mineral major- and minor element compositions were determined for 64 samples of the axial lower crust at Cardiff University using a Zeiss Sigma HD Scanning Electron Microscope (A-SEM; for methods see Chapter 3; data reported in Table VI). The samples were selected to reflect the diversity of lithologies present in the studied lithostratigraphic sections, which taken together provide an overall picture of the igneous lower crust (presented previously in Chapter 4 and comprising the axial gabbros, evolved varitextured gabbros and mantle plutons with axial affinity groups). They include 8 samples from Jabal Taymah, 7 samples from the Western ridge of Jabal Taymah, 3 samples from the ridge east of Jabal Taymah, 23 samples from Ra's al Ya, 3 samples from Jabal Bhala, 5 samples from Wadi Jibuti, 8 samples from Sur Masirah, 4 samples from Wadi Madi, 1 sample from Urf and 2 samples from the sheeted dyke complex (respectively north of Haql and west of Jabal Suwayr). For

each spot analysis the crystal number and position within the crystal (core, rim and intermediate) was recorded. The number of crystals analysed for a given phase in a single thin-section varied between 1 and 30, and the amount of spot analyses within crystals varied between 1 and 35. To

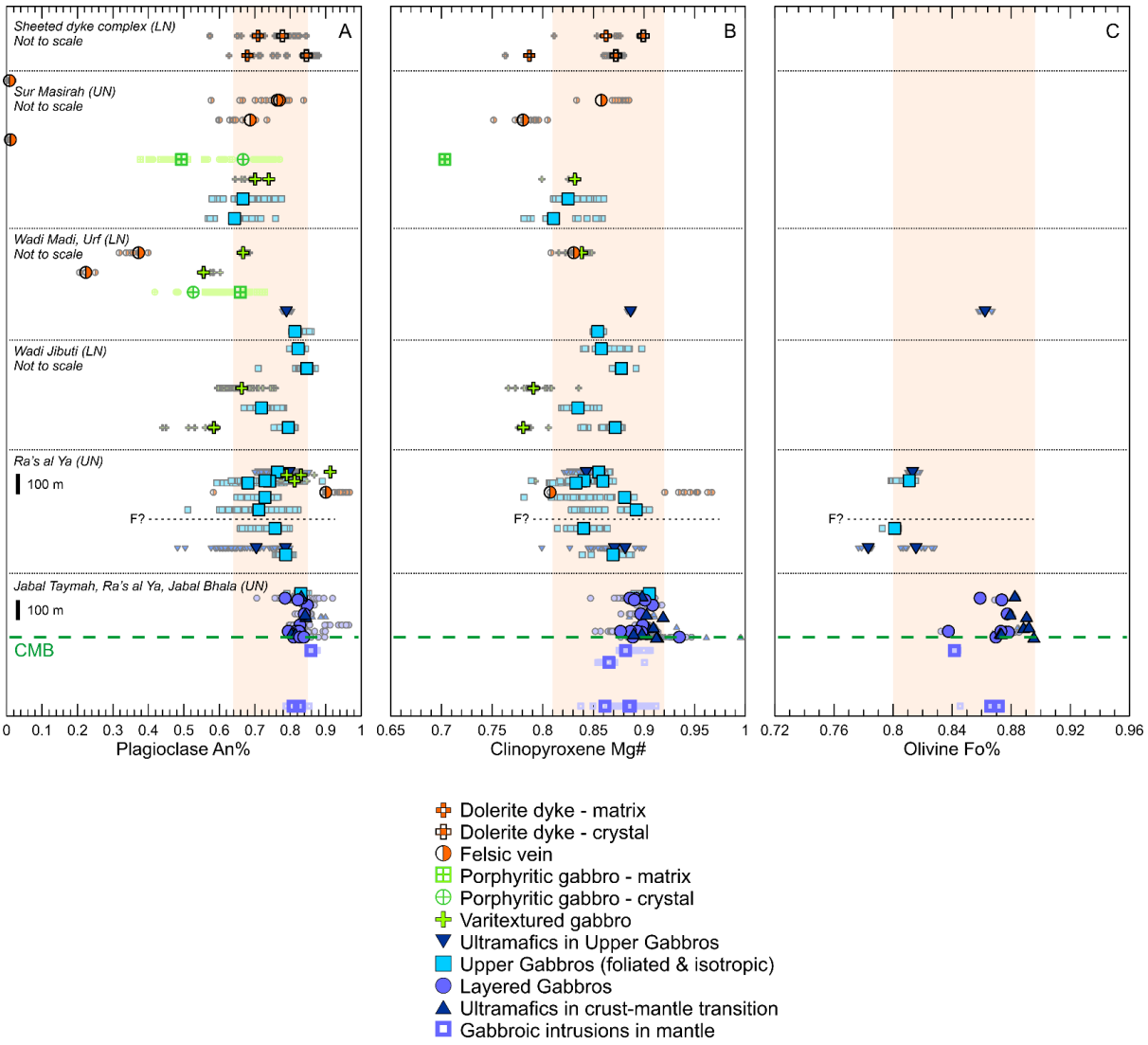

Figure 5.9: *Plagioclase (a), clinopyroxene (b) and olivine (c) mineral compositions for the various partial sections through the Masirah lower crust. The partial sections are ordered to reflect their relative stratigraphic position with respect to each other, with the mantle and crust-mantle boundary at the bottom and the sheeted dykes at the top. Vertical scale bars are included in sections where the relative stratigraphic height could be determined, whereas for other sections samples are ordered randomly at arbitrary heights. Large icons represent the average of crystal core analyses in a hand-sample, small faded icons represent individual analyses of crystal cores, intermediates and rims. The shaded boxes indicate the range in mineral core compositions found in the layered gabbros, the ultramafic suite in the crust-mantle transition and the foliated/isotropic upper gabbros (i.e., samples that represent the dominant lithologies within all combined partial sections). CMB = crust-mantle boundary, F? = Possible fault with unknown displacement, UN = Upper Nappe, LN = Lower Nappe.*

obtain a representative core (i.e., primary) or rim averages for a thin-section, first an average of all core (or rim) spot analyses was determined for each analysed crystal. All crystal-level averages for a given phase in a thin-section were then averaged to obtain an average crystal core (or rim) composition for a sample (results reported in Table VII).

Plagioclase An content (molar Ca / [Ca + Na]), clinopyroxene Mg# and olivine Fo content (both molar Mg / [Mg + Fe^{2+}], assuming all iron is Fe^{2+}) compositions for samples from each section are in relative stratigraphic order in Figure 5.9, with the large symbols representing the average core compositions per sample. A vertical scale bar is shown for the sections at Jabal Taymah and Ra's al Ya where the stratigraphic height could be reconstructed with reasonable confidence, whereas for the other sections the data are shown at arbitrary heights. The shaded areas indicate the compositional range of crystal cores in samples that are representative of the dominant lithologies in the section (i.e., the ultramafic suite and layered gabbros at the base of the lower crust, and the isotropic and foliated upper gabbros), whereas the data falling outside of that range are subordinate lithologies, such as felsic veins or varitextured segregations. Average core plagioclase An and clinopyroxene Mg# relations are broadly comparable to the primitive end of dry (magma H_2O < 0.5 wt%) fractionation trends observed in oceanic gabbros, but notably extend to more primitive compositions (Figure 5.10).

The layered gabbros and ultramafic suite from the base of the lower crust have the most primitive average mineral core compositions. The mineral compositions of the layered gabbros (An_{79-85}, average An_{82}; clinopyroxene Mg# = 0.88 – 0.91, average 0.89; Fo_{84}-Fo_{88}, average Fo_{87}) are broadly similar to those of the ultramafic rocks, although olivine is more primitive in the latter (An_{80-84}, average An_{83}; clinopyroxene Mg# = 0.89 – 0.92, average 0.90; Fo_{87}-Fo_{90}, average Fo_{89}). Mineral zoning is weak or absent (Figure 5.11a), with plagioclase showing intra-crystal An variations of 0.06 on average (maximum 0.12) in the gabbros and 0.03 (maximum 0.07) in the ultramafic rocks, and clinopyroxene showing intra-crystal Mg# variations of 0.02 on average (maximum 0.03) in both rock types. The observed zoning occurs both as normal and reversed, and less commonly in more complex forms (oscillatory or patchy).

The foliated and isotropic spotty gabbros, comprising the main lithology in the upper gabbros, have more evolved and more variable mineral compositions compared to the layered gabbros. Mineral compositions of the extensively sampled Ra's al Ya and Wadi Jibuti sections display a comparable range, and the main gabbroic lithologies from the less sampled Sur Masirah and Wadi Madi/Urf sections fall within this range. Plagioclase cores have An_{64-85} (average An_{75}) and clinopyroxene cores have Mg# of 0.81 – 0.91 (average 0.86). Rare olivine has Fo_{80}-Fo_{81}. Mineral zoning of plagioclase is

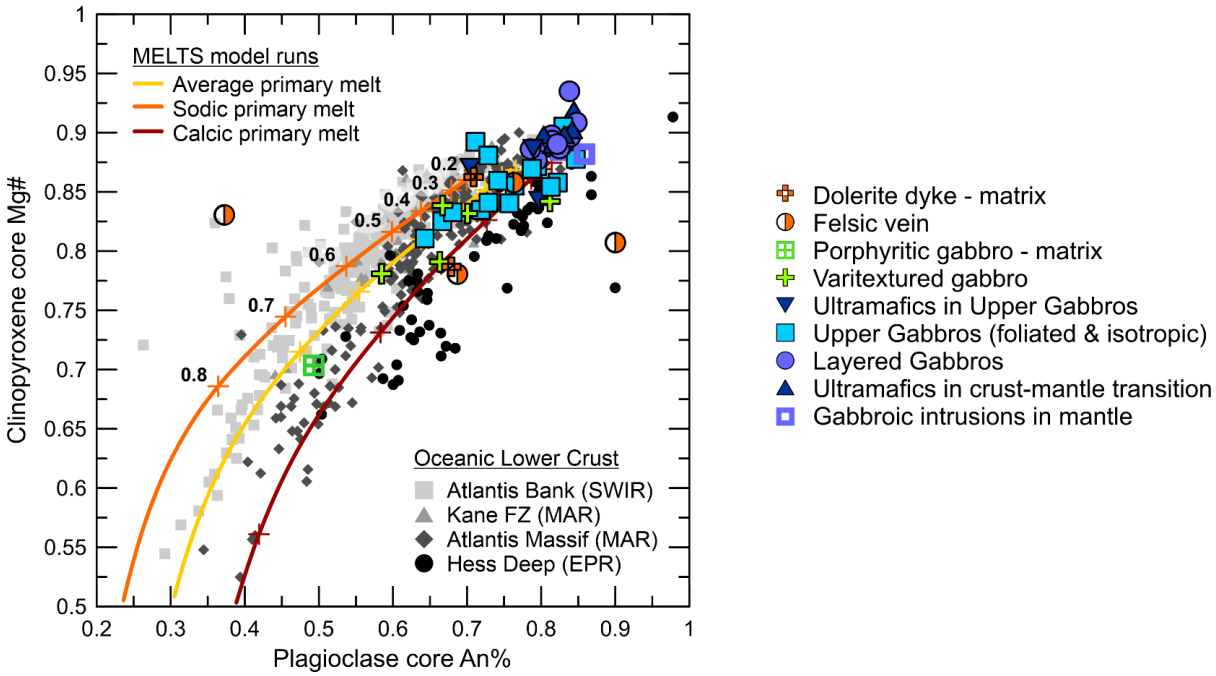

Figure 5.10: *Plagioclase anorthite and clinopyroxene Mg# relationships of the axial lower crust on Masirah. Each symbol represents the average of mineral core analyses in a hand-sample. The felsic vein that plots off the main trend at low anorthite is a segregating vein that has more evolved plagioclase compared to its host-rock, but clinopyroxene cores with similar Mg#. The high anorthite content (An_{90}) for the felsic vein plotting off the trend is likely due to alteration. The coloured lines are crystal lines of descent for primary MORBs undergoing fractional crystallisation calculated with MELTS (see discussion section 5.6.1.2 for details). Mineral compositions of oceanic gabbros from several locations shown as comparison (references in figure caption 5.19, subsection 5.6.1.2)*

more common and stronger than in the layered gabbros (intra-crystal An variations of 0.11 on average, maximum 0.25), and clinopyroxenes are zoned to a lesser extent than plagioclase (Mg# variations of 0.04 on average, maximum 0.08). Zoning in plagioclase crystals is often normal (Figure 5.11b) or oscillatory (Figure 5.11d), and less commonly patchy (Figure 5.11c) or reversed. Resorption of plagioclase is indicated in some samples by the truncation of zoning patterns (Figure 5.11b & c). Clinopyroxene zoning is commonly normal (Figure 5.11d), with rare instances of reverse or oscillatory zoning.

The ultramafic rocks within the upper gabbros typically have mineral compositions that are (slightly) more evolved than the layered gabbros but generally more primitive than the upper gabbros, often displaying strong compositional zoning. Plagioclase cores have An_{70-80} (average An_{77}) and intra-crystal variability is 0.16 on average (maximum 0.31), clinopyroxene cores have Mg# of 0.84 – 0.89 (average 0.87) with an average intra-crystal variability of 0.04 (maximum 0.10), and olivines have Fo_{78}-Fo_{86} (average Fo_{82}). Similar to the upper gabbros, mineral zoning exhibited in plagioclase is normal,

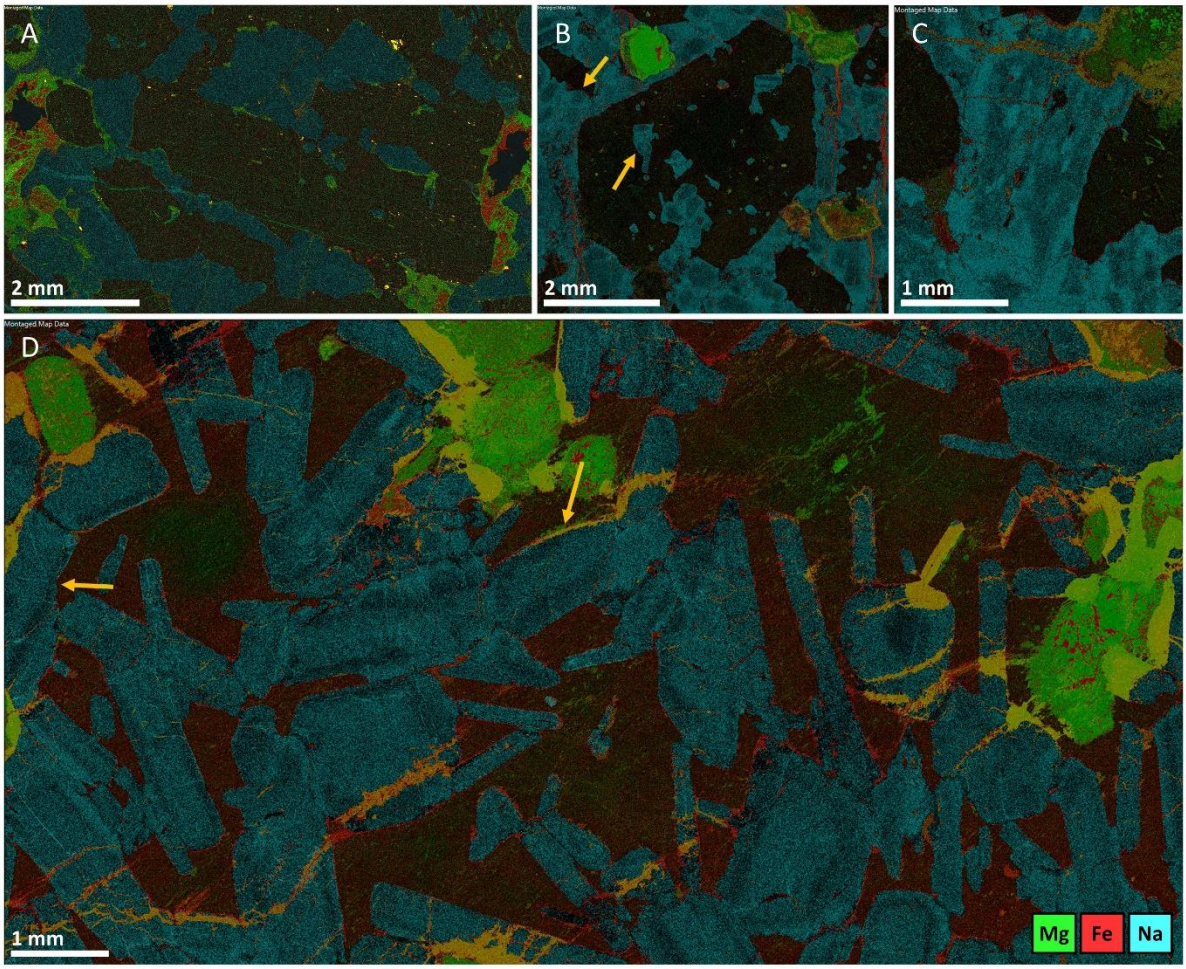

Figure 5.11: *Multi-element maps of Masirah gabbros, where plagioclase shows up in blue (Na), olivine in green (Mg) and clinopyroxene in dark-green (Mg) and red (Fe). (a) Olivine gabbro from the layered gabbros with unzoned plagioclase and clinopyroxene (Sample 18MM245, Western ridge of Jabal Taymah). (b) Spotty olivine gabbro from the upper gabbros with normally zoned plagioclase and unzoned clinopyroxene oikocrysts enclosing plagioclase chadsacrysts. Yellow arrows highlight truncation of zoning in the latter, indicating resorption (Sample 18MM197, Ra's al Ya). (c) Foliated gabbro from the upper gabbros, containing plagioclase with complex, patchy zoning (Sample 18MM193, Ra's al Ya). (d) Spotty gabbro from the upper gabbros with normally zoned clinopyroxene oikocrysts enclosing plagioclase crystals that display oscillatory zoning. Yellow arrows highlight truncation of zoning in the latter, indicating resorption (Sample 18MM196, Ra's al Ya).*

oscillatory or sometimes patchy, and in clinopyroxene zoning is most commonly normal and occasionally reverse.

Segregations, veins and pods of varitextured gabbro, porphyritic gabbro and felsic veins in the upper gabbros are variable in mineral composition and extend to more evolved compositions compared to the foliated and isotropic spotty gabbros. Primary mineral compositions were difficult to obtain from these rocks as they are more susceptible to weathering compared to other gabbroic lithologies. In

several samples no fresh clinopyroxenes were preserved, whereas plagioclase crystals showed patchy alteration-related variations in sodium content on a scale of (tens of) micrometres. To overcome these secondary effects on compositions, these plagioclase crystals were analysed by scanning a ~100x100 µm area rather than focusing the beam on a single spot. Nevertheless, an alteration control on the composition (especially analyses with high An of ~0.90) cannot be ruled out. In the varitextured gabbros, plagioclase cores have An_{56-91} (average An_{73}) and clinopyroxene cores have Mg# of 0.78 – 0.84 (average 0.82). In thin-sections with heterogeneous grainsizes, plagioclase core An is ~0.04 higher in the coarser grains compared to the finer grains. Moderate mineral zoning is present in some but not all rocks, with plagioclase showing normal, reverse and oscillatory zoning (average intra-crystal variability of An is 0.06, maximum 0.16), while zoning in clinopyroxene is either absent or normal (average intra-crystal Mg# variation of 0.03, maximum 0.07). The porphyritic gabbros have a relatively evolved matrix with plagioclase cores of An_{49-66} (average An_{58}) and rare fresh clinopyroxene cores with Mg# 0.70. The plagioclase megacrysts have distinct An compositions compared to their matrix and can be more primitive (e.g., core An of 0.61 and 0.73 compared to the average An_{49} of cores in the matrix in sample 18MM161) or more evolved (e.g., core An of 0.42 and 0.62 compared to the average An_{66} of cores in the matrix in sample 18MM340). Megacrysts are typically zoned either normally or reverse, such that their rims are of comparable composition to the matrix. Plagioclase crystals in the matrix display strong normal, oscillatory or patchy zoning (intra-crystal An variations of 0.16 on average, maximum 0.17). Felsic veins have the most evolved mineral compositions and disregarding two samples which contain pure albite (18MM033 and 18MM181, An_0) and one sample with (likely alteration-related) high An (18MM194, An_{90}), plagioclase average core compositions range An_{22}-An_{77} (average An_{56}) and clinopyroxene core Mg# ranges 0.78 – 0.86 (average 0.82). Plagioclase zoning, when it occurs, is normal or oscillatory (average intra-crystal An variation of 0.12, maximum 0.22), whereas zoning in clinopyroxene can be normal, reverse or oscillatory (Mg# variations of 0.04 on average, maximum 0.05).

The two porphyritic dykes have megacrysts and glomerocrysts with crystal cores that are more primitive than the crystals in the doleritic matrix. Dyke 18MM274 has plagioclase crystals with An_{78} cores and clinopyroxene crystals with core Mg# of 0.90, compared to matrix compositions of An_{71} and Mg# 0.86. Dyke 18MM262 contains glomerocrysts with plagioclase cores of An_{85} and clinopyroxene cores of Mg# 0.87, compared to groundmass crystals of An_{68} and Mg# of 0.79.

The contacts between the various lithologies in the upper gabbroic unit is often gradational and sometimes correlates with a change in mineral composition. The contact of a foliated gabbro and a varitextured gabbro vein (sample 18MM004, Wadi Jibuti) coincides with a change of average

plagioclase and clinopyroxene core compositions of respectively An_{79} and Mg# = 0.87 in the former to An_{58} and Mg# = 0.78 in the latter. Similarly, the contacts of felsic veins segregating from varitextured gabbros (samples 18MM323 and 18MM337 from Wadi Madi/Urf) are marked by a change in plagioclase composition from An_{56} and An_{67} in the varitextured gabbro to An_{22} and An_{37} in the felsic vein. Clinopyroxenes in sample 18MM323 do not show compositional variation across the contact (no fresh clinopyroxene was analysed in 18MM337) and a similar contact between a leucograbbroic vein and a foliated gabbro (sample 18MM163, Sur Masirah) shows no compositional change in plagioclase or clinopyroxene.

5.4.2 Bulk crust composition

5.4.2.1 Procedures and assumptions

During the magmatic accretion of an igneous oceanic crust, the aggregate melts derived from incremental polybaric batch melting (i.e., primary MORB melts) are delivered to the axial spreading ridge, where they are subsequently modified by magmatic differentiation, resulting in the formation of an upper and lower crust. According to this model, the bulk composition of the igneous crust should resemble the composition of the primary melt. This primary melt must be in equilibrium with mantle olivine and be a realistic parental melt for the dykes and lavas. Alternatively, if the process of magmatic differentiation in the crust is accompanied by lateral, along-axis melt migration in the form of lateral dyke intrusion (e.g., Staudigel et al., 1992) or melt flow in the lower crust (e.g., Magde et al., 2000), the bulk composition of a given section of crust is expected to deviate from a primary melt composition.

An estimation of the Masirah bulk crustal composition was made with a mass balance equation using whole-rock major and trace element geochemistry from MasirahDB and thickness estimates from this study and previous work (Peters et al., 1995; Marquer et al., 1998; results reported in Table XIII). The geochemical compilation MasirahDB (Table XII, see methods in Chapter 3 for details of this database) contains major and trace element whole-rock analyses for all major rock suites present on Masirah. Assuming that each suite was representatively sampled, it is possible to calculate a bulk composition estimate for each suite, as well as for the bulk crust. The Upper Nappe and Lower Nappe exposed on Masirah formed ~5 Ma apart (Chapter 4). Nevertheless, because units are not equally exposed and sampled in both Nappes, a bulk composition for Masirah as a whole was calculated, rather than a bulk composition for each individual nappe. Although the result is effectively a time-integrated bulk composition, this choice is justified by a lack of significant compositional differences between rocks from the Upper and Lower Nappes (i.e., within-nappe variations exceed between-nappe variations). Data was compiled for each rock unit by filtering MasirahDB according to the assigned rock suites, leaving out any sample with an unknown or

Table 5.1. Overview of samples used per rock unit for determining Masirah bulk crust composition

Rock Unit	MasirahDB Filters			Additional Data[1]	# samples
	Main Group	Sub Group	Assigned suite		
Mantle	Mantle	Mantle	Mantle	N/A	17
Layered Gabbro	Pluton	Axial Lower Crust	Axial Lower lower-crust gabbro	N/A	33
Ultramafic suite	Pluton	Axial Lower Crust	Axial Lower lower-crust ultramafic	N/A	14
Foliated / Isotropic Gabbro	Pluton	Axial Lower Crust	Axial Upper lower-crust gabbro	N/A	19
Varitextured Gabbro	-	-	-	2 samples	2
Felsics	Pluton	Axial Lower Crust	Axial Upper lower-crust plagiogranite	3 samples	4
Axial Dykes	Dyke	Axial sequence Dyke	Axial Dyke – Sheeted dykes & Axial Dyke – Gabbroic screens & Axial Dyke	13 samples	120
Late & Mantle Dykes	Dyke	Late Dyke & Mantle dyke	Late Dyke & Mantle dyke	16 samples	73
Axial Lavas	Lava	Axial Lava sequence	Axial Lava sequence	10 samples	72
Off-axis Gabbro & Dolerite	Pluton & Pluton/Dyke	Gb-Dol-Gr & Gb-Dol-Gr Dyke	Gb-Dol-Gr – Gabbro & Gb-Dol-Gr – Dolerite	N/A	47
Off-axis Granite	Pluton	Gb-Dol-Gr	Gb-Dol-Gr – Granite	N/A	26
Off-axis Lavas	Lava	Later lavas (interbedded in Maghilah sediments) & Seamount lavas & Seamount subvolcanics & Out-of-sequence (on Mantle and Kalban sediments) & Unknown	Lava – Sediment & Lava – Seamount & Dyke / subvolcanic – Seamount & Lava – Mantle/Sediment & Alkaline Lava	1 sample	64

[1] Data from this study, Chapter 4

ambiguous origin (Table 5.1). For major elements, oxide weights normalised to totals of 100% were used (i.e., anhydrous compositions). Because the chemical compositions of rocks are often not normally distributed, both the average and the median composition was calculated for major element oxides, following Coogan (2014). Since trace elements often follow a log-normal distribution in oceanic rocks, both the average and log-normal mean (LN-mean) were calculated, following Arevalo and McDonough (2010) and White and Klein (2014). In subsequent calculations the median (for major elements) and LN-mean (for trace elements) were regarded as more representative for the bulk composition than the average.

The Masirah crust was divided into five main stratigraphic units (Base of the Lower Crust, Upper Gabbro, Gabbro-Dyke Transition, Sheeted Dykes, and Lavas). For each stratigraphic unit, the volumetric contribution of each rock unit was estimated based on field observations (Table 5.2). The gabbro-dyke transition, for example, consists of gabbro intruded by variable proportions of dyke swarms ranging 0 – 100%, and was estimated to consist of 50% upper gabbro and 50% axial dykes on average. The upper gabbros themselves were further subdivided into foliated / isotropic gabbro (47.25%), varitextured gabbro (2.25%) and felsics (0.25%).

Table 5.2. Overview of the stratigraphic units used for determining Masirah bulk crust composition

Stratigraphic Unit	Bulk Masirah	
	Thickness	**Rock units (volume %)**
Base of the Lower Crust	200 m	70% Layered gabbro 30 % Ultramafic suite
Upper Gabbros	300 m	95% Foliated / isotropic gabbro 4.5% Varitextured gabbro 0.5% Felsics
Gabbro-Dyke Transition	500 m	50% Axial dykes 47.5% Foliated / isotropic gabbro 2.25% Varitextured gabbro 0.25% Felsics
Sheeted Dykes	500 m	100% Axial dykes
Lavas	500 m	100% Axial lavas
Total	**2000 m**	

Subsequently, using thickness estimates for each stratigraphic unit (Marquer et al., 1998), the volume proportion of each rock unit in the bulk crust was calculated and converted to a mass proportion using rock densities listed in Table 5.3. The bulk composition of the igneous crust, as well as the bulk composition of the cumulate lower crust (i.e., all plutonic rocks) and of the extracted melts forming the upper crust (i.e., all dykes and lavas), was calculated using a mass balance equation with the rock unit mass proportions and the bulk compositions.

The rock units on Masirah are Inherently heterogeneous, resulting in bulk compositions accompanied by large standard deviations and compositional ranges. If the unit was representatively and proportionally sampled throughout, however, each sample can be viewed as a repeat measurement of the mean (bulk) composition, where the standard error of the mean provides an estimate of the uncertainty of the determined bulk composition. For this reason, the standard error of the mean (S.E. = S.D. / SQRT[n]) was calculated per element for each rock unit and propagated through all subsequent calculations.

Table 5.3. Densities of rock units used for determining Masirah bulk crust composition

Rock Unit	Lithology	Density (kg/m^3)	Source
Axial Lavas, Off Axis Lavas	Metabasalt, basalt and spilite	2.73 x 10^3	Carlson and Raskin (1984)
Axial Dykes, Late & Mantle Dykes	Diabase and metadiabase	2.85 x 10^3	Carlson and Raskin (1984)
Layered Gabbro, Foliated / Isotropic Gabbro, Varitextured Gabbro, Off Axis Gabbro & Dolerite	Gabbro and olivine gabbro	2.95 x 10^3	Carlson and Raskin (1984)
Ultramafic suite	Dunite, olivine gabbro and troctolite	3.1 x 10^3	Estimate[1] based on Ol:Cpx:Plg proportions of 0.6 : 0.2 : 0.2
Felsics, Off Axis Granite	Felsic	2.7 x 10^3	Estimate[1] based on modal mineralogy dominated by Plg
Mantle	Peridotite	3.2 x 10^3	Estimate[1] based on modal mineralogy dominated by Ol & Opx

[1] Calculations assume mineral densities of 3.2 x 10^3 kg/m^3 (Ol & Opx/Cpx) and 2.7 x 10^3 kg/m^3 (Plg)

5.4.2.2 Bulk major elements

The estimate of the bulk Masirah crust major element composition is presented in Table 5.4 and has a Mg# (molar Mg / [Mg + Fe^{2+}], assuming a melt Fe^{3+}/Fe_{sum} = 0.12) of 0.733, in equilibrium with mantle olivine of Fo_{89}-Fo_{91} (using Fe-Mg liquid-olivine K_D = 0.3 ± 0.03; Roeder and Emslie, 1970), meeting the first requirement of a primary melt. Major elements are within ~0.2–- 2 wt% of the theoretical primary MORB melt compositions produced by polybaric incremental batch accumulative melting from Kinzler and Grove (1993) formed by 10% melting of a depleted mantle and primitive mantle source respectively (examples 3 and 6 in their paper, hereafter K&G3 and K&G6). Sodium

and potassium contents agree most closely with their estimate for a melt derived from a primitive mantle source (K&G6).

Table 5.4. Masirah bulk crust composition compared to theoretical primary MORB melt compositions

	Bulk Masirah			*K&G3*	*K&G6*
	Bulk Crust	**Lower crust**	**Upper crust**		
SiO_2	48.93	47.86	49.61	50.4	50.9
TiO_2	0.79	0.22	1.15	0.94	0.97
Al_2O_3	17.34	18.90	16.35	16.7	17.1
FeO^T	6.64	4.15	8.23	7.34	6.92
MnO	0.12	0.07	0.16	-	-
MgO	9.01	10.96	7.77	10.6	9.94
CaO	12.50	13.62	11.79	11.5	11
Na_2O	2.73	2.06	3.16	2.47	2.9
K_2O	0.24	0.10	0.32	0.07	0.31
P_2O_5	0.07	0.01	0.11	-	-
Mg#	0.733	0.843	0.657	0.745	0.744
Ca#	0.717	0.783	0.676	0.720	0.677

To test whether the bulk composition forms a likely parental melt, it is compared to the Masirah dyke and lava compositions in Mg-Harker diagrams (Figure 5.12). Despite the expected disruption of whole-rock major element compositions by the effects of alteration, the bulk estimate plots on the primitive end of major element trends. It has a slight deficit in MgO (~1.0 – 2.0 wt%), FeO^T (~1.0 wt%) and TiO_2 (~0.2 wt%), and an excess in CaO (~1.0 – 2.0 wt%), Al_2O_3 (~1.0 – 1.5 wt%) and Na_2O (~0.5 wt%) compared to the most primitive dykes and lavas. A number of effects can potentially account for these deviations. Firstly, a sampling bias may exist in MasirahDB towards more plagioclase-rich lithologies (CaO and Al_2O_3 bearing) compared to olivine-rich lithologies (MgO and FeO bearing), possibly resulting from the plagioclase-rich lithologies in the field being more resistant to weathering in general (particularly in the lower crust). Secondly, the net effect of alteration may have modified the bulk crustal composition. The observed deviations are notably the opposite for trends observed for melts that reacted with mantle peridotite along the Southwest Indian Ridge (which decreases CaO and Al_2O_3 and increases MgO through olivine dissolution; Paquet et al., 2016) or melts that reacted with primitive cumulates at Kane Megamullion (decreasing CaO and SiO_2 and increasing Al_2O_3 and MgO; Lissenberg and Dick, 2008), although it could be consistent with models that predict olivine crystallisation in the mantle during melt transport to the ridge axis (e.g., Niu, 1997).

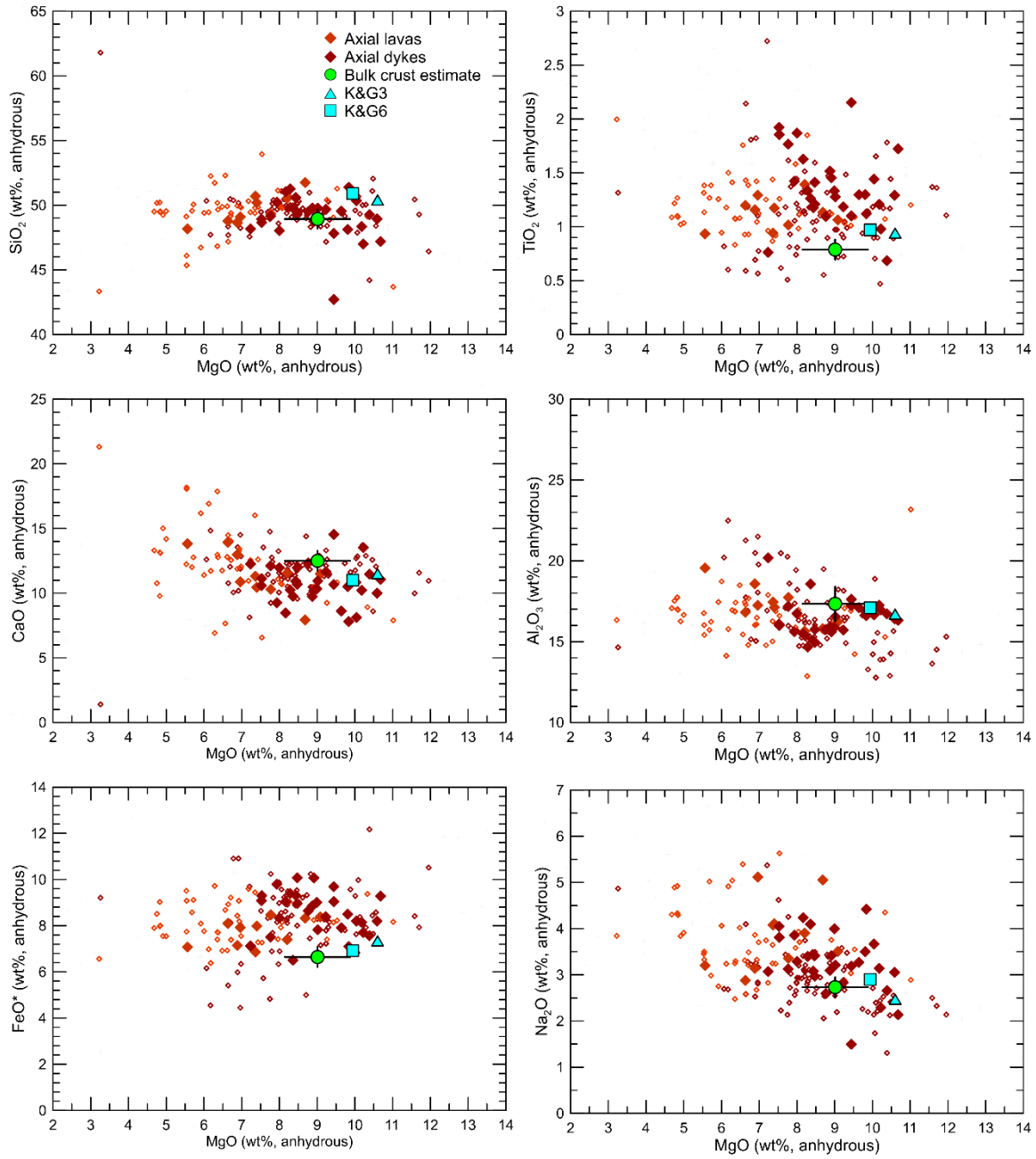

Figure 5.12: *Harker diagrams showing the Bulk crust composition in relation to dyke and lava compositions (large filled symbols represent data from this study, Chapter 4, whereas small open symbols represent data from MasirahDB). Primary melt estimates from Kinzler and Grove (1993) in cyan.*

The ultramafic suite of troctolites, dunites, plagioclase-dunites and plagioclase-wehrlites from the base of the oceanic crust has been interpreted previously as the product of mantle peridotite hybridised with MORB-like melts rather than representing pure cumulates (Suhr et al., 2008; Drouin et al., 2009, 2010). The cumulate versus mantle origin for the ultramafic suite at Masirah was not determined during this study. If, however, it is assumed that olivine in these rocks has a mantle origin and the interstitial phases (plagioclase and clinopyroxene) crystalised from a melt, the average

modal proportion of olivine in the ultramafic suite (~60%) can be used as an estimate for the mass of this hypothetical mantle component present in the igneous crust. When this mantle component (with a composition equal to the 'mantle' rock unit) is removed from the Masirah bulk estimate, the Mg# (0.719) of the new bulk estimate is still in equilibrium with (relatively fertile) mantle olivine (Fo_{88}-Fo_{90}), although this also further decreases MgO contents (by ~0.7 wt%) and further increases CaO (by ~0.2 wt%) and Al_2O_3 (by ~0.4 wt%).

5.4.2.3 Bulk trace elements

Selected trace element compositions of the bulk estimate as well as cumulate (bulk lower crust) and melt (bulk upper crust) compositions are shown in Figure 5.13. The compatible to moderately incompatible trace elements (Ni to Tb) of the bulk Masirah crust estimates are broadly similar to the bulk oceanic crust of White and Klein (2014; W&K14), but elements with greater incompatibility (i.e., Eu to Rb) are more enriched in the estimates for Masirah, consistent with the N-MORB to E-MORB character of the parental melts (Chapter 4). Positive Sr anomalies are present in both the lower crust as well as the bulk estimates, and also appear in the W&K14 estimate. This might be related to a sampling bias of plagioclase-rich lithologies or alternatively reflects an inherent feature of the oceanic upper mantle source (e.g., Niu and O'Hara, 2009). A positive Ba anomaly is present in the Masirah cumulates but less so in the melts or bulk compositions, and is possibly an alteration effect

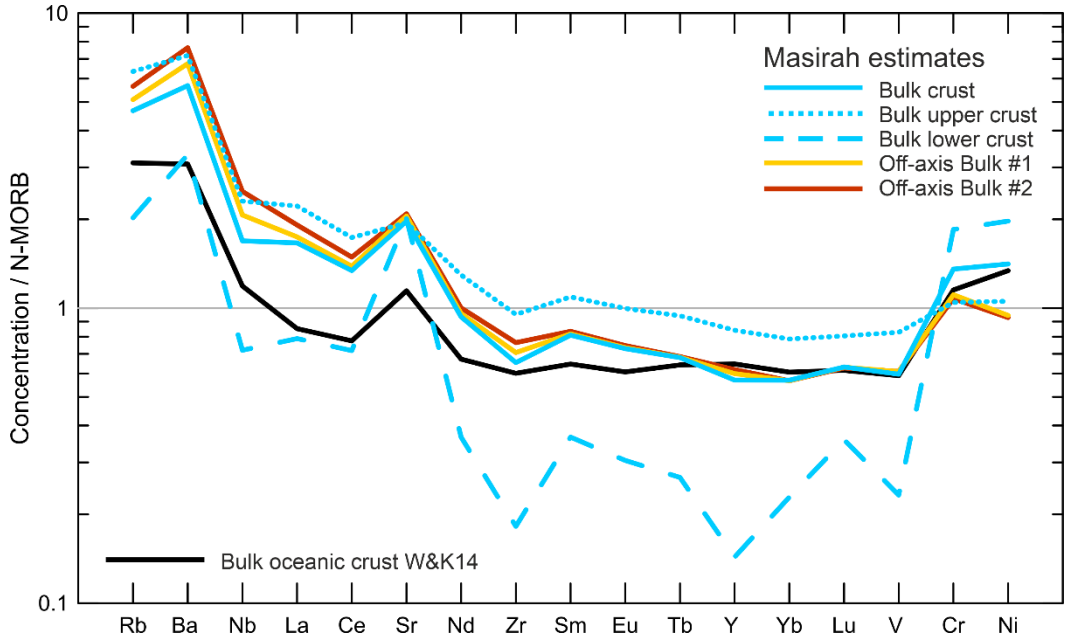

Figure 5.13: *N-MORB normalised trace element diagram of the Masirah bulk crust, bulk upper crust and bulk lower crust, as well as two bulk estimates for off-axis crust after the addition of near off-axis melts (see text for discussion). Bulk oceanic crust from White and Klein (2014) in black for comparison (normalisation values after Pearce and Parkinson, 1993).*

or alternatively a result of plagioclase accumulation, in which barium is only mildly incompatible (e.g., Blundy and Wood, 1991). The pronounced negative Zr and Y anomalies in the lower crust, and consequently similar but dampened anomalies in the bulk composition, are likely the effect of the scarcity of rare earth element (REE) data for the lower crust. In absence of more data, the presence and magnitude of the Zr and Y 'anomalies' is therefore assumed to be an artifact of the mass balance calculations as a consequence of the uncertainty of the adjacent REEs in the trace element diagram.

5.4.2.3 Near off-axis additions of melt to the crust

Due to the continuation of magmatism near off-axis, melts with a trace-element enriched composition were added to the Masirah igneous crust as it was transported away from the spreading ridge (Chapter 4). The modification of the oceanic bulk crust in such a manner is of potential interest for global geochemical cycling through subduction and mantle convection, and as such it is worthwhile to provide an estimate of this effect in Masirah as a reference value. To investigate this, two additional bulk estimates were calculated: off-axis Bulk #1 and off-axis Bulk #2, representing the addition of respectively 5% and 10% off-axis melts to the axial bulk estimate. For off-axis Bulk #1, 80% of the added melts were assumed to stall as the alkaline gabbro-dolerite-granite plutons while the remaining 20% formed late dykes and off-axis lavas, whereas in off-axis Bulk #2 the plutons comprised 60% of the late melts with late dykes and off-axis lavas making up the remainder. The composition of the alkaline plutons was determined by assuming 99% of these rocks consisted of off-axis gabbro & dolerite with a 1% contribution of off-axis granites, whereas the alkaline dykes and lavas were assumed to consist of equal proportions of late dykes and off-axis lavas.

The addition of on-axis and near off-axis melts produced by low degree melting of an enriched source to the bulk crust does not significantly affect the bulk major element composition. The trace element compositions for the two off-axis bulk estimates are shown in Figure 5.13. The addition of off-axis melts in the form of plutons, dykes and seamount lavas, is most noticeable in the most incompatible elements such as Nb, La, Ce and Zr. Compared to the axial bulk estimate, these elements are enriched by ~3 – 22% following the addition of 5% melts (80% plutons, 10% dykes and 10% lavas, off-axis Bulk #1) and by ~11 – 47% after adding 10% melts (60% plutons, 20% dykes and 20% lavas, off-axis Bulk #2).

5.5 Dyke melt-flow directions from AMS

The field observation of an extensive gabbro-dyke transition, with subparallel swarms of dykes commonly crosscutting gabbro, raises the question of where the dykes where sourced from. In this

section the dyke melt flow directions are investigated using AMS to assess the extent of lateral, along-axis melt transport via horizontal dyke intrusion.

5.5.1 Principles of AMS

Oriented block samples were taken of chilled dyke margins for the purpose of reconstructing melt flow lineations using the anisotropy of low-field magnetic susceptibility (AMS) as a proxy for the bulk petrofabric (e.g., Knight and Walker, 1988; Staudigel et al., 1992; Tauxe et al., 1998, Borradaile and Gauthier, 2003). Magnetic susceptibility is the induced ephemeral magnetisation a rock acquires in the presence of a low magnetic field (~ 0.1 mT). The anisotropy of this induced magnetic field can be determined by measuring the susceptibility of a rock specimen along several directions and is represented by the AMS tensor, an ellipsoid with the three principal axes (K_{max}, K_{int} and K_{min}; also K_1, K_2 and K_3) corresponding to the magnitude and direction of the susceptibility axes of the sample. The shape and orientation of the AMS tensor is almost exclusively determined by the bulk shape distribution of the minerals present in the specimen, thus providing a proxy for the net petrofabric (Borradaile and Jackson, 2004). An AMS tensor can be isotropic ($K_{min} = K_{int} = K_{max}$, indicating no preferential crystal orientation), oblate ($K_{min} << K_{int} \approx K_{max}$, indicating a preferred crystal orientation along a foliation plane), prolate ($K_{min} \approx K_{int} << K_{max}$, indicating a preferred crystal orientation along a lineation) or triaxial ($K_{min} < K_{int} < K_{max}$).

In mafic dykes the orientation of a petrofabric contains information on the direction of melt transport. When a dyke forms, magma is injected along a brittle fracture and elongate crystal particles are imbricated against the chilled margins such that their alignment indicates the direction of flow (Knight and Walker, 1988). Determining the orientation of the maximum principal axis (K_{max}) of the AMS tensor in chilled margins of dykes has therefore proven to be a particularly powerful tool for reconstructing the orientations of the axes along which melt flow took place (melt flow lineations), as well as the unique flow directions along these lineations (e.g., Knight and Walker, 1988; Staudigel et al., 1992; Tauxe et al., 1998, Borradaile and Gauthier, 2003).

In mafic dykes, the net AMS fabric generally consists of several magnetic subfabrics. The earliest crystallising phases form the crystal framework imbricated against the chilled margin and consist of paramagnetic mafic minerals such as olivine and pyroxene, with an overall low susceptibility and high modal concentration. Late-stage accessory ferromagnetic minerals, such as magnetite and titanomagnetite, have a low modal abundance but high susceptibility. The mineralogical differences in magnetic susceptibility are such that the susceptibility of a few percent of oxides will equal or exceed that of the paramagnetic matrix. Since late ferromagnetic minerals crystallise along the pre-existing silicate fabric of the matrix, however, their anisotropy tends to mirror that of the original

imbricated fabric (Hargraves et al., 1991; Stephenson, 1994). Lastly, crystallisation of secondary ferromagnetic minerals during hydrothermal alteration contributes to the bulk susceptibility of a specimen. Although the magnitude of the susceptibility of these secondary phases may exceed that of the primary fabric, the general lack of a preferred orientation of the former means that the overall orientation of the AMS tensor tends to remain unaffected (Borradaile and Gauthier, 2003).

5.5.2 AMS results

Single margins were sampled of 51 dykes from 9 localities spread out over both nappes of the Masirah ophiolite. The sampled dykes were generally 0.1 – 3 m thick and could be traced for metres to tens of metres in the field. They include 9 samples from the sheeted dyke complex north of Haql and west of Jabal Suwayr (Lower Nappe), 29 samples from the dyke swarms in the gabbro-dyke transition from Ra's al Ya and Sur Masirah (Upper Nappe) and Urf, Wadi Madi and Wadi Jibuti (Lower Nappe), and 13 samples from the dyke swarms in the mantle from Jabal Suwayr and Wadi Firaj. Oriented drill cores from the blocks were analysed for AMS with an Agico KLY-3S Kappabridge at the University of Plymouth and for data reduction Agico Anisoft v.4.2 and Stereonet v. 10.1.1 were used (Chadima and Jelínek, 2009; Allmendinger et al., 2013; Cardozo and Allmendinger, 2013). Details of the analytical methods and data reduction and quality control are described in Chapter 3.

The complete dataset of specimen-level AMS parameters is provided in Table X. The mean susceptibility (K_m) of the 293 analysed specimens ranges from 233 – 23 089 µSI, with a mean of 1956 µSI and a logarithmic mean of 1156 µSI (Figure 5.14a). This is lower than the magnetic susceptibility typically found in mafic dykes (>20 000 µSI, e.g., Borradaile and Gauthier, 2003) but nevertheless consistent with a bulk composition dominated by paramagnetic minerals and up to a few percent ilmenite, hematite and/or magnetite. Specimens from the same dyke margin generally show a limited variation in K_m (1387 µSI on average) and the magnitude of within-sample variation strongly correlates with the average K_m of a sample. The corrected degree of anisotropy (P_J, Jelínek, 1981) is generally low and varies from 1.0007 to 1.3877 (average = 1.0359, Figure 5.14c and 5.15a). Specimens with a higher K_m tend to have a greater anisotropy (Figure 5.15b). This correlation is especially strong for within-sample variability, suggesting that variations in mean susceptibility are not the result of secondary (and thus isotropic) ferromagnetic minerals. The shape of the AMS ellipsoids is variable and generally triaxial, with the shape factor (T, Jelínek, 1981) varying from -0.866 (prolate) to 0.945 (oblate), and 0.032 on average (triaxial, Figure 5.14d). Samples with the strongest degree of anisotropy (P_J > 1.1) tend to have a more prolate shaped AMS ellipsoid (Figure 5.15c).

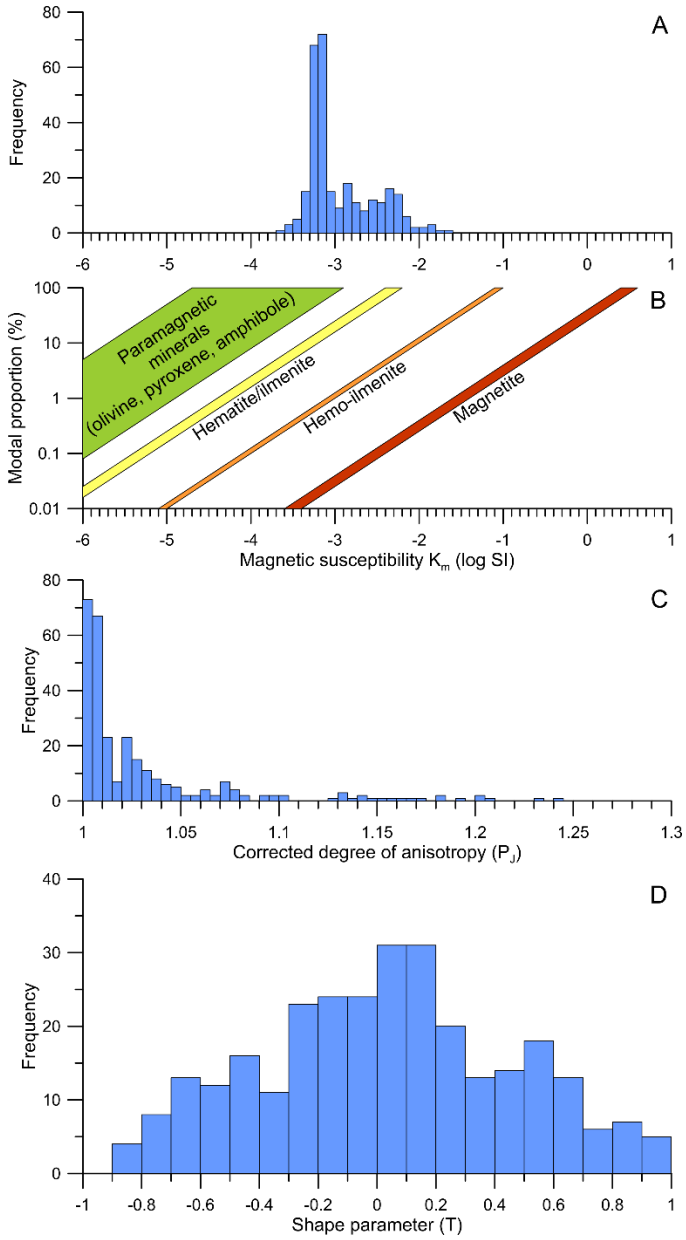

Figure 5.14: *Overview of AMS results showing: (a) the bulk magnetic susceptibility, (b) mineralogical controls on bulk susceptibility, (c) corrected degree of anisotropy in the magnetic susceptibility and (d) the shape parameter of the anisotropy (positive = oblate, negative = prolate)*

To investigate the reproducibility of AMS ellipsoid in a single dyke margin, five duplicate cores producing three core specimens each were drilled from the largest oriented rock sample (18MM307, Figure 5.16). The orientation of the principal axes of the AMS ellipsoid are well clustered, with K_{max} imbricated against the dyke margin and K_{min} at the pole. The orientation of K_{min} is consistent within ~10°, whereas K_{max} and K_{int} are more variable along the plane of the dyke margin, forming a slightly girdled spread of ~35°. The girdle indicates a triaxial fabric with a slight oblate tendency, also reflected in the mostly positive shape factor T (varies between -0.15 and 0.29). The corrected degree of anisotropy decreases with distance from the chilled margin (P_J = 1.020 – 1.023 at the margin and

P_J = 1.008 – 1.009 at ~5 cm from the margin), consistent with the idea that imbrication resulting from melt flow is strongest at the chilled margin. Not all dykes show a similar trend of decreasing anisotropy with increasing distance from the chilled margin, with some samples showing no variation while others show irregular variation. The most common relation is a fairly consistent low degree of anisotropy (P_J < 1.01) within 10 cm from the chilled margin (Figure 5.15a).

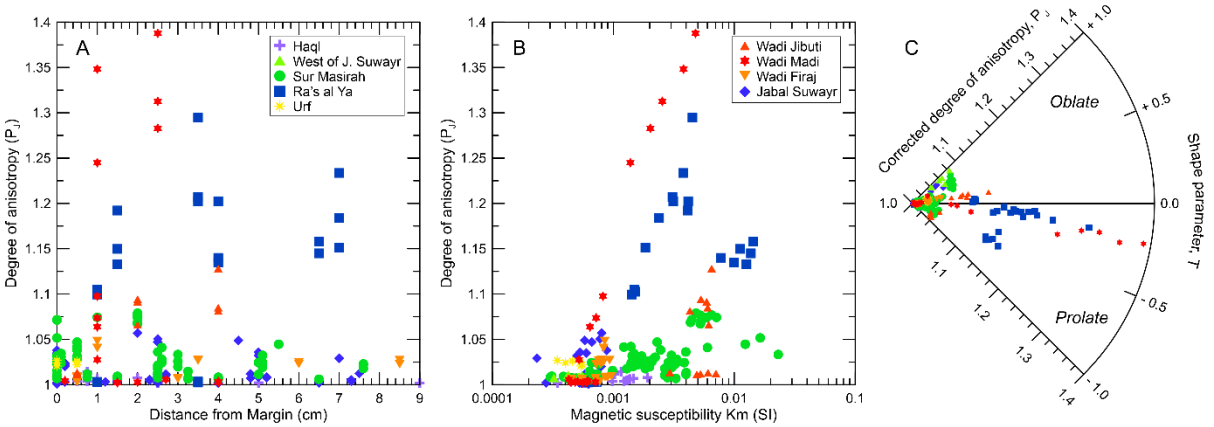

Figure 5.15: *(a) Relation between the degree of anisotropy and the distance of a sample from the dyke margin. (b) Relation between the degree of anisotropy and the bulk susceptibility. (c) Relation between the degree of anisotropy and the shape parameter.*

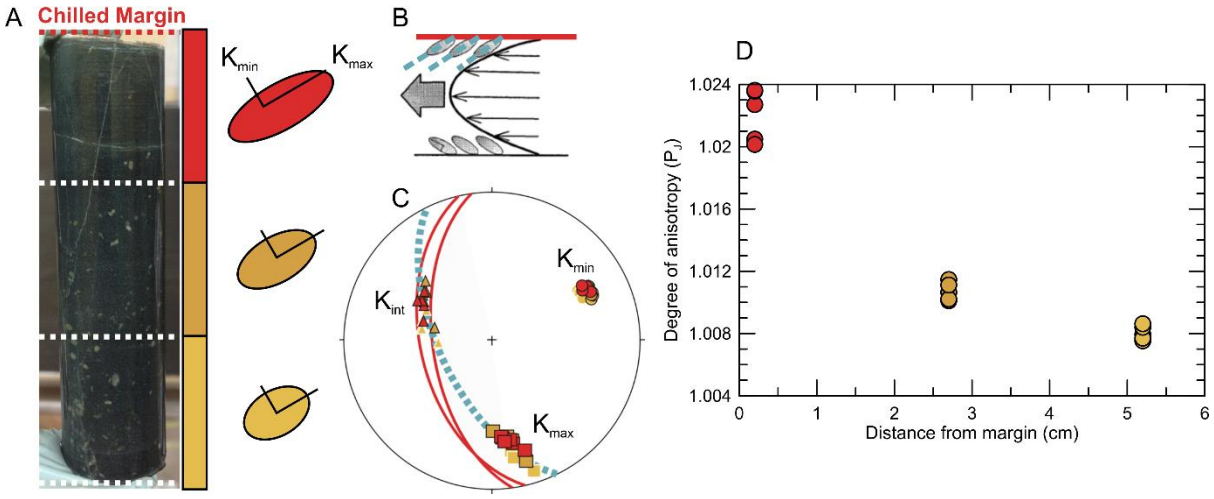

Figure 5.16: *Results from the dyke margin of sample 18MM307, illustrating the principles of AMS. (a) Drill core with schematic AMS ellipsoids showing a decrease in anisotropy with increasing distance from the margin. (b) Sketch illustrating the imbrication of the AMS ellipsoid as an effect of dyke flow. (c) Stereonet showing the orientations of K_{max}, K_{int} and K_{min} with relation to the dyke margin (red). The imbrication plane is shown in blue. (d) Relation between the degree of anisotropy and the distance of a sample from the dyke margin.*

5.5.3 Dyke melt flow lineations

Of the 51 dyke margins analysed for AMS, 36 were interpretable as a melt flow lineation (Table XI, see Chapter 3 for details). Macroscopic flow indicators such as surface lineations or stretched vesicles were not observed in the field and could therefore not be used to corroborate the AMS results. Previous studies into dyke-flow lineations in ophiolites, however, have demonstrated the robustness of the AMS technique (e.g., Rochette et al., 1991; Staudigel et al., 1992; Tauxe et al., 1998, Borradaile and Gauthier, 2003). Figure 5.17 presents stereonets displaying the relations between melt flow lineations (represented by the AMS principal component vector K_{max}) and dyke margins per sampling location in geographical coordinates, as well as histograms of the rake of the lineation with respect to the strike of the dyke margin.

Within single sampling locations in the sheeted dyke complex and dyke swarms in the gabbro-dyke transition, K_{max} tends to be less well clustered than the poles of dyke margins. This is especially apparent in the sheeted dykes north of Haql and the dyke swarms from the gabbro-dyke transition at Sur Masirah, where sampling was most extensive. At these locations dyke trends are fairly consistent (NE-SW in Haql; N-S at Sur Masirah), but K_{max} is scattered in the stereonets and the rake of K_{max} is variable, ranging from 5 – 64° at Sur Masirah and from 1 – 32° at Haql. The geochemical affinity of the dykes (indicated by colours in the histograms, data from Chapter 4) does not correlate with the orientation of K_{max}. Limited dyke flow lineations at Ra's al Ya suggest K_{max} is more consistent there, but that could be due to the small number of samples. Sampling was not sufficient to detect variations in K_{max} at Urf, Wadi Jibuti, Wadi Madi or the area west of Jabal Suwayr.

The dyke orientations of dyke swarms in the mantle (at Wadi Firaj and Jabal Suwayr) are a lot more variable (trends ranging from E-W, ESE-WNW, NE-SW to N-S at Jabal Suwayr, and from E-W, NE-SW to NW-SE at Wadi Firaj) and consequently K_{max} is scattered as well, with the rake of K_{max} varying from 21 – 68° at Wadi Firaj and from 16 – 87° at Jabal Suwayr. The locally sub-parallel sets of dykes do not provide enough samples to assess whether K_{max} is locally consistent.

In the absence of a paleomagnetic study, the net post-emplacement tectonic rotations that affected originally vertical dykes, and hence the relation between K_{max} and the paleo-horizontal and vertical, is unknown. It is therefore not straightforward to interpret the rake of a given K_{max} as representing vertical or lateral dyke intrusion. Nevertheless, the consistent steep and subparallel dyke trends north of Haql and at Sur Masirah suggest post-emplacement tectonics did not disrupt the dyke orientations with respect to each other within km-sized fault blocks. The observed range in K_{max} orientations therefore suggest that melt transport directions in dykes were variable at these locations, and by implication dyke intrusion facilitated both vertical as well as lateral melt transport.

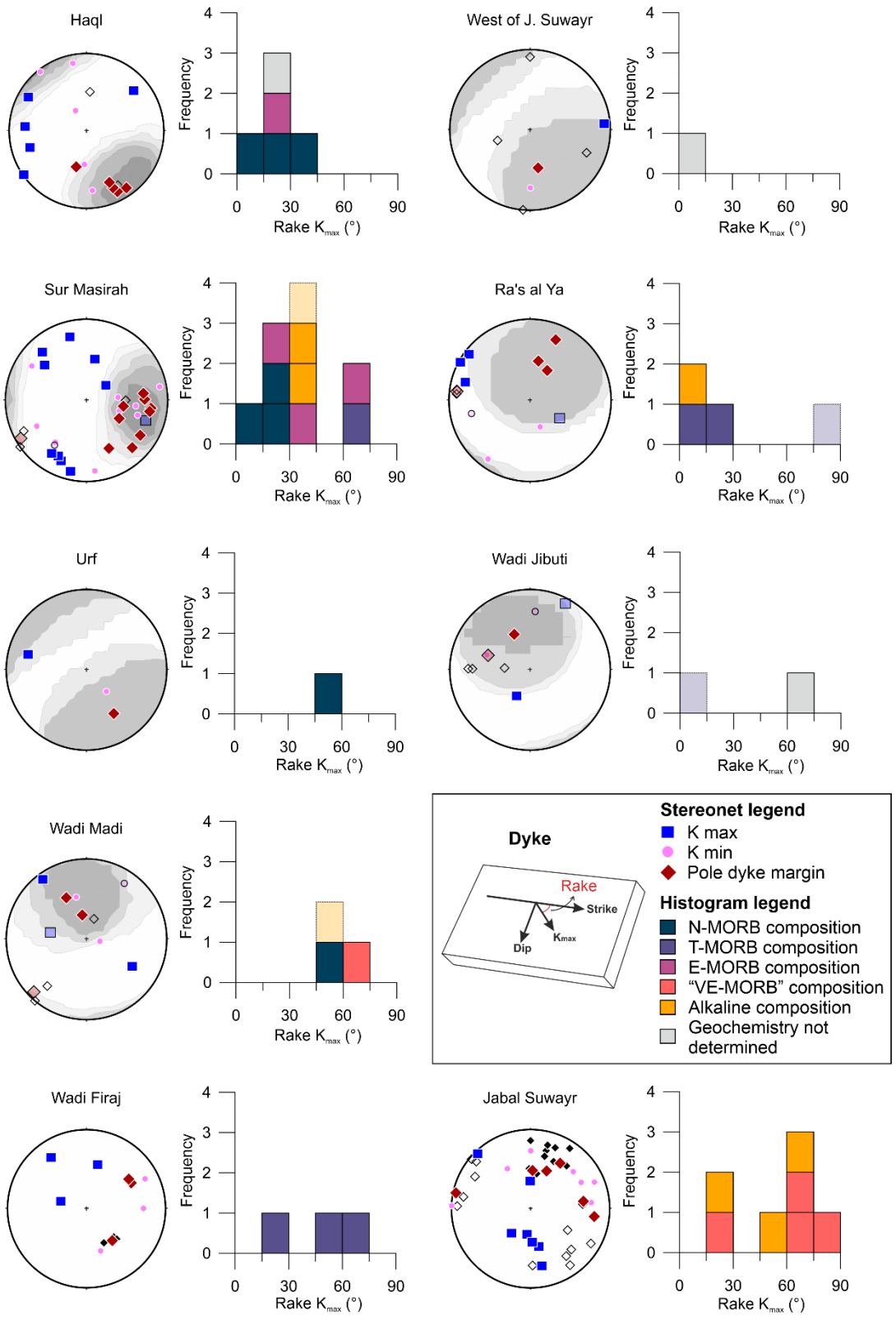

***Figure 5.17 (next page)**: AMS results shown per location. Stereonets show contour plots of the poles of the regional dyke trends. Poles of the dyke margins sampled for AMS are shown in dark red diamonds to compare to Kmax and Kmin orientations. Several dykes with an anomalous orientation compared to the regional trend are indicated by faded colouring. Histograms indicate the rake of the direction of melt flow (see sketch) and are coloured by geochemical composition (from Chapter 4).*

5.6 Discussion

The following section discusses the key implications of the results of this study for the magmatic accretion process recorded on Masirah. Subsequently the significance of the exceptions to the Penrose on a diet architecture is discussed. Finally, a comparison is made to observations from modern oceanic lithosphere.

5.6.1 Magmatic accretion at Masirah: what were the characteristics of the magma plumbing system?

5.6.1.1 To a first approximation the Masirah lower and upper igneous crust are chemically complementary

The bulk composition for the igneous crust calculated in this study is in equilibrium with mantle olivine and approximates a realistic parental melt for the erupted dykes and lavas (Section 5.4.2.2). Whole-rock major element compositions from MasirahDB show that lower crustal rocks (gabbroic plutons) consistently have a more primitive Mg# than the bulk composition, whereas the upper crustal rocks (dykes and lavas) are more evolved (Figure 5.12). Furthermore, there is no evidence for 'missing' melt, as would be expected if primitive melts stalled and fractionated at deeper levels in the lithospheric mantle or if the magmatic system was primarily fed by the lateral along-axis distribution of fractionated melts derived from a more magmatically robust part of the spreading segment. In both cases the bulk crustal composition would be more evolved than a primary melt due to the most primitive cumulates inferred to be missing from the present-day exposed crust in either model. This implies that the lower and upper igneous crust are chemically complimentary and is consistent with a genetic relationship between them through the fractionation of a MORB primary melt.

A similar conclusion is derived from the lower crustal mineral chemistry (Section 5.4.1), where the range in melts calculated to be in Mg-Fe equilibrium with olivine and clinopyroxene cores overlaps to a large extent with the range of Mg# observed in the dykes and lavas (Figure 5.18). Additionally, the plagioclase and clinopyroxene mineral compositions of the crystal cargo in the dykes are not in equilibrium with the groundmass, but their compositions do reflect the range found in the lower crust (Figure 5.9). Combined with the glomerocryst textures in dyke 18MM262, this is consistent with entrainment of crystals from a gabbroic mush during eruption, rather than closed-system phenocryst growth from a basaltic melt.

The small volume of lower crustal lithologies with more evolved mineral compositions do not have upper crustal counterparts and are likely the product of the final differentiation products in the gabbroic mush that failed to erupt (Figure 5.9). This is supported by field observations of varitextured gabbro and felsic lithologies segregating from- and back intruding into- their host

gabbros, indicating a near-solidus process involving a crystal-rich mush and the last remainder of melt. Porphyritic gabbros, with an evolved, varitextured to doleritic matrix and out-of-equilibrium megacrysts, may be analogous to crystal-rich dykes but failed to erupt.

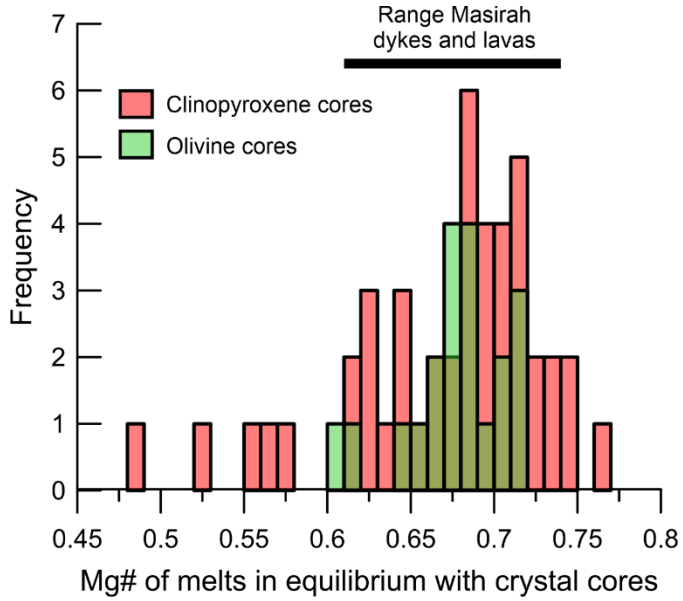

Figure 5.18: *Histogram of Mg# of melts calculated to be in equilibrium with hand-sample averaged clinopyroxene (red) and olivine (green) crystal core compositions from samples of the dominant lithologies of the partial sections (i.e., the layered gabbros, the ultramafic suite in the crust-mantle transition and the foliated/isotropic upper gabbros). The range of Mg# of the erupted dykes and lavas on Masirah is indicated by the black line (Mg# = 0.61 – 0.74; Chapter 4). Equilibrium melts were calculated using a Fe-Mg liquid-mineral partition coefficient K_D of 0.3 for olivine (Roeder and Emslie, 1970) and 0.109 + 0.186*Mg#$_{Cpx}$ for clinopyroxene (Eq. 35 from Wood and Blundy, 1997).*

5.6.1.2 The melts of the upper crust were extracted from the igneous lower crust after only small amounts of differentiation

Field observations and the reconstructed thicknesses of the various units indicate that the lower crust is thin (~500 – 1000 m) with respect to the upper crust (~ 1000 – 1500 m, with the ranges reflecting the difficulty in defining a boundary in the gabbro-dyke transition, Section 5.3.1). This lower-to-upper crust proportion contrasts sharply with the generally accepted 'classic' stratigraphy of oceanic crust. Crustal thickness estimates from seismic refraction surveys suggest that oceanic crust is dominated by lower crustal gabbros, with lower crust : upper crust ratios ranging ~0.70 : 0.30 to ~0.80 : 0.20 (e.g., White et al., 1992), whereas the upper crust is virtually absent at oceanic core complexes (e.g., Dick et al., 2008). A crustal configuration as present on Masirah is also not typically observed in other well-studied ophiolites: in the Semail ophiolite, for example, the same ratio approximates 0.60 : 0.40 (Lippard, 1986).

The field constraints are consistent with the results for the bulk composition of the igneous crust, which despite the unusual lower-to-upper crust proportion resembled the major element composition of a primary MORB melt in equilibrium with mantle olivine (Section 5.4.2.2). The volumetric ratio of the plutonic lower crust (cumulates) to the dykes and lavas of the upper crust (extracted melts) used for the bulk estimate was 0.38 : 0.62. Crucially, by varying different parameters in the mass balance calculation, it was found that in order to approximate a primary MORB composition, the crustal configuration required a thin lower crust relative to the upper crust, with an lower-to-upper crust ratio of 0.50 : 0.50 at most. To illustrate this point, a separate bulk estimate was calculated assuming a hypothetical 'normal' crustal configuration, with a lower crust of 4.5 km total thickness and an upper crust of 2.0 km (ratio 0.69 : 0.31). The Mg# of this bulk composition is too primitive to be in equilibrium with mantle olivine (Mg# = 0.807, Fo_{93}-Fo_{94}).

To obtain a first-order estimate of the amount of crystallisation that took place in the lower crust prior to melt extraction to the upper crust, the bulk trace element fractionation between the upper and lower crust is examined (Section 5.4.2.3). By assuming perfect fractional crystallisation (Rayleigh fractionation), it is possible to calculate the amount of crystallisation that the hypothetical primary melt (i.e., the bulk crustal composition) is required to undergo to reach the bulk upper crust trace element composition. The evolution of four immobile trace elements (Nb, Zr, Y and V) was modelled using bulk partition coefficients relevant for the lower oceanic crust compiled by White and Klein (2014). The results of the calculations for these four elements suggest that the bulk composition estimate for the upper crust can modelled by 28 – 45% crystallisation (average of 37%) of the primary melt. Rare earth element data is scarce for lower crustal rocks, but repeating the calculations for these elements yields similar, slightly lower, results (24 – 41% crystallisation, 32% average). The amount of crystallisation necessary to enrich trace elements in the upper crust is in close agreement with the lower-to-upper crust proportions required to obtain a major element composition that is realistic for a primary melt, and therefore a good indication that the determined Masirah bulk crust composition is internally consistent.

Figure 5.19 (next page) Top*: Histograms showing plagioclase anorthite (a), clinopyroxene Mg# (b) and olivine forsterite (c) contents of crystal cores of axial lower crust on Masirah (averaged per hand-sample). Dark bars represent the dominant lithologies of the partial crustal sections (i.e., the layered gabbros, the ultramafic suite in the crust-mantle transition and the foliated and isotropic upper gabbros), while the light-coloured bars represent subordinate lithologies (e.g., varitextured gabbros and felsics). Crystal lines of descent indicate the evolution of crystal compositions in equilibrium with melts undergoing fractional crystallisation (right-hand axis), calculated with MELTS (see discussion).* *(Caption continued on next page)*

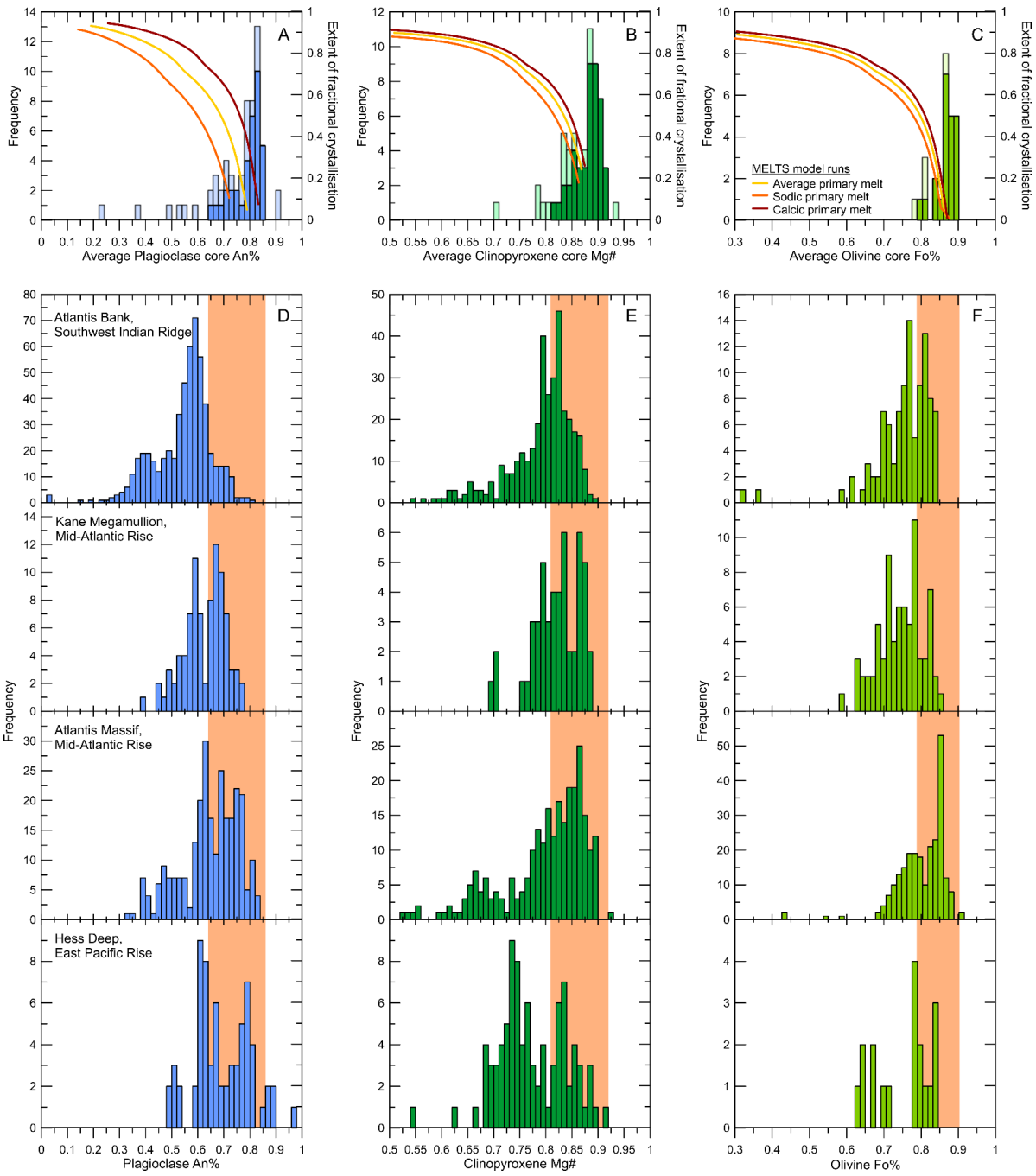

***Bottom**: Comparison of oceanic gabbros mineral compositions (d-f) to the range present in the dominant lithologies on Masirah (shaded box). Atlantis Bank (Southwest Indian Ridge) samples are from ODP Hole 735B, Leg 118/176 (Dick et al., 2002; Boulanger et al., 2020); Atlantis Massif (Mid-Atlantic Rise) samples are from IODP Hole 1309D, Leg 304/305 (Suhr et al., 2008; Drouin et al., 2009; Miller et al., 2009); Kane Megamullion (Mid-Atlantic Rise) samples are from ODP Holes 921 – 923 (Ross and Elthon, 1997; Coogan et al., 2000a, 2000b; Meurer and Gee, 2002); Hess Deep (East Pacific Rise) samples are from ODP Hole 894G, Leg 147 and several dives (Natland and Dick, 1996; Coogan et al., 2002; Lissenberg et al., 2013). For most published data, data were filtered for core analyses from which averages were calculated per hand-sample. For publications that did not report core-rim information, sample averages were calculated using all available spots. For publications that only reported averages, those averages were used.*

The limited extent of magmatic differentiation is also reflected in the primitive mineral chemistry of the gabbros. A compilation of plagioclase An content, clinopyroxene Mg# and olivine Fo content from the four most completely sampled sections of lower oceanic crust (ODP/IODP Hole 735B, Atlantis Bank, Southwest Indian Ridge; IODP Hole 1309D, Atlantis Massif, Mid-Atlantic Ridge; ODP Sites 920-924, Kane area, Mid-Atlantic Ridge; and ODP Site 894, Hess Deep, East Pacific Rise) shows that Masirah gabbros are on the primitive end of the spectrum and that mineral compositions cover a much smaller range (Figure 5.19). The median plagioclase core anorthite content on Masirah is 0.79, compared to 0.57 at Atlantis Bank, 0.65 at the Kane area, 0.66 at Atlantis Massif and 0.67 at Hess Deep. Median Mg# in clinopyroxene cores is 0.88 at Masirah, compared to 0.80 at Atlantis Bank, 0.83 at the Kane area, 0.82 at Atlantis Massif and 0.76 at Hess Deep. For olivine, the median core forsterite composition at Masirah is 0.87, compared to 0.77 for Atlantis Bank, 0.75 for the Kane area, 0.82 at Atlantis Massif and 0.78 at Hess Deep.

To test whether the Masirah gabbro compositions are consistent with the field estimates of the lower-to-upper crust ratio, the bulk amount of fractionation that an incoming primary melt needs to undergo to form the observed mineral compositions was estimated. A fractional crystallisation path was modelled using the MELTS algorithm for a pressure of 200 MPa and an oxygen fugacity 1 log unit below the quartz-fayalite-magnetite buffer. (Rhyolites-MELTS version 1.0.2 with the easyMelts 0.2.4 GUI available from https://magmasource.caltech.edu/gitlist/easyMelts.git/; Gualda et al., 2012; Ghiorso and Gualda, 2015). For a starting composition, an average parental melt composition was estimated by projecting linear regressions through the Masirah dyke and lava major element data back to Mg# = 0.72 and assuming 0.2 wt% H_2O. Although the previously determined bulk igneous crust estimate is in Mg-Fe equilibrium with mantle olivine, there are small deviations in major element concentrations with respect to the most primitive lavas and dykes on Masirah, most notably a lower MgO content (see section 5.4.2.2). Since it is not known if these deviations are primary or represent bulk alteration or a sampling bias, the bulk estimate is less suitable as a starting composition. To explore the effect of melt composition on plagioclase An content, two additional parental melt compositions were estimated (more calcic and sodic respectively) by regressing the upper and lower limits of the variation present in the Masirah liquid lines of descent of CaO, Na_2O, Al_2O_3 and SiO_2 (see Appendix I for details). Figure 5.19 (panel a-c) shows the solid lines of descent for plagioclase An, clinopyroxene Mg# and olivine Fo plotted against the extent of fractional crystallisation (i.e., 1 – melt mass remaining). Despite inherent uncertainties in this approximation, it is apparent that gabbros are in equilibrium with melts that have undergone only small amounts of fractional crystallisation (generally less than 50%, and for a substantial proportion less than 20%). Some of the more primitive plagioclase compositions can be modelled by assuming more calcic

melts were amongst the diverse melt compositions delivered to the crust (Chapter 4). The most primitive clinopyroxene and olivine crystals could not be reproduced by MELTS and hence the approximated degree of fractional crystallisation is accompanied by a degree of uncertainty. Nevertheless, these results indicate only minor amounts of melt differentiation took place in the lower crust, consistent with the field constraints.

5.6.1.3 Melt supply was low and melt extraction was local

The low degrees of magmatic differentiation imply that the crustal residence time of magmas prior to eruption was relatively short, and that the volume and frequency of melt supply was just enough to keep up with the timescale of the eruption cycle. This is consistent with the abundance of crystal-cargo present in the dykes and lavas, a common feature of slow-spreading ridges (e.g., Flower, 1980). Previous work has suggested that the crystal-cargo content in erupted magmas is related to the magma residence time in melt-rich lenses in the lower crustal crystal mush (Lange et al., 2013b). A robust melt supply at faster spreading ridges results in the formation of long-lived melt lenses, which allows the crystals that were entrained as melts ascended through the crystal-rich mush to settle out. Lower melt supplies at slower spreading ridges, in contrast, prevent the formation of long-lived melt lenses and entrained crystals consequently erupt at the seafloor (Lange et al., 2013b). Short crustal residence times of melts, and short-lived melt lenses, at Masirah, are also supported by the diversity of trace element and isotopic compositions of the dykes and lavas (Chapter 4), which imply inefficient melt homogenisation in the crust.

The gabbro-dyke relations on Masirah suggest that the spatial distribution of melt supply and extraction was highly variable. Instead of an abrupt gabbro-dyke transition over tens of metres marked by a fossil melt lens and dyke rooting zone underlying sheeted dykes (e.g., MacLeod and Rothery, 1992; MacLeod and Yaouancq, 2000), the transition takes place over several hundred metres and is dominated by dykes crosscutting gabbro. Short-lived residence times of magmas in the lower crust likely resulted in the episodic vertical migration of melt lenses (e.g., Hooft et al., 1997), and hence dykes are expected to root at variable depths. Additionally, as demonstrated earlier (section 5.5 above), the variable pitches of the AMS-derived melt-flow lineations in dyke margins from regions where dykes are subparallel indicate that dykes were fed both vertically as well as laterally, suggesting vertical and horizontal (along-axis) variations in melt distribution. Since the bulk crustal composition suggests that the igneous crust on the scale of the island represents a complete magmatic system, the length-scales of horizontal dyke intrusion and lateral variability in the presence of melt lenses were likely smaller (i.e., kilometres to tens of kilometres), suggesting a high degree of heterogeneity and three-dimensional complexity during magmatic accretion.

5.6.1.4 Melt-crystal disequilibrium is recorded throughout the lower crust

Evidence for melt-crystal disequilibrium is present in outcrops, petrography and mineral chemistry. In the base of the lower crust, resorption textures of olivine and Cr-spinel in the ultramafic rock unit, show that melts were in chemical disequilibrium with the crystalline matrix of the mush. The primitive compositions of clinopyroxene (Mg# = 0.89 – 0.92; Cr_2O_3 > 0.5 wt%) and olivine (Fo_{87}-Fo_{90}) compared to the first fractionating crystals in the MELTS models (Mg# = 0.87 and Fo_{87}) might be the result of assimilation of Mg and Cr-rich phases and can be explained by assuming that primitive olivine and Cr-spinel hybridised with incoming melts (e.g., Lissenberg and Dick, 2008; Lissenberg and MacLeod, 2016). The intrusive nature of some ultramafic rocks (see section 5.2.3.1, Figure 5.5h-i) suggests that an olivine-rich crystal mush with various proportions of incoming melt can, under the right conditions, form a crystal-melt slurry that is subsequently remobilised. Observations of disaggregating olivine rich bodies in the upper gabbros show this process occurs on a crustal scale. Where these relationships are preserved in the field, observations of warped layered gabbros, crosscutting gabbroic dykes with diffuse margins and a lack of shear strain recorded in minerals (see section 5.2.3.1), indicate these processes took place in the presence of melt but within a crystal mush that was close to the critical crystallinity at which the solid framework shows a dramatic increase in viscosity and is thus able to maintain a degree of internal coherence (e.g., Paterson et al., 1998; Rosenberg and Handy, 2005). Well-equilibrated layered gabbros, as well as a significant proportion of the upper gabbros, however, contain similarly Cr_2O_3 rich clinopyroxenes (Figure 5.20), suggesting that melt-rock reactions with ultramafic rocks were pervasive but were for the most part able to reach textural and phase equilibrium. Further work is needed to determine whether the primitive olivine and Cr-spinel inferred to have taken part in this reaction are of cumulate origin or represent mantle phases incorporated into the igneous crust (e.g., Suhr et al., 2008; Drouin et al., 2009, 2010).

The most common disequilibrium texture in the upper gabbros is resorbed plagioclase enclosed by clinopyroxene, often combined with complex An zoning (oscillatory, patchy). Complex zoning patterns in plagioclase can arise from repeated cycles of dissolution and recrystallisation due to undercooling, decompression and/or magma mixing during recharge events (Bennett et al., 2019). The presence of reverse zoning and interstitial olivine in some rocks indicates that late, primitive melts percolated through the relatively evolved crystal mush, whereas oscillatory zoning may record multiple influxes of primitive melts which subsequently evolve through crystallisation.

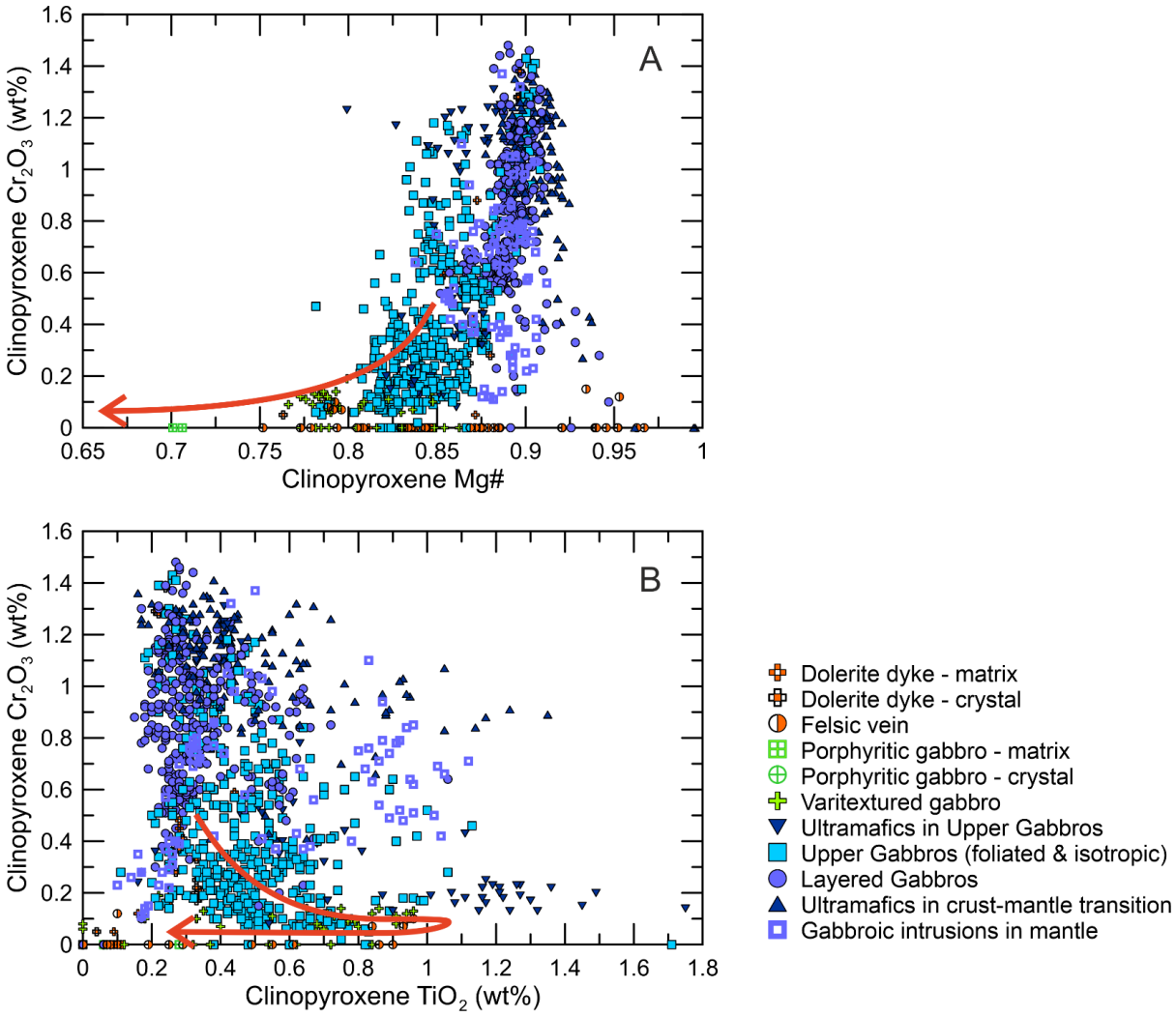

Figure 5.20: *Mg#-Cr_2O_3 (a) and TiO_2-Cr_2O_3 (b) relationships of clinopyroxene crystals (individual analyses of cores, rims and intermediate). Schematic fractional crystallisation trends of clinopyroxene in equilibrium with MORB undergoing low-pressure fractional crystallisation are marked with red arrows (after Lissenberg and MacLeod, 2016). A substantial amount of clinopyroxene compositions have higher Cr and Mg, as well as higher Cr for a given Ti content, than predicted by fractional crystallisation.*

5.6.2 Does the gabbro and dyke-intruded mantle record a different type of lithosphere?

In previous studies, the gabbro and dyke-intruded mantle (mantle types 2 and 3) forming the exceptions to the Penrose on a diet architecture (described above in section 5.3.4) were interpreted to be part of a later syn-magmatic intra-oceanic rifting event that took place ~20 Ma after seafloor spreading and the accretion of oceanic crust (Peters et al., 1995; Marquer et al., 1998). This was accompanied by localised rapid uplift to approximately sea level and the formation of the Barremian (~129.4 – 125 Ma) reefal platform carbonates exposed at Jabal Suwayr while deep-sea sedimentation continued elsewhere on Masirah (Immenhauser, 1996). New high-precision radiometric dates for the axial sequence of both nappes on Masirah (~135 – 130 Ma), combined with

the transitional nature of the axial and alkaline magmatism (Chapter 4), show that these events occurred much closer to the ridge axis (near off-axis, possibly on-axis), and mantle types 2 and 3 therefore potentially reflect the accretion of a second type of lithosphere.

The study of Marquer et al. (1998) describes ductile NW-SE extension and vertical shortening recorded as syn- and post-emplacement deformation within the alkaline plutons, as well as brittle extension recorded by the intrusion of late dykes, both in the Upper Nappe. In Lower Nappe, they describe the occurrence of asymmetric sediment-filled half-grabens (tens of metres in size) in the intruded mantle near Jabal Suwayr and syn-sedimentary faults (metre-scale) in the overlying sedimentary sequence (Marquer et al., 1998). They infer the normal fault structures must have been large based on (1) the exhumation of the mantle to the seafloor, (2) the uplift of the mantle to near sea-level as indicated by the platform carbonates at Jabal Suwayr, and (3) the deposition of breccia with gabbro and harzburgite clasts, indicating erosion (Immenhauser, 1996; Marquer et al., 1998).

There are two ways these observations can be reconciled with the new geochronological model for Masirah. The first is an updated version of the model proposed by Marquer et al. (1998) and proposes that mantle types 2 and 3 were initially overlain by a thin igneous crust similar to that present elsewhere on the island. On-axis detachment faults dismembered the igneous crust, resulting in exhumation of the mantle in the footwall block, while a relatively undisturbed, Penrose on a diet crust was preserved in the hanging wall block. Exhumation of the footwall was accompanied by the intrusion of the (mainly alkaline) plutons, ductile deformation, subsequent brittle dyke intrusion, brittle faulting leading to half-grabens, and continued uplift to near sea-level, followed by erosion and deposition of shallow-water sediments.

The second possibility proposes that the igneous crust that formed at the spreading ridge was not continuous along-axis, with parts of the axial ridge exposing mantle at the seafloor. Lateral along-axis differences in melt supply result in portions of the ridge that are able to sustain magmatic spreading, separated by regions of sparse magmatism where mantle is exhumed onto the seafloor. In the former region, melts are delivered to crustal crystal-melt mushes, whereas in the latter, melts may stall as impregnated peridotites or as gabbroic bodies that crystalise and differentiate *in situ* (see also Chapter 4, subsection 4.5.4). A transition zone between these two end-member states is marked by zones of lateral dyke intrusion with melts derived from the magmatic spreading centre. The recorded uplift and erosion may in this case be attributed to the change in plate tectonic motions in the Indian Ocean that roughly coincided with the formation of Masirah (Gaina et al., 2007, 2015; Phethean et al., 2016), with a cessation of seafloor spreading followed by local transpression and transtension due to the new plate motions along the former spreading ridge, as

proposed in Chapter 4 (subsection 4.5.5). Moreover, the two described alternatives are not mutually exclusive and a combination of both may have taken place.

Regardless of the origin of the mantle-intruded style lithosphere, however, it is noteworthy that a thin, melt-restricted, Penrose-on-a-diet-style magmatically-spread crust, as preserved on most of Masirah, is able to form (along sections of?) the same ridge. In the second alternative above this occurs symmetrically along a (only just) magmatically-robust segment of the ridge, whereas in the first this takes place on the conjugate plate to an ocean core complex (OCC). Not many studies have focussed on the plates conjugate to OCCs and as a result few constraints exist on the architecture of the lithosphere formed in such a setting. Notably, however, magmatic accretion in the hanging wall may not necessarily be impeded by the active formation of an OCC, since although the detachment fault takes up the bulk of extension, small amounts of magmatic spreading may be accommodated in the opposite plate depending on the degree to which melts are captured in the footwall and consequently the melt supply to the hanging wall. As such, there are potentially two viable tectonic settings for the magmatically spread crust of Masirah to have formed.

5.6.3 What thermal and mechanical conditions can result in Masirah-type lithosphere?

The 'Penrose on a diet' architecture observed at Masirah, where spreading is accommodated magmatically but at a low melt supply resulting in a thin crust, diverges from the prevailing models of slow-spreading oceanic crust (Figure 5.21). Plate separation at mid-ocean ridges is commonly viewed as the sum of tectonic extension (T) and the magmatic contribution to spreading (M). Numerical models show that when M drops to 0.3 – 0.5, an axial high-angle normal fault can develop into a large, low-angle detachment fault and accommodate run-away strain (Buck et al., 2005; Tucholke et al., 2008; Behn and Ito, 2008); ridge surveys of oceanic core complexes (OCC) suggest M can also approach 0 (MacLeod et al., 2009). Importantly, although M is correlated to the supply of magma to the spreading ridge, M and magma supply are not identical, demonstrated by the observation that core complexes can accrete substantial volumes of magma via footwall capture without contributing to magmatic spreading (e.g., MacLeod et al., 2009). More precisely, M is related to the amount of melt available to inject into the brittle lithosphere, whereas it is not affected by the amount of melt emplaced in the ductile portion of the ridge axis (Olive et al., 2010). When the melt supply is sufficient to fill fractures generated by spreading, a sheeted dyke complex is able to form. In this respect it is noteworthy that at Masirah, magmatic spreading was coupled to a relatively low degree of crystallisation, resulting in a thin plutonic crust and a large proportion of the melt being erupted as dykes and lavas (lower crust : upper crust = ~0.4 : 0.6).

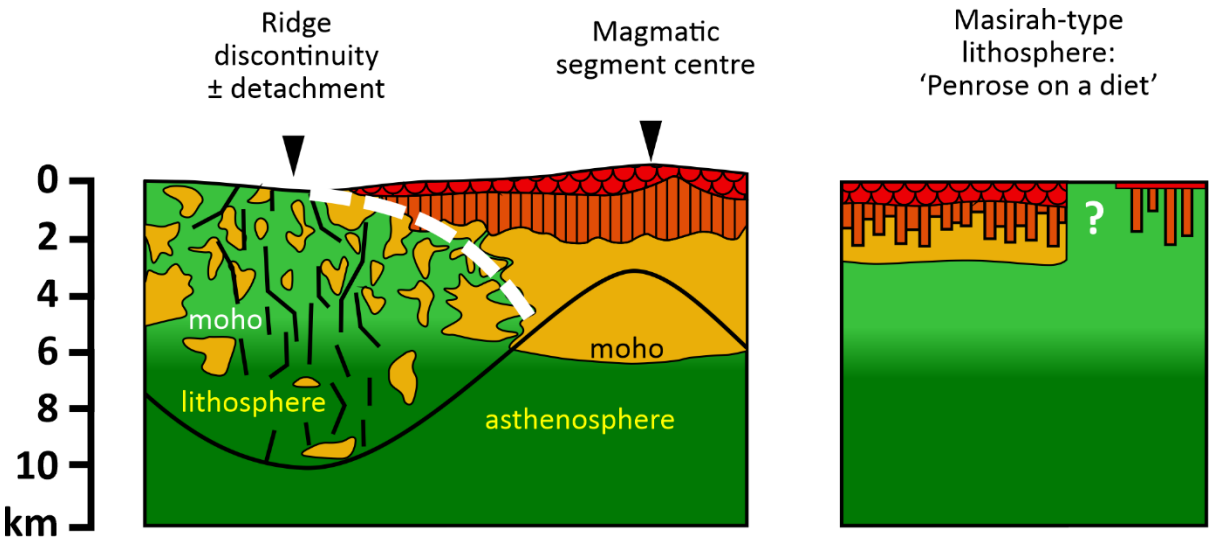

Figure 5.21: *Schematic diagram illustrating the differences between current models for slow-spreading oceanic crust (left, after Cannat, 1993; 1996) and the Penrose on a diet lithosphere described for Masirah (right). See text for discussion.*

Viewed mechanically, the magnitudes of M and T are the result of two competing physical processes at the ridge axis: tensile failure leading to dyke formation and seismic slip events along fault planes (Olive and Dublanchet, 2020). In their numerical model, Olive and Dublanchet (2020) found that the two main variables controlling this stress interaction were the thickness of the brittle on-axis lithosphere and the magmatic overpressure. For a given melt supply, they found that there is a threshold in lithospheric thickness at slow-spreading ridges marking the transition between detachment faulting (thick lithosphere) and magmatic spreading (thin lithosphere). Additionally, an increase in magmatic overpressure may enhance dyke formation and thus magmatic spreading (Olive and Dublanchet, 2020). Since the melt flux at Masirah was low, magmatic spreading was likely not enhanced as a result of an anomalously high magmatic overpressure. Instead, the possibility that a thin axial lithosphere enabled magmatic spreading to take place on Masirah is explored.

Although it is difficult to place definitive constraints on the thickness of the lithosphere, the sub-crustal mantle sections (type 1) on Masirah notably contain signs of channelised porous melt flow (orthopyroxene modal layering, e.g., Kelemen et al., 1995) but lack melt-impregnated peridotites. Additionally, gabbroic veins and intrusions in the mantle related to axial magmatism, are rare. These observations suggest that melts were transported through a mantle that was hot enough to prevent crystallisation and that the 1000°C isotherm (i.e., roughly the basaltic solidus) was above the crust-mantle boundary at the ridge axis. Further investigation is needed, however, to provide more quantitative constraints.

It nevertheless remains difficult to explain how a slow-spreading ridge with a low melt supply could develop a thin lithosphere. In general, the thermal structure of a spreading axis arises from a balance between heat input by melt intrusions and heat removal by hydrothermal circulation (Phipps Morgan and Chen, 1993). At faster spreading ridges, frequent melt replenishment results in long-lived axial melt lenses and crystal melt mushes within the crust, with asthenospheric mantle occurring up to the crust mantle boundary and the brittle-ductile transition (roughly the 650°C isotherm) at the gabbro-dyke transition. Microseismicity studies show that present-day slow and ultraslow spreading ridges, in contrast, are typically associated with a thick (~7 – 18 km) brittle axial lithosphere, consistent with lower rates of melt supply (Grevemeyer et al., 2019; Chen et al., 2023). Rare sections of slower spreading ridge axis where crustal magma mush zones have been seismically detected as low velocity anomalies, and where the brittle-ductile transition hence occurs at crustal levels, (e.g., at 50°28'E along the Southwest Indian Ridge, Jian et al., 2017; and the Lucky Strike segment along the Mid-Atlantic Ridge, Singh et al., 2006) are generally characterised by a thick magmatic crust (~9.5 km at 50°28'E along the Southwest Indian Ridge, Li et al., 2015). There are currently no known examples of a slow or ultra-spreading ridge axis with a thin magmatic crust and shallow brittle-ductile lithosphere.

Interestingly, the broadly linear relationship between an increased lithospheric thickness with decreasing magmatism breaks down at slower spreading rates. This is illustrated by comparing two spreading segments along the Southwest Indian Ridge (full spreading rate of ~14 mm/yr), where microseismicity studies show that the Dragon Horn segment (at 49°39'E), characterised by a sparsely magmatic detachment fault, has a thicker brittle lithosphere (~18 km, Yu et al., 2018) than the nearly amagmatic spreading segment at 64°30'E (~15 km, Chen et al., 2023). Thermal models suggest that besides the rate of melt supply to the ridge-axis, the periodicity in magmatism as well as the depth of melt emplacement exercise control on the thermal structure (Fan et al., 2021; Chen et al., 2022). Taking the episodic nature of melt supply at slower spreading ridges into account, Fan et al. (2021) were able to accurately model a steady-state 10 km thick brittle lithosphere and ~3 km magmatic crust at the Mid-Cayman Spreading Centre (spreading at 15 mm/yr) through emplacing 4 km-wide and 500 m-high magma sills at 14 km depth every 50 ka, as well as a 15 km thick brittle lithosphere and a ~0.2 km magmatic crust at the nearly amagmatic Southwest Indian Ridge segment at 64°30'E by emplacing smaller (1 km by 100 m) magmatic sills every 20 ka. Using an adapted version of this thermal model, Chen et al. (2022) showed that the depth of melt emplacement, which can vary from lava eruptions at the seafloor to gabbros crystalising at depth from trapped melts, affects the thermal structure of the ridge as well, with shallow melt sills contributing less to the over-all heat budget than deeper sills, due to more effective heat removal by hydrothermal circulation. Taken

together, these models suggest that more frequent and deeper melt injections result in a thinner lithosphere. Both these conditions do not appear to apply to Masirah, however, where melt supply was low and melt emplacement was shallow at crustal levels (<2 km).

Potentially, Masirah represents crustal accretion at a ridge-axis in a transient thermal regime. Chen et al. (2022) modelled how the thermal regime of the magmatically robust ridge-axis at 50°28'E along the Southwest Indian Ridge responded to the waxing and waning of magmatism in cycles of a few 100 ka, as suggested by seafloor observations (Chen et al., 2021). The efficiency of heat removal by hydrothermal fluid circulation exercises a key control on the time it takes for the thermal regime to respond to a change in magmatic activity, and the maximum depth of hydrothermal convection is modelled with a cracking front model that is itself dependent on the thermal state of the lithosphere (Olive and Crone, 2018; Fan et al., 2021). The models in the study of Fan et al. (2021) reach a thermal steady-state after ~1 – 2 Ma, although the authors note that their equilibration timescales may also reflect the average permeability of the convective domains in their models, as greater permeabilities result in faster cracking front migration in the absence of heat input (Olive and Crone, 2018). They conclude that future work should focus on constraining the timescales at which a ridge can switch to a different thermal steady-state in response to a rapid change in magmatism (Fan et al., 2021). In the case of Masirah, future thermal modelling could explore whether it is possible for a thin magmatic crust to accrete in a scenario where a formerly magmatically-robust ridge-axis experiences a sudden drop in magma supply and has a transient thermal structure. If inefficient hydrothermal cooling causes a significant delay in the response of the thermal structure of the ridge-axis, for instance, this could allow a hot and thin axial lithosphere to persist for some time during conditions of low melt supply.

Alternatively, the assumption that Masirah was slow-spreading could be wrong. At the moment, the spreading rate of the paleo-ridge axis at which Masirah formed is poorly constrained and the current estimate of 18 – 20 mm/yr (half-spreading rate; Peters and Mercolli, 1998) is not derived from direct observations but based on an analogy with the North and West Somali Basins (see also Chapter 4, section 4.5.6). Compared to slower-spreading ridges, a fast-spreading ridge requires a higher rate of melt supply, and therefore a greater heat input, to accrete a magmatic crust of the same thickness, due to the greater rate of plate separation. Consequently, a future thermal modelling study could explore at what spreading rates it is possible a ridge axis to develop a thin lithosphere and accrete a 2 km magmatic crust.

5.6.4 How common is Masirah-type lithosphere?

How common the Masirah-type lithosphere is in the present-day oceans, is an open question. 'Anomalously' thin (geophysically-defined) crust has been imaged seismically in spreading environments that range from ultraslow (e.g., 1.9 – 3.3 km at Gakkel Ridge; Jokat et al., 2003) to fast (3.5 – 4.5 km in the Wharton Basin, Indian Ocean, where seafloor spreading has since ceased; Singh et al., 2011)); however, it is an open question as to the extent to which seismic velocity layer thicknesses always accurately reflect magmatic crustal thicknesses in these diverse environments. Seismically imaged oceanic crust in the West-Somali Basin in the Indian Ocean, thought to have formed at a slow-spreading ridge that may have had a similar tectonic and paleogeographic setting as the Masirah palaeo-ridge (Gnos and Perrin, 1996; Peters, 2000), is also thin (3.7 – 6.4 km) with a shallow mantle present in some locations (Coffin et al., 1986). Magmatic spreading in the absence of oceanic core complexes has been observed at the ultraslow spreading Red Sea basin, where it may be related to a hotter mantle (Augustin et al., 2016). Crustal thicknesses derived from gravity anomalies suggest that melt supply appears to have been robust enough to form a ~5 km igneous crust in the Red Sea, thinner than 'classic' oceanic crust but not as thin as Masirah (Makris et al., 1991; Ligi et al., 2011, 2012). A seismic survey along a transect representing 70 Ma of slow seafloor spreading in the South Atlantic (31°S) also found no oceanic core complexes and concluded that the proportion of magmatic spreading, deduced from offsets along fault scarps as well as seafloor roughness, was greater than expected for the spreading rate (Christeson et al., 2020; Estep et al., 2021). Like the case in the Red Sea, these authors also related their observations to a hotter mantle, but unlike the Red Sea, wide-angle seismics along the 31°S profile in the Atlantic Ocean reveal a variable crustal thickness, reaching a minimum of 3.6 km (Christeson et al., 2020). Notably, this portion of oceanic crust has an upper crust (Layer 2, 2.2 km thick) versus lower crust (layer 3, 1.3 km thick; Christeson et al., 2020) proportion remarkably similar to Masirah. Taken together, these observations indicate there is potentially much more variability in seafloor spreading style and lithospheric architecture at very slow spreading rates, perhaps with second-order variations in magma supply having a disproportionate effect compared to faster spreading rates (>~20 – 30 mm/yr). Observations from Masirah are therefore uniquely valuable in informing what lithospheric configurations are permissible at slow-spreading ridges.

5.7 Conclusions

The study of slow-spreading oceanic lithosphere is complicated by the lack of complete sections through the crust. Most oceanic gabbros from slow-spreading ridges have hitherto only been sourced from oceanic core complexes, and hence may not be representative of large sections of the magmatic lower oceanic crust. It is often unclear – or not agreed – whether they represent a

dismembered lower part of a ‘full’ crustal section (e.g., Dick et al., 2000) or formed in a process that never produced an upper crust (e.g., Godard et al., 2009; Boulanger et al., 2020). In consequence, this lack of first-order constraint on the architecture of oceanic lithosphere leads to potentially specious debates about ‘missing’ primitive cumulates and sheeted dykes (e.g., Dick et al., 2000, 2008, 2019b).

The Masirah ophiolite is therefore potentially of great significance in this debate, as a fragment of oceanic lithosphere formed at a true mid-ocean ridge that has a complete upper and lower crust of which the three-dimensional lithospheric architecture can be studied. The results in this chapter suggest that crustal accretion at Masirah was highly heterogeneous and three independent lines of evidence are presented (field observations, subsection 5.3; mineral compositions of the gabbros, subsection 5.6.1.2; and the estimate for the bulk crust composition, subsection 5.6.1.2) that are consistent with the magmatic accretion of a thin igneous crust (2 km) and a thin lower crust with respect to the upper crust (lower crust : upper crust = ~0.4 : 0.6).

The generation of magmatically-spread crust at spreading ridges with a low melt supply contradicts current crustal accretion models, which predict the formation of 6 – 7 km thick crust for conditions of high melt supply and spreading dominated by detachment faulting when melt supply is low. The Masirah Ophiolite shows that the variability of permissible slow-spreading crustal geometries is greater than previously thought and that a basaltic seafloor should not automatically be interpreted to correlate with a thick magmatic crust. Future studies of oceanic crust should therefore consider Masirah-type lithosphere as a third possible end-member when interpreting seafloor bathymetry, seismic data and gravity anomalies.

6. A highly refractory mantle beneath anomalously thin slow-spreading oceanic crust in the Masirah Ophiolite

6.1 Introduction

The melt supply at mid-ocean ridges (MOR) exercises a first order control on oceanic crustal accretion and the resulting lithospheric architecture, and is ultimately a function of the amount of melt produced in the underlying mantle. Slow-spreading ridges (<40 mm/yr full spreading rate) represent 50% of the present-day MOR system and are generally thought to have a variable but reduced melt supply compared to their fast-spreading counterparts (>80 mm/yr), leading to heterogeneous crustal accretion that significantly departs from the original Penrose model (Cannat, 1993). Current models propose that as melt supply varies in space and time, the mode of crustal accretion alternates between the formation of 'classic' magmatically-robust crust (e.g., Lin et al., 1990) and oceanic core complexes (OCC, e.g., Cann et al., 1997). Furthermore, as spreading rates transition from slow to ultraslow, amagmatic ridges may occur (e.g., Dick et al., 2003). However, establishing a direct link between mantle melting, melt supply and lithospheric architecture is difficult. Few ridge segments expose full lithospheric cross sections; hence, there is significant uncertainty in the synthetic models that have been developed for lithospheric architecture. It is not clear, for example, what the thickness of the crust is in magmatically active slow-spreading ridge segments. Furthermore, it is difficult to establish relationships between crustal magmatism and mantle melting, as mantle is typically only exposed when crust is either dismembered or absent. Another challenge is that existing data indicate that the degree of mantle melting does not always correlate positively with melt supply: refractory harzburgites may be recovered from portions of the ridge that lack a significant basaltic crust (e.g., Seyler et al., 2007).

An investigation on Masirah enables direct observations to be made on the link between the mantle and the crust. As shown in Chapter 4 and by previous work (Peters and Mercolli, 1998), Masirah is believed to originate from a true, 'open-ocean' slow-spreading ridge, rather than near a subduction zone, where the melting regime is influenced by the presence of water. Chapter 5 presented the unusual lithospheric architecture of Masirah and demonstrated that the igneous crust is thin (~2 – 2.5 km) but nevertheless formed by magmatic spreading. The conditions necessary the accretion of this style of lithosphere are thought to involve a low melt supply but nevertheless a thin brittle lithosphere (see discussion Chapter 5). In this chapter, the mantle section on Masirah will be investigated to see what conditions could have led to a reduced melt supply. This chapter will present mineral chemistry for the mantle peridotites and link it to observations on the architecture of the overlying crust. It will show that despite having a thin igneous crust, the mantle section at

Masirah is highly refractory, therefore likely requiring an ancient melting event to have previously depleted the mantle, resulting in a mantle that was on average less fertile and fusible. This indicates that the time-integrated melting history of the mantle, rather than just the upwelling rate, controls degrees of mantle melting, and hence the architecture of ocean lithosphere.

6.2 Summary of the lithospheric architecture of Masirah

Masirah Island is a ~600 km^2 exposure of oceanic lithosphere off the southeast coast of Oman and is unrelated to the better known Semail Ophiolite onshore. Detailed mapping revealed that the Masirah ophiolite consists of two nappes each containing a near-complete sequence of mantle, lower crust, upper crust and sedimentary cover (Peters et al., 1995). Accretion of the ocean lithosphere took place ~135 – 130 Ma and was followed by continued near 'off-axis' magmatism that emplaced alkaline plutons and volcanics in parts of the island (Chapter 4). Although no single complete section through the lithosphere is preserved due to tectonic disruption, detailed field observations have allowed a reconstruction of the lithospheric architecture (Figure 6.1; Peters and Mercolli, 1998; Peters, 2000; Chapter 5). All of the classical ophiolite lithostratigraphic units are present on Masirah. However, the magmatic crust is thin compared to conventional models of oceanic crust, never exceeding 2 – 2.5 km. Most notably, the gabbroic lower crustal sequence is extremely thin (~500 m). Where exposed, the lower crust consists of a sequence of modally layered olivine-gabbros, intercalated with plagioclase and clinopyroxene-bearing dunites and troctolites at the base, followed upwards by a sequence of non-layered gabbro that is intruded by an increasing proportion of dykes. Dykes and lavas range from N-MORB to E-MORB compositions that are fairly primitive compared to typical MORB (average Mg# = 0.65, average TiO_2 = 1.2 wt%; Peters and Mercolli, 1998; Chapter 4), consistent with low amounts of crystallisation prior to eruption. In the lower nappe the lavas are concordantly overlain by autochthonous pelagic sediments. Despite emplacement-related tectonic disruption, continuous sections through all major units and undisturbed transitions between units are preserved. Together with a well-developed sub-vertical dyke complex that is regionally perpendicular to the crust-mantle boundary and an absence of evidence for on-axis rotations or the juxtaposition of different lithologies on pre-emplacement structures, these observations suggest that the thin crust is the result of magmatic accretion under melt-poor conditions, rather than tectonic thinning through detachment faulting (Peters and Mercolli, 1998; Chapter 5).

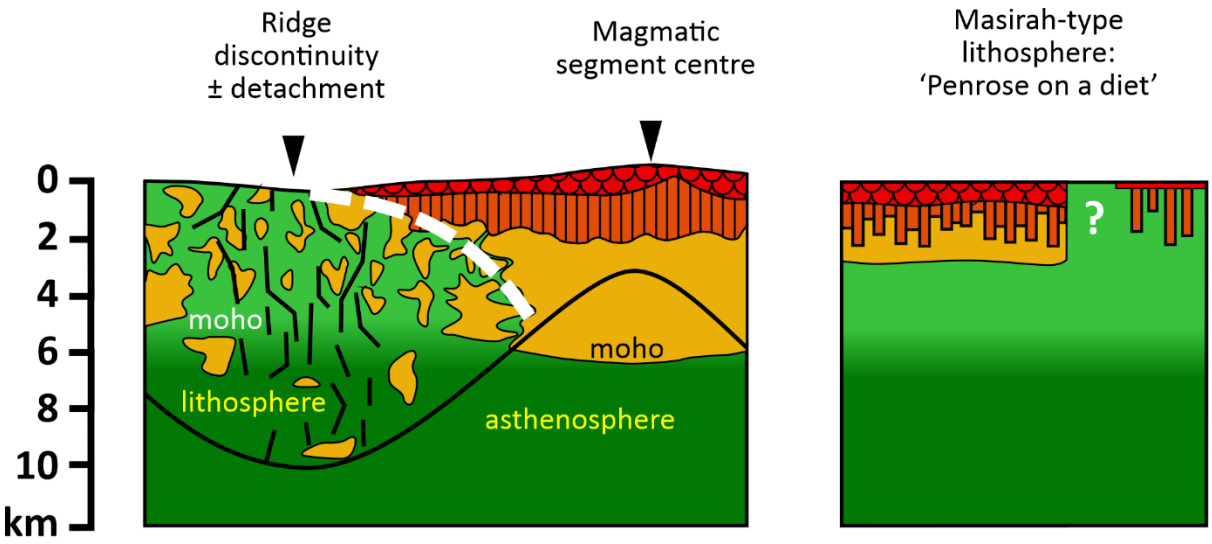

***Figure 6.1**: Lithospheric architecture of the Masirah Ophiolite (right) compared to the prevailing models for slow-spreading oceanic crust (left, after Cannat, 1993, 1996) (see Chapter 5 for discussion).*

6.3 The mantle section

6.3.1 Key field observations

Mantle exposures on Masirah are extensively to completely serpentinised and occur as peridotites overlain by a gabbroic igneous lower crust (herein referred to as 'sub-crustal mantle', equivalent to mantle Type 1 in Chapter 5) and as tectonically dismembered outcrops. The sub-crustal mantle is characterised by the presence of metre-sized dunite lenses and modal orthopyroxene-olivine banding (cm to m scale) that is steeply orientated with respect to the crust-mantle boundary, and contains rare gabbroic intrusions (generally <1 vol% of outcrop); plagioclase peridotites are absent. Peridotite localities that lack outcrop of overlying igneous crust (locally) contain more abundant metre-sized gabbroic intrusions (5 – 70 vol%), most of which have an alkaline affinity (Chapter 4), as well as rare plagioclase peridotites and in some cases swarms of cross-cutting dolerite dykes with chilled margins and compositions that range from MORB-like tholeiites to alkaline basalts (Chapter 4). This 'intruded mantle' facies (mantle Types 2 and 3 in Chapter 5) contains no visible modal layering and the peridotites generally have a distinctly darker appearance due to the formation of magnetite veins during serpentinization. It is generally spatially associated with the km-scale alkaline plutons related to the near off-axis magmatism and in a few cases is overlain by sediments of Barremian age (~129.4 – 125 Ma), indicating that mantle was exposed at the seafloor by that time (Immenhauser, 1996). There is no firm evidence, however, that suggests peridotites were exposed at the seafloor at the paleo-ridge (see discussions in Chapters 4 and 5).

6.3.2 Petrography

A total of 23 peridotite samples were collected from several mantle localities on Masirah, with the area east of Jabal Taymah sampled in detail (Figure 6.2). Modal mineral abundances were estimated visually from thin-sections (Figure 6.3) and a detailed petrography is presented in Table III. The Masirah peridotites are dominantly refractory with little to no clinopyroxene (0 – 5%), and include 16 spinel harzburgites, 5 spinel dunites, 1 spinel lherzolite and 1 plagioclase peridotite (a melano-olivine gabbro *sensu stricto*). Only one of the dunites (sample 18MM054, from the subcrustal mantle) consists of pure olivine plus minor spinel.

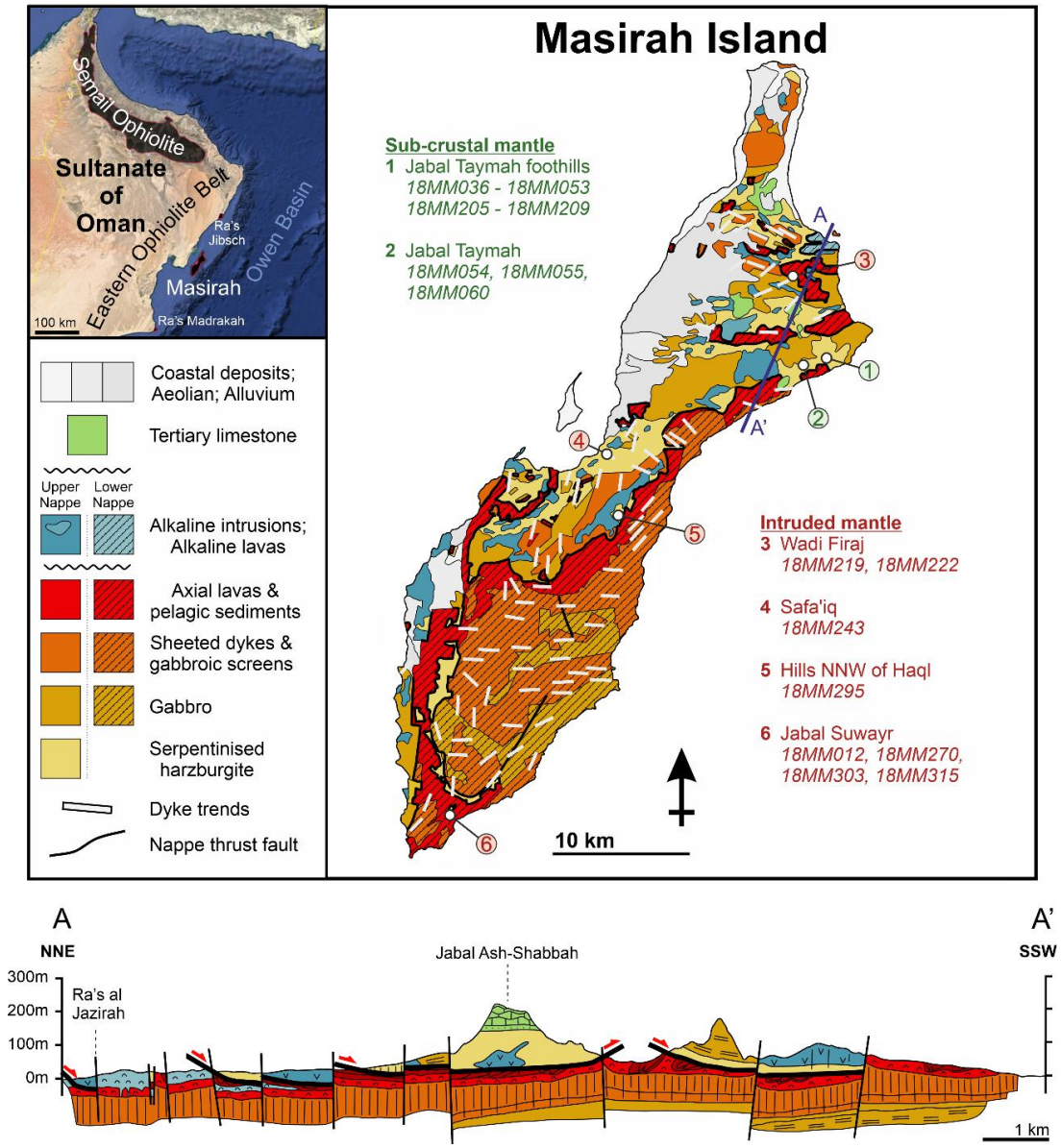

Figure 6.2: *Geological map of Masirah indicating mantle exposures and sample locations. Sub-crustal mantle sections were studied at Jabal Taymah and its foothills (1 & 2) and the intruded mantle sections were studied at Wadi Firaj (3), Safa'iq (4), the hills north-northwest of Haql (5) and at Jabal Suwayr (6). Figure adapted from Peters et al. (1995).*

Most peridotites have undergone extensive to complete serpentinization but preserve relic primary mineral assemblages (estimated modal proportions of alteration minerals range from 40%-100%, average 87%). The post-olivine serpentine mesh is commonly replaced by fine bladed serpentine, whereas orthopyroxene generally preserves bastite pseudomorphs. Clinopyroxene is more resistant to alteration and weathering and shows only partial replacement. The contrasting modes of 170erpentinization noted in the field is reflected in thin-section by the serpentine textures and magnetite abundance. Sub-crustal mantle peridotites generally have finer serpentine mesh cells (0.1 – 0.2 mm) and magnetite mineralisation along serpentine veins is sparse to absent, producing a light beige-brown appearance in hand specimens. In contrast, the serpentine mesh of intruded mantle peridotites has coarser cells (0.1 – 1 mm) and abundant magnetite precipitated in fine-grained aggregates forming a diffuse vein network. The presence of magnetite results in a darker appearance in hand specimens and occasionally forms red colouration due to oxidation to hematite.

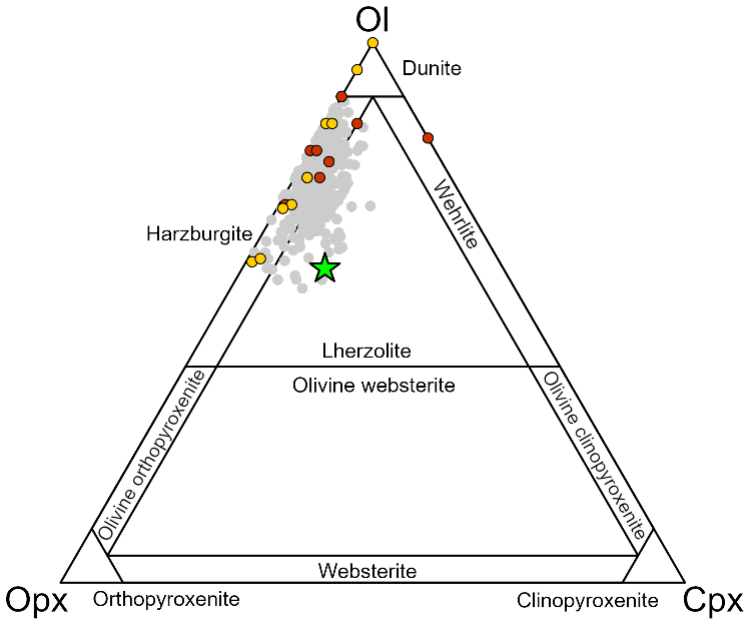

Figure 6.3: *Modal compositions of the Masirah peridotites from sub-crustal mantle locations (yellow) and intruded mantle locations (red). Abyssal peridotites in grey (Warren, 2016) and the model depleted mantle source composition of Workman and Hart (2005) indicated with the green star.*

6.3.2.1 Cr-Spinel

Cr-spinel is present in almost all samples in trace amounts (<1 %) and has various morphologies that can be grouped into three main textural types: (1) irregular holly-leaf grains (Figure 6.4a and Figure 6.5a & b), (2) clinopyroxene-spinel symplectites (hereafter Cpx-Sp symplectites, Figure 6.4b & 6.5e), and (3) euhedral diamond-shaped crystals (Figure 6.4c & 6.5d). Spinel textures can be hybrid, as

some smaller holly-leaf spinels resemble the Cpx-Sp symplectites (Figure 6.4d & f and Figure 6.5c), while larger holly-leaf grains may have rims that are intergrown with clinopyroxene.

The holly-leaf shaped spinels can vary in size from 0.2 to 4 mm. This spinel type is present in all mantle peridotite samples, except for the pure dunite sample (18MM054). The complex shapes of holly-leaf morphologies result in some spinels having a more equidimensional granular habit whereas others have a more extreme negative curvature that sometimes give rise to embayments and poikilitic textures (Figure 6.4a & 6.5a). The irregularly curved grain-boundaries are often intergrown with orthopyroxene, clinopyroxene and sometimes olivine. Spinel-clinopyroxene intergrowths occasionally form thin (~100 µm) discontinuous films around orthopyroxene porphyroclasts (Figure 6.4d & 6.5c).

The intricately intergrown Cpx-Sp symplectites occur in a majority of the peridotites. Cr-Spinel is most often intergrown with clinopyroxene and to a lesser extent with orthopyroxene and olivine (Figure 6.4b). Their morphology can be transitional into some of the finer holly leaf spinel grains, here symplectites are defined as intricate intergrowths with individual vermicular spinel domains of <~0.1 mm. The largest symplectites are ~2.5 mm and the smallest can occur as a single vermicular sliver of Cr-spinel.

Figure 6.4 (next page): *Microphotographs illustrating the petrographic relations of the Masirah peridotites. (a) A harzburgite with holly-leaf spinel and porphyroclastic orthopyroxene and clinopyroxene (plane-polarised light, PPL; sample 18MM048, foothills east of Jabal Taymah). (b) Harzburgite with a spinel-clinopyroxene symplectite. Kinkbands in olivine indicated by yellow arrows (cross-polarised light, XPL; sample 18MM055, Jabal Taymah). (c) Dunite with diamond-shaped euhedral spinel crystals (PPL, sample 18MM054, Jabal Taymah). (d) Harzburgite spinel and clinopyroxene intergrown around an orthopyroxene crystal (XPL, sample 18MM052, foothills east of Jabal Taymah). I Harzburgite with thin interstitial clinopyroxene grains along olivine and orthopyroxene grain-boundaries. Adjacent clinopyroxene grains have a similar angle of extinction (PPL, sample 18MM050, foothills east of Jabal Taymah). (f) Harzburgite with olivine embayments in an orthopyroxene grain, resulting in a highly curved grain-boundary and narrow protrusions from the orthopyroxene (indicated by yellow arrow; XPL, sample 18MM052, foothills east of Jabal Taymah). (g) Harzburgite with a large orthopyroxene porphyroclast containing exsolution lamella and blebs of clinopyroxene (XPL, sample 18MM205, ridge east of Jabal Taymah). (h) Plagioclase-bearing lherzolite with mosaic (neoblastic?) clinopyroxene and orthopyroxene grains (XPL, sample 18MM367, Ra's Madrakah). Sp = spinel; Ol = olivine; Cpx = clinopyroxene; Opx = orthopyroxene; alt = altered.*

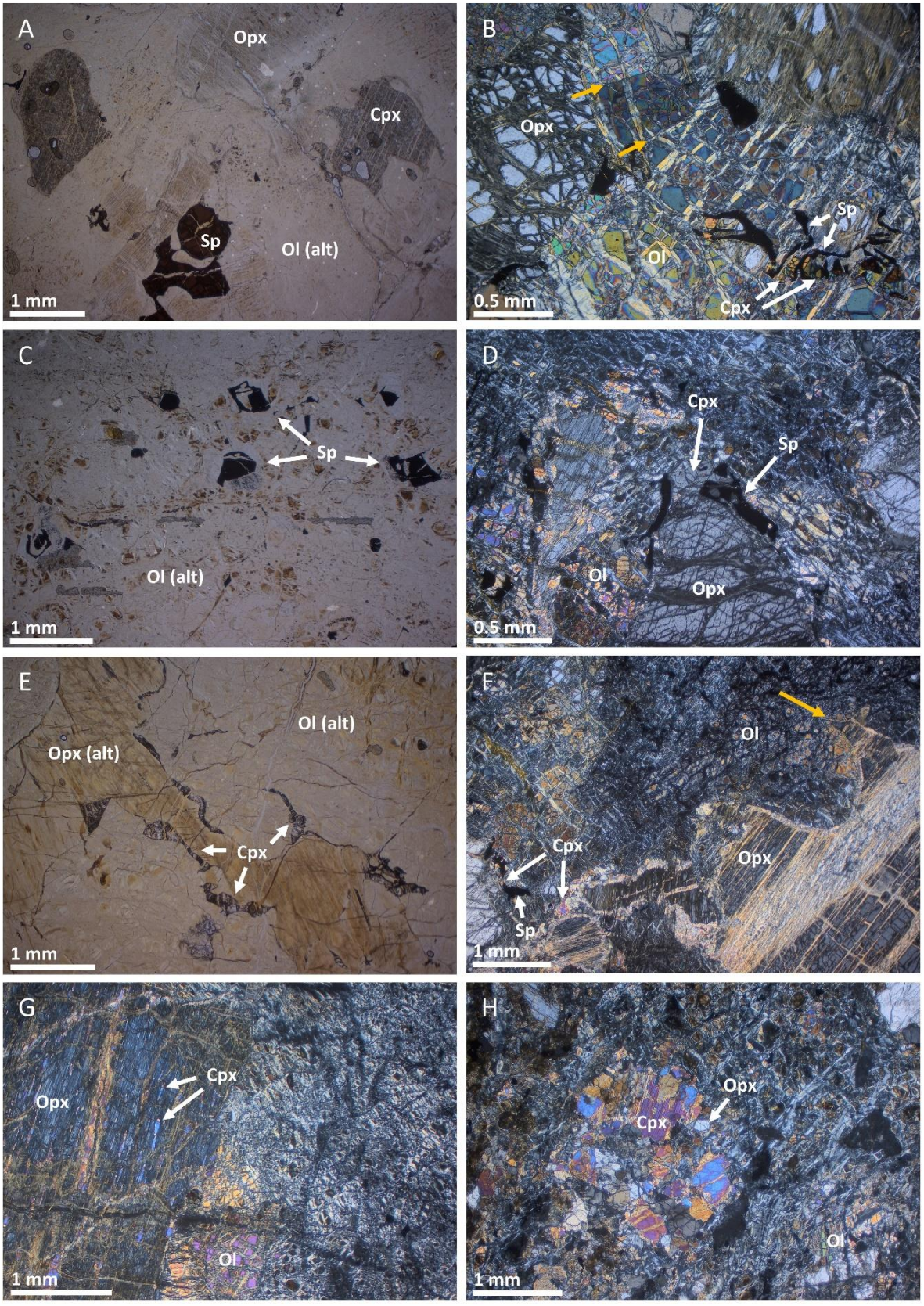
A
Opx
Cpx
Sp
Ol (alt)
1 mm
B
Opx
Sp
Ol
Cpx
0.5 mm
C
Sp
Ol (alt)
1 mm
D
Cpx
Sp
Ol
Opx
0.5 mm
E
Ol (alt)
Opx (alt)
Cpx
1 mm
F
Ol
Cpx
Opx
Sp
1 mm
G
Cpx
Opx
Ol
1 mm
H
Opx
Cpx
Ol
1 mm

The euhedral spinels have a diamond to blocky morphology and occasional twins (Figure 6.4c). They occur exclusively in dunites and Opx-poor harzburgites (<20 %), although they are not present in all dunites. Crystals are usually distributed within the post-olivine serpentine mesh, but in some samples the Cr-spinels cluster together in blocky aggregates. The crystal shape is commonly slightly rounded, potentially a sign of resorption by a melt. In dunite sample 18MM054 the rims of some euhedral spinels preserve micrometre-scale symplectite reaction textures (Figure 6.5d). This type of Cr-spinel can also contain small round inclusions with olivine and altered minerals.

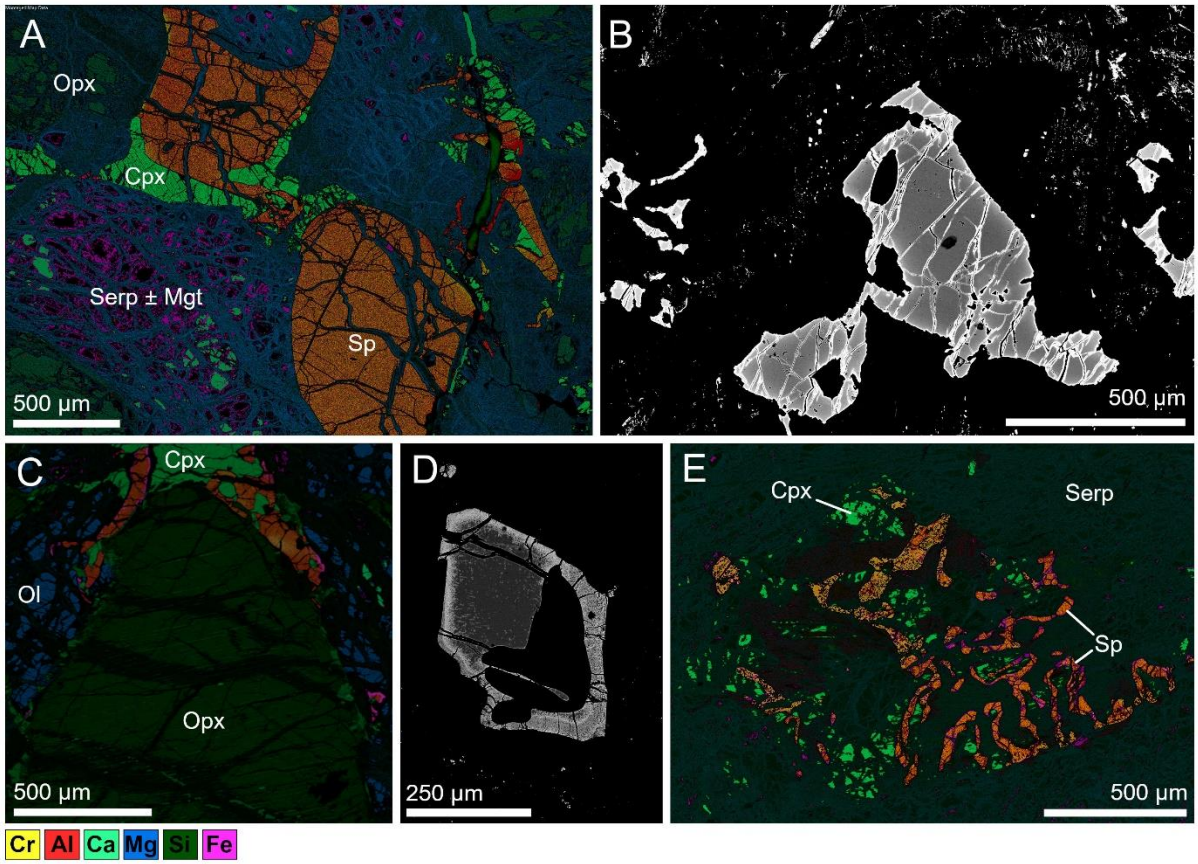

Figure 6.5: *Multi-element maps and backscattered electron images illustrating textures of the Masirah peridotites. (a) Residual holly-leaf spinel (Group 4) with rims intergrown with interstitial clinopyroxene in a serpentine matrix. (b) Strong concentric zoning (Al-rich core, Cr-rich rim) in a residual holly-leaf spinel (Group 4) with ferrit-chromite alteration along rim and fractures (Group 1). (c) Clinopyroxene intergrown with a zoned residual holly-leaf spinel (Group 4) forms a thin film along the rim of an orthopyroxene porphyroclast. (d) Euhedral spinel (Group 3) with symplectite reaction-rim in a serpentinised dunite. I Cpx-Sp symplectite (Group 3) with portions of the spinel corroded and affected by low temperature metamorphism (Group 2).*

No spinel foliation was observed. Brittle deformation is often present in the form of micro-fractures filled with serpentine veinlets, suggesting a genetic link to the volume-change during the serpentinization of the peridotites. The colour of Cr-spinel generally corresponds well to its chemical

composition, making it possible to detect chemical zoning in thin-section for some grains (Al-rich: yellowish light-brown, Cr-rich: deep-red, dark-brown to black). Some Cr-spinels contain micrometre-scale pores that are visible under a reflected light microscope as well as in BSE images, and likely related to some form of alteration or weathering.

6.3.2.2 Olivine

Due to its sensitivity to alteration, olivine is often better preserved in pyroxene-bearing peridotites compared to dunites. Olivine grains are generally coarse-grained (1-10 mm, 5 mm average) and have curved grain boundaries (Figure 6.4b), and more rarely form fine-grained mosaic aggregates with triple junctions. They commonly exhibit embayments protruding into orthopyroxene grains (Figure 6.4f). In the plagioclase peridotite, olivine has rounded contacts with plagioclase and clinopyroxene, interpreted as a resorption texture. Fresh olivine relics often display crystal-plastic deformation features and include undulose extinction (from weak to strong), kink-bands and the formation of subgrains (Figure 6.4b). The coexistence of deformed and undeformed grains suggests a dynamic, high-temperature deformation-recrystallisation process typical of mantle flow.

6.3.2.3 Orthopyroxene

Orthopyroxene is commonly replaced by bastite pseudomorphs (Figure 6.4e), although fresh orthopyroxene occurs in about 40% of the samples (Figure 6.4a & b). Less commonly, ultrafine-grained, high-birefringence alteration minerals form a rim around orthopyroxene grains, sometimes completely replacing it. Orthopyroxene generally occurs as coarse porphyroclasts (1 – 8 mm, 3 mm average) with a rounded morphology with common (sometimes extreme) olivine embayments that can result in a holly leaf shape (Figure 6.4f). Calcium exsolution lamella are common but not present in all grains and occur mostly as sharp, discrete lamella and more rarely as broader diffuse lamella. All three varieties often co-exist in the same hand specimen. In other grains, clinopyroxene is present in orthopyroxene grains as discontinuous lenses or irregularly shaped blebs (Figure 6.4g). Although foliation was not commonly observed in the field, orthopyroxene grains in several samples are weakly aligned in mm-sized bands and occasionally a crystal preferred orientation is apparent from the alignment of cleavage and exsolution lamella orientations. Pristine orthopyroxene porphyroclasts often display little to no crystal-plastic deformation, with occasional undulose extinction present. Bastite pseudomorphs are more commonly deformed and display microfolding, undulose extinction, kink-bands and the formation of subgrains. Other, less common occurrences of orthopyroxene include fine-grained (~1 mm) orthopyroxene in (neoblastic?) mosaic aggregates, occurring next to clinopyroxene and olivine (Figure 6.4h), and orthopyroxene intergrown as rims around Cr-spinel grains.

6.3.2.4 Clinopyroxene

Clinopyroxene is generally present in small amounts (<5 %) or absent, and can be subdivided into five textural types. The first type is clinopyroxene intricately intergrowth with Cr-spinel (Cpx-Sp symplectites, Figure 6.4b; see section 6.3.2.1 on Cr-spinel for a description) and occurs commonly in most samples. The symplectites are 0.1 – 2.5 mm in size and the individual crystal domains range from 20 to 100 µm.

The second type is defined as interstitial, vermicular to lobular grains of clinopyroxene that occur along grain-boundaries, often forming rims and tips on orthopyroxene porphyroclasts and occasionally embayed at orthopyroxene-olivine contacts (Figure 6.4e). They commonly occur intergrown with Cr-spinel, although not as intricately as the Cpx-Sp symplectites. Nearby clinopyroxene grains will often have a similar extinction angle, suggesting a poikilitic texture arising from a thin, three-dimensional veining network along grain boundaries. In a few instances clinopyroxene of this type, as well as Cpx-Sp symplectites, display undulose extinction.

The third type of clinopyroxene is less common and occurs as coarser porphyroclastic grains (0.1 – 4 mm, 1.5 mm average) with curved grain-boundaries that can form embayments in olivine and orthopyroxene grains (Figure 6.4a). Exsolution of orthopyroxene occurs as sharp and discrete lamella or more rarely as broad and diffuse lamella. Sometimes grains of this type are overgrown by near-poikilitic cpx, forming a rim with a different extinction angle. Some clinopyroxene has slight undulose extinction and grains are often micro-fractured.

The fourth type is also less common and is characterised by (neoblastic?) mosaic aggregates of fine-grained clinopyroxene (0.1 – 1 mm) with triple boundaries coexisting with other silicates such as orthopyroxene and olivine (Figure 6.4h). Generally, clinopyroxene of this type shows no deformation and, in some instances, twinning is preserved in them.

Lastly, the fifth type of clinopyroxene occurs solely in the plagioclase-bearing peridotite and constitutes large (1 – 20 mm) oikocrysts that enclose rounded olivine grains. Clinopyroxene of this type shows no crystal-plastic deformation and has no exsolution of orthopyroxene.

6.3.2.5 Plagioclase

Plagioclase occurs in relatively few samples and is completely replaced. In the plagioclase peridotite from Wadi Firaj (18MM222) it forms interstitial to poikilitic pockets around rounded olivine.

A rare but notable occurrence of plagioclase is as euhedral lath-shaped inclusions in spinel. These plagioclase inclusions were found in two harzburgites from the intruded mantle section at Jabal Suwayr (samples 18MM315 and 18MM270, Figure 6.6). The larger plagioclase-bearing spinel grains

(> ~0.5 mm) are strongly zoned with an inclusion-free, Al-rich core, and a Cr-rich and inclusion-rich rim. In smaller (mostly dark, Cr-rich) spinel grains, no zoning is visible and inclusions are present through-out.

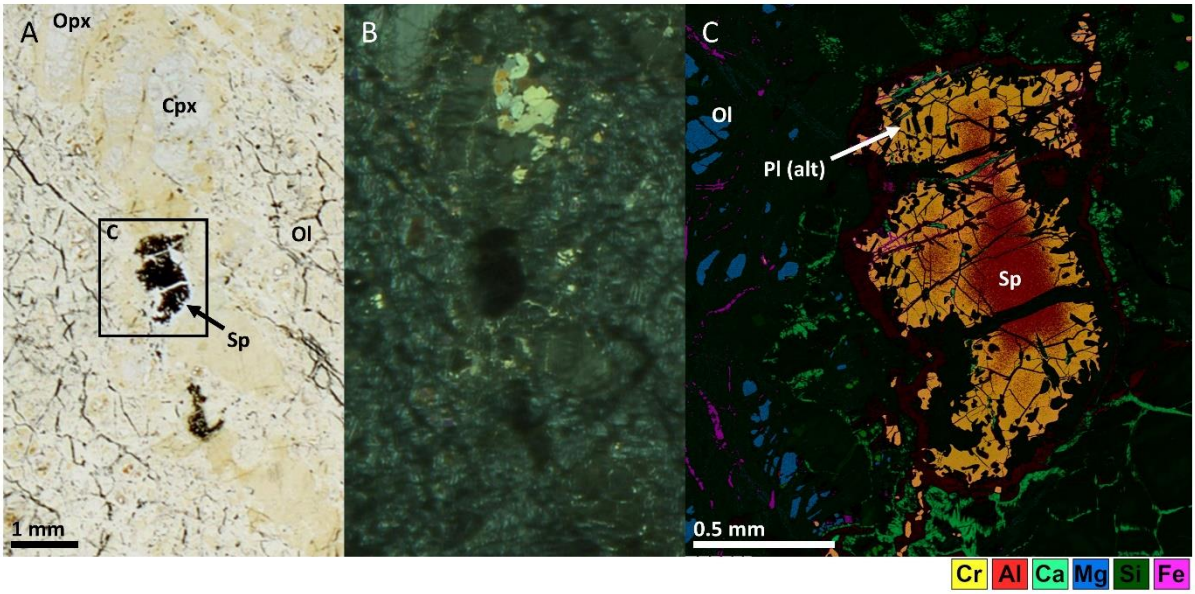

Figure 6.6: *Pockets of spinel and mosaic clinopyroxene within harzburgite matrix in sample 18MM315 from the mantle section at Jabal Suwayr. The spinel crystals are highly zoned (core Cr# = 0.36; rim Cr# = 0.52) and the rims contain chadacrysts consisting of near-euhedral plagioclase laths. Microphotographs in (a) plane-polarised light and (b) cross-polarised light, and (c) multi-element map.*

6.4 Results

6.4.1 Mineral chemistry

Mineral major element compositions of Cr-spinel, together with relicts of any coexisting olivine, orthopyroxene and clinopyroxene, were determined in 16 plagioclase-free harzburgites and 5 dunites at Cardiff University using a Zeiss Sigma HD EDS-SEM (spinel mineral chemistry is reported in Table VIII and silicate mineral chemistry is reported in Table VI). In these samples, a total of 77 Cr-spinel grains were analysed and several spots were analysed per grain. Fourteen samples (10 harzburgites and 4 dunites) are from the sub-crustal mantle sections and 7 samples (6 harzburgites and 1 dunite) are from the intruded mantle sections (Figure 6.2). Iron redox states for Cr-spinels were determined with the use of Mössbauer-calibrated secondary standards following Wood and Virgo (1989) (see Chapter 3 for more details).

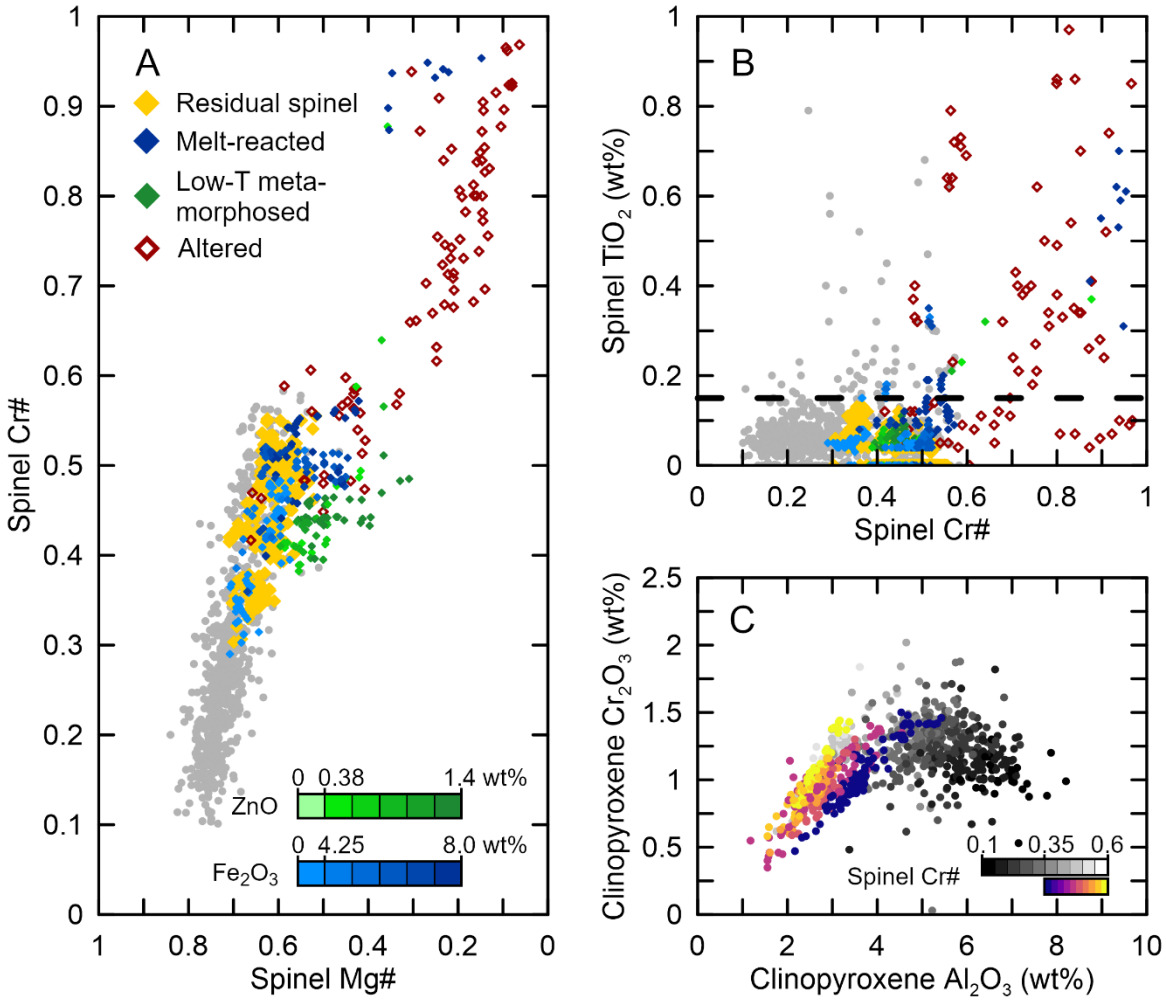

Figure 6.7: *(a) and (b) Cr-spinel mineral chemistry. Residual compositions fall on the depleted end of the global abyssal peridotites. (c) Clinopyroxenes are likewise depleted in Al_2O_3, correlating well with Cr-spinel compositions. Abyssal peridotites in grey (from Warren, 2016).*

Fresh Cr-spinels analyses fall on the depleted end of the abyssal peridotite array in a Cr#-Mg# diagram, with a subset extending to higher Mg# and Cr# (Figure 6.7a, Mg# = molar Mg / [Mg + Fe^{2+}] and Cr# = molar Cr / [Cr + Al]). Eighteen of the 21 samples have low TiO_2 (<0.15 wt%, Figure 6.7b) and of the three samples with elevated spinel TiO_2, one is a harzburgite from the intruded mantle near Jabal Suwayr (18MM303) and two (a pure dunite, 18MM054, and a harzburgite, 18MM060) are from the sub-crustal mantle at Jabal Taymah. The compositions of the three textural groups overlap significantly, with holly-leaf spinels occupying the entire range in Cr# (0.29 – 0.57), euhedral spinels limited to the depleted end (Cr# = 0.43 – 0.55) and Cpx-Sp symplectites on average slightly more aluminous (Cr# = 0.30 – 0.49).

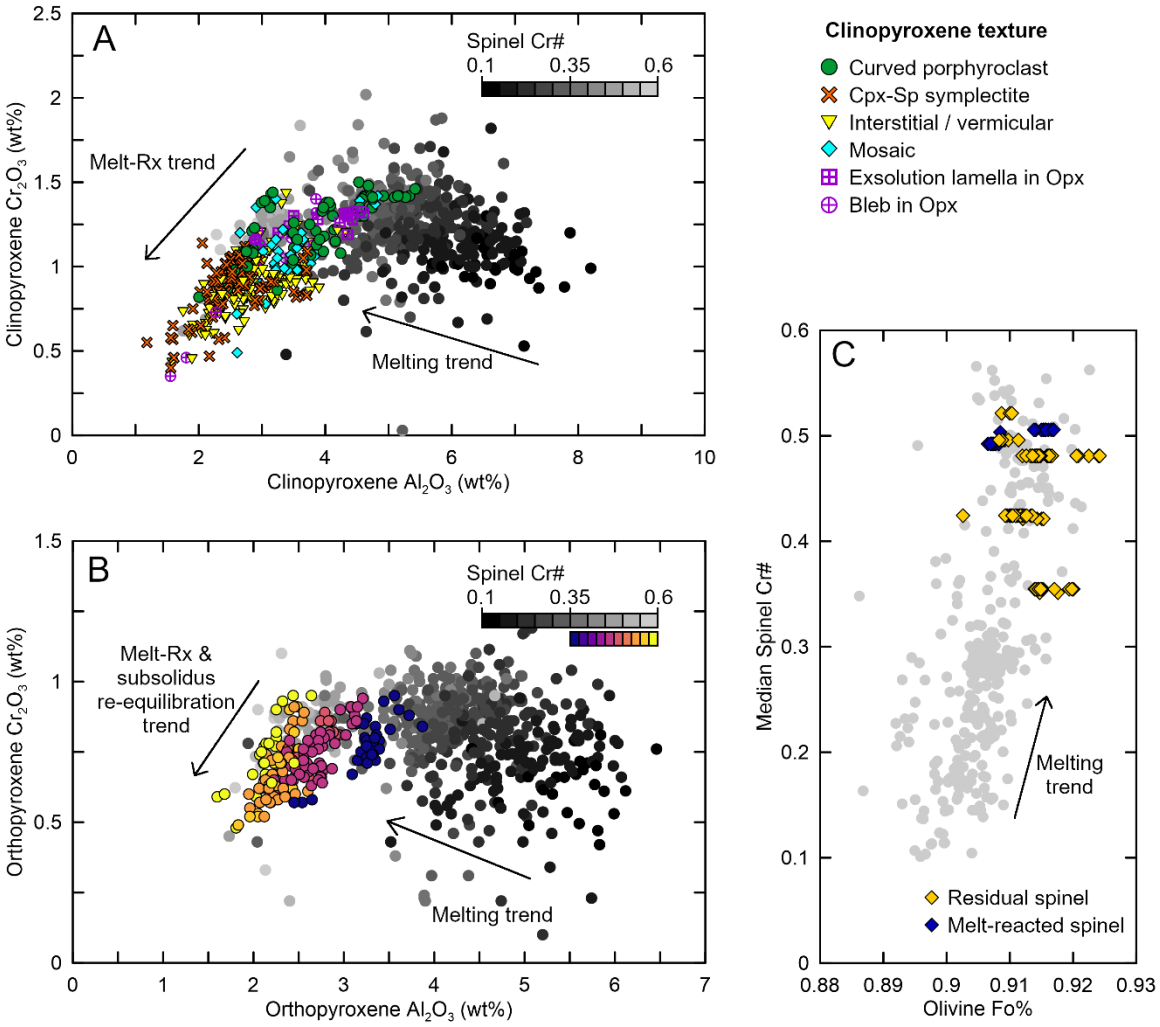

Figure 6.8: *Silicate mineral compositions of (a) clinopyroxene, (b) orthopyroxene and (c) olivine fall on the depleted end of the global abyssal peridotite fields (Warren, 2016). Clinopyroxenes that are interpreted to have formed through melt-reaction (Cpx-Sp symplectites and interstitial grains) are depleted in both Al_2O_3* ***and Cr_2O_3.*** *Orthopyroxene compositions correlate with the Cr# of coexisting spinel. A subset of orthopyroxene trends to lower Al_2O_3 and Cr_2O_3 contents, either due to melt-reaction or subsolidus re-equilibration. Olivine forsterite and spinel Cr# are not clearly correlated.*

The depleted character of the peridotites is also reflected in the forsteritic compositions of olivine (Fo = 90.3 – 92.4, avg. 91.2) and high Mg# in orthopyroxene (90.6 – 92.2, avg. of 91.5) and clinopyroxene (90.9 – 94.9, avg. 93.0; Figure 6.8). Orthopyroxene and clinopyroxene Al_2O_3 depletion correlates systematically with the average Cr# of coexisting spinel, and their compositions are comparable to the most refractory abyssal peridotites (Figure 6.7c and 6.8a-b). A subset of clinopyroxene grains, consisting of Cpx-Sp symplectites and interstitial grains that are interpreted as the products of late melt-reactions, extends to lower Al_2O_3 and Cr_2O_3 contents and a higher Mg#.

6.4.2 Characterisation of Cr-spinels: identifying residual compositions

With the aim of identifying those spinels which may be residual, the analyses are subdivided into four groups on the basis of petrographic observations and compositional relationships as follows: (1) altered ferrichromite present in most spinel grains along rims and fractures; (2) spinels (generally rims) that show geochemical evidence of metamorphism through ZnO enrichment (Figure 6.9a; Barnes, 2000); (3) spinels with indications for melt-reaction in the form of Fe^{3+} enrichment (Figure 6.9b; Dick and Bullen, 1984), Cpx-Sp symplectite textures (Seyler et al., 2001, 2007), or a dunite host-rock (Kelemen et al., 1995); (4) residual holly-leaf spinel compositions. The olivine-spinel geothermometer, based on Fe-Mg exchange, of Li et al. (1995) was used to determine equilibration temperatures for spinels that occurred with fresh relic olivine. The following section details the criteria and rationale of this classification scheme.

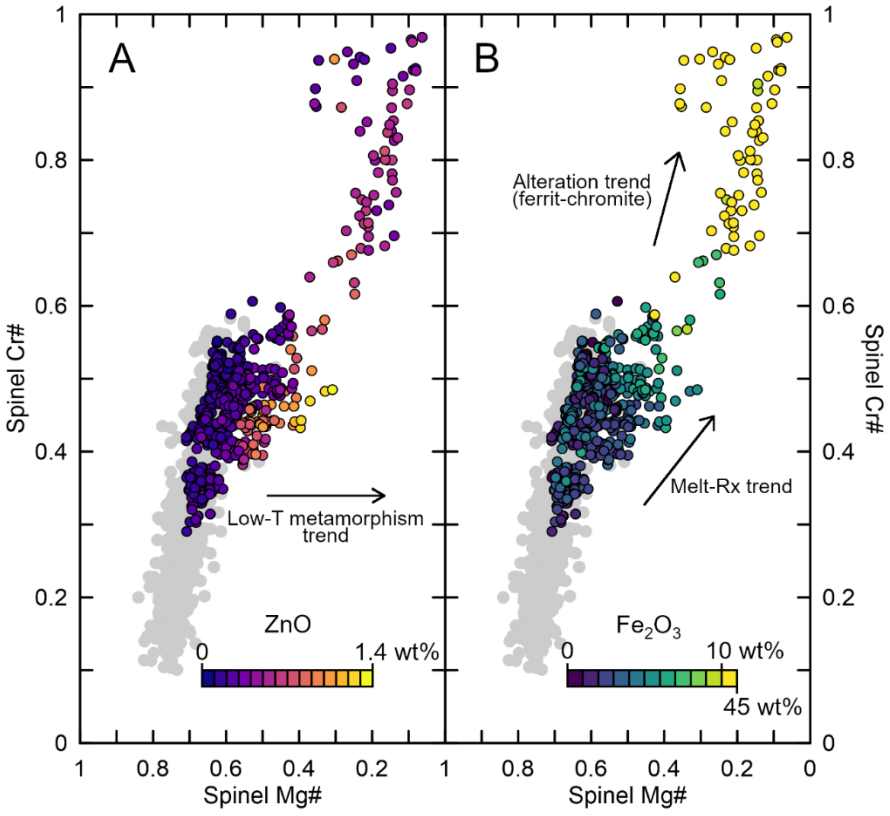

Figure 6.9 *(a) An increase in Cr-spinels ZnO content is highly correlated with a decrease in Mg#, extending to values lower than residual abyssal peridotites. (b) An increase in Cr-spinel Fe_2O_3 content correlates with increasing Cr# and decreasing Mg#, extending past the limits of the residual abyssal peridotite field. Abyssal peridotites in grey (from Warren, 2016).*

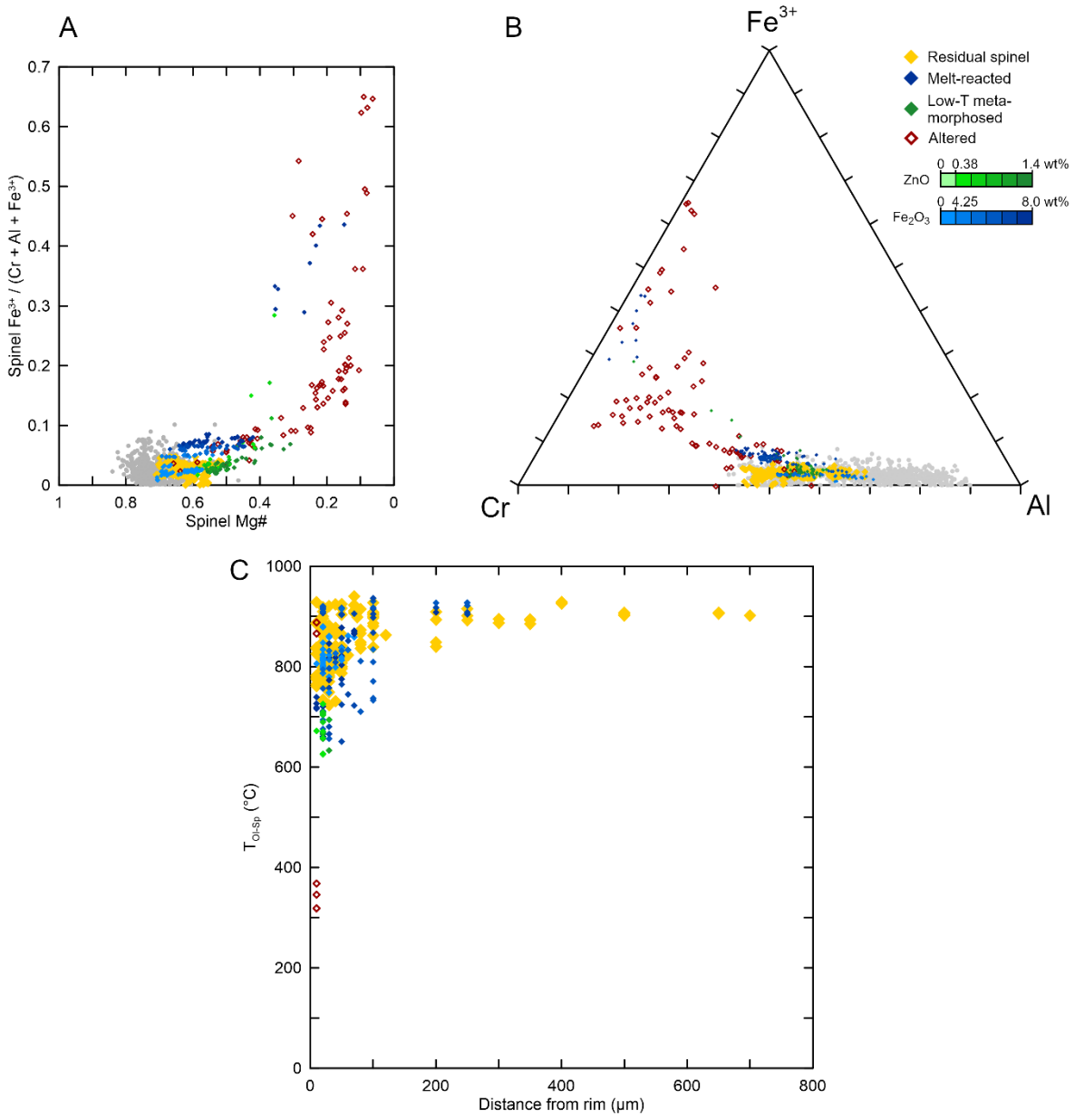

Figure 6.10: *(a) and (b) Cr-spinel mineral chemistry. Abyssal peridotites in grey (from Warren, 2016). (c) Equilibration temperatures recorded in spinels as function of the distance to the crystal rim. Residual cores of large grains record amongst the highest temperatures, whereas ZnO enriched rims record lower temperatures. Temperatures calculated using the olivine-spinel thermometer of Li et al. (1995).*

6.4.2.1 Group 1: Altered spinels

Analyses in group 1 consist of ferrichromite that formed along the rims and fractures of most spinel grains through alteration. In a small number of samples, the alteration is more pervasive throughout the grain. These altered regions are opaque in thin-section and distinctly bright on backscattered electron (BSE) images. Their compositions form an alteration trend that is characterised by a loss of Al_2O_3 and MgO and an increase in FeO and (initially) Cr_2O_3, followed by an increase in Fe_2O_3 and loss

of Cr_2O_3 (Figure 6.7a and 6.10a & b). A similar trend has been observed in other ophiolites and was linked to regional Prehnite-Pumpellyite to lower greenschist facies metamorphism (e.g., Burkhard, 1993). This interpretation is consistent with the low equilibration temperatures recorded in these spinels (318 – 888°C, median 368°C), which are interpreted to represent a loss of MgO rather than equilibrium temperatures.

6.4.2.2 Group 2: Low-T metamorphic spinels

Analyses in group 2 are characterised by elevated ZnO contents (up to 1.3 wt%) that correlate with a decrease in Mg# (Figure 6.9a). The zinc-enriched zones in spinel grains are generally limited to within 100 µm from the grain boundary and predominantly occur in the most intensely serpentinised samples. The olivine-spinel thermometer yields temperatures (625 – 726°C, median 671°C) that are cooler when compared to the spinels in group 3 and 4, and similar to the temperatures recorded by Group 1 spinels, they are interpreted to not reflect equilibrium temperatures (Figure 6.10c). A lack of correlation with Fe^{3+} contents suggests the process responsible for ZnO enrichment occurred under reducing conditions. Similar enrichments have previously been noted in spinels from Hess Deep (Allan and Dick, 1996) as well as various ophiolites (e.g., Gahlan and Arai, 2007) and is attributed to greenschist to mid-amphibolite facies metamorphism (Barnes 2000). A compilation of abyssal peridotites for which ZnO contents in spinel are available show that 95% of the analyses are <0.38 wt% (samples from Lena Trough at Gakkel Ridge, Hellebrand and Snow, 2003; Lassiter et al., 2014; Kane FZ at the MAR, Dick et al., 2010; and Hess Deep at the EPR, Allan and Dick, 1996; Edwards and Malpas, 1996; Hesse et al., 2015). Based on the above, group 2 spinels are defined as having ZnO contents >0.38 wt%.

6.4.2.3 Group 3: Melt-reacted spinels

Although most of the Masirah spinels have low TiO_2 contents (< 0.15 wt%), there are geochemical and textural indications that a subset of the spinels have been modified by melt-rock reaction. Some spinels show enrichment in Fe^{3+} (Fe_2O_3 > ~4.25 wt%), similar to the abyssal dunites and plagioclase peridotites described by Dick and Bullen (1984) and interpreted to result from interaction with a (relatively) oxidised melt (Figure 6.9b and 6.10a & b). They span the same range in Cr# as residual spinels, although they have a higher average Cr# (0.50). Spinels coexisting within a single sample display similar extents of Fe^{3+} enrichment, but generally do not show textural evidence of the melt-reaction. Two exceptions are sample 18MM054, a pure dunite, where spinels are euhdral and preserve symplectite reaction rims (Figure 6.4c & 6.5d) and sample 18MM315, which contains strongly zoned spinels with plagioclase inclusions in the rims (Figure 6.6).

Some spinels showed petrographical indications of melt-reaction without an enrichment in Fe^{3+}. Amongst these are spinels occurring in dunites (>90 vol.% olivine), which are generally believed to form through dissolution of orthopyroxene during shallow, focussed melt-flow (Kelemen et al., 1995). Also included in this group are the spinel-clinopyroxene symplectites, which have been interpreted either as crystallisation products of a trapped melt (Seyler et al., 2001) and/or by an orthopyroxene-consuming melt-reaction at low pressures (Seyler et al., 2007). A trapped reactive-melt origin is consistent with observations of deep embayments of olivine intruding into orthopyroxene and spinel-clinopyroxene films along orthopyroxene grain-boundaries, as well as a slightly more aluminous composition for symplectite spinels compared to residual spinels (Al_2O_3 being more incompatible and therefore expected to be enriched in the melt with respect to Cr_2O_3).

Group 3 spinels record temperatures of 651 – 936°C (median 818°C), largely overlapping with group 4 but extending to cooler temperatures.

6.4.2.4 Group 4: Residual spinels

The residual spinels are defined by a process of elimination based on the criteria of the three groups described above. Residual spinels have a holly-leaf texture and a large compositional range (Cr# 0.30 – 0.56). They record temperatures of 724 – 940°C (median 839°C). The large variation in residual Cr# is not related to mantle type, sample location, modal variations or spinel grain-size, and there are no systematic chemical variations in outcrops with banding defined by orthopyroxene contents.

Significant variation in Cr# occurs within thin-sections (ΔCr# 0 – 0.19, avg. 0.08) as well as within grains (ΔCr# 0 – 0.17, avg. 0.04). Compositional zoning is present in the majority of the Cr-spinels, with only 30% of the analysed grains showing a variation in Cr# of <0.01. The degree of zoning varies between weak (38%, Cr# variation <0.025), moderate (21%, Cr# variation < 0.05) and strong (10%, Cr# variation <0.20). Zoning is continuous and occurs in a range of textures, most commonly as patchy zoning (40%), followed by concentric zoning (i.e., core-rim zoning, 22%). Concentric zoning is mostly 'normal' (Al and Mg rich cores, Cr and Fe^{2+} rich rims), and in rare cases 'reverse'.

We interpret these large variations to represent residual compositions and hence related to mantle melting for three reasons. Firstly, the cores of the largest spinels in this group, which record the highest equilibration temperatures and are most likely to preserve residual compositions, show a similarly large range. Secondly, most of the intra-sample and intra-grain co-variations of Cr# and Mg# follow a slope parallel to the abyssal peridotite melting trend, rather than a melt-reaction trend (Figure 6.7a and 6.11). Thirdly, the depletion of spinel correlates closely to the depletion of other silicate minerals (Figure 6.7c and 6.8).

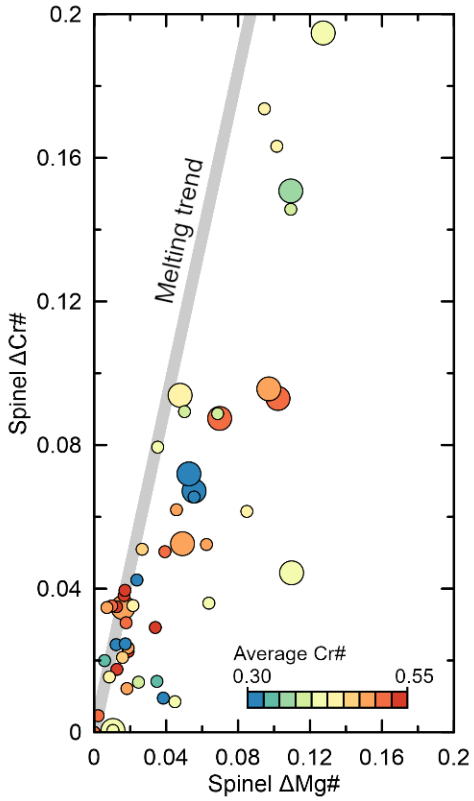

Figure 6.11: *Covariations of Cr# and Mg# in the residual spinel (group 4) illustrated as differences in Cr# and Mg# within hand samples (large circles) and individual grains (small circles) coloured by average Cr# composition (relative scale of axes is similar to the normal Cr#-Mg# diagram). Cr# and Mg# co-vary in proportions close to the melting trend defined by residual abyssal peridotites, regardless of the degree of Cr# depletion.*

6.5 Discussion

6.5.1 A high degree of melting and a thin igneous crust at Masirah

The mantle section at Masirah is petrologically and geochemically depleted, consistent with a high degree of melt extraction. The sampled peridotites likely represent the top of the melting column and their depletion is therefore likely to constrain the maximum extent of partial melting. Since the large variation in residual spinel Cr# is coupled with Mg# variation along a melting trend and correlates strongly with pyroxene depletion, this is interpreted to be a primary feature, caused by heterogeneous melt flow during mantle upwelling and melting. As such, the amount of melt extraction for Masirah as a whole is reflected by the average spinel Cr# (0.45), calculated as the median rather than the mean to reduce the effect of outliers, and corresponds to 15.8% partial melting of a hypothetical fertile mantle source (following the parameterisation by Warren, 2016).

To compare Cr-spinel compositions in the Masirah peridotites to modern mid-ocean ridges, the residual abyssal peridotite compilation of Warren (2016) was examined. Due to the variable nature

of spinel compositions at single localities, only locations for which there were 10 or more spinel analyses available were included in the comparison made here. The St Paul TF (MAR) and Atlantis II TF (SWIR) are each subdivided into three areas in the original database, but were treated as one for the purposes of this comparison. The three sub-areas at the Kane TF (MAR), however, showed significant variation in spinel composition and are therefore displayed separately. Locations where the interaction between a ridge and a hotspot is well established were excluded (Table 6.1). The comparison of Masirah to modern abyssal peridotites is shown in Figure 6.12. Masirah is unusually depleted for a slow-spreading ridge and more similar to the depletion expected for fast-spreading, magmatically-robust ridges.

Table 6.1. Overview of ridge-hotspot interaction locations

Ridge	Location	Hotspot	References
MAR	Ridge at 43°N	Azores hotspot	Michael and Bonatti, 1985; Dick et al., 1984
MAR	Kurchatov TF	Azores hotspot	Michael and Bonatti, 1985; Dick et al., 1984
MAR	Pico TF	Azores hotspot	Michael and Bonatti, 1985; Dick et al., 1984
MAR	Famous TF	Azores hotspot	Michael and Bonatti, 1985; Dick et al., 1984
MAR	Oceanographer TF	Azores hotspot	Michael and Bonatti, 1985; Dick et al., 1984
AAR	Conrad TF	Bouvet hotspot	Johnson et al., 1990; Kurz et al., 1998; Georgen et al., 2003
AAR	Bullard TF: East	Bouvet hotspot	Johnson et al., 1990; Kurz et al., 1998; Georgen et al., 2003
SWIR	Bouvet TF	Bouvet hotspot	Johnson et al., 1990; Kurz et al., 1998; Georgen et al., 2003
SWIR	Islas Orcadas TF	Bouvet hotspot	Johnson et al., 1990; Kurz et al., 1998; Georgen et al., 2003
SWIR	Shaka TF	Bouvet hotspot	Johnson et al., 1990; Kurz et al., 1998; Georgen et al., 2003
SWIR	Prince Edward TF	Marion Hotspot	Johnson et al., 1990; Georgen et al., 2001

A large amount of melt extraction from the Masirah mantle appears contradictory to the thin character of the igneous crust at Masirah. In the following subsections, three hypotheses to explain this discrepancy are explored: that a reduced melt supply at the Masirah paleo-ridge was the consequence of (1) a cold mantle, (2) the focussing of melts along-axis away from Masirah towards more magmatically robust segment centres, or (3) an ancient refractory domain in the mantle.

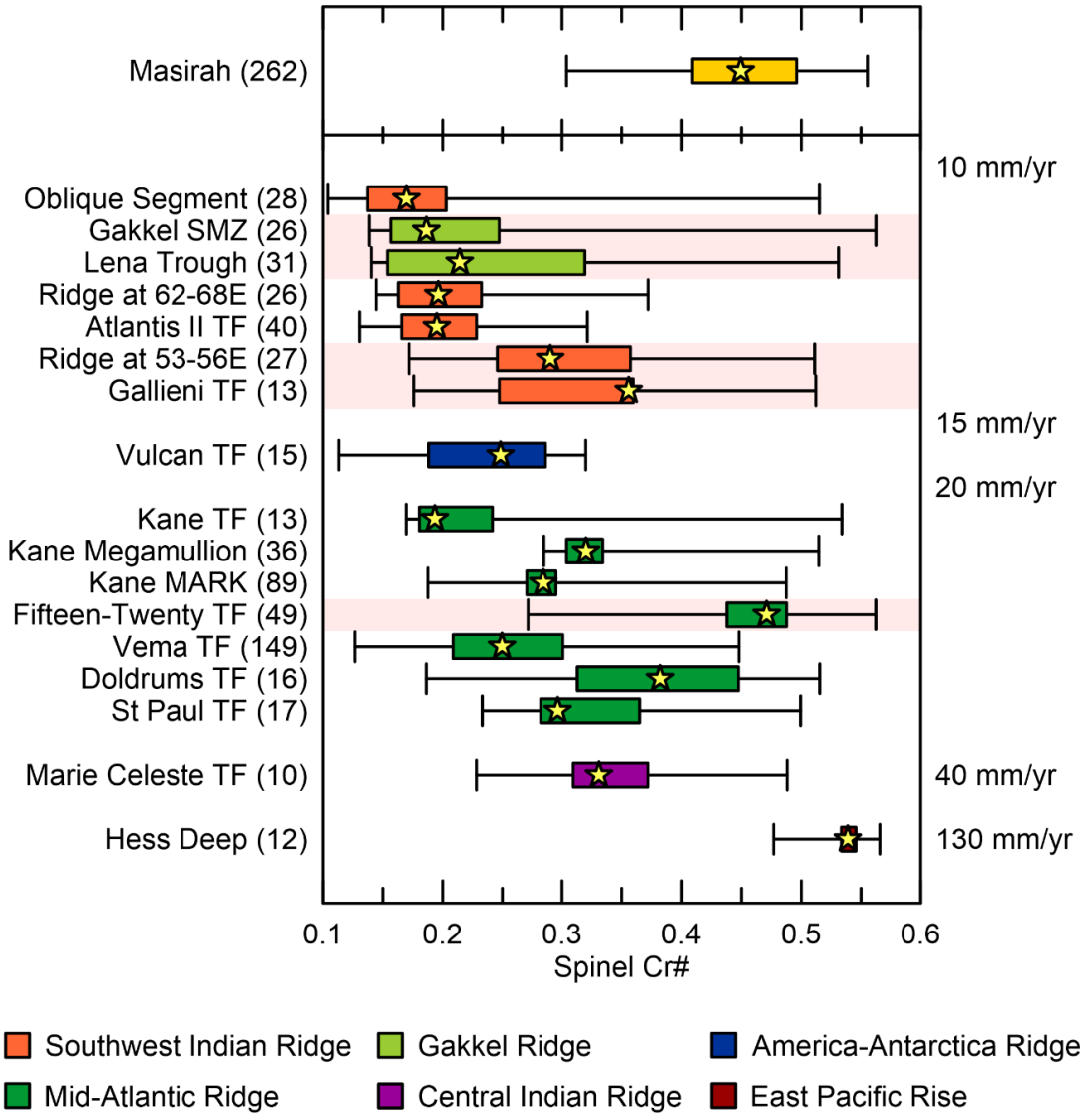

Figure 6.12: *Global abyssal peridotites grouped by sampling-location (from Warren, 2016; see text for further details) show a broad correlation between increasing spreading-rate (right) and Cr-spinel depletion. Masirah spinels, together with several locations highlighted in pink, are significantly more depleted than expected from this trend (see text for discussion). Data presented as boxplots, indicating medians (yellow stars), minima, maxima and first and third quartiles. Number of samples at each site indicated between brackets after location name.*

6.5.2 The effect of mantle temperature

Firstly, it has been suggested that melting at the Masirah paleo-ridge was reduced, due to a cooling effect from either an inferred transform fault or proximity to continental plates with a cold, thick lithosphere (Peters and Mercolli, 1998). Reduced melting can be the result of a suppressed mantle potential temperature (T_p) or a thick lithosphere, both of which decrease the height of the melting column.

An estimate of the Masirah T_p can be obtained using the PRIMELT3 model of Herzberg and Asimow (2015), which calculates T_p from the major element composition of an accumulated fractional primary melt. The primary melt composition is approximated by reverse modelling the fractional crystallisation of olivine and therefore requires a primitive melt composition as input (i.e., a melt that has only undergone olivine fractionation). If the melt instead has undergone olivine + plagioclase fractionation, the calculated T_p will too high. The model assumes a fertile mantle source, but the effects of variable peridotite fertility on T_p are minor (Herzberg and O'Hara, 2002; Herzberg and Asimow, 2008).

Axial dyke and lava analyses from MasirahDB (Table XII) were filtered for likely primitive melt compositions based on field descriptions (i.e., fine-grained, no phenocrysts) and alteration (loss on ignition < 3%), resulting in 9 dykes and 2 lavas. All compositions were primitive, with MgO contents in the dykes ranging 7.95 – 10.17 wt% (8.13 – 10.48 wt% recalculated anhydrous) and Mg# of 0.63 – 0.73 (calculated anhydrous, for Fe^{3+}/Fe_{sum} = 0.1), and MgO in the two lavas ranging 6.2 – 7.05 wt% (6.36 – 7.18 wt% anhydrous) with Mg# of 0.60 – 0.62. Six compositions (5 dykes and 1 lava) were flagged with a pyroxenite source error by PRIMELT3, indicating primary melt CaO contents are too low to be derived from peridotite melting (although this can also result from CaO mobility during alteration, Herzberg and Asimow, 2015). The remaining five compositions (4 dykes and 1 lava) resulted in calculated primary melts that are in equilibrium with mantle olivine of Fo% = 90.5 – 91.4, consistent with olivine compositions in the Masirah peridotites (Fo% = 90.3 – 92.4, avg. 91.2). The resulting mantle potential temperatures range between ~1350 – 1480°C (Table 6.2). The most primitive dyke (MA236) required the least amount of olivine addition (3.8%) and therefore probably provides the most accurate estimate for the mantle potential temperature (~1350°C). This temperature is close to the result for the most primitive lava (~1370°C) which required 16.2% olivine addition. The higher temperatures, corresponding to the more evolved dykes and lavas respectively, can potentially be explained by variable amounts of plagioclase fractionation, resulting in erroneously high temperature estimates (Herzberg and Asimow, 2015). These calculations show that the T_p of Masirah (~1350°C) is not anomalously low compared to other MORs (e.g., Putirka et al., 2007; Herzberg et al., 2007; Gregg et al., 2009).

Making inferences about the thickness of the on-axis lithosphere is more prone to uncertainty. Nevertheless, it is noteworthy that the sub-crustal mantle at Masirah is devoid of plagioclase-peridotites and contains minor volumes of gabbroic intrusions (see also Chapter 5, section 5.2.2), which does not fit the plum-pudding model for slow-spreading oceanic crust with a thick lithosphere (e.g., Cannat 1993). Furthermore, if melting was limited due to a thick lithosphere truncating the top of the melting column, relatively fertile peridotite compositions would be expected, rather than the

depleted ones observed. It is therefore concluded that there is no evidence in favour of a reduced melting column underneath the paleo-ridge.

Table 6.2. Summary of input and results of PRIMELT3 modelling

Sample details					Output from PRIMELT3					
Sample	**Type**	**MgO (wt% hydr.)**	**Mg#**	**LOI**	**%Ol addition**	**Primary MgO (wt%)**	**T_p (°C)**	**Ol Fo%**	**Residual Lithology**	**Error code**
J095	Dyke	8.25	0.65	2.81	17.9	15.02	1435.5	0.911	Spinel Peridotite	Pyroxenite Source … no solution
J148	Dyke	8.01	0.64	2.01	22.5	16.18	1465.8	0.914	Harzburgite	Pyroxenite Source … no solution
Z225	Dyke	8.32	0.65	2.02	19.5	15.63	1451.4	0.913	Spinel Peridotite	No Error
Z334	Dyke	7.95	0.64	2.52	22.6	16.16	1465.3	0.913	Harzburgite	Pyroxenite Source … no solution
Z335	Dyke	8.00	0.63	2.65	23.4	16.55	1475.4	0.914	Harzburgite	Pyroxenite Source … no solution
MA367	Dyke	9.29	0.67	2.35	17.1	15.65	1451.9	0.912	Harzburgite	No Error
MA266	Dyke	9.62	0.67	2.64	19.0	16.59	1476.3	0.914	Harzburgite	No Error
MA236	Dyke	10.09	0.72	1.93	3.8	11.80	1350.7	0.905	Spinel Peridotite	No Error
X176	Dyke	10.17	0.73	2.96	3.8	12.00	1356.1	0.908	Harzburgite	Pyroxenite Source … no solution
J210	Lavas	6.20	0.62	2.68	16.2	12.46	1368.2	0.906	Spinel Peridotite	No Error
P024	Lavas	7.05	0.60	2.07	28.1	17.07	1488.8	0.915	Spinel Peridotite	Pyroxenite Source … no solution

6.5.3 The role of melt focussing

A second possibility is that strong along-axis melt-focussing in the asthenospheric mantle resulted in the juxtaposition of a thin igneous crust on top of a relatively depleted mantle. This process is thought to prominent along slow-spreading ridges, where melt, aided by topographic gradients along the base of the lithosphere, is focussed to segment centres resulting in thicker igneous crust away from transform faults (the so-called bull's-eye pattern, e.g., Lin et al., 1990). To asses whether this mechanism can account for the 'missing melt' at Masirah, a comparison is made to the Vema Fracture Zone (FZ) along the slow-spreading Mid-Atlantic Ridge (MAR), where the mantle Bouguer anomaly indicates the presence of a bull's-eye crustal structure (Bonatti et al., 2003). Furthermore, the igneous crust at Vema has similarities to Masirah in terms of thickness (~2 – 3 km) and pseudo-

stratigraphy (Auzende et al., 1989). Residual peridotite Cr-spinel at Vema FZ is far less depleted however (median Cr# = 0.25; F_{melt} = 10.5%), suggesting that melt-focusing is unlikely to be solely responsible for the unusual depletion at Masirah.

6.5.4 Ancient refractory domains in the upper mantle

The third, and preferred, hypothesis is that the upper mantle underneath the Masirah paleo-ridge was dominated by highly refractory domains that have experienced previous (ancient) melting events. Such a scenario has been proposed based on Os isotopic ratios, which are able to record an age of melt extraction due to the parent isotope (^{187}Re) behaving as an incompatible element during mantle melting whereas the daughter isotope (^{187}Os) is compatible (e.g., Harvey et al., 2006). Extrapolating this observation to Masirah, and adding the constrains on both lithospheric architecture and melt compositions offered by Masirah, it is proposed that ancient melt depletion of the mantle, lithospheric architecture and MORB compositions are interrelated (Figure 6.13). Upwelling of refractory peridotites substantially decreases the total amount of melt produced in the melting column. Furthermore, because these peridotites contribute relatively little melt, melts derived from more fertile mantle components, such as pyroxenite veins reintroduced into the refractory matrix through mantle convection, should be comparatively over-represented in erupted MORBs. Consequently, the igneous crust that is produced is thinner and the erupted MORBs may extend to more enriched trace-element compositions (i.e., E-MORB; Wilson et al., 2013). MORB compositions at Masirah are variable and extend to enriched trace element and isotope compositions, consistent with preferential melting of fertile source regions in an otherwise refractory mantle (Mahoney et al., 1998; Chapter 4).

Observations from Masirah are therefore consistent with a model involving ancient refractory mantle domains and suggest that crustal architecture along slow-spreading ridges may be controlled by heterogeneous source fertility in the mantle. Similar highly refractory mantle domains have been identified along modern slow-spreading ridges at the Fifteen-Twenty FZ region of the MAR (Harvey et al., 2006), the Gallieni FZ and the Ridge at 53 – 56° E along the Southwest Indian Ridge (SWIR) on the flank of Marion Rise (Zhou and Dick, 2013; Li et al., 2019) and the Sparsely Magmatic Zone and Lena Trough along Gakkel Ridge (Liu et al., 2008; Lassiter et al., 2014). At these locations (highlighted in pink in Figure 6.12), the concurrence of extensive mantle exposures at the seafloor, significantly depleted Cr-spinels, and unradiogenic osmium isotopes in peridotites, are interpreted to require long-term melt depletion. Nevertheless, apart from the Fifteen-Twenty FZ region, spinels from these locations are less depleted than those from Masirah, suggesting Masirah is an extreme case.

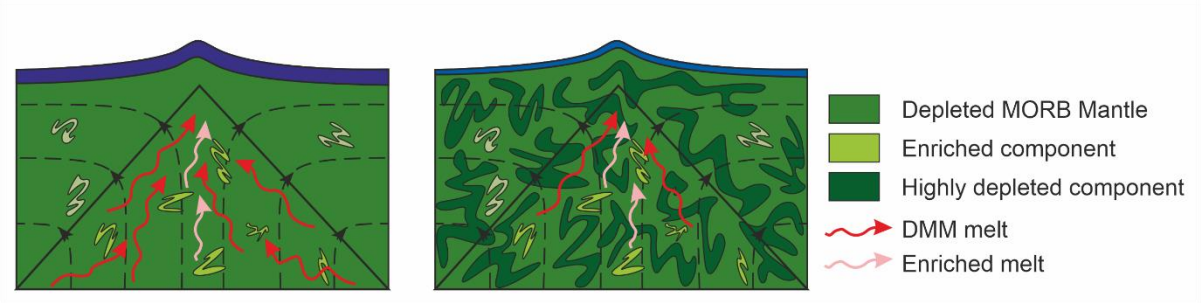

Figure 6.13: *Schematic diagram showing the effect of the inferred ancient, depleted mantle domain in the melting triangle underneath the Masirah paleo-ridge. Compared to a typical mid-ocean ridge that overlies a depleted MORB mantle (left) the Masirah mantle (right) is dominated by refractory mantle that is able to produce less melt. As a result, less melt (arrows) is produced, the igneous crust (blue) is thinner and enriched melts (pink arrows) are relatively over-represented in the total melt volume.*

Studies of the ridge segment between Marathon FZ and Fifteen-Twenty FZ (13° N – 15°20' N along the MAR) have proposed a link between magma supply and mode of crustal accretion, where the sporadic waning of magma-supply leads to the termination of magmatic accretion and the formation of detachment faults and OCCs (Smith et al., 2006; Escartin et al., 2008; MacLeod et al., 2009). Wilson et al. (2013) linked the recurring waxing and waning of the magma supply and MORB compositions at this ridge segment directly to variations in source fertility in a heterogenous upper mantle. However, this study suggests that the variation in possible crustal architecture is greater than previously thought, as Masirah does not conform readily to an OCC or thick igneous crust from a segment centre. Instead of a simple 'on-off' switch to detachment fault controlled spreading and formation of OCCs, a variable magma supply and the resulting thermal structure and rheology of the lithosphere is able to produce a spectrum of architectures.

6.6 Conclusion

The Masirah ophiolite is characterised by thin crust with enriched trace element compositions, yet is underlain by highly refractory peridotites. These observations can be reconciled in a model where upwelling of an ancient domain of depleted mantle led to an overall reduced melt supply and a high proportion of melts from fertile mantle components relative to those from the depleted peridotites. Such refractory domains may be common in the present-day upper mantle underneath MORs and as a result may be a key factor in understanding the variations of crustal accretion and MORB compositions that occur along slow-spreading ridges. Masirah shows that a reduced melt supply does not necessarily form OCCs, however, indicating the variation in crustal architecture at mid-ocean ridges may be greater than previously thought.

7. Conclusions and outlook

7.1 Conclusions

This thesis presents an investigation into the Masirah ophiolite from a modern mid-ocean ridge perspective. Unlike many other ophiolites, Masirah is thought to have formed at a slow-spreading, 'true' MOR, as indicated by dyke and lava major element compositions that fall on dry magma differentiation trends, MORB-like trace element compositions that lack the elevated Th/Yb and supressed Ti/V characteristic of supra-subduction zone settings, and mantle Cr-spinels with Cr# < 0.60 consistent with dry oceanic melting. It is therefore uniquely suited to test current theories of ocean lithosphere accretion at slower spreading ridges.

The existing model for the formation and evolution of Masirah is reviewed and updated with new geochemical and high-precision geochronological constraints. The dykes and lavas that formed on-axis display a wide range of trace element compositions that form a continuous trend towards, and partly overlap with, the later alkaline dyke and lava suite. Conversely, some dykes and lavas originally thought to be alkalic due to their stratigraphic relationships (e.g., the dyke swarms in the mantle), are MORB-like tholeiites. Mineral compositions of axial and alkalic gabbros similarly form a single differentiation trend. Uranium-lead dates of single zircons from the axial gabbroic sequence indicate that the Lower and Upper Nappe present on the island formed respectively ~135 Ma and ~131 Ma, instead of ~150 Ma as proposed in earlier models. Consequently, the alkalic magmatism, originally thought to have occurred ~20 Ma off-axis, directly succeeded seafloor spreading and records a transition from on-axis to near off-axis magmatism. The broad trend observed in dyke and lava trace elements compositions can be attributed to the stochastic tapping of a heterogeneous mantle, but with an overall progressive decrease in the degree of melting coupled with a proportionally increased contribution of a more enriched and fusible mantle source.

Two potential mechanisms are proposed for this evolution. The first possibility is that Masirah records a process that could be an intrinsic part of ocean crustal accretion, with seamounts forming close to the ridge axis due to imperfect melt focussing. The second possibility is that the event is related to the tectonic reorganisation of plate motions that took place in the Indian Ocean around that time, potentially resulting in complex plate boundary geometries that caused seafloor spreading to halt and localised compression leading to uplift and extension leading to small degree melting and renewed magmatism. Further work is needed to test these possibilities.

The architecture of the ocean lithosphere at Masirah departs from current theories of slow-spreading ridges, which predict a 6 – 7 km thick layered igneous crust at magmatically robust spreading centres and a discontinuous, plum-pudding crust at the magma poor segment-ends.

Instead, the igneous crustal sequence at Masirah is thin (~2 km) but nevertheless preserves a complete Penrose-style layered sequence. Furthermore, the upper-to-lower crust volumetric ratio (~0.4 : 0.6) contrasts with most (seismically imaged) oceanic crust (~0.7 : 0.3 to ~0.8 : 0.2). The field observations at Masirah are consistent with the mineral compositions of the gabbroic lower crust, which are significantly more primitive than oceanic gabbros sampled along modern MORs and suggest that magmas in the lower crust underwent only small amounts of crystallisation before being extracted to form the upper crust. The bulk composition of the Masirah igneous crust is consistent with a primary MORB melt in equilibrium with mantle olivine, indicating there is no 'missing melt', and trace element fractionation between the upper and lower crust is consistent with small amounts of crystallisation. The presence of a sheeted dyke complex and the absence of indicators for significant tectonic strain on-axis, argue for crustal accretion by magmatic spreading. As such, although the thin crust demonstrates Masirah formed under melt poor conditions, melt supply was nevertheless spatially and temporally robust enough for magmatism to accommodate plate separation. The thick gabbro-dyke transition (~500 m) and variability in dyke-flow direction as reconstructed by AMS, indicate this was a highly three-dimensional process with a significant role for horizontal dyke injection.

Despite the low melt supply inferred from the thickness of the igneous crust, the underlying mantle section is characterised by highly refractory peridotites. Residual mantle Cr-spinel compositions are amongst the most depleted found in present-day abyssal peridotites and record a degree of melting that is unusually high when compared to other slow-spreading ridges. These contrasting observations can be reconciled in a model where a large portion of the upwelling mantle consisted of a domain that was previously depleted in an ancient melting event, leading to an overall reduced melt supply at Masirah. The reintroduction of enriched and more fusible components through mantle convection, stirred over time with this ancient refractory domain, accounts for the relative overrepresentation of E-MORB compositions in the total melt volume produced, as reflected in the erupted dykes and lavas. These observations indicate that besides mantle potential temperature and the thickness of the lithosphere, mantle fertility exercises an important primary control on the degree of melting and hence lithospheric architecture and MORB compositions.

The Masirah ophiolite shows that the variability of permissible slow-spreading crustal geometries is greater than previously thought and that a basaltic seafloor should not automatically be interpreted to correlate with a thick magmatic crust. Future studies of oceanic crust should therefore consider Masirah-type lithosphere as a third possible end-member when interpreting seafloor bathymetry, seismic data and gravity anomalies.

7.2 Future work on Masirah:

The new constraints for the evolution of Masirah presented in this study form the basis for further work on the island. Some outstanding questions as well as potential avenues for future research are outlined below.

7.2.1 Geochronological constraints for the alkaline magmatism and the nappe structure of Masirah

Following the determination of an age for seafloor spreading at the Masirah ophiolite using modern techniques, a next important step is to constrain the precise timing and duration of the near off-axis magmatism. As discussed in Chapter 4, current age constraints contain large uncertainties and as a result, the mechanisms that produced off-axis magmatism remain poorly constrained. Detailed geochronology on the later, crosscutting alkaline units can provide further support for the model of a transitional magmatic event, as well as test the tectonic setting in which they formed. If seamount volcanism was an intrinsic part of seafloor spreading at Masirah due to imperfect focussing of melts to the ridge axis, the alkaline magmatism should affect both nappes roughly equally and continued off-axis magmatism is expected to last roughly the same amount of time in each nappe. If the magmatism is related to the reorganisation of plate-motions in the Indian Ocean, however, alkaline rocks might be expected to be more common in the younger Upper Nappe and of a similar age as those in the Lower Nappe.

The finding that crustal accretion of the Masirah Lower and Upper Nappes took place at distinct times (respectively ~135.1 – 135.0 Ma and 131.4 – 130.6 Ma), supports the nappe structure of the Masirah ophiolite that was mapped by Peters et al. (1995) and inferred from seismic studies (Beauchamp et al., 1995; Rodriguez et al., 2020). It also suggests that precisely determined crystallisation ages can be a useful and independent criterium for determining the nappe-provenance of outcrops for which it is otherwise unclear. When a nappe thrust fault structure was not observed in the field, criteria of comparison were used with known occurrences of the Upper and Lower Nappes. This is complicated, however, by the fact that few lavas and no sediments are preserved in the Upper Nappe, while no clear mantle section is preserved in the lower Nappe. This introduces the potential for a circular line of reasoning where all mantle exposures must be Upper Nappe and all sediments Lower Nappe. Notably, mantle outcrops in the southwest of the island, many of them intruded by alkaline plutons and dyke swarms, are generally attributed to the Upper Nappe on the geological map, whereas nearby sediments (mainly the Kalban Unit) and lavas (mainly the out-of-sequence lavas) were assigned on the Lower Nappe. Similarly, the alkaline seamount structures near Shi'inzi, surrounded by exposures of mantle and gabbro in the north of the island, are interpreted to be a Lower Nappe exposure in a tectonic window in the Upper Nappe. An alternative interpretation is that the intruded mantle, lavas and sediments actually belong to the

same nappe, and can be tested by a careful comparison of radiometric dates. Furthermore, recent models for the emplacement of the Eastern Oman Ophiolites involve the formation of a doubly-vergent thrust stack of numerous ophiolite sheets, formed during transpressive strike-slip plate motions (Rodriguez et al., 2020). The potential complexities of such a system raise the possibility that the structurally complex regions of Masirah may expose fragments of additional nappes beyond the currently recognised Lower and Upper Nappe.

7.2.2 Paleomagnetic constraints on the on-axis architecture of the lithosphere

The model for the formation of Masirah-style 'Penrose on a diet' crust through magmatic spreading is supported by the presence of a sheeted dyke complex. Although a significant part of the dyke complex on Masirah consists of dykes intruding gabbro, the formation of a stratigraphic level consisting of 100% dykes is strong evidence for magmatically accommodated spreading. A second prediction of the magmatic spreading model, namely that dykes primarily intrude sub-parallel to the ridge-axis, remains to be investigated, however. Whereas dyke trends on Masirah are locally consistent, they can be variable on the nappe- and island-scale and it is not possible from field observations alone to constrain how much of this variability can be related to later tectonic rotation. Previous studies that described the dominantly ENE-WSW trending sheeted dyke complex in the interior of the southern part on island, proposed that this orientation remained intact during obduction and could therefore be interpreted to reflect the strike of the Masirah paleo-spreading ridge (e.g., Peters and Mercolli, 1998). This hypothesis can be tested by measuring the paleomagnetic remanence direction recorded in the dykes. Using this approach, it is possible to constrain all net tectonic rotations that affected a dyke after formation, allowing the original orientation (i.e., at the moment of intrusion) to be reconstructed (e.g., Bonhommet et al., 1988; MacLeod et al., 1990; Morris et al., 1990). Assuming dykes originally formed as vertical structures, there are two solutions for rotating a dyke back to its original orientation in the paleo-north coordinate system. The reliability of this net rotation can subsequently be evaluated by the effect it has on the orientation of the overlying lavas or layering in gabbros. For the original dyke orientation to be realistic, both of these should be rotated towards the horizontal. By comparing the original dyke trends derived in such a manner, it is possible to reconstruct the on-axis architecture and answer several important questions: Is the orientation of the sheeted dyke complex consistent within the nappes and across the island? Did the crustal dyke swarms in the gabbro-dyke transition, as well as the dyke swarms intruding the mantle sections, form parallel to the sheeted dykes? How prevalent was horizontal versus vertical AMS-derived melt flow within dykes in the paleo-coordinate system? Were the crustal and mantle dyke-swarms primarily fed laterally or from below? Additionally, by comparing the magnetic remanence directions recorded by carefully selected early

and late dykes, as well as dykes and intruded gabbros, it is possible to provide some constraints on the amount of rotation that took place on-axis during crustal accretion. This last test could potentially provide further support for the case against a significant role for tectonic spreading at Masirah, which is typically accommodated along rotational detachment faults (e.g., MacLeod et al., 2011).

7.2.3 Masirah: a natural laboratory for the melt poor endmember of slow-spreading ridges

The melt poor conditions during the accretion of the Masirah oceanic crust make it a valuable case study for determining how MORB melts are modified at crustal levels prior to eruption. Trace element and isotope compositions of erupted MORB glasses are commonly used to assess the heterogeneity of the upper mantle (e.g., Zindler et al., 1984; Hofmann et al., 1986). The full scale of the heterogeneity of the mantle source region is obscured, however, though the process of melt aggregation and magma mixing in crustal melt lenses (e.g., Rubin and Sinton, 2007). At melt-poor slow-spreading ridges the observed variability in MORB trace element and isotope compositions is greater than at faster spreading, magmatically robust ridges, where long-lived melt lenses facilitate homogenisation. Recent studies have shown that the gabbroic cumulates preserve a greater degree of the mantle-inherited variability and that this can be measured by analysing isotope compositions of single micro-drilled clinopyroxene and plagioclase crystals (Jansen et al., 2018; Lambart et al., 2019). Using similar techniques to the crystal cargo caried by MORBs, other studies have come to the same conclusion (e.g., Lange et al., 2013a). Applying the same techniques to Masirah is valuable for two reasons. Firstly, a comparison between the compositions of the gabbroic cumulates, the erupted dykes and lavas, and the crystal cargo in melts, enables an assessment of the degree of homogenisation that occurs at a melt poor endmember of slow spreading ridges with a well-defined architecture, compared to more magmatically robust spreading segments. The primitive nature of the gabbroic lower crust, indicating short magma residence times, predict that crustal-level magma mixing was not an extensive process. Secondly, such an exercise will provide more information on the accretion of the lower crust at Masirah. The observed diversity in gabbro mineral compositions should reflect the variability in the erupted N-MORB to E-MORB melts, but it remains to be investigated whether all erupted melts contributed equally to the crystallisation of the gabbros. Similarly, it remains unknown whether alkaline hornblende gabbros represent the cumulate counterpart of the alkaline lavas or whether they are highly differentiated MORB-like melts that stalled in the lithosphere.

7.2.4 The search for Masirah-style lithosphere:

It remains to be investigated whether the lithospheric configuration at Masirah is an anomaly or represents a third end-member for slow-spreading oceanic lithosphere. As noted in Chapter 5, the

observed magmatic spreading under melt poor conditions contradicts the expectation of a thick brittle lithosphere under those conditions. Nevertheless, several tectonic settings are potential candidates for hosting Masirah-style lithosphere. The combination of a refractory mantle (as proposed in Chapter 6) and a hotter ambient mantle may create the right conditions: a thin lithosphere overlying an asthenosphere that was unable to produce large volumes of melt despite being hot. Furthermore, the thickness of the lithosphere might be a highly transient feature that varies strongly with melt supply to the ridge. Periods of a relatively robust melt supply would according to this hypothesis be able to thin the lithosphere and accommodate magmatic spreading, alternating with periods of magma-starved tectonic spreading. In this model, Masirah might be analogous to certain domains of volcanic seafloor along amagmatic ultraslow spreading ridges (e.g., Cannat et al., 2006). Although these ridges are notable for their extensive exposures of mantle peridotite, they are also characterised by a discontinuous magmatic crust, the architecture of which remains poorly constrained (more than half of the seafloor at the easternmost southwest Indian Ridge is volcanic for example, Cannat et al., 2006).

Alternatively, crust may be magmatically accreted on the conjugate plate to an oceanic core complex (OCC). In this scenario, spreading is mostly tectonic but since strain is concentrated along the detachment fault and internal deformation mostly restricted in the core-complex footwall block, the hanging wall may be expected to record little tectonic strain, while it is able to accommodate magmatic spreading when melt supply allows it. Such a configuration is often assumed in numerical models of detachment faulting to provide a mechanism for magmatic spreading (M) and tectonic spreading (T) to alternate when M = ~0.5 (Buck et al., 2005; Tucholke et al., 2008). There are no direct observations of hanging walls across from OCCs to test if this configuration is realistic. Further surveys of the conjugate plates at OCCs are needed to investigate this.

One more possible occurrence of Masirah-type crust in particular is highlighted in more detail. IODP expedition 390/393 set sail early June 2022 and will drill cores along an off-axis transect in the South Atlantic Ocean at 31° S. A survey of the transect has indicated that the seismically imaged igneous crust at one of the planned drill sites (CREST05) is thin (3.6 ± 0.3 km) and that the relative difference in thickness between the upper and lower crust is similar to Masirah (2.2 ± 0.6 km and 1.3 ± 0.6 km respectively; Christeson et al., 2020). Additionally, a study analysing fault scarps on the sea floor along this transect concluded that spreading was dominantly magmatic (Estep et al., 2021). Since the primary scientific objectives are the investigation of low-temperature hydrothermal systems in older oceanic crust, only the uppermost parts of the basaltic crust are targeted. A first order test to compare the recovered lavas to Masirah, however, would be to see if they record the same low levels of magmatic differentiation (i.e., high Mg#) and short magma-residence times (i.e., a high

variability in the trace element and isotope compositions of erupted melts) as in this study. Furthermore, bathymetry surveys have identified numerous small volcanic seamounts along the South Atlantic transect, indicating off-axis magmatism (Christeson et al., 2020). Although these mounts are not targeted for drilling, the drill cores may recover off-axis lava flows covering the axial lavas. In that case it would be interesting to compare their compositions with the near off-axis lavas from Masirah and test whether near off-axis magmatism is a common process at mid-ocean ridges and whether these late melts significantly change the bulk composition of the ocean crust.

8. References

Abbotts, I. L. (1978). High-potassium granites in the Masirah ophiolite of Oman occurs as xenolithic blocks , the pegmatite as a breccia matrix , and the gabbro and dolerite occur. *Geological Magazine*. Cardiff University **115**, 415–425.

Abbotts, I. L. (1979a). A field, petrological and geochemical study of the Masirah Ophiolite, Oman. University of Birmingham.

Abbotts, I. L. (1979b). Intrusive processes at ocean ridges: Evidence from the sheeted dyke complex of Masirah, Oman. *Tectonophysics* **60**, 217–233.

Abelson, M., Baer, G. & Agnon, A. (2001). Evidence from gabbro of the Troodos ophiolite for lateral magma transport along a slow-spreading mid-ocean ridge. *Nature* **409**, 72–75.

Alabaster, T., Pearce, J. A. & Malpas, J. (1982). The volcanic stratigraphy and petrogenesis of the Oman ophiolite complex. *Contributions to Mineralogy and Petrology* **81**, 168–183.

Allan, J. F., Batiza, R., Perfit, M. R., Fornari, D. J. & Sack, R. O. (1989). Petrology of lavas from the lamont seamount chain and adjacent East Pacific rise, 10° N. *Journal of Petrology* **30**, 1245–1298.

Allan, J. F. & Dick, H. J. B. (1996). Cr-Rich Spinel as a Tracer for Melt Migration and Melt–Wall Rock Interaction in the Mantle: Hess Deep, Leg 147. *Proceedings of the Ocean Drilling Program, 147 Scientific Results* **147**.

Allmendinger, R. W., Cardozo, N. C. & Fisher, D. (2013). *Structural Geology Algorithms: Vectors & Tensors*. Cambridge, England: Cambridge University Press.

Anderson, M., Wanless, V. D., Perfit, M., Conrad, E., Gregg, P., Fornari, D. & Ridley, W. I. (2021). Extreme Heterogeneity in Mid-Ocean Ridge Mantle Revealed in Lavas From the 8°20'N Near-Axis Seamount Chain. *Geochemistry, Geophysics, Geosystems* **22**, 1–22.

Anenburg, M. (2020). Rare earth mineral diversity controlled by REE pattern shapes. *Mineralogical Magazine* **84**, 629–639.

Annen, C., Blundy, J. D. & Sparks, R. S. J. (2006). The Genesis of Intermediate and Silicic Magmas in Deep Crustal Hot Zones. *Journal of Petrology* **47**, 505–539.

Anonymous (1972). Penrose field conference on ophiolites. *Geotimes* **17**, 24–25.

Arai, S. (1994). Characterization of spinel peridotites by olivine-spinel compositional relationships: Review and interpretation. *Chemical Geology* **113**, 191–204.

Arevalo, R. & McDonough, W. F. (2010). Chemical variations and regional diversity observed in MORB. *Chemical Geology* **271**, 70–85.

Augustin, N., van der Zwan, F. M., Devey, C. W., Ligi, M., Kwasnitschka, T., Feldens, P., Bantan, R. A. & Basaham, A. S. (2016). Geomorphology of the central Red Sea Rift: Determining spreading processes. *Geomorphology*. Elsevier B.V. **274**, 162–179.

Auzende, J.-M., Bideau, D., Bonatti, E., Cannat, M., Honnorez, J., Lagabrielle, Y., Malavieille, J., Mamaloukas-Frangoulis, V. & Mevel, C. (1989). Direct observation of a section through slow-spreading oceanic crust. *Nature* **337**, 726–729.

Bach, W. & Früh-Green, G. L. (2010). Alteration of the Oceanic Lithosphere and Implications for Seafloor Processes. *Elements* **6**, 173–178.

Barnes, S. J. (2000). Chromite in komatiites, II. Modification during greenschist to mid-amphibolite

facies metamorphism. *Journal of Petrology* **41**, 387–409.

Barton, P. J., Owen, T. R. E. & Wright, R. S. (1990). Preliminary Results and Interpretation Extensional. *Tectonophysics* **173**, 319–331.

Batiza, R. (1996). Magmatic segmentation of mid-ocean ridges: a review. *Geological Society Special Publication* **118**, 103–130.

Beauchamp, W. H., Ries, A. C., Coward, M. P. & Miles, J. A. (1995). Masirah Graben, Oman: a hidden Cretaceous rift basin? *American Association of Petroleum Geologists Bulletin* **79**, 864–879.

Behn, M. D. & Ito, G. (2008). Magmatic and tectonic extension at mid-ocean ridges: 1. Controls on fault characteristics. *Geochemistry, Geophysics, Geosystems* **9**.

Bennett, E. N., Lissenberg, C. J. & Cashman, K. V. (2019). The significance of plagioclase textures in mid-ocean ridge basalt (Gakkel Ridge, Arctic Ocean). *Contributions to Mineralogy and Petrology*. Springer Berlin Heidelberg **174**, 1–22.

Beurrier, M. (1987). Géologie de la nappe ophiolitique de Samail dans les parties orientale et centrale des montagnes d'Oman. Université Pierre-et-Marie-Curie, Paris VI.

Bird, R. T. & Naar, D. F. (1994). Intratransform origins of mid-ocean ridge microplates. *Geology* **22**, 987–990.

Blackman, D. K., Cann, J. R., Janssen, B. & Smith, D. K. (1998). Origin of extensional core complexes: Evidence from the Mid-Atlantic Ridge at Atlantis Fracture Zone. *Journal of Geophysical Research: Solid Earth*. John Wiley & Sons, Ltd **103**, 21315–21333.

Blackman, D. K., Ildefonse, B., John, B. E., Ohara, Y., Miller, D. J., MacLeod, C. J. & And, the E. 304/305 S. (2006). Expedition 304/305 summary. *Proceedings of the Integrated Ocean Drilling Program* **304/305**.

Blundy, J. D. & Wood, B. J. (1991). Crystal-chemical controls on the partitioning of Sr and Ba between plagioclase feldspar, silicate melts, and hydrothermal solutions. *Geochimica et Cosmochimica Acta* **55**, 193–209.

Bonatti, E., Brunelli, D., Buck, W. R., Cipriani, A., Fabretti, P., Ferrante, V., Gasperini, L. & Ligi, M. (2005). Flexural uplift of a lithospheric slab near the Vema transform (Central Atlantic): Timing and mechanisms. *Earth and Planetary Science Letters* **240**, 642–655.

Bonatti, E., Ligi, M., Brunelli, D., Cipriani, A., Fabretti, P., Ferrante, V., Gasperini, L. & Ottolini, L. (2003). Mantle thermal pulses below the Mid-Atlantic Ridge and temporal variations in the formation of oceanic lithosphere. *Nature* **423**, 499–505.

Bonhommet, N., Roperch, P. & Calza, F. (1988). Paleomagnetic arguments for block rotations along the Arakapas fault (Cyprus). *Geology* **16**, 422–425.

Borradaile, G. J. & Gauthier, D. (2003). Interpreting anomalous magnetic fabrics in ophiolite dikes. *Journal of Structural Geology* **25**, 171–182.

Borradaile, G. J. & Jackson, M. (2004). Anisotropy of magnetic susceptibility (AMS): Magnetic petrofabrics of deformed rocks. *Geological Society Special Publication* **238**, 299–360.

Boschi, C., Früh-Green, G. L. & Escartín, J. (2006). Occurrence and significance of serpentinite-hosted, talc-and amphibole-rich fault rocks in modern oceanic settings and ophiolite complexes: An overview. *Ofioliti* **31**, 129–140.

Bosellini, A. (1986). East Africa continental margins. *Geology* **14**, 76–78.

Boudier, F. & Nicolas, A. (2007). Comment on “dating the geologic history of Oman’s Semail ophiolite: Insights from U-Pb geochronology” by C. J. Warren, R. R. Parrish, D. J. Waters and M. P. Searle. *Contributions to Mineralogy and Petrology* **154**, 111–113.

Boudier, F., Nicolas, A. & Ildefonse, B. (1996). Magma chambers in the Oman ophiolite: fed from the top and the bottom. *Earth and Planetary Science Letters* **144**, 239–250.

Boulanger, M., France, L., Deans, J., Ferrando, C., Lissenberg, J. & von der Handt, A. (2020). Magma Reservoir Formation and Evolution at a Slow-Spreading Center (Atlantis Bank, Southwest Indian Ridge) . *Frontiers in Earth Science* .

Bowen, N. L. (1922). The Reaction Principle in Petrogenesis. *The Journal of Geology* **30**, 177–198.

Buck, W. R., Lavier, L. L. & Poliakov, A. N. B. (2005). Modes of faulting at mid-ocean ridges. *Nature* **434**, 719–723.

Burkhard, D. J. M. (1993). Accessory chromium spinels: Their coexistence and alteration in serpentinites. *Geochimica et Cosmochimica Acta* **57**, 1297–1306.

Cann, J. R. (1970). New model for the structure of the ocean crust. *Nature* **226**, 928–930.

Cann, J. R. (1974). A Model for Oceanic Crystal Structure Developed. *Geophysical Journal of the Royal Astronomical Society* **39**, 169–187.

Cann, J. R., Blackman, D. K., Smith, D. K., McAllister, E., Janssen, B., Mello, S., Avgerinos, E., Pascoe, A. R. & Escartin, J. (1997). Corrugated slip surfaces formed at ridge-transform intersections on the Mid-Atlantic Ridge. *Nature* **385**, 329–332.

Cannat, M. (1993). Emplacement of Mantle Rocks in the Seafloor. *Journal of Geophysical Research* **98**, 4163–4172.

Cannat, M. *et al.* (1995). Thin crust, ultramafic exposures, and rugged faulting patterns at the Mid-Atlantic Ridge (22°-24°N). *Geology* **23**, 49–52.

Cannat, M. (1996). How thick is the magmatic crust at slow spreading oceanic ridges? *Journal of Geophysical Research: Solid Earth* **101**, 2847–2857.

Cannat, M., Céline, R. J. & Fujimoto, H. (2003). Melt supply variations to a magma-poor ultra-slow spreading ridge (Southwest Indian Ridge 61° to 69°E). *Geochemistry, Geophysics, Geosystems* **4**, 1–21.

Cannat, M., Rommevaux-Jestin, C., Sauter, D., Deplus, C. & Mendel, V. (1999). Formation of the axial relief at the very slow spreading Southwest Indian Ridge (49° to 69°E). *Journal of Geophysical Research: Solid Earth* **104**, 22825–22843.

Cannat, M., Sauter, D., Mendel, V., Ruellan, E., Okino, K., Escartin, J., Combier, V. & Baala, M. (2006). Modes of seafloor generation at a melt-poor ultraslow-spreading ridge. *Geology* **34**, 605–608.

Carbotte, S. M., Marjanović, M., Carton, H., Mutter, J. C., Canales, J. P., Nedimović, M. R., Han, S. & Perfit, M. R. (2013). Fine-scale segmentation of the crustal magma reservoir beneath the East Pacific Rise. *Nature Geoscience*. Nature Publishing Group **6**, 866–870.

Carbotte, S. M., Smith, D. K., Cannat, M. & Klein, E. M. (2016). Tectonic and magmatic segmentation of the Global Ocean Ridge System: A synthesis of observations. *Geological Society Special Publication* **420**, 249–295.

Cardozo, N. & Allmendinger, R. W. (2013). Spherical projections with OSXStereonet. *Computers and Geosciences*. USA: Pergamon Press, Inc. **51**, 193–205.

Carlson, R. L. & Raskin, G. S. (1984). Density of the ocean crust. *Nature* **311**, 555–558.

Chadima, M. & Jelinek, V. (2009). Anisoft 4.2: Anisotropy data browser for windows. *Agico Inc., Brno*.

Chen, J., Cannat, M., Tao, C., Sauter, D. & Munschy, M. (2021). 780 Thousand Years of Upper-Crustal Construction at a Melt-Rich Segment of the Ultraslow Spreading Southwest Indian Ridge 50°28'E. *Journal of Geophysical Research: Solid Earth* **126**, 1–19.

Chen, J., Crawford, W. C. & Cannat, M. (2023). Microseismicity and lithosphere thickness at a nearly-amagmatic oceanic detachment fault system. *Nature Communications*. Springer US **14**, 430–436.

Chen, J., Olive, J.-A. & Cannat, M. (2022). Thermal Regime of Slow and Ultraslow Spreading Ridges Controlled by Melt Supply and Modes of Emplacement. *Journal of Geophysical Research: Solid Earth* **127**, 1–19.

Chen, Y. & Morgan, W. J. (1990). Rift valley/no rift valley transition at mid-ocean ridges. *Journal of Geophysical Research: Solid Earth*. John Wiley & Sons, Ltd **95**, 17571–17581.

Chen, Y., Niu, Y., Wang, X., Gong, H., Guo, P., Gao, Y. & Shen, F. (2019). Petrogenesis of ODP Hole 735B (Leg 176) Oceanic Plagiogranite: Partial Melting of Gabbros or Advanced Extent of Fractional Crystallization? *Geochemistry, Geophysics, Geosystems* **20**, 2717–2732.

Christensen, N. I. (1978). Ophiolites, Seismic Velocities and Oceanic Crustal Structure. *Tectonophysics* **47**, 131–157.

Christeson, G. L., McIntosh, K. D. & Karson, J. A. (2007). Inconsistent correlation of seismic layer 2a and lava layer thickness in oceanic crust. *Nature* **445**, 418–421.

Christeson, G. L., Reece, R. S., Kardell, D. A., Estep, J. D., Fedotova, A. & Goff, J. A. (2020). South Atlantic Transect: Variations in Oceanic Crustal Structure at 31°S. *Geochemistry, Geophysics, Geosystems* **21**, 1–19.

Christie, D. M. & Sinton, J. M. (1981). Evolution of abyssal lavas along propagating segments of the Galapagos spreading center. *Earth and Planetary Science Letters* **56**, 321–335.

Cochran, J. R. (1988). Somali Basin, Chain Ridge, And Origin Of The Northern Somali Basin Gravity And Geoid Low. *Journal of Geophyscial Research* **93**, 11985–12008.

Cochran, J. R. (2008). Seamount volcanism along the Gakkel Ridge, Arctic Ocean. *Geophysical Journal International* **174**, 1153–1173.

Cochran, J. R. & Sempéré, J. C. (1997). The Southeast Indian Ridge between 88°E and 118°E: Gravity anomalies and crustal accretion at intermediate spreading rates. *Journal of Geophysical Research: Solid Earth*. Wiley-Blackwell **102**, 15463–15487.

Coffin, M. F., Rabinowitz, P. D. & Houtz, R. E. (1986). Crustal structure in the Western Somali Basin. *Geophysical Journal of the Royal Astronomical Society* **86**, 331–369.

Cohen, K. M., Finney, S. C., Gibbard, P. L. & Fan, J.-X. (2013). The ICS International Chronostratigraphic Chart. *Episodes* **36**, 199–204.

Coleman, R. G. (1971). Plate Tectonic Emplacement of Upper Mantle Peridotites along Continental Edges. *Journal of Geophysical Research* **76**, 1212–1222.

Condon, D. J., Schoene, B., McLean, N. M., Bowring, S. A. & Parrish, R. R. (2015). Metrology and traceability of U–Pb isotope dilution geochronology (EARTHTIME Tracer Calibration Part I). *Geochimica et Cosmochimica Acta* **164**, 464–480.

Coogan, L. A. (2014). 4.14 - The Lower Oceanic Crust. In: Holland, H. D. & Turekian, K. K. B. T.-T. on G. (Second E. (eds) *Treatise on Geochemistry: Second Edition*. Oxford: Elsevier, 497–541.

Coogan, L. A., Gillis, K. M., MacLeod, C. J., Thompson, G. M. & Hékinian, R. (2002). Petrology and geochemistry of the lower ocean crust formed at the East Pacific Rise and exposed at Hess Deep: A synthesis and new results. *Geochemistry, Geophysics, Geosystems* **3**, 1–30.

Coogan, L. A., Kempton, P. D., Saunders, A. D. & Norry, M. J. (2000a). Melt aggregation within the crust beneath the Mid-Atlantic Ridge: Evidence from plagioclase and clinopyroxene major and trace element compositions. *Earth and Planetary Science Letters* **176**, 245–257.

Coogan, L. A., Saunders, A. D., Kempton, P. D. & Norry, M. J. (2000b). Evidence from oceanic gabbros for porous melt migration within a crystal mush beneath the Mid-Atlantic Ridge. *Geochemistry, Geophysics, Geosystems* **1**.

Cooper, G. F., Davidson, J. P. & Blundy, J. D. (2016). Plutonic xenoliths from Martinique, Lesser Antilles: evidence for open system processes and reactive melt flow in island arc crust. *Contributions to Mineralogy and Petrology*. Springer Berlin Heidelberg **171**.

Crawford, W. C. & Webb, S. C. (2002). Variations in the distribution of magma in the lower crust and at the Moho beneath the East Pacific Rise at 9°-10°N. *Earth and Planetary Science Letters* **203**, 117–130.

Davidson, J., Turner, S., Handley, H., Macpherson, C. & Dosseto, A. (2007). Amphibole “sponge” in arc crust? *Geology* **35**, 787–790.

Davis, A. S., Clague, D. A., Bohrson, W. A., Dalrymple, G. B. & Greene, H. G. (2002). Seamounts at the continental margin of California: A different kind of oceanic intraplate volcanism. *Bulletin of the Geological Society of America* **114**, 316–333.

Davis, F. A., Cottrell, E., Birner, S. K., Warren, J. M. & Lopez, O. G. (2017). Revisiting the electron microprobe method of spinel-olivine-orthopyroxene oxybarometry applied to spinel peridotites. *American Mineralogist* **102**, 421–435.

Davis, J. K., Lawver, L. A., Norton, I. O. & Gahagan, L. M. (2016). New Somali Basin magnetic anomalies and a plate model for the early Indian Ocean. *Gondwana Research*. International Association for Gondwana Research **34**, 16–28.

de Graaff, S. J., Goodenough, K. M., Klaver, M., Lissenberg, C. J., Jansen, M. N., Millar, I. & Davies, G. R. (2019). Evidence for a Moist to Wet Source Transition Throughout the Oman-UAE Ophiolite, and Implications for the Geodynamic History. *Geochemistry, Geophysics, Geosystems*. John Wiley & Sons, Ltd **20**, 651–672.

de Roever, W. P. (1957). Sind die alpinotypen Peridotitmassen vielleicht tektonisch verfrachtete Bruchstücke der Peridotitschale? *Geologische Rundschau* **46**, 137–146.

Detrick, R. S., Buhl, P., Vera, E., Mutter, J., Orcutt, J., Madsen, J. & Brocher, T. (1987). Multi-channel seismic imaging of a crustal magma chamber along the East Pacific Rise. *Nature* **326**, 35–41.

Dick, H. J. B. (1989). Abyssal peridotites, very slow spreading ridges and ocean ridge magmatism. *Geological Society Special Publication* **42**, 71–105.

Dick, H. J. B. *et al.* (2000). A long in situ section of the lower ocean crust: results of ODP Leg 176 drilling at the Southwest Indian Ridge. *Earth and Planetary Science Letters* **179**, 31–51.

Dick, H. J. B. *et al.* (2002). Primary silicate mineral chemistry of a 1.5-km section of very slow spreading lower ocean crust: ODP hole 735B, Southwest Indian ridge. *Proceedings of Ocean Drilling Program, Scientific Results* **176**, 1–61.

Dick, H. J. B. *et al.* (2017). Expedition 360 summary. *Proceedings of the International Ocean Discovery Program* **360**.

Dick, H. J. B. *et al.* (2019a). Dynamic Accretion Beneath a Slow-Spreading Ridge Segment: IODP Hole 1473A and the Atlantis Bank Oceanic Core Complex. *Journal of Geophysical Research: Solid Earth*. John Wiley & Sons, Ltd **124**, 12631–12659.

Dick, H. J. B. & Bullen, T. (1984). Chromian spinel as a petrogenetic indicator in abyssal and alpine-type peridotites and spatially associated lavas. *Contributions to Mineralogy and Petrology* **86**, 54–76.

Dick, H. J. B., Fisher, R. L. & Bryan, W. B. (1984). Mineralogic variability of the uppermost mantle along mid-ocean ridges. *Earth and Planetary Science Letters* **69**, 88–106.

Dick, H. J. B., Johan Lissenberg, C. & Warren, J. M. (2010). Mantle melting, melt transport, and delivery beneath a slow-spreading ridge: The paleo-MAR from 23°15'N to 23°45'N. *Journal of Petrology* **51**, 425–467.

Dick, H. J. B., Kvassnes, A. J. S., Robinson, P. T., MacLeod, C. J. & Kinoshita, H. (2019b). The Atlantis Bank Gabbro Massif, Southwest Indian Ridge. *Progress in Earth and Planetary Science*. Progress in Earth and Planetary Science **6**, 1–70.

Dick, H. J. B., Lin, J. & Schouten, H. (2003). An ultraslow-spreading class of ocean ridge. *Nature* **426**, 405–412.

Dick, H. J. B., Meyer, P. S., Bloomer, S., Kirby, S., Stakes, D. & Mawer, C. (1991). Lithostratigraphic evolution of an in-situ section of oceanic layer 3. *Proceeding of the Ocean Drilling Program, Scientific Results*. Ocean Drilling Program Texas, 439–538.

Dick, H. J. B., Natland, J. H. & Miller, D. J. (1999). Leg 176 summary. *Proceedings of the Ocean Drilling Program. Part A, Initial report*.

Dick, H. J. B., Tivey, M. A. & Tucholke, B. E. (2008). Plutonic foundation of a slow-spreading ridge segment: Oceanic core complex at Kane Megamullion, 23°30'N, 45°20'W. *Geochemistry, Geophysics, Geosystems* **9**.

Dietz, R. S. (1963). Alpine serpentines as oceanic rind fragments. *GSA Bulletin* **74**, 947–952.

Dilek, Y. (2003). Ophiolite concept and its evolution. *Special Paper of the Geological Society of America* **373**, 1–16.

Dilek, Y. & Furnes, H. (2011). Ophiolite genesis and global tectonics: Geochemical and tectonic fingerprinting of ancient oceanic lithosphere. *Bulletin of the Geological Society of America* **123**, 387–411.

Drouin, M., Godard, M., Ildefonse, B., Bruguier, O. & Garrido, C. J. (2009). Geochemical and petrographic evidence for magmatic impregnation in the oceanic lithosphere at Atlantis Massif, Mid-Atlantic Ridge (IODP Hole U1309D, 30°N). *Chemical Geology*. Elsevier B.V. **264**, 71–88.

Drouin, M., Ildefonse, B. & Godard, M. (2010). A microstructural imprint of melt impregnation in slow spreading lithosphere: Olivine-rich troctolites from the Atlantis Massif, Mid-Atlantic Ridge, 30°N, IODP Hole U1309D. *Geochemistry, Geophysics, Geosystems* **11**, 1–21.

Dumitrica, P., Immenhauser, A. & Dumitrica-Jud, R. (1997). Mesozoic Radiolarian Biostratigraphy from Masirah Ophiolite, Sultanate of Oman - Part 1: Middle Triassic, Uppermost Jurassic and Lower Cretaceous Spumellarians and Multisegmented Nassellarians. *Bulletin of National Museum of Natural Science* **9**, 1–106.

Dunn, R. A., Lekić, V., Detrick, R. S. & Toomey, D. R. (2005). Three-dimensional seismic structure of the Mid-Atlantic Ridge (35°N): Evidence for focused melt supply and lower crustal dike injection. *Journal of Geophysical Research: Solid Earth* **110**, 1–17.

Dziak, R. P., Fox, C. G. & Schreiner, A. E. (1995). The June-July 1993 seismo-acoustic event at CoAxial segment, Juan de Fuca Ridge: Evidence for a lateral dike injection. *Geophysical Research Letters* **22**, 135–138.

Edwards, S. J. & Malpas, J. (1996). Melt-Peridotite Interactions in Shallow Mantle at the East Pacific Rise: Evidence from ODP Site 895 (Hess Deep). *Mineralogical Magazine* **60**, 191–206.

Eggins, S. M. (2003). Laser Ablation ICP-MS Analysis of Geological Materials Prepared as Lithium Borate Glasses. *Geostandards Newsletter*. John Wiley & Sons, Ltd **27**, 147–162.

Escartín, J. & Canales, J. P. (2011). Detachments in Oceanic Lithosphere: Deformation, Magmatism, Fluid Flow, and Ecosystems. *Eos, Transactions American Geophysical Union*. John Wiley & Sons, Ltd **92**, 31.

Escartín, J., Smith, D. K., Cann, J., Schouten, H., Langmuir, C. H. & Escrig, S. (2008). Central role of detachment faults in accretion of slow-spreading oceanic lithosphere. *Nature* **455**, 790–794.

Estep, J., Reece, B., Christeson, G. L., Kardell, D. A. & Carlson, R. L. (2021). 70 million years of seafloor spreading and magmatism in the South Atlantic. *Earth and Planetary Science Letters*. Elsevier B.V. **574**.

Ewart, A. & Hawkesworth, C. J. (1987). The pleistocene-recent tonga-kermadec arc lavas: Interpretation of new isotopic and rare earth data in terms of a depleted mantle source model. *Journal of Petrology* **28**, 495–530.

Fan, Q., Olive, J.-A. & Cannat, M. (2021). Thermo-Mechanical State of Ultraslow-Spreading Ridges With a Transient Magma Supply. *Journal of Geophysical Research: Solid Earth* **126**, 1–20.

Fitton, J. G. (2007). The OIB paradox. *Special Paper of the Geological Society of America* **430**, 387–412.

Fitton, J. G., Saunders, A. D., Norry, M. J., Hardarson, B. S. & Taylor, R. N. (1997). Thermal and chemical structure of the Iceland plume. *Earth and Planetary Science Letters* **153**, 197–208.

Flower, M. F. J. (1980). Accumulation of calcic plagioclase in ocean-ridge tholeiite: an indication of spreading rate? *Nature* **287**, 530–532.

Fornari, D. J., Haymon, R. M., Perfit, M. R., Gregg, T. K. & Edwards, M. H. (1998). Axial summit trough of the East Pacific Rice 9°–10°N: Geological characteristics and evolution of the axial zone on fast spreading mid-ocean ridge. *Journal of Geophysical Research: Solid Earth*. Wiley-Blackwell **103**, 9827–9855.

Fox, P. J., Schreiber, E. & Peterson, J. J. (1973). The Geology of the Oceanic: Compressional Wave Velocities of Oceanic Rocks. *Journal of Geophysical Research* **78**, 5155–5172.

France, L., Ildefonse, B. & Koepke, J. (2009). Interactions between magma and hydrothermal system in Oman ophiolite and in IODP Hole 1256D: Fossilization of a dynamic melt lens at fast spreading ridges. *Geochemistry, Geophysics, Geosystems* **10**, 1–30.

Fryer, P., Sinton, J. M. & Philpotts, J. A. (1981). Basaltic Glasses from the Mariana Trough. *Initial Reports of the Deep Sea Drilling Project* **60**, 601–609.

Gaetani, G. A. & Grove, T. L. (1998). The influence of water on melting of mantle peridotite. *Contributions to Mineralogy and Petrology* **131**, 323–346.

Gahlan, H. A. & Arai, S. (2007). Genesis of peculiarly zoned Co, Zn and Mn-rich chromian spinel in serpentinite of Bou-Azzer ophiolite, Anti-Atlas, Morocco. *Journal of Mineralogical and Petrological Sciences* **102**, 69–85.

Gaina, C., Müller, R. D., Brown, B., Ishihara, T. & Ivanov, S. (2007). Breakup and early seafloor spreading between India and Antarctica. *Geophysical Journal International* **170**, 151–169.

Gaina, C., Van Hinsbergen, D. J. J. & Spakman, W. (2015). Tectonic interactions between India and Arabia since the Jurassic reconstructed from marine geophysics, ophiolite geology, and seismic tomography. *Tectonics* **34**, 875–906.

Gale, A., Dalton, C. A., Langmuir, C. H., Su, Y. & Schilling, J. G. (2013). The mean composition of ocean ridge basalts. *Geochemistry, Geophysics, Geosystems* **14**, 489–518.

Gass, I. G. (1968). Is the Troodos Massif of Cyprus a Fragment of Mesozoic Ocean Floor? *Nature*. Nature Publishing Group **220**, 39–42.

Gass, I. G., Neary, C. R., Plant, J., Robertson, A. H. F., Simonian, K. O., Smewing, J. D., Spooner, E. T. C. & Wilson, R. A. M. (1975). Comments on "The Troodos ophiolitic complex was probably formed in an island arc", by A. Miyashiro and subsequent correspondence by A. Hynes and A. Miyashiro. *Earth and Planetary Science Letters* **25**, 236–238.

Georgen, J. E., Kurz, M. D., Dick, H. J. B. & Lin, J. (2003). Low 3He/4He ratios in basalt glasses from the western Southwest Indian Ridge (10°-24°E). *Earth and Planetary Science Letters* **206**, 509–528.

Geshi, N., Umino, S., Kumagai, H., Sinton, J. M., White, S. M., Kisimoto, K. & Hilde, T. W. (2007). Discrete plumbing systems and heterogeneous magma sources of a 24 km3 off-axis lava field on the western flank of East Pacific Rise, 14°S. *Earth and Planetary Science Letters* **258**, 61–72.

Ghiorso, M. S. & Gualda, G. A. R. (2015). An H2O–CO2 mixed fluid saturation model compatible with rhyolite-MELTS. *Contributions to Mineralogy and Petrology* **169**, 53.

Gibbons, W. & Thompson, L. (1991). Ophiolitic mylonites in the Lizard Complex: ductile extension in the lower oceanic crust. *Geology* **19**, 1009–1012.

Gillis, K. M. (1996). Rare earth element constraints on the origin of amphibole in gabbroic rocks from site 894, Hess Deep. *Proceedings of the Ocean Drilling Program, Scientific Results*. National Science Foundation, 59–76.

Gillis, K. M. (2008). The roof of an axial magma chamber: A hornfelsic heat exchanger. *Geology* **36**, 299–302.

Glennie, K. W., Boeuf, M. G. A., Hughes Clarke, M. W., Moody-Stuart, M., Pilaar, W. F. H. & Reinhardt, B. M. (1974). Geology of the Oman Mountains. *Verhandelingen van het Koninklijk Nederlands Geologisch Mijnbouwkundig Genootschap* **31**, 423.

Gnos, E., Immenhauser, A. & Peters, T. (1997). Late Cretaceous/early Tertiary convergence between the Indian and Arabian plates recorded in ophiolites and related sediments. *Tectonophysics* **271**, 1–19.

Gnos, E. & Perrin, M. (1996). Formation and evolution of the Masirah ophiolite constrained by paleomagnetic study of volcanic rocks. *Tectonophysics* **253**, 53–64.

Godard, M. *et al.* (2009). Geochemistry of a long in-situ section of intrusive slow-spread oceanic lithosphere: Results from IODP Site U1309 (Atlantis Massif, 30°N Mid-Atlantic-Ridge). *Earth and Planetary Science Letters*. Elsevier B.V. **279**, 110–122.

Godard, M., Bosch, D. & Einaudi, F. (2006). A MORB source for low-Ti magmatism in the Semail ophiolite. *Chemical Geology* **234**, 58–78.

Goodenough, K. M., Styles, M. T., Schofield, D., Thomas, R. J., Crowley, Q. C., Lilly, R. M., McKervey, J., Stephenson, D. & Carney, J. N. (2010). Architecture of the Oman-UAE ophiolite: Evidence for a multi-phase magmatic history. *Arabian Journal of Geosciences* **3**, 439–458.

Goodenough, K. M., Thomas, R. J., Styles, M. T., Schofield, D. I. & MacLeod, C. J. (2014). Records of Ocean Growth and Destruction in the Oman–UAE Ophiolite. *Elements* **10**, 109–114.

Goričan, Š., O'Dogherty, L., Baumgartner, P. O., Carter, E. S. & Matsuoka, A. (2018). Mesozoic radiolarian biochronology – current status and future directions. *Revue de Micropaleontologie* **61**, 165–189.

Gregg, P. M., Behn, M. D., Lin, J. & Grove, T. L. (2009). Melt generation, crystallization, and extraction beneath segmented oceanic transform faults. *Journal of Geophysical Research: Solid Earth* **114**, 1–16.

Grevemeyer, I., Hayman, N. W., Lange, D., Peirce, C., Papenberg, C., Van Avendonk, H. J. A., Schmid, F., de La Peña, L. G. & Dannowski, A. (2019). Constraining the maximum depth of brittle deformation at slow- and ultraslow-spreading ridges using microseismicity. *Geology* **47**, 1069–1073.

Griffin, B. J. & Varne, R. (1980). The Macquarie Island ophiolite complex: Mid-Tertiary oceanic lithosphere from a major ocean basin. *Chemical Geology* **30**, 285–308.

Gualda, G. A. R., Ghiorso, M. S., Lemons, R. V & Carley, T. L. (2012). Rhyolite-MELTS: a Modified Calibration of MELTS Optimized for Silica-rich, Fluid-bearing Magmatic Systems. *Journal of Petrology* **53**, 875–890.

Hall, L. S., Mahoney, J. J., Sinton, J. M. & Duncan, R. A. (2006). Spatial and temporal distribution of a C-like asthenospheric component in the Rano Rahi Seamount Field, East Pacific Rise, 15°-19°S. *Geochemistry, Geophysics, Geosystems* **7**.

Hansen, L. N., Cheadle, M. J., John, B. E., Swapp, S. M., Dick, H. J. B., Tucholke, B. E. & Tivey, M. A. (2013). Mylonitic deformation at the Kane oceanic core complex: Implications for the rheological behavior of oceanic detachment faults. *Geochemistry, Geophysics, Geosystems* **14**, 3085–3108.

Hargraves, R. B., Johnson, D. & Chan, C. Y. (1991). Distribution anisotropy: The cause of AMS in igneous rocks? *Geophysical Research Letters* **18**, 2193–2196.

Harvey, J., Gannoun, A., Burton, K. W., Rogers, N. W., Alard, O. & Parkinson, I. J. (2006). Ancient melt extraction from the oceanic upper mantle revealed by Re-Os isotopes in abyssal peridotites from the Mid-Atlantic ridge. *Earth and Planetary Science Letters* **244**, 606–621.

Hayes, D. E. & Kane, K. A. (1994). Long-lived mid-ocean ridge segmentation of the Pacific-Antarctic Ridge and the Southeast Indian Ridge. *Journal of Geophysical Research: Solid Earth*. Wiley-Blackwell **99**, 19679–19692.

Hellebrand, E. & Snow, J. E. (2003). Deep melting and sodic metasomatism underneath the highly oblique-spreading Lena Trough (Arctic Ocean). *Earth and Planetary Science Letters* **216**, 283–299.

Herzberg, C. & Asimow, P. D. (2008). Petrology of some oceanic island basalts: PRIMELT2.XLS software for primary magma calculation. *Geochemistry, Geophysics, Geosystems*. John Wiley & Sons, Ltd **9**.

Herzberg, C. & Asimow, P. D. (2015). PRIMELT3 MEGA.XLSM software for primary magma calculation: Peridotite primary magma MgO contents from the liquidus to the solidus. *Geochemistry, Geophysics, Geosystems* **16**, 563–578.

Herzberg, C., Asimow, P. D., Arndt, N., Niu, Y., Lesher, C. M., Fitton, J. G., Cheadle, M. J. & Saunders, A. D. (2007). Temperatures in ambient mantle and plumes: Constraints from basalts, picrites, and komatiites. *Geochemistry, Geophysics, Geosystems* **8**, 1–34.

Herzberg, C. & O'Hara, M. J. (2002). Plume-Associated Ultramafic Magmas of Phanerozoic Age. *Journal of Petrology* **43**, 1857–1883.

Hess, H. H. (1962). History of Ocean Basins. *Petrologic Studies: A Volume to Honor A. F. Buddington* 599–620.

Hess, H. H. (1964). The oceanic crust, the upper mantle and the Mayaguez serpentinized peridotite. *A study of serpentinite*. Publ, 169.

Hesse, K. T., Gose, J., Stalder, R. & Schmädicke, E. (2015). Water in orthopyroxene from abyssal spinel peridotites of the East Pacific Rise (ODP Leg 147: Hess Deep). *Lithos*. Elsevier B.V. **232**, 23–34.

Hey, R., Duennebier, F. K. & Morgan, W. J. (1980). Propagating Rifts on Midocean Ridges. *Journal of Geophysical Research: Solid Earth*. Wiley-Blackwell **85**, 3647–3658.

Hey, R. N., Naar, D. F., Kleinrock, M. C., Phipps Morgan, W. J., Morales, E. & Schilling, J. G. (1985). Microplate tectonics along a superfast seafloor spreading system near Easter Island. *Nature* **317**, 320–325.

Hiess, J., Condon, D. J., McLean, N. & Noble, S. R. (2012). 238U/235U Systematics in Terrestrial Uranium-Bearing Minerals. *Science*. American Association for the Advancement of Science **335**, 1610–1614.

Hirano, N. *et al.* (2006). Volcanism in Response to Plate Flexure. *Science* **313**, 1426–1428.

Hofmann, A. W., Jochum, K. P., Seufert, M. & White, W. M. (1986). Nb and Pb in oceanic basalts: new constraints on mantle evolution. *Earth and Planetary Science Letters* **79**, 33–45.

Hooft, E. E. E., Detrick, R. S. & Kent, G. M. (1997). Seismic structure and indicators of magma budget along the Southern East Pacific Rise. *Journal of Geophyscial Research* **102**, 27319–27340.

Hooft, E. E. E., Detrick, R. S., Toomey, D. R., Collins, J. A. & Lin, J. (2000). Crustal thickness and structure along three contrasting spreading segments of the Mid-Atlantic Ridge, 33.5°–35°N. *Journal of Geophysical Research: Solid Earth*. Wiley-Blackwell **105**, 8205–8226.

Hori, R. S., Cho, C. -F & Umeda, H. (1993). Origin of cyclicity in Triassic-Jurassic radiolarian bedded cherts of the Mino accretionary complex from Japan. *Island Arc* **2**, 170–180.

Hynes, A. (1975). Comment on "The Troodos ophiolitic complex was probably formed in an island arc", by A. Miyashiro. *Earth and Planetary Science Letters* **25**, 213–216.

Ildefonse, B. *et al.* (2007). Oceanic core complexes and crustal accretion at slow-speading ridges. *Geology* **35**, 623–626.

Immenhauser, A. (1995). The autochthonous mesozoic sediment record on the Masirah Island Ophiolite (Sultanate of Oman). Universität Bern.

Immenhauser, A. (1996). Cretaceous sedimentary rocks on the Masirah Ophiolite (Sultanate of Oman): Evidence for an unusual bathymetric history. *Journal of the Geological Society* **153**,

539–551.

Immenhauser, A., Schreurs, G., Gnos, E., Oterdoom, H. W. & Hartmann, B. (2000). Late Palaeozoic to Neogene geodynamic evolution of the northeastern Oman margin. *Geological Magazine*. Cardiff University **137**, 1–18.

Immenhauser, A., Schreurs, G., Peters, T., Matter, A., Hauser, M. & Dumitrica, P. (1998). Stratigraphy, sedimentology and depositional environments of the Permian to uppermost Cretaceous Batain Group, eastern-Oman. *Eclogae Geologicae Helvetiae* **91**, 217–235.

Irvine, T. N. & Baragar, W. R. A. (1971). A guide to the chemical classification of the common volcanic rocks. *Canadian journal of earth sciences*. NRC Research Press Ottawa, Canada **8**, 523–548.

Ishikawa, T., Nagaishi, K. & Umino, S. (2002). Boninitic volcanism in the Oman ophiolite: Implications for thermal condition during transition from spreading ridge to arc. *Geology* **30**, 899–902.

Jaffey, A. H., Flynn, K. F., Glendenin, L. E., Bentley, W. C. & Essling, A. M. (1971). Precision Measurement of Half-Lives and Specific Activities of 235mU and 238U. *Physical Review C*. American Physical Society **4**, 1889–1906.

Janney, P. E., Macdougall, J. D., Natland, J. H. & Lynch, M. A. (2000). Geochemical evidence from the Pukapuka volcanic ridge system for a shallow enriched mantle domain beneath the South Pacific Superswell. *Earth and Planetary Science Letters* **181**, 47–60.

Jansen, M. N., Lissenberg, C. J., Klaver, M., Graaff, S. J. de, Koornneef, J. M., Smeets, R. J., MacLeod, C. J. & Davies, G. R. (2018). Isotopic variation in Semail Ophiolite lower crust reveals crustal-level melt aggregation. *Geochemical Perspectives Letters* **8**, 37–42.

Jelínek, V. (1977). *The statistical theory of measuring anisotropy of magnetic susceptibility of rocks and its application*. Brno: Geofyzika.

Jelínek, V. (1981). Characterization of the magnetic fabric of rocks. *Tectonophysics* **79**, 63–67.

Jian, H., Singh, S. C., Chen, Y. J. & Li, J. (2017). Evidence of an axial magma chamber beneath the ultraslow- spreading Southwest Indian Ridge. *Geology* **45**, 143–146.

Jiang, Q. *et al.* (2021). Origin of geochemically heterogeneous mid-ocean ridge basalts from the Macquarie Ridge Complex, SW Pacific. *Lithos*. Elsevier B.V. **380**–**381**, 105893.

Jochum, K. P. *et al.* (2011). Determination of Reference Values for NIST SRM 610–617 Glasses Following ISO Guidelines. *Geostandards and Geoanalytical Research*. John Wiley & Sons, Ltd **35**, 397–429.

Jochum, K. P., Nohl, U., Herwig, K., Lammel, E., Stoll, B. & Hofmann, A. W. (2005). GeoReM: A New Geochemical Database for Reference Materials and Isotopic Standards. *Geostandards and Geoanalytical Research*. John Wiley & Sons, Ltd **29**, 333–338.

Jochum, K. P., Weis, U., Schwager, B., Stoll, B., Wilson, S. A., Haug, G. H., Andreae, M. O. & Enzweiler, J. (2016). Reference Values Following ISO Guidelines for Frequently Requested Rock Reference Materials. *Geostandards and Geoanalytical Research*. John Wiley & Sons, Ltd **40**, 333–350.

Johnson, K. T. M., Dick, H. J. B. & Shimizu, N. (1990). Melting in the Oceanic Upper Mantle: An Ion Microprobe Study of Diopsides in Abyssal Peridotites. *Journal of Geophyscial Research* **95**, 2661–2678.

Jokat, W., Ritzmann, O., Schmidt-Aursch, M. C., Drachev, S., Gauger, S. & Snow, J. (2003). Geophysical evidence for reduced melt production on the Arctic ultraslow Gakkel mid-ocean ridge. *Nature* **423**, 962–965.

Kamenetsky, V. S., Everard, J. L., Crawford, A. J., Varne, R., Eggins, S. M. & Lanyon, R. (2000). Enriched end-member of primitive MORB melts: Petrology and geochemistry of glasses from Macquarie Island (SW Pacific). *Journal of Petrology* **41**, 411–430.

Kamenetsky, V. S. & Maas, R. (2002). Mantle-melt evolution (dynamic source) in the origin of a single MORB suite: A perspective from magnesian glasses of Macquarie Island. *Journal of Petrology* **43**, 1909–1922.

Kane, K. A. & Hayes, D. E. (1992). Tectonic corridors in the south Atlantic: Evidence for long-lived mid-ocean ridge segmentation. *Journal of Geophysical Research: Solid Earth*. Wiley-Blackwell **97**, 17317–17330.

Karig, D. E. (1970). Ridges and Basins of the Tonga-Kermadec Island Arc System. *Journal of Geophyscial Research* **75**, 239–254.

Karig, D. E. (1971a). Origin and Development of Marginal Basins in the Western Pacific. *Journal of Geophyscial Research* **76**, 2542–2561.

Karig, D. E. (1971b). Structural history of the mariana island arc system. *Bulletin of the Geological Society of America* **82**, 323–344.

Karson, J. A. *et al.* (2002). Structure of uppermost fast-spread oceanic crust exposed at the Hess Deep Rift: Implications for subaxial processes at the East Pacific Rise. *Geochemistry, Geophysics, Geosystems* **3**.

Karson, J. A., Kelley, D. S., Fornari, D. J., Perfit, M. R. & Shank, T. M. (2015). *Discovering the deep: a photographic atlas of the seafloor and ocean crust*. Cambridge University Press.

Kelemen, P. B., Koga, K. & Shimizu, N. (1997). Geochemistry of gabbro sills in the crust-mantle transition zone of the Oman ophiolite: implications for the origin of the oceanic lower crust. *Earth and Planetary Science Letters* **146**, 475–488.

Kelemen, P. B., Shimizu, N. & Salters, V. J. M. (1995). Extraction of mid-ocean-ridge basalt from the upwelling mantle by focused flow of melt in dunite channels. *Nature*, 747–753.

Keller, C. B., Schoene, B. & Samperton, K. M. (2018). A stochastic sampling approach to zircon eruption age interpretation. *Geochemical Perspectives Letters* **8**, 31–35.

Kidd, R. G. W. (1977). A model for the process of formation of the upper oceanic crust. *Geophysical Journal of the Royal Astronomical Society* **50**, 149–183.

Kinzler, R. J. & Grove, T. L. (1993). Corrections and Further Discussion of the Primary Magmas of Mid-Ocean Ridge Basalts, 1 and 2. *Journal of Geophyscial Research* **98**, 22339–22347.

Kirby, G. A. (1979). The Lizard complex as an ophiolite. *Nature* **282**, 58–61.

Klaver, M., Blundy, J. D. & Vroon, P. Z. (2018). Generation of arc rhyodacites through cumulate-melt reactions in a deep crustal hot zone: Evidence from Nisyros volcano. *Earth and Planetary Science Letters* **497**, 169–180.

Klein, E. M. & Langmuir, C. H. (1987). Global correlations of ocean ridge basalt chemistry with axial depth. *Journal of Geophyscial Research* **92**, 8089–8115.

Knight, M. D. & Walker, G. P. L. (1988). Magma flow directions in dikes of the Koolau Complex, Oahu, determined from magnetic fabric studies. *Journal of Geophysical Research: Solid Earth*. John Wiley & Sons, Ltd **93**, 4301–4319.

Koepke, J. *et al.* (2008). Petrography of the dike-gabbro transition at IODP Site 1256 (equatorial

Pacific): The evolution of the granoblastic dikes. *Geochemistry, Geophysics, Geosystems* **9**, 1–29.

Koepke, J., Feig, S. T., Berndt, J. & Neave, D. A. (2021). Wet magmatic processes during the accretion of the deep crust of the Oman Ophiolite paleoridge: Phase diagrams and petrological records. *Tectonophysics* **817**.

Koepke, J., Schoenborn, S., Oelze, M., Wittmann, H., Feig, S. T., Hellebrand, E., Boudier, F. & Schoenberg, R. (2009). Petrogenesis of crustal wehrlites in the Oman ophiolite: Experiments and natural rocks. *Geochemistry, Geophysics, Geosystems* **10**, 1–26.

Kurz, M. D., Roex, A. P. L. E. & Dick, H. J. B. (1998). Isotope geochemistry of the oceanic mantle near the Bouvet triple junction. *Geochimica et Cosmochimica Acta* **62**, 841–852.

Kvassnes, A. J. S., Strand, A. H., Moen-Eikeland, H. & Pedersen, R. B. (2004). The Lyngen Gabbro: The lower crust of an Ordovician Incipient Arc. *Contributions to Mineralogy and Petrology* **148**, 358–379.

Lambart, S., Koornneef, J. M., Millet, M.-A., Davies, G. R., Cook, M. & Lissenberg, C. J. (2019). Highly heterogeneous depleted mantle recorded in the lower oceanic crust. *Nature Geoscience* **12**, 482–486.

Lambart, S., Laporte, D. & Schiano, P. (2009). An experimental study of pyroxenite partial melts at 1 and 1.5 GPa: Implications for the major-element composition of Mid-Ocean Ridge Basalts. *Earth and Planetary Science Letters*. Elsevier B.V. **288**, 335–347.

Lange, A. E., Nielsen, R. L., Tepley, F. J. & Kent, A. J. R. (2013a). Diverse sr isotope signatures preserved in mid-oceanic-ridge basalt plagioclase. *Geology* **41**, 279–282.

Lange, A. E., Nielsen, R. L., Tepley, F. J. & Kent, A. J. R. (2013b). The petrogenesis of plagioclase-phyric basalts at mid-ocean ridges. *Geochemistry, Geophysics, Geosystems* **14**, 3282–3296.

Langmuir, C. H., Bender, J. F. & Batiza, R. (1986). Petrological and tectonic segmentation of the East Pacific Rise, 5°30′–14°30′ N. *Nature*. Nature Publishing Group **322**, 422–429.

Langmuir, C. H. & Hanson, G. N. (1980). An evaluation of major element heterogeneity in the mantle sources of basalts. *Philosophical Transactions of the Royal Society of London. Series A, Mathematical and Physical Sciences* **297**, 383–407.

Langmuir, C. H., Klein, E. M. & Plank, T. (1992). Petrological Systematics of Mid-Ocean Ridge Basalts: Constraints on Melt Generation Beneath Ocean Ridges. *Geophysical Monograph* **71**, 183–280.

Lassiter, J. C., Byerly, B. L., Snow, J. E. & Hellebrand, E. (2014). Constraints from Os-isotope variations on the origin of Lena Trough abyssal peridotites and implications for the composition and evolution of the depleted upper mantle. *Earth and Planetary Science Letters*. Elsevier B.V. **403**, 178–187.

Le Bas, M. J., Le Maitre, R. W., Streckeisen, A. & Zanettin, B. (1986). A chemical classification of volcanic rocks based on the total alkali-silica diagram. *Journal of Petrology* **27**, 745–750.

Le Métour, J., Béchennec, F., Roger, J., Platel, J. P. & Wyns, R. (1992). Explanatory Notes to the Geological map of Al Masirah, Sheet NF 40–16, Scale: 1: 250,000. *Directorate General of Minerals, Oman Ministry of Petroleum and Minerals*.

Lees, G. M. (1928). The Geology and Tectonics of Oman and of Parts of South-Eastern Arabia. *Journal of the Geological Society* **84**, 585–670.

Lehnert, K., Su, Y., Langmuir, C. H., Sarbas, B. & Nohl, U. (2000). A global geochemical database

structure for rocks. *Geochemistry, Geophysics, Geosystems*. John Wiley & Sons, Ltd **1**.

Li, J. *et al.* (2015). Seismic observation of an extremely magmatic accretion at the ultraslow spreading Southwest Indian Ridge. *Geophysical Res* **42**, 2656–2663.

Li, J., Kornprobst, J. & Vielzeuf, D. (1995). An Improved Experimental Calibration of the Olivine-Spinel Geothermometer. *Chinese Journal of Geochemistry* **14**, 68–77.

Li, W., Liu, C., Tao, C. & Jin, Z. (2019). Osmium isotope compositions and highly siderophile element abundances in abyssal peridotites from the Southwest Indian Ridge: Implications for evolution of the oceanic upper mantle. *Lithos*. Elsevier B.V. **346**–**347**, 105167.

Ligi, M. *et al.* (2011). Initial burst of oceanic crust accretion in the Red sea due to edgedriven mantle convection. *Geology* **39**, 1019–1022.

Ligi, M., Bonatti, E., Bortoluzzi, G., Cipriani, A., Cocchi, L., Caratori Tontini, F., Carminati, E., Ottolini, L. & Schettino, A. (2012). Birth of an ocean in the Red Sea: Initial pangs. *Geochemistry, Geophysics, Geosystems* **13**, 1–29.

Lin, J., Purdy, G. M., Schouten, H., Sempere, J. C. & Zervas, C. (1990). Evidence from gravity data for focused magmatic accretion along the Mid-Atlantic Ridge. *Nature* **344**, 627–632.

Lippard, S. J. (1986). The ophiolite of northern Oman. *Geological Society London Memoir* **11**, 178.

Lissenberg, C. J. & Dick, H. J. B. (2008). Melt-rock reaction in the lower oceanic crust and its implications for the genesis of mid-ocean ridge basalt. *Earth and Planetary Science Letters* **271**, 311–325.

Lissenberg, C. J. & MacLeod, C. J. (2016). A reactive porous flow control on mid-ocean ridge magmatic evolution. *Journal of Petrology* **57**, 2195–2220.

Lissenberg, C. J., MacLeod, C. J., Howard, K. A. & Godard, M. (2013). Pervasive reactive melt migration through fast-spreading lower oceanic crust (Hess Deep, equatorial Pacific Ocean). *Earth and Planetary Science Letters*. Elsevier **361**, 436–447.

Lissenberg, C. J., Rioux, M., Shimizu, N., Bowring, S. A. & Mével, C. (2009). Zircon dating of oceanic crustal accretion. *Science* **323**, 1048–1050.

Liu, C. Z., Snow, J. E., Hellebrand, E., Brügmann, G., Von Der Handt, A., Büchl, A. & Hofmann, A. W. (2008). Ancient, highly heterogeneous mantle beneath Gakkel ridge, Arctic Ocean. *Nature* **452**, 311–316.

Lizarralde, D., Gaherty, J. B., Collins, J. A., Hirth, G. & Kim, S. D. (2004). Spreading-rate dependence of melt extraction at mid-ocean ridges from mantle seismic refraction data. *Nature* **432**, 744–747.

Longerich, H. P., Jackson, S. E. & Günther, D. (1996). Inter-laboratory note. Laser ablation inductively coupled plasma mass spectrometric transient signal data acquisition and analyte concentration calculation. *Journal of Analytical Atomic Spectrometry*. The Royal Society of Chemistry **11**, 899–904.

Lundstrom, C. C., Sampson, D. E., Perfit, M. R., Gill, J. & Williams, Q. (1999). Insights into mid-ocean ridge basalt petrogenesis: U-series disequilibria from the Siqueiros Transform, Lamont Seamounts, and East Pacific Rise. *Journal of Geophysical Research: Solid Earth* **104**, 13035–13048.

Macdonald, K. C. (1986). The crest of the Mid-Atlantic Ridge: Models for crustal generation processes and tectonics. *The Western North Atlantic Region*. Geological Society of America, 0.

Macdonald, K. C., Fox, P. J., Perram, L. J., Eisen, M. F., Haymon, R. M., Miller, S. P., Carbotte, S. M., Cormier, M. H. & Shor, A. N. (1988). A new view of the mid-ocean ridge from the behaviour of ridge axis discontinuities. *Nature* **335**, 217–225.

Macdonald, K. C., Scheirer, D. S. & Carbotte, S. M. (1991). Mid-Ocean Ridges: Discontinuities, Segments and Giant Cracks. *Science* **253**, 986–994.

Macdonald, K., Sempere, J. C. & Fox, P. J. (1984). East Pacific Rise from Siqueiros to Orozco Fracture Zones: Along-strike continuity of axial neovolcanic zone and structure and evolution of overlapping spreading centers. *Journal of Geophysical Research: Solid Earth*. Wiley-Blackwell **89**, 6049–6069.

Macgregor, L. M., Constable, S. & Sinha, M. C. (1998). The RAMESSES experiment—III. Controlled-source electromagnetic sounding of the Reykjanes Ridge at 57°45'N. *Geophysical Journal International* **135**, 773–789.

MacLeod, C. J. *et al.* (2002). Direct geological evidence for oceanic detachment faulting: The Mid-Atlantic Ridge, 15°45'N. *Geology* **30**, 879–882.

MacLeod, C. J., Allerton, S., Gass, I. G. & Xenophontos, C. (1990). Structure of a fossil ridge–transform intersection in the Troodos ophiolite. *Nature* **348**, 717–720.

MacLeod, C. J., Carlut, J., Escartín, J., Horen, H. & Morris, A. (2011). Quantitative constraint on footwall rotations at the 15°45'N oceanic core complex, Mid-Atlantic Ridge: Implications for oceanic detachment fault processes. *Geochemistry, Geophysics, Geosystems* **12**, 1–29.

MacLeod, C. J., Johan Lissenberg, C. & Bibby, L. E. (2013). "Moist MORB" axial magmatism in the Oman ophiolite: The evidence against a mid-ocean ridge origin. *Geology* **41**, 459–462.

MacLeod, C. J. & Rothery, D. A. (1992). Ridge axial segmentation in the Oman ophiolite: Evidence from along-strike variations in the sheeted dyke complex. *Geological Society Special Publication* **60**, 39–63.

MacLeod, C. J., Searle, R. C., Murton, B. J., Casey, J. F., Mallows, C., Unsworth, S. C., Achenbach, K. L. & Harris, M. (2009). Life cycle of oceanic core complexes. *Earth and Planetary Science Letters*. Elsevier B.V. **287**, 333–344.

Macleod, C. J. & Yaouancq, G. (2000). A fossil melt lens in the Oman ophiolite: Implications for magma chamber processes at fast spreading ridges. *Earth and Planetary Science Letters* **176**, 357–373.

Maffione, M., Thieulot, C., van Hinsbergen, D. J. J., Morris, A., Plümper, O. & Spakman, W. (2015). Dynamics of intraoceanic subduction initiation: 1. Oceanic detachment fault inversion and the formation of supra-subduction zone ophiolites. *Geochemistry, Geophysics, Geosystems* **16**, 1753–1770.

Magde, L. S., Barclay, A. H., Toomey, D. R., Detrick, R. S. & Collins, J. A. (2000). Crustal magma plumbing within a segment of the Mid-Atlantic Ridge, 35°N. *Earth and Planetary Science Letters* **175**, 55–67.

Mahoney, J. J., Frei, R., Tejada, M. L. G., Mo, X. X., Leat, P. T. & Nägler, T. F. (1998). Tracing the Indian Ocean mantle domain through time: isotopic results from old west Indian, east Tethyan, and South Pacific seafloor. *Journal of Petrology* **39**, 1285–1306.

Makris, J., Henke, C. H., Egloff, F. & Akamaluk, T. (1991). The gravity field of the Red Sea and East Africa. *Tectonophysics* **198**, 369–381.

Marquer, D., Mercolli, I. & Peters, T. (1998). Early Cretaceous intra-oceanic rifting in the Proto-Indian

Ocean recorded in the Masirah Ophiolite, Sultanate of Oman. *Tectonophysics* **292**, 1–16.

Marquer, D., Peters, T. & Gnos, E. (1995). A new structural interpretation for the emplacement of the Masirah ophiolites (Oman): a main Paleocene intra-oceanic thrust. *Geodinamica Acta* **8**, 13–19.

Mattinson, J. M. (2005). Zircon U-Pb chemical abrasion ("CA-TIMS") method: Combined annealing and multi-step partial dissolution analysis for improved precision and accuracy of zircon ages. *Chemical Geology* **220**, 47–66.

Mattioli, M., Upton, B. G. J. & Renzulli, A. (1997). Sub-volcanic crystallization at Sete Cidades volcano, São Miguel, Azores, inferred from mafic and ultramafic plutonic nodules. *Mineralogy and Petrology* **60**, 1–26.

McDonough, W. F. & Sun, S. -s. (1995). The composition of the Earth. *Chemical Geology* **120**, 223–253.

McLean, N. M., Bowring, J. F. & Bowring, S. A. (2011). An algorithm for U-Pb isotope dilution data reduction and uncertainty propagation. *Geochemistry, Geophysics, Geosystems*. John Wiley & Sons, Ltd **12**.

McLean, N. M., Condon, D. J., Schoene, B. & Bowring, S. A. (2015). Evaluating uncertainties in the calibration of isotopic reference materials and multi-element isotopic tracers (EARTHTIME Tracer Calibration Part II). *Geochimica et Cosmochimica Acta* **164**, 481–501.

Mehl, L. & Hirth, G. (2008). Plagioclase preferred orientation in layered mylonites: Evaluation of flow laws for the lower crust. *Journal of Geophysical Research: Solid Earth* **113**, 1–19.

Mendel, V., Sauter, D., Parson, L. & Vanney, J.-R. (1997). Segmentation and Morphotectonic Variations Along a Super Slow-Spreading Center: The Southwest Indian Ridge (57° E-70° E). *Marine Geophysical Researches* **19**, 505–533.

Meurer, W. P. & Gee, J. (2002). Evidence for the protracted construction of slow-spread oceanic crust by small magmatic injections. *Earth and Planetary Science Letters* **201**, 45–55.

Meyer, J., Mercolli, I. & Immenhauser, A. (1996). Off-ridge alkaline magmatism and seamount volcanoes in the Masirah island ophiolite, Oman. *Tectonophysics* **267**, 187–208.

Michael, P. J. *et al.* (2003). Magmatic and amagmatic seafloor generation at the ultraslow-spreading Gakkel ridge, Arctic Ocean. *Nature* **423**, 956–961.

Michael, P. J. & Bonatti, E. (1985). Peridotite composition from the North Atlantic: regional and tectonic variations and implications for partial melting. *Earth and Planetary Science Letters* **73**, 91–104.

Miller, D. J. *et al.* (2009). Data report: microprobe analyses of primary mineral phases from Site U1309, Atlantis Massif, IODP Expedition 304/305. *Proceedings of the Integrated Ocean Drilling Program* **304/305**, 1–4.

Miyashiro, A. (1973). The Troodos ophiolitic complex was probably formed in an island arc. *Earth and Planetary Science Letters* **19**, 218–224.

Miyashiro, A. (1975a). Origin of the troodos and other ophiolites: A reply to Hynes. *Earth and Planetary Science Letters* **25**, 217–222.

Miyashiro, A. (1975b). Origin of the Troodos and other ophiolites: a reply to Moores. *Earth and Planetary Science Letters* **25**, 227–235.

Molinie, A. J. & Ogg, J. G. (1992). Milankovitch cycles in Upper Jurassic and Lower Cretaceous radiolarites of the equatorial Pacific: spectral analysis and sedimentation rate curves. *Proceedings of the Ocean Drilling Program, Scientific Results* **129**, 529–547.

Molli, G. (1995). Pre-orogenic High Temperature Shear Zones in an Ophiolite Complex (Bracco Massif, Northern Apennines, Italy). In: Vissers, R. L. M. & Nicolas, A. (eds) *Mantle and Lower Crust Exposed in Oceanic Ridges and in Ophiolites*. Dordrecht: Springer Netherlands, 147–161.

Moores, E. M. (1975). Discussion of "Origin of Troodos and other ophiolites: a reply to Hynes", by Akiho Miyashiro. *Earth and Planetary Science Letters* **25**, 223–226.

Moores, E. M. & Jackson, E. D. (1974). Ophiolites and oceanic crust. *Nature* **250**, 136–139.

Moores, E. M. & Vine, F. J. (1971). The Troodos Massif, Cyprus and other ophiolites as oceanic crust: evaluation and implications. *Philosophical Transactions of the Royal Society of London. Series A, Mathematical and Physical Sciences* **268**, 443–467.

Morgan, J. P. & Chen, Y. J. (1993). Dependence of ridge-axis morphology on magma supply and spreading rate. *Letters to Nature* **364**, 706–708.

Morris, A., Creer, K. M. & Robertson, A. H. F. (1990). Palaeomagnetic evidence for clockwise rotations related to dextral shear along the Southern Troodos Transform Fault, Cyprus. *Earth and Planetary Science Letters* **99**, 250–262.

Moseley, F. (1969). The upper Cretaceous ophiolite complex of Masirah island, Oman. *Geological Journal* **6**, 293–306.

Moseley, F. (1990). The structure of Masirah Island, Oman. *Geological Society Special Publication* **49**, 665–671.

Moseley, F. & Abbotts, I. L. (1979). The ophiolite mélange of Masirah, Oman. *Journal of the Geological Society* **136**, 713–724.

Moseley, F. & Abbotts, I. L. (1984). A geological map of the Masirah ophiolite complex, Oman. *Overseas Geology and Mineral Resources* **62**, 1–5.

Mountain, G. S. & Prell, W. L. (1990). A multiphase plate tectonic history of the southeast continental margin of Oman. *Geological Society Special Publication* **49**, 725–743.

Muller, M. R., Minshull, T. A. & White, R. S. (2000). Crustal structure of the Southwest Indian Ridge at the Atlantis II Fracture Zone. *Journal of Geophyscial Research* **105**, 25809 – 25828.

Muller, M. R., Robinson, C. J., Minshull, T. A., White, R. S. & Bickle, M. J. (1997). Thin crust beneath ocean drilling program borehole 735B at the Southwest Indian Ridge? *Earth and Planetary Science Letters* **148**, 93–107.

Nägler, T. F. & Frei, R. (1997). True K-feldspar granites in oceanic crust (Masirah ophiolite, Sultanate of Oman): A U-Pb and Sm-Nd isotope study. *Chemical Geology* **138**, 119–126.

Natland, J. H. & Dick, H. J. B. (1996). Melt Migration through High-Level Gabbroic Cumulates of the East Pacific Rise at Hess Deep: The Origin of Magma Lenses and the Deep Crustal Structure of Fast-Spreading Ridges. *Proceedings of the Ocean Drilling Program, Scientific Results* **147**, 21–58.

Neumann, E. R., Sørensen, V. B., Simonsen, S. L. & Johnsen, K. (2000). Gabbroic xenoliths from La Palma, Tenerife and Lanzarote, Canary Islands: Evidence for reactions between mafic alkaline Canary Islands melts and old oceanic crust. *Journal of Volcanology and Geothermal Research* **103**, 313–342.

Neumann, G. A. & Forsyth, D. W. (1993). The paradox of the axial profile: isostatic compensation along the axis of the Mid-Atlantic Ridge? *Journal of Geophysical Research* **98**, 17891–17910.

Nicolas, A. (1989). *Structures of ophiolites and dynamics of oceanic lithosphere*. Dordrecht: Kluwer Academic Publishers.

Nicolas, A. & Boudier, F. (2011). Structure and dynamics of ridge axial melt lenses in the Oman ophiolite. *Journal of Geophysical Research: Solid Earth* **116**, 1–16.

Nicolas, A., Ceuleneer, G., Boudier, F. & Misseri, M. (1988a). Structural mapping in the Oman ophiolites: Mantle diapirism along an oceanic ridge. *Tectonophysics* **151**, 27–56.

Nicolas, A., Reuber, I. & Benn, K. (1988b). A new magma chamber model based on structural studies in the Oman ophiolite. *Tectonophysics* **151**, 87–105.

Niu, Y. (1997). Mantle melting and melt extraction processes beneath ocean ridges: Evidence from abyssal peridotites. *Journal of Petrology* **38**, 1047–1074.

Niu, Y. & Batiza, R. (1997). Trace element evidence from seamounts for recycled oceanic crust in the Eastern Pacific mantle. *Earth and Planetary Science Letters* **148**, 471–483.

Niu, Y., Gilmore, T., Mackie, S., Greig, A. & Bach, W. (2002). Mineral chemistry, whole-rock compositions, and petrogenesis of Leg 176 gabbros: data and discussion. *Proceedings of the Ocean Drilling Program, Scientific Results* **176**, 1–60.

Niu, Y. & O'Hara, M. J. (2009). MORB mantle hosts the missing Eu (Sr, Nb, Ta and Ti) in the continental crust: New perspectives on crustal growth, crust–mantle differentiation and chemical structure of oceanic upper mantle. *Lithos* **112**, 1–17.

Norris, A. & Danyushevsky, L. (2018). Towards estimating the complete uncertainty budget of quantified results measured by LA-ICP-MS. *Goldschmidt: Boston, MA, USA*.

O'Hara, M. J. (1968). Are Ocean Floor Basalts Primary Magma? *Nature* **220**, 683–686.

O'Neill, H. S. C. (2016). The smoothness and shapes of chondrite-normalized rare earth element patterns in basalts. *Journal of Petrology* **57**, 1463–1508.

Ohara, Y., Yoshida, T., Kato, Y. & Kasuga, S. (2001). Giant Megamullion in the Parece Vela Backarc Basin. *Marine Geophysical Researches* **22**, 47–61.

Olive, J.-A. & Crone, T. J. (2018). Smoke Without Fire : How Long Can Thermal Cracking Sustain Hydrothermal Circulation in the Absence of Magmatic Heat? *Journal of Geophysical Research: Solid Earth* **123**, 4561–4581.

Olive, J. A., Behn, M. D. & Tucholke, B. E. (2010). The structure of oceanic core complexes controlled by the depth distribution of magmaemplacement. *Nature Geoscience*. Nature Publishing Group **3**, 491–495.

Olive, J. A. & Dublanchet, P. (2020). Controls on the magmatic fraction of extension at mid-ocean ridges. *Earth and Planetary Science Letters*. Elsevier B.V. **549**, 116541.

Paquet, M., Cannat, M., Brunelli, D., Hamelin, C. & Humler, E. (2016). Effect of melt/mantle interactions on MORB chemistry at the easternmost Southwest Indian Ridge (61°–67°E). *Geochemistry, Geophysics, Geosystems* **17**, 4605–4640.

Paterson, S. R., Fowler, T. K., Schmidt, K. L., Yoshinobu, A. S., Yuan, E. S. & Miller, R. B. (1998). Interpreting magmatic fabric patterns in plutons. *Lithos* **44**, 53–82.

Pearce, J. A. (1975). Basalt geochemistry used to investigate past tectonic environments on Cyprus.

Tectonophysics **25**, 41–67.

Pearce, J. A. (1996). A user's guide to basalt discrimination diagrams. *Geological Association of Canada, Short Course Notes*, 79–113.

Pearce, J. A. (2008). Geochemical fingerprinting of oceanic basalts with applications to ophiolite classification and the search for Archean oceanic crust. *Lithos* **100**, 14–48.

Pearce, J. A. (2014). Immobile Element Fingerprinting of Ophiolites. *Elements* **10**, 101–108.

Pearce, J. A., Alabaster, T., Shelton, A. W. & Searle, M. P. (1981). The Oman Ophiolite as a Cretaceous Arc-Basin Complex: Evidence and Implications. *Philosophical Transactions of the Royal Society of London. Series A, Mathematical and Physical Sciences* **300**, 299–317.

Pearce, J. A. & Cann, J. R. (1971). Ophiolite Origin Investigated By Discriminant Analysis Using Ti, Zr And Y. *Earth and Planetary Science Letters* **379**, 339–349.

Pearce, J. A. & Cann, J. R. (1973). Tectonic setting of basic volcanic rocks determined using trace element analyses. *Earth and Planetary Science Letters* **19**, 290–300.

Pearce, J. A., Lippard, S. J. & Roberts, S. (1984). Characteristics and tectonic significance of supra-subduction zone ophiolites. *Geological Society Special Publication* **16**, 77–94.

Pearce, J. A. & Norry, M. J. (1979). Petrogenetic implications of Ti, Zr, Y, and Nb Variations in volcanic rocks. *Contributions to Mineralogy and Petrology* **69**, 33–47.

Pearce, J. A. & Stern, R. J. (2006). Origin of back-arc basin magmas: Trace element and isotope perspectives. *Geophysical Monograph Series* **166**, 63–86.

Perfit, M. R. & Chadwick, W. W. (1998). Magmatism at mid-ocean ridges: Constraints from volcanological and geochemical investigations. *Geophysical Monograph-American Geophysical Union* **106**, 59–116.

Peters, T. (2000). Formation and evolution of the western Indian Ocean as evidenced by the Masirah ophiolite: A review. *Geological Society of America Special Paper* **349**, 525–536.

Peters, T., Immenhauser, A., Mercolli, I. & Meyer, J. (1995). Geological map of Masirah North and Masirah South with Explanatory Notes. Sheet K768-North and Sheet K768-South, Scale 1:50,000. Directorate General of Minerals, Oman Ministry of Petroleum and Minerals, 80.

Peters, T. & Mercolli, I. (1997). Formation and evolution of the Masirah Ophiolite (Sultanate of Oman). *Ofioliti* **22**, 15–34.

Peters, T. & Mercolli, I. (1998). Extremely thin oceanic crust in the Proto-Indian Ocean: Evidence from the Masirah Ophiolite, Sultanate of Oman. *Journal of Geophysical Research: Solid Earth* **103**, 677–689.

Phethean, J. J. J., Kalnins, L. M., van Hunen, J., Biffi, P. G., Davies, R. J. & McCaffrey, K. J. W. (2016). Madagascar's escape from Africa: A high-resolution plate reconstruction for the Western Somali Basin and implications for supercontinent dispersal. *Geochemistry, Geophysics, Geosystems* **17**, 5036–5055.

Prell, W. L. & 117, S. P. of O. L. (1990). Neogene tectonics and sedimentation of the SE Oman continental margin: Results from ODP Leg 117. *Geological Society Special Publication* **49**, 745–758.

Price, R. C., Johnson, L. E. & Crawford, A. J. (1990). Basalts of the North Fiji Basin: the generation of back arc basin magmas by mixing of depleted and enriched mantle sources. *Contributions to*

Mineralogy and Petrology **105**, 106–121.

Putirka, K. D., Perfit, M., Ryerson, F. J. & Jackson, M. G. (2007). Ambient and excess mantle temperatures, olivine thermometry, and active vs. passive upwelling. *Chemical Geology* **241**, 177–206.

Rabinowitz, P. D., Coffin, M. F. & Falvey, D. (1983). The Separation of Madagascar and Africa. *Science*. American Association for the Advancement of Science **220**, 67–69.

Raitt, R. W. (1956). Seismic-Refraction Studies of the Pacific Ocean Basin: Part I: Crustal Thickness of the Central Equatorial Pacific. *Bulletin of the Geological Society of America* **67**, 1623–1640.

Reeves, C. V., Teasdale, J. P. & Mahanjane, E. S. (2016). Insight into the eastern margin of Africa from a new tectonic model of the Indian Ocean. *Geological Society Special Publication* **431**, 299–322.

Rioux, M., Bowring, S., Kelemen, P., Gordon, S., Dudás, F. & Miller, R. (2012a). Rapid crustal accretion and magma assimilation in the Oman-U.A.E. ophiolite: High precision U-Pb zircon geochronology of the gabbroic crust. *Journal of Geophysical Research: Solid Earth* **117**, 1–12.

Rioux, M., Bowring, S., Kelemen, P., Gordon, S., Miller, R. & Dudás, F. (2013). Tectonic development of the Samail ophiolite: High-precision U-Pb zircon geochronology and Sm-Nd isotopic constraints on crustal growth and emplacement. *Journal of Geophysical Research: Solid Earth* **118**, 2085–2101.

Rioux, M., Johan Lissenberg, C., McLean, N. M., Bowring, S. A., MacLeod, C. J., Hellebrand, E. & Shimizu, N. (2012b). Protracted timescales of lower crustal growth at the fast-spreading East Pacific Rise. *Nature Geoscience*. Nature Publishing Group **5**, 275–278.

Roberts, S., Andrews, J. R., Bull, J. M. & Sanderson, D. J. (1993). Slow-spreading ridge-axis tectonics: evidence from the Lizard complex, UK. *Earth and Planetary Science Letters* **116**, 101–112.

Rochette, P., Jenatton, L., Dupuy, C., Boudier, F. & Reuber, I. (1991). Diabase dikes emplacement in the Oman ophiolite: a magnetic fabric study with reference to geochemistry. *Ophiolite genesis and evolution of the oceanic lithosphere*. Dordrecht: Springer, 55–82.

Rodriguez, M. *et al.* (2020). Successive shifts of the India-Africa transform plate boundary during the Late Cretaceous-Paleogene interval: Implications for ophiolite emplacement along transforms. *Journal of Asian Earth Sciences*. Elsevier **191**, 104225.

Rodriguez, M., Huchon, P., Chamot-Rooke, N., Fournier, M., Delescluse, M. & François, T. (2016). Tracking the paleogene India-Arabia plate boundary. *Marine and Petroleum Geology*. Elsevier Ltd **72**, 336–358.

Roeder, P. L. & Emslie, R. F. (1970). Olivine-liquid equilibrium. *Contributions to Mineralogy and Petrology* **29**, 275–289.

Rosenberg, C. L. & Handy, M. R. (2005). Experimental deformation of partially melted granite revisited: Implications for the continental crust. *Journal of Metamorphic Geology* **23**, 19–28.

Ross, K. & Elthon, D. (1997). Cumulus and postcumulus crystallization in the oceanic crust: major- and trace-element geochemistry of Leg 153 gabbroic rocks. *Proceedings of the Ocean Drilling Program, Scientific Results* **153**, 333–350.

Rothery, D. A. (1983). The base of a sheeted dyke complex, Oman ophiolite: implications for magma chambers at oceanic spreading axes. *Journal of the Geological Society* **140**, 287–296.

Royer, J. Y., Chaubey, A. K., Dyment, J., Bhattacharya, G. C., Srinivas, K., Yatheesh, V. & Ramprasad, T. (2002). Paleogene plate tectonic evolution of the Arabian and Eastern Somali basins. *Geological*

Society Special Publication **195**, 7–23.

Rubin, K. H. & Sinton, J. M. (2007). Inferences on mid-ocean ridge thermal and magmatic structure from MORB compositions. *Earth and Planetary Science Letters* **260**, 257–276.

Salis, K. Von & Immenhauser, A. (1997). Mesozoic calcareous nannofossils from Masirah Island (Sultanate of Oman). *Journal of Nannoplankton Research* **19**, 95–101.

Sauter, D. *et al.* (2013). Continuous exhumation of mantle-derived rocks at the Southwest Indian Ridge for 11 million years. *Nature Geoscience*. Nature Publishing Group **6**, 314–320.

Sauter, D., Ringenbach, J. C., Cannat, M., Maurin, T., Manatschal, G. & McDermott, K. G. (2018). Intraplate Deformation of Oceanic Crust in the West Somali Basin: Insights From Long-offset Reflection Seismic Data. *Tectonics* **37**, 588–603.

Schlindwein, V. & Schmid, F. (2016). Mid-ocean-ridge seismicity reveals extreme types of ocean lithosphere. *Nature*. Nature Publishing Group **535**, 276–279.

Schouten, H. & Klitgord, K. D. (1982). The memory of the accreting plate boundary and the continuity of fracture zones. *Earth and Planetary Science Letters* **59**, 255–266.

Schreurs, G. & Immenhauser, A. (1999). West-northwest directed obduction of the Batain Group on the eastern Oman continental margin at the Cretaceous-Tertiary boundary. *Tectonics* **18**, 148–160.

Schroeder, T. & John, B. E. (2004). Strain localization on an oceanic detachment fault system, Atlantis Massif, 30°N, Mid-Atlantic Ridge. *Geochemistry, Geophysics, Geosystems* **5**, 1–30.

Searle, R. C., Cannat, M., Fujioka, K., Mével, C., Fujimoto, H., Bralee, A. & Parson, L. (2003). FUJI Dome: A large detachment fault near 64°E on the very slow-spreading southwest Indian Ridge. *Geochemistry, Geophysics, Geosystems*. Wiley-Blackwell **4**.

Segoufin, J. (1978). Anomalies magnétiques mésozoïques dans le bassin du Mozambique. *Comptes rendus de l'Académie des Sciences* **287**, 109–112.

Segoufin, J. & Patriat, P. (1980). Existence d'anomalies mesozoiques dans le bassin de Somalie. Implications pour les relations Afrique-Antarctique-Madagascar. *Comptes rendus de l'Académie des Sciences* **291**, 85–88.

Sempéré, J.-C., Lin, J., Brown, H. S., Schouten, H. & Purdy, G. M. (1993). Segmentation and morphotectonic variations along a slow-spreading center: The Mid-Atlantic Ridge (24°00' N–30°40' N). *Marine Geophysical Researches* **15**, 153–200.

Sempéré, J. & Cochran, J. R. (1997). The Southeast Indian Ridge between 88°E and 118°E: Variations in crustal accretion at constant spreading rate. *Journal of Geophysical Research: Solid Earth*. Wiley-Blackwell **102**, 15489–15505.

Seyler, M., Cannat, M. & Mé vel, C. (2003). Evidence for major-element heterogeneity in the mantle source of abyssal peridotites from the Southwest Indian Ridge (52° to 68°E). *Geochemistry, Geophysics, Geosystems* **4**, 1–33.

Seyler, M., Lorand, J. P., Dick, H. J. B. & Drouin, M. (2007). Pervasive melt percolation reactions in ultra-depleted refractory harzburgites at the Mid-Atlantic Ridge, 15° 20'N: ODP Hole 1274A. *Contributions to Mineralogy and Petrology* **153**, 303–319.

Seyler, M., Toplis, M. J., Lorand, J. P., Luguet, A. & Cannat, M. (2001). Clinopyroxene microtextures reveal incompletely extracted melts in abyssal peridotites. *Geology* **29**, 155–158.

Shackleton, R. M. & Ries, A. C. (1990). Tectonics of the Masirah Fault Zone and eastern Oman. *Geological Society Special Publication* **49**, 715–724.

Shackleton, R. M., Ries, A. C., Bird, P. R., Filbrandt, J. B., Lee, C. W. & Cunningham, G. C. (1990). The Batain Melange of NE Oman. *Geological Society Special Publication* **49**, 673–696.

Shaw, P. R. (1992). Ridge segmentation, faulting and crustal thickness in the Atlantic Ocean. *Nature* **358**, 490–493.

Shervais, J. W. (1982). Ti-V plots and the petrogenesis of modern and ophiolitic lavas. *Earth and Planetary Science Letters* **59**, 101–118.

Singh, S. C. *et al.* (2006). Discovery of a magma chamber and faults beneath a Mid-Atlantic Ridge hydrothermal field. *Nature* **442**, 1029–1032.

Singh, S. C., Carton, H., Chauhan, A. S., Androvandi, S., Davaille, A., Dyment, J., Cannat, M. & Hananto, N. D. (2011). Extremely thin crust in the Indian Ocean possibly resulting from Plume-Ridge Interaction. *Geophysical Journal International* **184**, 29–42.

Sinton, J. M. & Detrick, R. S. (1992). Mid-ocean ridge magma chambers. *Journal of Geophysical Research* **97**, 197–216.

Sinton, J. M. & Fryer, P. (1987). Mariana Trough lavas from 18°N: Implications for the origin of back arc basin basalts. *Journal of Geophysical Research* **92**, 12782–12802.

Sinton, J. M., Smaglik, S. M., Mahoney, J. J. & Macdonald, K. C. (1991). Magmatic processes at superfast spreading mid-ocean ridges: Glass compositional variations along the East Pacific Rise 13°–23°S. *Journal of Geophysical Research: Solid Earth*. Wiley-Blackwell **96**, 6133–6155.

Sisson, T. W. & Grove, T. L. (1993). Experimental investigations of the role of H2O in calc-alkaline differentiation and subduction zone magmatism. *Contributions to Mineralogy and Petrology* **113**, 143–166.

Smewing, J. D., Abbotts, I. L., Dunne, L. A. & Rex, D. C. (1991). Formation and emplacement ages of the Masirah ophiolite, Sultanate of Oman. *Geology* **19**, 453–456.

Smewing, J. D., Simonian, K. O. & Gass, I. G. (1975). Metabasalts from the Troodos Massif, Cyprus: Genetic implication deduced from petrography and trace element geochemistry. *Contributions to Mineralogy and Petrology* **51**, 49–64.

Smith, D. J. (2014). Clinopyroxene precursors to amphibole sponge in arc crust. *Nature Communications* **5**, 4329.

Smith, D. K. *et al.* (1995). Mid-Atlantic Ridge volcanism from deep-towed side-scan sonar images, 25°–29°N. *Journal of Volcanology and Geothermal Research* **67**, 233–262.

Smith, D. K. & Cann, J. R. (1993). Building the crust at the Mid-Atlantic Ridge. *Nature* **365**, 707–715.

Smith, D. K., Cann, J. R. & Escartín, J. (2006). Widespread active detachment faulting and core complex formation near 13°N on the Mid-Atlantic Ridge. *Nature* **442**, 440–443.

Sobolev, A. V & Shimizu, N. (1993). Ultra-depleted primary melt included in an olivine from the Mid-Atlantic Ridge. *Nature*. Nature Publishing Group **363**, 151–154.

Standish, J. J., Dick, H. J. B., Michael, P. J., Melson, W. G. & O'Hearn, T. (2008). MORB generation beneath the ultraslow spreading Southwest Indian Ridge (9-25°E): Major element chemistry and the importance of process versus source. *Geochemistry, Geophysics, Geosystems* **9**, 1–39.

Standish, J. J. & Sims, K. W. W. (2010). Young off-axis volcanism along the ultraslow-spreading

Southwest Indian Ridge. *Nature Geoscience*. Nature Publishing Group **3**, 286–292.

Staudigel, H. (2014). 4.16 - Chemical Fluxes from Hydrothermal Alteration of the Oceanic Crust. In: Holland, H. D. & Turekian, K. K. B. T.-T. on G. (Second E. (eds) *Treatise on Geochemistry: Second Edition*. Oxford: Elsevier, 583–606.

Staudigel, H., Gee, J., Tauxe, L. & Varga, R. J. (1992). Shallow intrusive directions of sheeted dikes in the Troodos ophiolite: anisotropy of magnetic susceptibility and structural data. *Geology* **20**, 841–844.

Steinmann, G. (1927). Die ophiolitischen zonen in den Mediterranean Kettengebirgen. *Compte-Rendu, XIVe Congrès Géologique International, 1926, Madrid, Gráficas Reunidas* **2**, 637–667.

Stephenson, A. (1994). Distribution anisotropy: two simple models for magnetic lineation and foliation. *Physics of the Earth and Planetary Interiors* **82**, 49–53.

Suhr, G., Hellebrand, E., Johnson, K. & Brunelli, D. (2008). Stacked gabbro units and intervening mantle: A detailed look at a section of IODP Leg 305, Hole U1309D. *Geochemistry, Geophysics, Geosystems* **9**, 1–31.

Sun, S. S. & McDonough, W. F. (1989). Chemical and isotopic systematics of oceanic basalts: Implications for mantle composition and processes. *Geological Society Special Publication* **42**, 313–345.

Tauxe, L., Gee, J. S. & Staudigel, H. (1998). Flow directions in dikes from anisotropy of magnetic susceptibility data: The bootstrap way. *Journal of Geophysical Research: Solid Earth* **103**, 17775–17790.

Thayer, T. P. (1969). Peridotite-gabbro complexes as keys to petrology of mid-oceanic ridges. *Geological Society of America Bulletin* **80**, 1515–1522.

Tolstoy, M., Harding, A. J. & Orcutt, J. A. (1993). Crustal Thickness on the Mid-Atlantic Ridge: Bull's-Eye Gravity Anomalies and Focused Accretion. *Science* **262**, 726–729.

Tucholke, B. E., Behn, M. D., Buck, W. R. & Lin, J. (2008). Role of melt supply in oceanic detachment faulting and formation of megamullions. *Geology* **36**, 455–458.

Tucholke, B. E., Lin, J. & Kleinrock, M. C. (1998). Megamullions and mullion structure defining oceanic metamorphic core complexes on the Mid-Atlantic Ridge. *Journal of Geophysical Research: Solid Earth* **103**, 9857–9866.

Upadhyay, H. D. & Neale, E. R. W. (1979). On the tectonic regimes of ophiolite genesis. *Earth and Planetary Science Letters* **43**, 93–102.

Varne, R., Brown, A. V. & Falloon, T. (2000). Macquarie Island: Its geology, structural history, and the timing and tectonic setting of its N-MORB to E-MORB magmatism. *Special Paper of the Geological Society of America* **349**, 301–320.

Vermeesch, P. (2018). IsoplotR: A free and open toolbox for geochronology. *Geoscience Frontiers* **9**, 1479–1493.

Vine, F. J. & Moores, E. M. (1972). A model for the gross structure, petrology, and magnetic properties of oceanic crust. *Studies in Earth and Space Sciences: A Memoir in Honor of Harry Hammond Hess*. Geological Society of America Boulder, Colorado 195–205.

Vuagnat, M. (1964). Remarques sur la Trilogie Serpentinites-Gabbros-Diabases dans le Bassin de la Méditerranée Occidentale. *Geologische Rundschau* **53**, 336–358.

Wakabayashi, J. & Dilek, Y. (2003). What constitutes “emplacement” of an ophiolite?: Mechanisms and relationship to subduction initiation and formation of metamorphic soles. *Geological Society Special Publication* **218**, 427–447.

Warren, C. J., Parrish, R. R., Waters, D. J. & Searle, M. P. (2005). Dating the geologic history of Oman’s Semail ophiolite: Insights from U-Pb geochronology. *Contributions to Mineralogy and Petrology* **150**, 403–422.

Warren, C. J., Searle, M. P., Parrish, R. R. & Waters, D. J. (2007). Reply to Comment by F. Boudier and A. Nicolas on “Dating the geologic history of Oman’s Semail Ophiolite: Insights from U-Pb geochronology” by C.J. Warren, R.R. Parrish, M.P. Searle and D.J. Waters. *Contributions to Mineralogy and Petrology* **154**, 115–118.

Warren, J. M. (2016). Global variations in abyssal peridotite compositions. *Lithos* **248**–**251**, 193–219.

Wendt, I. & Carl, C. (1991). The statistical distribution of the mean squared weighted deviation. *Chemical Geology* **86**, 275–285.

White, R. S., McKenzie, D. & O’Nions, R. K. (1992). Oceanic crustal thickness from seismic measurements and rare earth element inversions. *Journal of Geophysical Research* **97**, 19683–19715.

White, R. S., Minshull, T. A., Bickle, M. J. & Robinson, C. J. (2001). Melt generation at very slow-spreading oceanic ridges: Constraints from geochemical and geophysical data. *Journal of Petrology* **42**, 1171–1196.

White, S. M., Haymon, M. R., Fornari, D. J., Perfit, M. R. & Macdonald, K. C. (2002). Correlation between volcanic and tectonic segmentation of fast-spreading ridges: Evidence from volcanic structures and lava flow morphology on the East Pacific Rise at 9°–10°N. *Journal of Geophysical Research: Solid Earth*. Wiley-Blackwell **107**, EPM 7-1-EPM 7-20.

White, W. M. & Klein, E. M. (2014). 4.13 - Composition of the Oceanic Crust. In: Holland, H. D. & Turekian, K. K. B. T.-T. on G. (Second E. (eds) *Treatise on Geochemistry: Second Edition*. Oxford: Elsevier, 457–496.

Whitmarsh, R. B. (1974). Some aspects of plate tectonics in the Arabian Sea. *Initial Reports of the Deep Sea Drilling Project* **23**, 527–536.

Whitmarsh, R. B. (1979). The Owen Basin off the south-east margin of Arabia and the evolution of the Owen Fracture Zone. *Geophysical Journal of the Royal Astronomical Society* **58**, 441–470.

Wilkens, R. H., Fryer, G. J. & Karsten, J. (1991). Evolution of porosity and seismic structure of upper oceanic crust: importance of aspect ratios. *Journal of Geophysical Research* **96**, 17981–17995.

Wilson, S. C., Murton, B. J. & Taylor, R. N. (2013). Mantle composition controls the development of an Oceanic Core Complex. *Geochemistry, Geophysics, Geosystems* **14**, 979–995.

Winchester, J. A. & Floyd, P. A. (1977). Geochemical discrimination of different magma series and their differentiation products using immobile elements. *Chemical Geology* **20**, 325–343.

Wood, B. J. & Blundy, J. D. (1997). A predictive model for rare earth element partitioning between clinopyroxene and anhydrous silicate melt. *Contributions to Mineralogy and Petrology* **129**, 166–181.

Wood, B. J. & Virgo, D. (1989). Upper mantle oxidation state: Ferric iron contents of lherzolite spinels by 57Fe Mössbauer spectroscopy and resultant oxygen fugacities. *Geochimica et Cosmochimica Acta* **53**, 1277–1291.

Woodhead, J., Eggins, S. & Gamble, J. (1993). High field strength and transition element systematics in island arc and back-arc basin basalts: evidence for multi-phase melt extraction and a depleted mantle wedge. *Earth and Planetary Science Letters* **114**, 491–504.

Workman, R. K. & Hart, S. R. (2005). Major and trace element composition of the depleted MORB mantle (DMM). *Earth and Planetary Science Letters* **231**, 53–72.

Yu, Z. *et al.* (2018). Lithospheric Structure and Tectonic Processes Constrained by Microearthquake Activity at the Central Ultraslow-spreading Southwest Indian Ridge (49.2° to 50.8°E). *Journal of Geophysical Research: Solid Earth* **123**, 6247–6262.

Zhang, C., Koepke, J., France, L. & Godard, M. (2017). Felsic plutonic rocks from IODP Hole 1256D, Eastern Pacific: Implications for the nature of the axial melt lens at fast-spreading mid-ocean ridges. *Journal of Petrology* **58**, 1535–1566.

Zhang, S. Q., Mahoney, J. J., Mo, X. X., Ghazi, A. M., Milani, L., Crawford, A. J., Guo, T. Y. & Zhao, Z. D. (2005). Evidence for a widespread Tethyan upper mantle with Indian-Ocean-type isotopic characteristics. *Journal of Petrology* **46**, 829–858.

Zhou, H. & Dick, H. J. B. (2013). Thin crust as evidence for depleted mantle supporting the Marion Rise. *Nature* **494**, 195–200.

Zindler, A., Staudigel, H. & Batiza, R. (1984). Isotope and trace element geochemistry of young Pacific seamounts: implications for the scale of upper mantle heterogeneity. *Earth and Planetary Science Letters* **70**, 175–195.

Appendix I: Primary melt compositions for MELTS modelling

An average primary melt composition was estimated from the major element compositions of Masirah dykes and lavas (Chapter 4). Each individual major and minor element oxide was plotted against Mg# and a regression was made for each array to determine its composition at Mg# = 0.72. Iron was regressed as $Fe_2O_3^T$ and then split into FeO and Fe_2O_3 using $Fe^{3+}/Fe_{sum} = 0.12$. Water content was set at 0.2 wt%. Due to the non-linear nature of the liquid lines of descent for many elements, resulting from the changes in slope as plagioclase and clinopyroxene appear as stable phases on the liquidus, numerical regressions through the data are inherently inaccurate. Instead, a visual inspection of the data was used to obtain petrologically realistic regressions.

By examining the scatter in the dyke and lava trends for Ca, Na, Al and Si, it was found that samples that tended to have elevated CaO, also had elevated Al_2O_3 and lowered Na_2O and SiO_2, and vice versa. This trend was not found to be controlled by crystal accumulation and was interpreted as related to primary melt composition. To explore the effect of Ca-Na variations in the primary melt on the plagioclase crystal line of descent, a 'calcic' and 'sodic' primary melt was derived using a similar regression technique as for the average primary melt. For Ca, Na, Al and Si, however, instead of taking an average through the data, the upper and lower bounds of the scatter were regressed to obtain a calcic melt (high CaO and Al_2O_3, low Na_2O and SiO_2) and a sodic melt (low CaO and Al_2O_3, high Na_2O and SiO_2). The scatter likely results from a combination of primary magmatic processes and alteration effects. By regressing the upper and lower bounds of the scatter, a maximum of the permissible variation in primary compositions is obtained.

The visual regressions resulted in totals of 100.24 wt% (average melt composition), 99.81 wt% (calcic melt) and 100.09 (sodic melt), lending some confidence to the applied method. Oxide contents were subsequently normalised to totals of 100 wt% for MELTS modelling (Table A1).

Table A1. Masirah primary melt composition estimates from major element versus Mg# regressions

	Average melt	Calcic melt	Sodic melt	Normalised to 100%		
	(1)	(2)	(3)	(1)	(2)	(3)
SiO_2	49	47.2	50.7	48.88	47.29	50.66
TiO_2	1	1	1	1.00	1.00	1.00
Al_2O_3	17.2	18.15	16.1	17.16	18.19	16.09
FeO	6.65	6.65	6.65	6.64	6.66	6.65
Fe_2O_3	1.01	1.01	1.01	1.01	1.01	1.01
MnO	0.135	0.135	0.135	0.13	0.14	0.13
MgO	9.9	9.9	9.9	9.88	9.92	9.89
CaO	11.8	12.9	10.3	11.77	12.93	10.29
Na_2O	3	2.32	3.75	2.99	2.32	3.75
K_2O	0.17	0.17	0.17	0.17	0.17	0.17
P_2O_5	0.12	0.12	0.12	0.12	0.12	0.12
Cr_2O_3	0.05	0.05	0.05	0.05	0.05	0.05
H_2O	0.2	0.2	0.2	0.20	0.20	0.20
Total	**100.24**	**99.81**	**100.09**	**100.00**	**100.00**	**100.00**
Mg#	0.726	0.726	0.726	0.726	0.726	0.726
Ca#	0.754	0.603	0.685	0.754	0.603	0.685